Characterizing Degradation in Organic Redox Flow Batteries

by

Charlotte Clegg

Submitted in partial fulfilment of the requirements

for the degree of Doctor of Philosophy

at

Dalhousie University

Halifax, Nova Scotia

December 2022

Table of Contents

*

List of Tables

List of Figures

Abstract

Organic redox flow batteries (ORFB)s are a promising energy storage technology that may facilitate the grid-integration of renewable energy. ORFB development is challenged by poor calendar lifetime and cycling stability. Currently, the most promising ORFB electrolytes are projected to last several years (whereas lifetimes must exceed 10 years to be feasible for grid-level storage) [1–3]. The majority of ORFB literature focuses on the development of stable redox molecules, which is crucial to extending cell lifetimes. However, electrode properties are known to significantly impact cell performance. Therefore, it is equally important to understand how the electrodes are affected by cell degradation.

This thesis aims to understand how electrode properties change with cycling in promising ORFB systems. We used a combination of electrochemical and spectroscopic methods to characterize changes to cycled cell components. These methods were developed on non-aqueous vanadium(III) acetylacetonate flow cells, which were used to validate our experimental set-up [4]. We employed this methodology to further examine an anthraquinone derivative (2,6-DPPEAQ) and potassium ferrocyanide as a model aqueous system, which was previously developed by Ji *et al.* [2]. We also examined a non-aqueous phenothiazine and viologen system, which was developed by Professor Odom and co-workers [5,6]. The temperature sensitivity of the non-aqueous system was also explored at 0, 25 and 40 °C.

Despite the exceptional chemical stability reported (and observed) for the aqueous electrolytes, a concerning loss in energy efficiency was observed with charge-discharge cycling. The performance loss is correlated with growth in charge-transfer resistance observed in full-cell impedance spectra during cycling. X-ray photoelectron spectroscopy (XPS) did not reveal significant foreign material on the cycled electrodes; however, systemic changes in oxygen bonding environment were observed, which may explain the observed performance loss.

In the non-aqueous system, stable cell capacity was observed at room temperature; whereas, rapid capacity loss was observed at 0 and 40°C. XPS revealed considerable accumulation of foreign material on electrodes cycled at 25 and 40 °C, including unexpected electrolyte impurities. Separator fouling was also observed, and correlated with reduced separator porosity and self-discharge current, which results in increased coulombic and energy efficiency with cycling.

List of Abbreviations and Symbols Used

Abbreviations

a	Exponent accounting for XPS analyzer configuration (given in manufacturer specifications)
I_A	Integrated peak intensity (used in XPS analysis)
R_A	Relative sensitivity factor
$T(\text{KE})$	Analyzer transmission function for electrons detected with kinetic energy KE
X_A	Percentage atomic concentration of an element (A)
2,6-DPPEAQ	(((9,10-dioxo-9,10-dihydroanthracene-2,6-diyl)bis(oxy)) bis(propane-3,1-diyl))bis(phosphonic acid)
Ag/Ag$^+$	Silver/silver ion (non-aqueous) reference electrode
Ag/AgCl	Silver/silver chloride (aqueous) reference electrode
AgNO$_3$	Silver nitrate
ATR	Attenuated total reflectance

BE	Binding energy	eV
CE	Coulombic efficiency	
CE	Counter electrode	
CEM	Cation exchange membranes	
CLS	Capacity limiting side	
CO_2	Carbon dioxide	
CPE	Constant phase element	
CV	Cyclic voltammetry	
DRT	Distribution of relaxation times	
ECSA	Electrochemically active surface area	
EE	Energy efficiency	
EES	Electrochemical energy storage	
EIS	Electrochemical impedance spectroscopy	
ETC	Environmental testing chamber	
FTIR	Fourier transform infrared spectroscopy	
GCE	Glassy carbon electrode	
H NMR	Nuclear magnetic resonance	
IEMs	Ion exchange membranes	
IR	Infrared	
KCl	Potassium chloride	

KE	Kinetic energy	eV
KE_A	Kinetic energy measured by XPS analyzer	eV
KOH	Potassium hydroxide	
LIBs	Lithium-ion batteries	
MAP	*Maxiumum a priori* distribution	
MEEPT	10-[2-(2-methoxyethoxy)- ethyl]-10H-phenothiazine	
MEEV	bis[2-(2-methoxyethoxy)ethyl]viologen bis(bis(trifluoromethane sulfonyl)imide)	
NPW	Nanopure water	
O	Oxygen	
OCV	Open-circuit voltage, equivalently OCP (open-circuit potential)	
ORFB	Organic redox flow battery	
OSFs	Oxygen surface functionalities	
PAN	Polyacrylnitride	
Pt	Platinum	
RBF	Radial basis function	
RE	Reference electrode	
RFB	Redox flow battery	
SE	Supporting electrolyte	
SEM	Scanning electron microscopy (or microscope)	

SHE	Standard hydrogen electrode
SOC	State-of-charge
TEABF$_4$	Tetraethylammonium tetrafluoroborate
TEATFSI	Tetraethylammonium bis(trifluoromethanesulfonyl)imide
UHV	Ultra-high vacuum
V(acac)$_3$	Vanadium(III) acetylacetonate
VE	Voltage efficiency
VO(acac)$_2$	Vanadyl acetylacetonate
WE	Working electrode
XPS	X-ray photoelectron spectroscopy

Symbols

$[Ox_{+/-}]$	Concentration of oxidized species in the positive or negative half-cell	
$[Red_{+/-}]$	Concentration of reduced species in the positive or negative half-cell	
α	Exponent describing the magnitude of the phase response for a constant phase element	
ΔE_p	Separation between the anodic and cathodic peak potentials (used in CV)	V
$\Delta V_{c/d}$	Change in cell voltage at the end of each charge discharge step	V
η	Overpotential	V

ω	EIS perturbation frequency	$\mathrm{rad\,s^{-1}}$
σ	The Warburg diffusion coefficient	
A	Electrode geometric surface area	$\mathrm{m^{-2}}$
C_{dl}	Double layer capacitance	F
$C_{o/r}$	Concentration of oxidized or reduced electrolyte species	
$D_{o/r}$	Diffusion coefficient of oxidized or reduced species	
E	Working electrode poential	V
E^0	Standard reduction potential of an electrochemically active species	V
$E^{0\prime}$	Formal reduction potential specific to the experimental conditions (used in CV)	V
E_1	Starting potential (used in cyclic voltammetry)	V
E_+^0	Standard reduction potential for positive half-cell	Volts
E_-^0	Standard reduction potential for negative half-cell	Volts
$E_{p,a}$	Anodic peak potential (used in CV)	V
$E_{p,c}$	Cathodic peak potential (used in CV)	V
F	Faraday constant, 96485	$\mathrm{C\,mol^{-1}}$
i	Charging current	A
i_p	Peak current	A
n	Number of electrons involved in a charge-transfer reaction	

$Q_{t,+/-}$	Theoretical capacity of the positive and negative half-cells Coulombs	
R	Universal gas contant, 8.314	$\mathrm{J\,K^{-1}\,mol^{-1}}$
R_{cell}	Internal cell resistance	Ω
R_{ct}	Charge-transfer resistance	Ω
R_s	Series resistance	Ω
T	Temperature	K
t	Time	s
v	Scan rate (used in cyclic voltammetry)	$\mathrm{V\,s^{-1}}$
$V_{+/-}$	Electrolyte volume in the positive or negative half-cell	L
Z'	Real component of complex impedance (Re[Z])	Ω
Z''	Imaginary component of complex impedance (Im[Z])	Ω
Φ_{A}	Analyzer workfunction	eV
Φ_{S}	Sample workfunction	eV
T	Magnitude of response for a constant phase element	

Acknowledgements

First, I want to express a deep thank you to my supervisor Professor Ian Hill. This work would not be possible without your advice and feedback. Over the years your tuition has taught me to develop effective research plans and think more critically about my work, and I will leave Dal as a better researcher because of it. Just as importantly, I want to thank you for your professional advice, understanding and accommodation of different mentorship needs.

I also want to thank my examining committee: Professors Heather Andreas, Jeff Dahn, and Fikile Brushett for volunteering your time to review this work, and attend our meetings and exams throughout the years. Your constructive criticism and insights have been extremely helpful for project development and writing. Thank you as well Jeff for sharing your lab and equipment with us, which allowed us to begin and complete these studies. As well, thank you Dr. Brushett for sharing your knowledge and cell design with us – your visit to Dal was a well-timed answer to our problems with leaky cells and faulty designs.

The work presented in Chapter 7 would not be possible without our colleagues at the University of Kentucky: Professor Susan Odom, Dr. Aman Kaur, and PhD student Rahul Jha. Rahul kindly lent his time to synthesize the negative electrolyte material required for this investigation, and provided counselling for many experimental details.

I am also very grateful for all the assistance provided by the technical staff in the department (Michel Johnson, Andrew George, Kevin Borgel and John Noddin), who helped me with various characterization techniques and machine shop tasks. A special thank you also to Tanya Timmins (who treats every student like family) and makes sure we all meet our FGS deadlines.

Finally, I need to thank my family for supporting my decision to take this journey; and, both my colleagues and friends from the lab, physics department, and beyond: Ajan Ramachandran, Chris Sutherland, Brandon Taylor, Malachy Maguire, Eric Bergmann, Ryan Ambrose, Sam March, Irina Valitova, Lexie Mitchell, Chris Lee, Elizabeth Lawrence and especially Luke Knopp. Thank you for letting me complain to you after many a failed experiment. Your encouragement and friendship outside of work have been invaluable.

Chapter 1

Introduction

1.1 Background

Since the industrial revolution global energy consumption has skyrocketed, reaching approximately 160,000 TWh in 2020 (Figure 1.1a). These needs are primarily met through fossil fuel combustion, which has caused the atmospheric carbon dioxide (CO_2) concentration to nearly double in the last 200 years (Figure 1.1b). There are strong motivators to transition away from fossil fuels: mean global temperatures have risen by 1.1 ºC (and are expected to exceed 1.5 ºC without further intervention [7]); air pollution from fuel combustion causes an estimated 3.6 million premature deaths each year [8]; and, global events and supply chain issues lead to volatile oil prices, and inequity in its availability between high- and low- income countries.

Transitioning towards a renewable energy economy is essential to combat these problems. The cost of renewable energy has dropped significantly in the last decade due to increased production and efficiency [9]. Figure 1.1c shows the levelized cost of renewable energy compared to conventional production methods in 2009 and 2019. (Levelized cost refers to the average price per unit of electricity that would be required for a generating plant to "break-even" with its capital and operational investments). Even without subsidies, photovoltaic and wind energy is cheaper than that produced
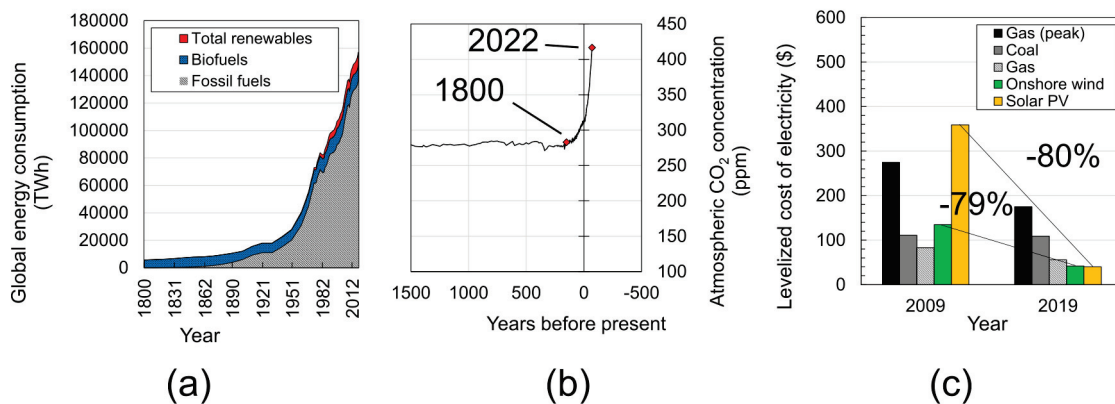
Figure 1.1: Figure showing the annual global energy consumption provided by renewable sources compared to fossil fuels is shown in (a). The measured atmospheric carbon dioxide concentration is shown in (b). (By convention "years before present" is referenced with respect to 1950, the origin of practical radiocarbon dating.) The levelized cost of renewable energy in 2009 and 2019 is shown in (c). Gas (peaker) refers to power plants that are run to supply electricity during times of peak demand.

by fuel combustion [9, 10]. In 2019, renewable energy accounted for nearly 17.3 % of Canada's energy production (approximately 60 % from hydroelectricity); globally, this figure was up to 13 % [9, 10]. This is an improvement over previous decades, but deployment of renewable energy generators must increase considerably to meet net-zero CO_2 emissions targets by 2050.

1.1.1 Redox flow batteries for energy storage

Supply intermittency remains the largest impediment to grid-scale integration of solar and wind energy. A safe, low-cost and efficient form of energy storage is needed to address this problem. Electrochemical energy storage (EES) is a flexible option to address this need. Lithium-ion batteries (LIBs) represent the current state-of-the-art for EES, and are now ubiquitous in portable electronics and electric vehicles. However, there is concern that material scarcity and high costs will limit their widespread deployment for grid-level storage.

Redox flow batteries (RFB)s are a possible alternative. Vanadium redox flow bat-

teries are recognized as the current state-of-the-art flow battery technology – several systems already operate at a commercial level. In 2005, a 4 MW/6 MWh demonstration facility was installed by Sumitomo Electric Industries at Subaru Wind Farm in Hokkaido, Japan [11]. The system was reported to demonstrate stable and safe operation for wind energy storage and power output stabilization (270,000+ cycles) over a three year period [12]. Since then, Sumitomo has installed numerous systems internationally [13], and has been contracted to supply Hokkaido Electric Power Network Inc. with 51 MWh/17 MW vanadium RFB storage systems for grid expansion [14]. The scale of vanadium RFB facilities has increased over the last couple of decades; in 2022, Rongke Power began construction of the largest vanadium RFB system (a 200 MW/800 MWh facility) in Dailan, China [15].

1.2   Inside a flow battery: structure and operation

Unlike other rechargeable batteries, energy in RFBs is stored in a liquid electrolyte, which is housed in reservoirs outside the cell (Figure 1.2). During charging, the electrolyte flows between the reservoirs and a porous carbon electrode inside the cell. An applied current (or voltage) drives redox reactions to change the oxidation state of the negative and positive electrolyte (negolyte and posolyte, respectively), thus storing electrochemical energy in the electrolyte. During discharge these reactions proceed spontaneously in reverse. A separator, or selective membrane keeps the active electrolytes separated, but allows ions from the supporting electrolyte (SE) to pass freely. The supporting electrolyte does not participate in charge-storage reactions. Its main purpose is to maintain charge neutrality, and improve ionic conductivity in the cell (which lowers solution resistance and improves the voltage efficiency).

Separation of the electrolyte storage from the cell body allows the energy and power capabilities of RFBs to scale independently, which is beneficial for large-scale energy storage. The energy capacity is determined by the reservoir volume and elec-

trolyte concentration, while the power capabilities are determined by the active area of the cell body. Using a liquid electrolyte to store energy has the drawback of reduced energy density; however, in stationary storage applications this disadvantage is less compromising. Table 1.1 compares the energy density and other key features of RFBs to LIBs and other promising grid energy storage technologies.
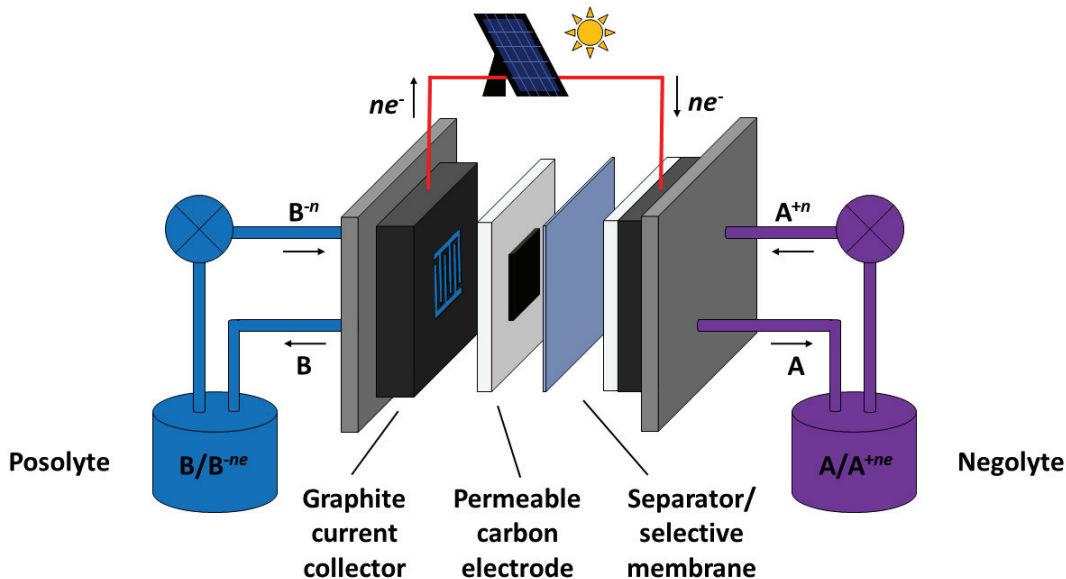
Figure 1.2: Schematic depicting the components and charging process for a redox flow battery. (Discharging operates in reverse).

Vanadium flow batteries are the most technologically developed system, but the relatively low abundance and high cost of vanadium is expected to limit deployment of this technology. With further development, organic electrolytes may offer a suitable alternative as they are created from low-cost, earth-abundant materials. In addition, the properties of organic species (solubility, reduction potential, kinetics, stability and number of oxidation states) can be tuned with careful molecular design.

The majority of ORFB research in the last few years has focused on the development of aqueous electrolytes; however, interest in non-aqueous systems is steadily growing. Non-aqueous solvents afford a higher electrochemical stability window than

water. In theory, cell potentials up to $4 - 5$ V are achievable (contrasted with 1.5 V for water), which could enable higher energy density systems [16–20]. Other benefits of non-aqueous RFBs include a wider operating temperature range and fast charge-transfer kinetics. However, these advantages are balanced by increased solvent cost, toxicity, flammability and lowered electrolyte conductivity compared to aqueous electrolytes [16, 17, 21].

1.3 Challenges facing organic RFBs

Two major issues must be addressed to develop commercially relevant organic redox flow battery (ORFB) systems: (1) material and component costs must be minimized to reach economically attractive targets [16, 22]; and, (2) electrochemical and chemical lifetimes must be improved. The U.S. Department of Energy suggests a capital cost target of $100-120/kWh for new energy storage systems [22, 23]. This figure represents an "allowable" upper limit on capital investment such that the cost of stored energy per kilowatt hour (kWh) will match the cost of electricity over a system's operational lifetime. These aggressive targets reflect the cheap price of electricity in North America. Techno-economic studies suggest that aqueous ORFBs can meet these targets with further development [12, 16, 17, 24]. A parameter space bounded by high cell voltage $(1 - 1.5$ V), low molecular weight (150 g (mol e)$^{-1}$) and high solubility $(1 - 2$ M) is recommended to maintain low aqueous systems costs [16, 17]. Non-aqueous RFBs should achieve higher cell voltages (3 V) and solubility targets (4 − 5 M) to offset the higher solvent costs.

Improving cell stability and chemical lifetimes will also contribute to lower systems costs. Many studies continue to push the frontiers of electrolyte stability; but, until recently have focused primarily on the discovery or design of stable electrolyte species [2, 3, 6, 25–30]. The last two years have seen new studies undertaking a more wholistic examination of how factors such as ambient atmosphere and cycling protocols affect

cell stability [31–34]. Adding to this body of knowledge will facilitate the design of new materials, or cycling protocols to extend ORFB lifetimes.

Table 1.1: Table comparing key features of major energy storage technologies. Figures are taken from references: [12, 35–39]. *Note that the indicated lifetimes do not reflect the maintenance/servicing requirements for the marked technologies.

Method	Power rating (MW)	Capital Cost ($/kWh)	Energy efficiency (%)	Lifetime (yrs)	Energy density (Wh/L)	Limitations
Vanadium RFBs	kW − MW	180 − 400	75 − 85	> 10*	25 − 35	Lower energy density and requires more supporting equipment
Lithium-ion	kW − MW	110	> 90	10 − 20+	350 − 780	Material abundance
Lead acid	kW − MW	350 − 900	70 − 76	5 − 10	80	Low to medium energy density, poor deep discharge performance
Compressed air	MW - GW	50 − 200	60 − 79	10 − 30*	5	Special geographic requirements
Pumped hydro	MW - GW	80 − 200	70 − 85	30*	1	Specific geographic requirements

1.4 Thesis objectives

Until recently little has been done to understand the degradation at electrode interfaces in ORFBs. It is well understood that the properties of carbon electrodes affect the electronic, kinetic and mass-transport properties in RFBs, which impact the overall cell performance [40–49]. For example, Sun *et al.* investigated the effect of heat and acid treatments on the properties of carbon felt electrodes for use in vanadium RFBs [50, 51]. Both treatments were found to significantly improve cell performance. These effects were correlated with increased physical wetting and a higher density of oxygen functional groups on the electrode surface. Understanding how these properties change with cycling will be important to maintaining long-term cell performance. Studies by Nibel *et al.*, Derr *et al.* and some others have characterized changes in the properties of vanadium RFB electrodes after extended cycling [52–56]; however, to our knowledge comprehensive studies examining electrode degradation have not been performed in ORFBs.

This thesis aims to develop a holistic understanding of degradation in promising ORFB systems. Specifically, we plan to: (1) identify sources of capacity loss; and, (2) characterize the degradation of key cell components (specifically impedance growth at the membrane/separator and electrodes). Because both aqueous, and non-aqueous chemistries have unique advantages, we will examine a promising system for each. As an aqueous ORFB, we will examine the use of an anthraquinone derivative (as a negolyte) paired with a standard potassium ferrocyanide posolyte. This system uses a near pH-neutral electrolyte, and is reported to show outstanding chemical stability [2]. A viologen (negolyte)/phenothiazine (posolyte) system will be examined as an example of a non-aqueous chemistry in acetonitrile. This system has been demonstrated stable cycling in acetonitrile for up to 100 cycles [5]; however, degradation of the electrodes and separator were not characterized (likewise for the aqueous chemistry). Details regarding the selected electrolytes are provided in the following chapter.

1.5　Outline of the thesis

The aim of this chapter was to frame our research objectives with regards to the main challenges facing ORFB development. The following chapter focuses on a literature review of RFB electrode properties, and four promising electrolyte molecules that are examined in Chapters 6-7. A brief survey of studies characterizing the effect of electrode properties on RFB cell performance are also summarized. The intention of Chapter 2 is to establish context for the results discussed in Chapters 5-7.

Chapter 3 discusses the theory behind common flow battery performance metrics in the context of cell cycling and stability. A background to relevant electrochemical, spectroscopic and thermal characterization techniques is also given with the context of understanding changes in the properties of cycled cell components. The experimental methods used to build, cycle and characterize three different flow battery systems are detailed in Chapter 4. The described methods are applied to a proof-of-concept flow battery using a non-aqueous vanadium (III) acetylacetonate electrolyte. Although not extensively studied in the literature, this chemistry was selected for its assumed simplicity, and was used to validate our experimental set-up in comparison to existing publications. This system was used to explore different electrochemical and spectroscopic techniques to characterize changes to the electrodes and electrolyte *ex situ* after cycling. The background and results from this study are presented in Chapter 5.

The same methods are used in Chapter 6, to evaluate the critical factors which limit the lifetime and operation of RFBs using an aqueous anthraquinone derivative (2,6-DPPEAQ) (((9,10-dioxo-9,10-dihydroanthracene-2,6-diyl)bis(oxy)) bis(propane-3,1-diyl))bis(phosphonic acid) as a negolyte. This molecule was previously paired with a standard potassium ferro/ferricyanide posolyte to show outstanding molecular stability under relevant cycling conditions [2]. In this work, we focus on understanding the evolution of cell impedance with cycling, and develop an informed equivalent

circuit model to account for the observed changes. Changes to the three major cell components (electrodes, electrolyte and membrane) are characterized *ex situ* after cycling in comparison to uncycled samples.

In Chapter 7 we examine the cycling performance of a novel non-aqueous organic system, which employs a phenothiazine (MEEPT) and a viologen (MEEV) derivative as the posolyte and negolyte, respectively. Similar to the aqueous system, we monitor the evolution of cell impedance with cycling. Interestingly, we observe improvements in certain efficiency metrics. Changes to the three major cell components are characterized *ex situ* after cycling in comparison to uncycled samples. The effect of ambient temperature on cycling performance and stability is evaluated at room temperature, 40 °C and 0 °C.

General trends and conclusions derived from Chapters 5 – 7 are presented in Chapter 8. These observations are used to outline recommendations for future study.

Chapter 2

Literature Review

2.1 Electrodes and electrode properties

Fibrous carbon paper or felt electrodes are almost universally used in RFB literature, owing to their high fluid permeability, specific surface area, electrochemical activity, conductivity and low cost [57]. Carbon electrodes also offer a strong chemical resistance and large overpotential for water-splitting reactions, which makes it a preferred material in aqueous systems [57, 58]. Carbon electrodes for RFBs are manufactured in a variety of forms, including paper, felt and woven cloth. Cell designs using carbon paper ($100 - 300 \ \mu$m thick) electrodes have become a preferred choice for RFB systems in the last decade due to reductions in ohmic and mass-transport losses [59]. Electrolyte convection through the thin carbon paper electrodes is facilitated by an adjacent flow field (as depicted in Figure 1.2). Graphite felt electrodes ($\sim$ 3 mm thickness) were used primarily in vanadium RFB literature. Electrolyte convection through graphite felt electrodes was primarily achieved by directing electrolyte flow in the felt plane. Growing research in the last two years has led to increased interest in woven carbon cloth electrodes for ORFBs due to its improved electrolyte transport properties [43, 60, 61]. The following subsections outline the effects of electrode pre-treatment, microstructure and precursor material on flow cell performance.

2.1.1 Pre-treatment effects

In 1991, the Sun *et al.* described the effects of thermally and chemically treated graphite felt on vanadium RFB performance [50, 51]. Heating the electrodes at 400 °C in air was observed to significantly reduce cell polarization resistance compared to untreated samples. As a result the cell energy efficiency increased from 78 % (untreated) to 88 % (treated). The heat treated electrodes exhibited improved electrode wetting, and increased surface oxygen content (specifically phenolic C-OH functional groups) as measured by XPS. The oxygen surface functionalities (OSFs) were hypothesized to facilitate electron transfer for the V(IV)/V(V) (dis)charge reactions, thereby lowering the cell activation overpotential [50]. The authors also found that boiling electrodes in 90 % H_2SO_4 for 5 hours also reduced the cell polarization resistance, resulting in 91 % energy efficiency (compared to 78 % for the untreated cell) [51]. The improved cell performance was similarly correlated with enhanced wetting and increased OSFs (determined by XPS).

Since the original publications by Sun *et al.* there has been unanimous agreement that thermal (and other) pre-treatment methods yield improved electrode performance; however, the origin of improvement is debated. Like Sun *et al.*, many other authors attribute the improved performance to functionalization of the carbon surface with oxygen-containing groups [45, 46, 50, 62–65]. Other theories include increased graphitic edge site concentration [46, 49, 66–68], improved electrode wetting [68], increased electrochemically active surface area (ECSA) [45, 62, 63, 65], or some combination of these mechanisms.

In 2018 Greco *et al.* published a comprehensive study investigating thermal treatment effects on electrode properties [42]. Electrode capacitance and ECSA of typical RFB electrodes increased after treating at 400 °C in air for 30 hours. Above 400 °C, however, the electrode areal density, capacitance and ECSA decreased steadily with temperature. In contrast, the surface oxygen content observed by XPS steadily

increased. Improved electrode wetting was also observed for the thermally treated samples. Vanadium flow batteries assembled with heat treated electrodes were used to measure cell performance, electrochemical impedance spectroscopy (EIS) and polarization curves. Charge-transfer, mass-transfer (and total) cell resistance observed by EIS were significantly lowered for treated electrodes. The exchange current density determined from polarization curves was used to estimate a rate constant for cells assembled with each type of electrode. The rate constants (normalized to ECSA) were observed to increase linearly with the oxygen to carbon ratio (and treatment temperature). However, the reduction in ECSA at higher treatment temperatures was observed to reduce the overall exchange current density – resulting in a trade-off in cell performance. The maximum exchange current density and cell energy efficiency (80 %) were recorded using electrodes treated at 450 °C in air.

2.1.2 Effects of physical structure

In addition to electrode surface chemistry (see above), the physical microstructure of electrodes can significantly impact cell operation. In addition to facilitating redox reactions, electrodes must enable facile liquid transport throughout the entirety of the cell to supply (and remove) reactants (and products) from the electrode surface. Understanding the mass-transport limitations for different electrodes has become recognized as an important limiting factor in RFB performance [69–73]. Some authors have studied the effects of engineered electrode modifications such as perforation by CO_2 lasers [74], or KOH pitting treatments [57, 75, 76]. In both cases, the authors ascribed performance enhancements to broadened pore sizes, which increased electrolyte accessibility through the electrode structure.

In 2019 Forner-Cuenca *et al.* performed a systematic investigation into the effect of electrode microstructure on electrochemical performance for a range of commercially available carbon paper, felt and woven cloth electrodes. Electrode porosity,

microstructure and pressure drop under operating conditions were evaluated for a range of samples. The woven carbon cloth electrodes were found to exhibit the lowest charge-transfer and mass-transfer resistance under a range of operating conditions (in comparison to felt and paper electrodes). The improved performance was hypothesized to result from the bimodal pore size distribution characteristic of the carbon cloth weave. In particular, large and regularly spaced through-plane pores (from the weave pattern) result in low hydraulic and mass-transfer resistances – thereby enabling rapid electrolyte replenishment to smaller microscopic pores on the fibre surfaces [43]. These results are consistent with other studies, which conclude that large pores are needed to facilitate reactant transport throughout the electrode (despite the side-effect of reduced surface area) [73, 75, 76]. Because of these findings the last two years have seen increased interest in employing cloth structured carbon electrodes in ORFBs with kinetically facile redox reactions [43, 60, 61, 77]. While understanding changes in electrode structure are not the focus of this thesis, it is important to recall that changes in these structural properties may impact cell performance during ageing.

2.1.3 Electrode precursors

Carbon electrodes are commonly made from carbonized or graphitized polyacrylamide (PAN) or Rayon (cellulose) fibres. Electrode precursor has been found by several authors to influence the electrochemical activity for vanadium redox reactions. Zhong *et al.* report reduced electrical resistivity and preferential formation of C–O bonds (over C=O) for PAN-based electrodes in comparison to those made with Rayon precursors [78]. Schweiss *et al.* showed that in non-graphitic carbon fibers, PAN-based electrodes showed higher H_2 evolution rates compared with Rayon-based felts [79]. Understanding the effect of electrode precursors on cell performance is beyond the scope of this thesis; however, it is worth considering in the context of understanding

electrode impacts on cell performance (and possibly stability).

2.1.4 Electrode changes with cycling/ageing

Electrode pre-treatment methods are known to yield improved electrochemical performance (section 2.1.1); however, long-term cycling of vanadium RFBs has revealed significant losses in electrode performance over time [52, 53, 55, 80, 81]. Theories accounting for the performance loss include: reduction of electrochemically active surface area [54], electrode pitting [52], and increased oxygen surface functionalities (OSFs) [52–54, 81] (some of which are suggested to result from competing hydrogen evolution reactions [48, 79, 82]).

A consensus regarding the main characteristics of electrode degradation has not yet been reached. Rudolph *et al.* reported that extended cycling of vanadium RFBs caused a loss of OSFs (especially at the negative electrode), which led to increased polarization resistance [83, 84]. In contrast, other studies report an increase in OSFs at the negative [81, 85] and positive electrodes [52, 53, 55] after extended cycling. Increased OSFs at positive electrodes were generally linked to high state-of-charge conditions; however, Pezeshki *et al.* suggest that oxygen content alone cannot sufficiently explain degradation in electrochemical performance [55]. Indeed, Derr *et al.* showed that electrolyte exposure alone can cause significant changes in OSF concentration and loss of electrode capacitance, even without electrochemical cycling [54]. It remains likely that a combination of factors are responsible for lost electrochemical performance, including: changes in OSF content [52, 53, 53], damage to carbon fibers [52, 53], loss of electrode capacitance [54], and changes to relative fraction of ordered and disordered graphitic domains [52, 80].

A major limitation of electrode degradation studies thus far is the difficulty in drawing conclusions from a wide variety of complex commercial electrodes (often with proprietary materials composition). Carbon papers, for example, can be manu-

factured using different techniques, which may produce widely varied electrode morphologies [43]. Electrodes purchased from different manufacturers will exhibit notable changes in physical properties [43]. Recently, Taylor *et al.* characterized electrode degradation using a simplified set of samples – discs of edge and basal plane graphite [80]. Extended cyclic voltammetry performed in vanadium solutions was observed to diminish electrochemical reversibility in both samples, with a greater impact observed on the basal plane electrode. Both samples showed significant loss of OSFs after cycling, although the basal plane surface showed the greatest loss. The basal plane electrode also exhibited a notable loss of microscopic surface texture after cycling – large graphitic flakes appeared to be lost. Reducing the negative limit for the voltage window (from -0.8 V to -0.6 V vs SHE) was observed to reduce degradation effects. Although these electrode samples are not fully representative of RFB electrodes under realistic operating conditions, the study represents a step towards developing a systematic understanding of electrode degradation.

Until recently, organic electrolytes lagged solubility, voltage and stability targets required to compete with vanadium flow cells. However, recent works have significantly advanced organic electrolyte stability, enabling competitive long-term cycling (section 2.3.1). To our knowledge electrode degradation studies remain unexplored in ORFB literature at this time. Developing this area of understanding will be important for improving ORFB lifetimes.

2.2   Membranes and separators

The primary function of membranes/separators in RFBs is to conduct ions from the supporting electrolyte between the two half-cells, while maintaining separation of redox active species. RFB membranes should additionally restrict excessive solvent crossover between the two half-cells. RFB membranes are broadly be divided into two technologies: ion-exchange membranes (IEMs) and microporous separators. The

following paragraphs provide a brief description of each in the context of RFBs.

A majority of aqueous RFBs use IEMs, which are manufactured from a type of polymer electrolyte. The polymer material contains a certain type of fixed charge, which enables some selectivity to conduct the corresponding counterions in solution [86]. Vanadium RFBs typically use cation exchange membranes (CEMs) such as Nafion®, which take advantage of the high mobility of acidic protons in solution. While Nafion CEMs have a high conductivity, they are not perfectly selective against the small, charged vanadium cations. Nafion CEMs are also manufactured from expensive fluorinated polymers, and currently account for up to 30 – 40 % of cell material costs [86]. Anion exchange membranes (e.g. fumatech®-brand membranes) can also be used; these tend to exhibit better selectivity against vanadium cations at the expense of lower ionic conductivity [86]. The improved selectivity of fumatech® membranes has also been demonstrated in ORFB systems [2,3].

Microporous materials such as Daramic, or Celgard are commonly used as separators in non-aqueous RFBs. Microporous materials enable passage of ions in supporting electrolyte through micron-sized pores, but lack a physical barrier against active material crossover. IEMs have also been demonstrated in non-aqueous flow cells; however, these materials exhibit high membrane resistance in non-aqueous electrolyte (which has an inherently low ionic conductivity) [5,87]. At this time, thin or high porosity microporous separators are preferred for non-aqueous RFBs to achieve higher through-plane membrane conductivity. High porosity, however, results in high permeability towards reactive species, so lower Coulombic efficiencies are expected [88]. Until further advancements in non-aqueous separators are made, non-aqueous RFB performance will likely be limited by a trade-off between achieving low through-plane membrane resistance (high voltage efficiency) at the cost of reduced Coulombic efficiency.

In this thesis we use Daramic 175 as a microporous separator for non-aqueous

systems (Chapters 5 and 7). Daramic 175 is a 175 μm thick PET-based separator which has an average porosity of 58 % and pore diameter of 0.1 μm [87]. This material has already been shown to demonstrate low membrane resistance and good energy efficiency during flow cell cycling compared to other options [5]. Fumasep E-620 (K) (a potassium ion-exchange membrane) was selected as a CEM for the aqueous chemistry studied in Chapter 6. As reported by Kwabi *et al.* and Ji *et al.*, this material shows reduced permeability to the quinone and ferrocyanide active species under examination in comparison to historically used Nafion membranes [2,3]. Fumasep E-620 (K) has the additional benefit of being manufactured from low-cost, non-fluorinated polymers, and is expected to achieve low materials costs at large production volumes [3].

2.3 Organic electrolytes of interest

2.3.1 Aqueous chemistry: a near-neutral quinone flow cell

Potassium ferro/ferricyanide: (a standard aqueous posolyte)

Potassium ferrocyanide is a commonly used redox material with established applications in metal processing, steel hardening and electroplating [89]. The compound consists of an iron center, which is strongly coordinated to six cyanide ions (Figure 2.2 (a)) [29]. Potassium ferrocyanide is reported to cycle stably between the iron 2+ ($[Fe(CN)_6]^{4-}$, ferrocyanide) and iron 3+ ($[Fe(CN)_6]^{3-}$, ferricyanide) oxidation states. Because of its low toxicity, cycling stability and moderately high solubility, it has become a standard posolyte in many aqueous RFB studies [2,3,90,91].

The long-term stability of potassium ferro/ferricyanide has been debated in the literature. It is well-established that neutral and high pH solutions of potassium ferrocyanide decompose into pentacyanide/iron hydroxides under UV exposure; whereas, solutions that are stored under dark, or diffuse light conditions are reported to be

stable [89, 92, 93]. The proposed decay mechanisms involved slow dissociation in the presence of oxygen; while, others suggested substitution of a hydroxide for a cyanide ion in the presence of sunlight (resulting in the production of free cyanide ions in solution) [89, 94]. These effects were reported to accelerate under low pH and high pH conditions [29, 94]. In the context of aqueous RFB literature, ferricyanide was reported to spontaneously reduce to ferrocyanide in the presence of carbon electrodes within days [28]; however, this process was determined to be reversible and was not expected to cause irrecoverable capacity loss in RFBs. A study by Luo *et al.* reported rapid capacity fade while cycling in capacity balanced symmetric flow cells [29]. The capacity fade was observed to accelerate at high pH, and was hypothesized to occur via dissociation of a cyanide ligand, followed by irreversible hydroxylation of the iron centre. Other reports by Cazot *et al.* and Paez *et al.* did not observe such rapid capacity fade, and suggested that growing ohmic losses and/or cell imbalancing due to oxygen evolution reactions may have been conflated with the capacity loss observed by Luo *et al.* [95, 96].

Recent work by Fell *et al.* (under review) agrees with these later findings. Their results suggest that while ferro/ferricyanide is chemically stable (in the dark, pH 7 – 14), ferricyanide can undergo electroless reduction to ferrocyanide (which is balanced by oxygen evolution reactions). The reduction rate was found to be aggravated under alkaline conditions and in the presence of porous carbon electrodes (which agrees with observations by Goulet *et al.*) [28, 97]. The parasitic reduction of ferricyanide (via oxygen evolution) was thermodynamically unfavourable below pH 11. Reaction rates were also reduced by: (i) maintaining high oxygen partial pressure, (ii) reducing the graphitic binder content of carbon electrodes; and, (iii) increasing the total number of ferricyanide ions relative to the electrode surface area. The recent evidence from these studies suggests that potassium ferro/ferricyanide should not be discounted as a stable, competitive posolyte in alkaline ORFB applications [95–97].

Anthraquinones: (and 2,6-DPPEAQ as a negolyte)

Quinones are arguably the most well-studied electrolyte family for aqueous ORFBs. Quinones undergo (generally reversible) two-electron reduction and oxidation. The exact mechanism is pH-dependent as the electron-transfer is coupled with proton exchange [25, 98, 99]. At low pH the reaction involves two protons, and the reduction potential decreases by 59 mV for every pH unit. Quinone reduction is generally described by the following reaction steps:

$$Q + e^- \rightleftharpoons Q^{\bullet -} \tag{2.1}$$

$$Q^{\bullet -} + H^+ \rightleftharpoons QH^{\bullet} \tag{2.2}$$

$$QH^{\bullet} + e^- \rightleftharpoons QH^- \tag{2.3}$$

$$QH^- + H^+ \rightleftharpoons QH_2 \tag{2.4}$$
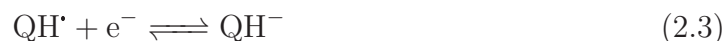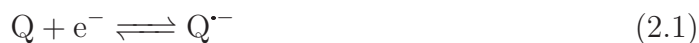
Under acidic conditions the protonation step is often so fast that the entire reaction can be described by a single two-electron transfer step ($Q + 2\,H^+ + 2\,e^- \rightleftharpoons QH_2$). At high pH the quinones may become fully de-protonated. When this is the case no protons are involved in the reduction reaction ($Q + 2\,e^- \rightleftharpoons Q^{2-}$), and the reaction and reduction potential become pH independent. A scheme depicting these reactions for *para*-benzoquinone is shown in Figure 2.1.
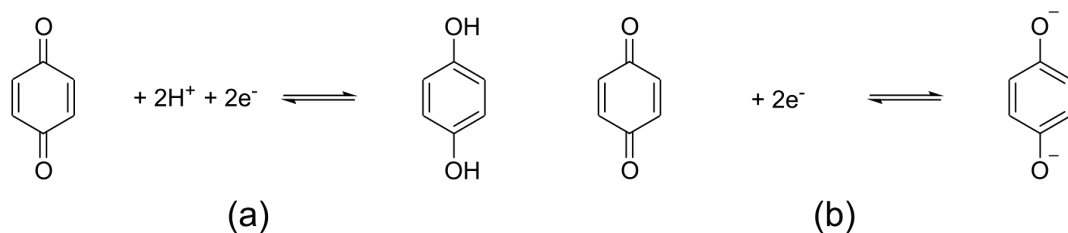
Figure 2.1: Schematic illustrating quinone reduction in acidic (a) and alkaline (b) media. *para*-benzoquinone is used as an example.

Comprehensive studies have shown that the solubility, redox potential and stability of quinones can be tuned by varying the nature, position and number of functional groups on the quinone centre [25, 100]. Numerous ORFBs have employed both commercially purchased quinones and novel derivatives [25, 27, 90, 100–104]. However, many of these earlier works were affected by rapid and irreversible capacity loss (up to several percent of the starting capacity per day).

In 2018, Kwabi *et al.* developed 4,4'-((9,10-anthraquinone-2,6-diyl)dioxy) dibutyrate (2,6-DBEAQ), which was synthesized from a previous redox molecule – 2,6-dihydroxyanthraquinone (2,6-DHAQ) [3, 90]. The addition of ether-linked alkyl chains terminated with carboxylate functional groups resulted in enhanced room-temperature solubility (1.1 M at pH 14, compared to 0.6 M for 2,6-DHAQ). The 2,6-DBEAQ negolyte demonstrated a record-breaking capacity fade rate of only 0.04 %/day when paired with an excess of potassium ferro/ferricyanide (posolyte). Long-term cycling studies and H NMR analysis determined that 2,6-DBEAQ was susceptible to irreversible chemical degradation via nucleophilic substitution, which results in cleavage of the solubilizing side chains. Both carboxylate and hydroxide ions were reported to act as nucleophiles; therefore, it was expected the stability could be improved by neutralizing the electrolyte pH, and substituting the carboxylate termination on the solubilizing alkyl chains.

In 2019, Ji *et al.* replaced the carboxylate side-chains with phosphonate-terminated functional groups to produce (((9,10-dioxo-9,10-dihydroanthracene-2,6-diyl)bis(oxy)) bis(propane-3,1-diyl))bis(phosphonic acid) (2,6-DPPEAQ) [2]. The phosphonate-functionalized quinone was reported to exhibit reversible reduction in unbuffered pH 9 and pH 12 solution, and has enhanced solubility at pH 9 (0.75 M) compared to 2,6-DBEAQ (35 mM), which enables cell operation in nearly-neutral electrolyte. Paired with a potassium ferro/ferricyanide posolyte, Ji *et al.* reported a 0.5 M 2,6-DPPEAQ flow cell with an OCV of 1.0 V a capacity fade rate of < 0.014 %/day – a new record

at the time. 2,6-DPPEAQ is commercially sold by Strem (15-8245), and was chosen for further investigation in this thesis owing to its promising solubility and stability in nearly neutral electrolyte.

Since then, efforts in understanding the degradation mechanisms and environmental factors affecting quinones have furthered improvements in chemical stability [25, 32, 34]. In 2020, Wu *et al.* reported two high-performance quinone molecules: 3,3'-(9,10-anthraquinone-diyl)bis(3-methyl- butanoic acid) (DPivOHAQ), and 4,4'-(9,10-anthraquinone-diyl)dibutanoic acid (DBAQ). The side chains in DPivOHAQ and DBAQ are carbon-linked, which makes them less susceptible to degradation by nucleophilic substitution than 2,6-DBEAQ and 2,6-DPPEAQ. At pH 12, DPivOHAQ and DBAQ were reported to have a solubility of 0.7 M and 1.0 M, respectively. Paired with a potassium ferro/ferricyanide posolyte, these compounds were shown to demonstrate an OCV of 1.0 V and a record stability of less than 0.014 % and 0.0084 % capacity fade per day. Wu *et al.* reported that by increasing the supporting electrolyte pH to 14, the stability of DPivOHAQ was improved to less than 0.0014 % capacity fade per day.

Some of these novel anthraquinones are on the path to large-scale commercialization. Advances in synthetic chemistry allow progressively higher yields and the use of more common, inexpensive precursors [105]. Cost analysis projects that with upscaling and batch production (on the order of gigatonnes) these high-performance molecules could be produced for as little as $ 2.4/kg, which is on par with electrolyte target costs recommended by techno-economic analysis [16, 105]. Given these advancements, it would not unreasonable to expect commercialization of quinone flow batteries in the future [106]. In fact, a recent break-through has shown that the decomposition of 2,6-DHAQ (previously mentioned) can be reversed in the presence of oxygen [107]. This material recently secured more that $7.8 million in funding for a new flow battery start-up company, Quino Energy [108].

While significant work has been done to extend the lifetime of quinone electrolytes, little has been done to understand the degradation of electrode interfaces in ORFBs. As previously described, the chemical and physical properties of carbon electrodes can have a significant impact on charge-transfer kinetics and cell performance [49, 52], so understanding the factors affecting electrode degradation is important for maintaining cell performance. In this thesis, we characterize electrode degradation in a promising aqueous quinone system – 2,6-DPPEAQ. (Although newer quinone derivatives have been reported, 2,6-DPPEAQ is commercially available from STREM). We cycle this negolyte against a potassium ferro/ferricyanide posolyte (Figure 2.2) using a similar cell design and cycling protocol reported by Ji *et al.* [2]. In addition to capacity retention, we monitor changes in cell impedance by performing *in situ* electrochemical impedance spectroscopy every 10 cycles. The effects of electrochemical cycling are determined by comparing the physical, electrical and chemical properties of the carbon electrodes with uncycled samples for both the positive and negative electrodes.

2.3.2 Non-aqueous chemistry: phenothiazine- and viologen-based derivatives

Phenothiazines: (and MEEPT as a posolyte)

Phenothiazines are a group of redox active molecules that act as a (generally) stable electron-donor. These molecules have established uses in the textile and pharmaceutical industries, and are also used as biological indicators [109]. Recently, these materials have become interesting for applications in electrochemical energy storage systems. For example, *N*-Ethylphenothiazine (EPT) can be used as an additive to protect against overcharging in lithium ion batteries [6].

Since 2015, Dr. Odom's group at the University of Kentucky has pioneered research of phenothiazine derivatives for use as catholytes in non-aqueous ORFBs [6, 110–113]. In 2016, Milshtein *et al.* developed a high solubility, long lifetime mate-
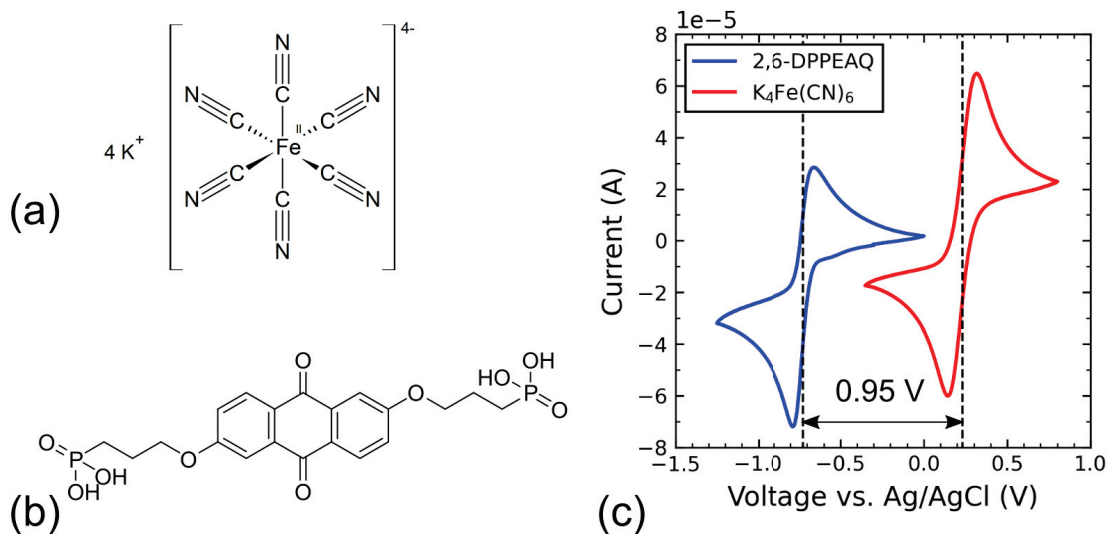
Figure 2.2: Figure showing the chemical structure of potassium ferrocyanide (a), 2,6-DPPEAQ (b), and cyclic voltammograms of the two electrolytes at 10 mM concentration in 2 M potassium chloride adjusted to pH 9 (c). Full current-compensation was used during these measurements. The predicted open-circuit voltage for the cell under these conditions is 0.95 V.

rial (10-[2-(2-methoxyethoxy)- ethyl]-10H-phenothiazine (MEEPT)), which was produced *via* one-step synthesis from EPT [6]. While EPT has a solubility limit of 0.1 M in carbonate- and nitrile-based solvents, MEEPT is functionalized with a linear oligoglycol chain to increase solubility. MEEPT is in fact a liquid at room temperature and fully miscible with non-aqueous media in its uncharged state [6]. The volumetric capacity of a MEEPT flow cell is limited by its radical cation salt, which is known to be soluble up to 1.0 M with appropriate choice of supporting electrolyte [113]. MEEPT undergoes a chemically and electrochemically reversible one-electron oxidation (Figure 2.3a) and has been shown to cycle stably at high current-density for 100 cycles with no capacity loss [6]. This was a significant advancement in the non-aqueous ORFB field, which is relatively young compared to aqueous systems. MEEPT is now commercially available from TCI (M3068) to use as a standard non-aqueous posolyte.

Many phenothiazines also posses a third oxidation state (Figure 2.3a). The sec-

ond oxidation process for MEEPT was believed to be irreversible; however, more recent work suggests that careful choice of solvent and supporting electrolyte may allow the third oxidation state to be reversibly accessed [6, 113]. In addition, other phenothiazine derivatives have been developed to undergo reversible two-electron oxidation [111, 112].

Although MEEPT is a promising step forward in the development of non-aqueous catholytes, further work must be done to understand its chemical stability under operating conditions. Early work suggested that MEEPT cations were affected by nucleophiles (such as water); meanwhile, neutral (uncharged) MEEPT was reported to degrade slowly in the presence of oxygen [6]. Kaur *et al.* later reported that water (in low concentrations) did not appear to affect the stability of the MEEPT cation [113], and further elaborated that the degradation was caused by impurities in acetonitrile (when MEEPT was present in low concentrations) [113]. They also showed that the MEEPT stability was strongly affected by choice of supporting salt, with the following stability trend: $TFSI^- > PF_6^- > ClO_4^- > BF_4^-$. The decomposition mechanism is still undetermined. Under full-cell operating conditions, MEEPT is reported to cycle stably (with reversible fluctuations in cell capacity) [5]. Minimal degradation was reported in the electrolyte after 100 cycles (as evaluated by cyclic voltammetry and H NMR studies) [5]. These results are promising, and further work should be done to understand the stability of the separator and carbon electrodes with long-term cycling of a MEEPT catholyte. This is a problem that we examine in this thesis.

Viologens: (and MEEV-TFSI$_2$ as a negolyte)

Viologens have a long history of electrochemical applications, including use as: biological indicators, herbicides and electrochemical display devices [114]. Recently, viologen derivatives have also shown promise as negative redox materials in ORFBs
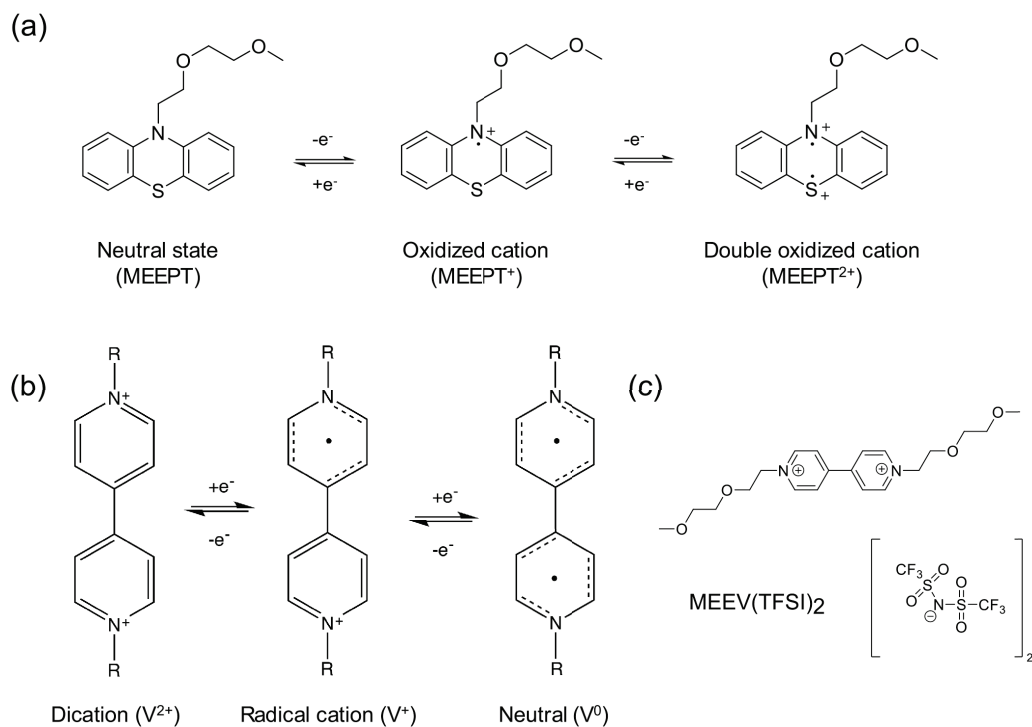
Figure 2.3: Illustrating the non-aqueous molecules examined in this thesis: a schematic of the three oxidation states for MEEPT (a), a schematic showing the three reduction states for viologen molecules (b); and, a diagram of the chemical structure of MEEV-TFSI$_2$ (c).

owing to their high solubility, tunable reduction potential, fast chemical kinetics, and facile/inexpensive synthesis [115–120]. The viologen molecule consists of two pyridyl groups, and may exist in three reduction states: $V^{2+} \rightleftharpoons V^{\bullet+} \rightleftharpoons V^0$ (Figure 2.3b).

Early viologens (such as methyl-viologen, Figure 2.3b R$= -$CH$_3$) showed poor calendar lifetime in flow battery applications, with capacity fade rates of up to 1 %/day. The stability of methyl viologen is limited by a bimolecular decomposition mechanism involving the dimerization of two charged cations [28, 115, 116, 119, 121, 122]. Dimers can precipitate if they are insoluble, and can also disproportionate into an uncharged (V^{2+}) and doubly reduced (V^0) species. The latter can be protonated in the presence of water to form a redox-inactive material [123]. Recent reports have shown that functionalization with bulky and/or charged side-chains can inhibit

26

unfavorable dimerization, leading to some of the highest lifetimes in ORFBs to date [115, 118–120, 124]. Viologen cations have also been reported to react with oxygen and water, ultimately leading to the deprotonation and loss of solubilizing functional groups (−R) [125].

One unique advantage of viologens is that they have three reduction states. While the first reduction step is highly reversible, the second step is less-frequently so (due to the production of an insoluble and uncharged species) [114, 120, 124]. Accessing the third reduction state (V^0) is an excellent opportunity to increase the energy density of viologen derivatives, and has already been demonstrated in aqueous environments [120]. Dr. Odom's research group at the University of Kentucky has shown that appropriately functionalized viologens can also be successful as a negolyte in non-aqueous ORFBs. The novel electrolyte – bis[2-(2-methoxyethoxy)ethyl]viologen bis(bis(trifluoromethanesulfonyl)imide) (MEEV-TFSI$_2$, Figure 2.3(c)) – contains glycol side chains on the N centres, and two TFSI anions to simultaneously improve solubility and electrolyte conductivity [126]. The authors report both reduction events to be both chemically and electrochemically reversible in the presence of supporting electrolyte [126]. MEEV-TFSI$_2$ has also been used as a two-electron receptor under both room temperature and low-temperature conditions [5, 126–128]. Negligible degradation products are reported by cyclic voltammetry and NMR spectroscopy of cycled electrolyte samples. However, issues with capacity loss have yet to be fully understood.

In this thesis we examine a MEEV-TFSI$_2$ negolyte paired with a MEEPT posolyte as a non-aqueous flow battery system in acetonitrile. Due to its common anion, tetraethylammonium bis(trifluoromethanesulfonyl)imide (TEATFSI) is used as a supporting electrolyte to improve solution conductivity [126]. Daramic 175 is selected as a separator due to its low impedance; however, previous studies report high crossover rates for MEEPT and MEEV-TFSI$_2$ with Daramic 175 (due to its microporous struc-

ture) [5]. Following protocols developed by Dr. Odom and co-workers, we pre-mix the MEEV-TFSI$_2$ and MEEPT in equal concentrations to be used in both the posolyte and negolyte [5,126,127]. Although this results in higher materials usage, it minimizes crossover driven by concentration gradients across the cell, thereby enabling a more reliable assessment of capacity retention. We seek to characterize the performance and stability of MEEPT-MEEV flow cells at 25 °C, 40 °C and 0 °C. Understanding the temperature sensitivity of ORFBs is critical to their intended application in grid-storage systems; however, the effects of temperature are under-explored in flow cell literature at this time.

Chapter 3

Theory

3.1 Cell attributes and performance metrics

3.1.1 Theoretical capacity

In most RFBs, the electroactive materials are dissolved in a liquid electrolyte. As discussed in Chapter 1, this enables the stored energy to be upscaled by increasing the electrolyte volume, and/or by increasing the amount of dissolved electroactive materials. The theoretical capacity of the positive ($Q_{t,+}$) and negative ($Q_{t,-}$) half-cells is easily expressed in Coulombs as:

$$Q_{t,+/-} = n_{+/-} F C_{+/-} V_{+/-} \tag{3.1}$$

where $n_{+/-}$ is the number of electrons transferred/molecule, F is Faraday's constant (96845 C/mol), $C_{+/-}$ is the electrolyte concentration (mol/L) and $V_{+/-}$ is the electrolyte volume (L). (The subscripts denote the positive and negative half-cells) [129]. This is easily converted to a commonly used unit, Amp hours, by applying the factor (1 hr /3600 s). In research-scale flow batteries the negolyte and posolyte capacities are often unmatched, i.e. one half-cell is assembled with excess material, while the other is deficient. The material deficient half-cell is termed the capacity limiting side

(CLS). This set-up enables the stability of the CLS to be assessed independently from the other half-cell [28].

Capacity may also be reported in terms of the volumetric capacity (electrolyte capacity normalized to the electrolyte volume).

$$Q_{v,+/-} = \frac{Q_{+/-}}{V_{+/-}} \tag{3.2}$$

where $V_{+/-}$ is the electrolyte volume in the positive or negative half-cell [129]. The overall energy density of the cell is the volumetric capacity normalized to the total electrolyte volume [129].

$$Q_{v,cell} = \frac{Q_{discharge}}{V_+ + V_-} \tag{3.3}$$

3.1.2 Cell voltage and state-of-charge

The thermodynamic limit for the average cell voltage (at 50 % state-of-charge) is determined by the difference in standard reduction potential between the two half-cells:

$$E_{cell}^0 = E_+^0 - E_-^0 \tag{3.4}$$

where E_+^0 is the standard reduction potential for the positive half-cell and E_-^0 is the standard reduction potential for the negative half-cell. More generally, the concentration of oxidized and reduced species in the negative and positive half-cells determines the total cell voltage according to the Nernst equation

$$E_{cell}^0 = (E_+^0 + \frac{RT}{nF} \ln \frac{[Ox_+]}{[Red_+]}) - (E_-^0 + \frac{RT}{nF} \ln \frac{[Ox_-]}{[Red_-]}) \tag{3.5}$$

The quantities $[Ox_{+/-}]$ and $[Red_{+/-}]$ indicate the concentration of oxidized and reduced species in the positive and negative half-cells, and the R is the universal gas
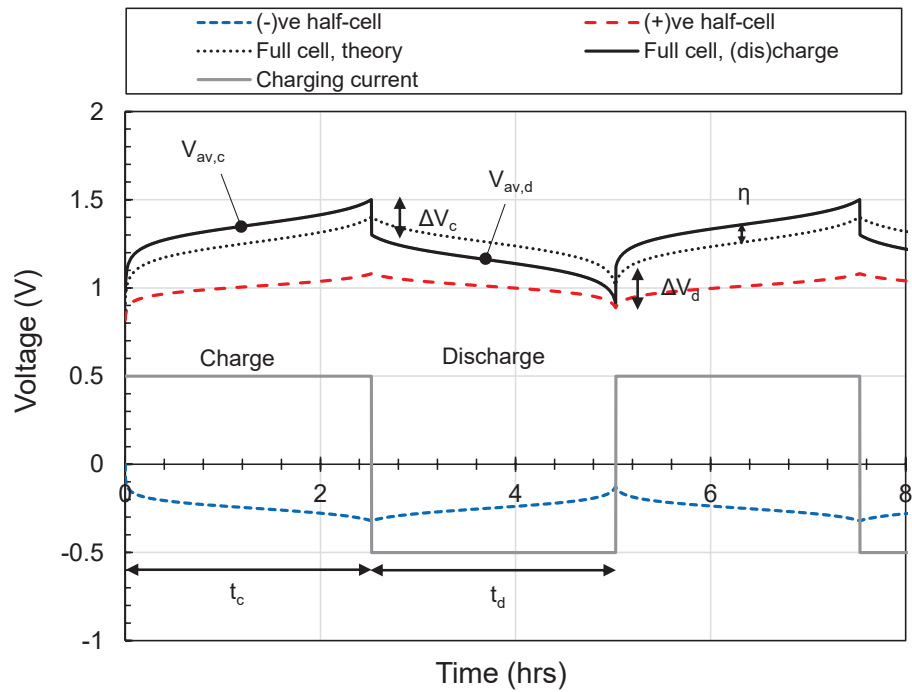
Figure 3.1: Theoretical voltage profiles for a full cell during charging and discharging. The thermodynamic voltage is indicated by the black dashed trace, while the voltage under constant-current charging is indicated by the solid black trace. Relevant variables in sections 3.1.2 and 3.1.3 are indicated.

constant. A theoretical voltage profile for charging and discharging is shown in Figure 3.1.

Under operation a constant-current (and/or constant-voltage) may be used to (dis)charge the cell, which causes the cell voltage to deviate from the thermodynamic limit by an amount iR_{cell} when (dis)charging (Figure 3.1). Here i is the charging current and R_{cell} refers to the internal resistance of the cell. This voltage difference (labelled η in Figure 3.1) results from kinetic, ohmic and mass-transport losses [59]. Kinetic losses result from activation control (i.e. charge-transfer of either an electron or ion between an the electrode surface and redox-active electrolyte) [59]. Ohmic losses include electronic and contact resistances at the cell electrode, ionic resistance of the solution and membrane/separator resistance to charge migration [41]. Finally, mass transport losses refer to the delivery of active electrolyte species to the electrode surface [70].

The internal cell resistance can be estimated by using the change in voltage at the end of each charge/discharge step ($\Delta V_{c,d}$) when the current immediately switches directions (Figure 3.1). The cell resistance can be estimated from

$$R_{cell} = \frac{\Delta V_{c/d}}{2i} \tag{3.6}$$

The difference between the theoretical and measured voltage profiles is sometimes referred to as the overpotential (η), which results from the kinetic, ohmic and mass-transport losses described above [59, 70, 71, 130].

The state-of-charge (SOC) for a cell refers to the ratio of capacity stored/charged over the theoretical cell capacity [129].

$$\text{SOC} = \frac{Q_{charge}}{Q_t} \tag{3.7}$$

When electrochemically reversible electrolyte materials are used, the SOC can also

be estimated from the cell open-circuit voltage (OCV) as described below

$$\text{OCV} = E^0_{cell} + \frac{RT}{nF} \ln[(\frac{\text{SOC}}{1 - \text{SOC}})^2] \tag{3.8}$$

3.1.3 Cell efficiency

Three metrics are typically used to define cell efficiency: coulombic efficiency (CE), voltage efficiency (VE) and energy efficiency (EE).

The Coulombic efficiency describes the ratio of charge extracted from a cell on discharge to the amount needed to charge the cell (equation 3.9) [129]. If constant-current cycling alone is used to (dis)charge the cell, it can be determined from the ratio of discharge to charge time. However, many studies use a combination of constant-current and constant-voltage (dis)charging; when this is the case, the charge passed in both constant-current and constant-voltage steps must be considered when determining the Coulombic efficiency. The Coulombic efficiency of a cell may be affected by processes such as parasitic reactions and membrane cross-over (which are described in section 3.1.4).

$$\text{CE} = \frac{Q_{discharge}}{Q_{charge}} \tag{3.9}$$

The voltage efficiency describes the ratio of the average discharge to charge voltages. As the cell resistance and/or charging current increase, the cell overpotential will increase, which causes the voltage efficiency to decrease.

$$\text{VE} = \frac{V_{av,d}}{V_{av,ch}} \tag{3.10}$$

The energy efficiency describes the overall cell efficiency from the ratio of energy provided on discharge to the energy needed to charge the cell [129]. It can be determined from the product of the Coulombic and voltage efficiencies. Relevant variables

used to determine these cell efficiency metrics are depicted in Figure 3.1.

$$EE = CE \text{ x } VE \tag{3.11}$$

In this thesis we define an additional quantity called the current efficiency, which refers to the ratio of charge extracted at constant-current on discharge to the charge added during constant-current charging. Unlike the Coulombic efficiency, this metric excludes charge passed during constant-voltage holds. The current efficiency is sensitive to the cell overpotential (which causes the charging limits to be exceeded prematurely); whereas the Coulombic efficiency is not (when constant-voltage (dis)charging is present).

3.1.4 Stability and capacity loss

Capacity fade rates are used to quantify the stability of RFBs. Capacity fade is either expressed in terms of calendar time (% loss/day), or cycle numbers (% loss/cycle). Lower capacity cells and high cycling rates tend to exaggerate apparent stability when reported as % loss/cycle, especially when decay mechanisms are time-dependent. It is generally agreed that calendar fade rates are a more informative stability metric [131].

Capacity fade may result from a number of mechanisms including: material crossover, chemical decomposition and parasitic side reactions. These are described briefly in the following sections.

Crossover

Crossover typically refers to the diffusion or migration of electrochemically active species from one half-cell to the other. An ideal membrane/separator would be perfectly selective against the redox active species and only enable transport of supporting ions, but this is difficult to achieve in practice. Crossover of (charged) active species causes the cell to self-discharge and leads to low CE, capacity decay and in

some cases irreversible reactions. It is also possible for solvent and supporting ions to preferentially migrate to one half-cell resulting in volume and pressure imbalancing [129].

Some tactics to minimize crossover effects include: using low electrolyte concentrations, or pre-mixing positive and negative electrolytes to reduce the diffusion driven by concentration gradients [5, 126]. Symmetric cells may also be used to eliminate some effects from crossover. These cells are described in section 3.1.5.

Chemical decomposition

Chemical decomposition refers to the inherent stability of the redox-active material. This decay mechanism is more problematic in organic RFBs. Several chemical decomposition pathways have been suggested, including: nucleophilic substitution, disproportionation, dimerization and polymerization [2, 3, 25, 28, 115, 116, 119, 121, 122, 132, 133]. These reaction pathways lead to irrecoverable capacity loss if the degradation product is not redox active (or not redox active within the charging window), or less soluble (which results in material precipitation). Some of these decomposition mechanisms are known to be affected by material concentration (in the case of bimolecular decomposition pathways), cell voltage and ambient atmosphere [32, 115, 132, 133].

Parasitic side-reactions

Parasitic side-reactions may occur due to solvent decomposition (such as water-splitting reactions), or reactions involving electrolyte impurities (either in the raw material, or sometimes due to dissolved oxygen). Typically parasitic reactions manifest as a lower CE; however, in some cases they can also accelerate chemical decomposition. Water-splitting reactions lead to pH changes, which may result in nucleophilic substitution pathways [2, 3]. Parasitic reactions can be dependent on the voltage cycling window, so selecting appropriate charging limits can be important (especially

for minimizing solvent decomposition reactions).

3.1.5   Types of cells
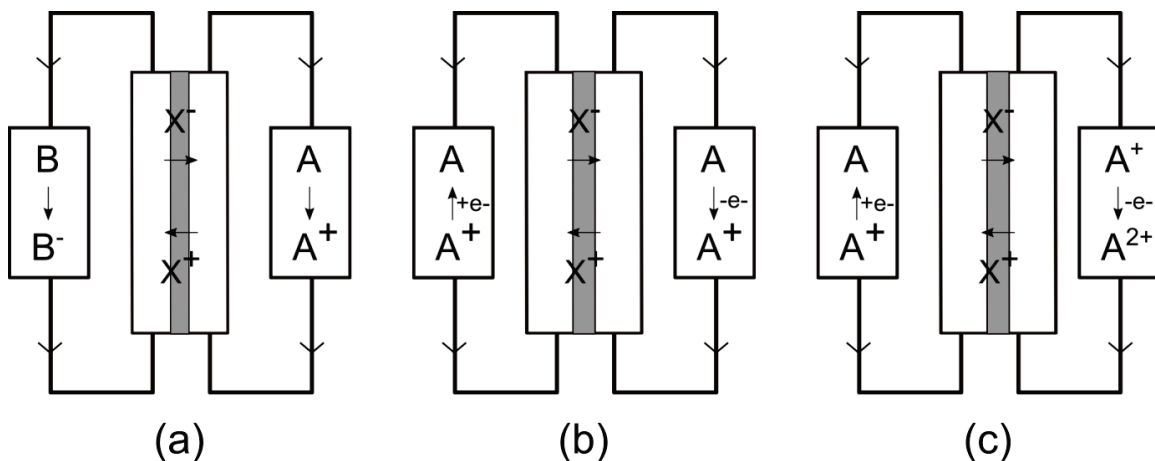
Figure 3.2: Schematic illustrating three commonly used cell configurations: (a) asymmetric, (b) symmetric (definition I), and (c) symmetric (definition II).

Asymmetric cells

An asymmetric cell describes a flow cell when different materials are used in each half-cell. Typically the electrolyte of interest is capacity limiting, while the other half-cell has a material excess. This is done to minimize the impact of the excess material on the full-cell stability. Asymmetric cells yield data about full cell performance, including: cell efficiencies, impedance, power density, and capacity fade. A schematic of an asymmetric flow cell is shown in Figure 3.2a.

Symmetric cells

A symmetric cell refers to a flow cell with the same electrolyte used in both half-cells. The electrolyte is cycled between the same two oxidation states in both half-cells (charging in one half-cell, while discharging in the other). As a result the average cell voltage is 0 V; however, this cell configuration is useful for understanding the intrinsic

molecular stability of the electrolyte material in the absence of membrane crossover effects [6, 28, 129]. A schematic of a symmetric flow cell is illustrated in Figure 3.2b.

It is important to clarify that the term "symmetric cell" is also commonly used in the literature to describe a similar cell design. The second usage is a hybrid of symmetric and asymmetric cells that utilizes a redox material with more than 2 oxidation states. The electrolyte is symmetric in the sense that the same material is used in both half-cells; however, each half-cell cycles between different oxidation states. Because the standard reduction potential differs between the two half-cells a non-zero cell voltage is achieved (in contrast to our previous definition for symmetric cells). A schematic for this definition of symmetric cell is also shown in Figure 3.2c.

Two examples of these symmetric cells include the vanadium(III) acetylacetonate electrolyte (which is examined in Chapter 5 and exists in 3 oxidation states), and the ubiquitous aqueous vanadium electrolyte (which utilizes 4 vanadium oxidation states). So long as there is no net mass transfer between the two half-cells crossover does not lead to significant irreversible capacity fade in these types of symmetric cells as the material may also be charged in the opposite half-cell.

3.2 Electrode characterization techniques

3.2.1 Three electrode cells

Three-electrode cells are used to accurately control the potential of a single electrode. The potential at the electrode of interest (the working electrode, WE) is defined with respect to a reference electrode (RE) – an electrode with a stable and known reduction potential. The RE is non-polarizable, which means that its potential changes very little as it passes current. This enables the potential difference between the WE and RE to be more accurately defined. A counter electrode (CE) is used to complete the circuit, and balance charge passed at the WE. The CE must also be selected to meet

specific requirements. An ideal counter electrode should be non-polarizable (i.e. have fast reaction kinetics) and have a large surface area; it is recommended for the CE surface area to be approximately ten times larger than the WE when possible.

Two equivalent schematics for a three-electrode set-up measured using a potentiostat are shown in Figure 3.3. The working electrode potential is set with respect to the RE by passing current through the CE until the specified potential difference is achieved. (Preparation methods for electrodes and three-electrode cells are discussed in section 4.1.3.) This set-up significantly reduces the uncertainty in the working electrode potential compared to a two-electrode measurement; however, an unknown voltage drop still occurs due to solution resistance between the working and reference electrodes. Methods to minimize the solution resistance include: (1) placing the RE as close to the WE as possible (without blocking the current path to the CE), (2) using a highly conductive supporting electrolyte, and (3) running experiments using a lower current. The remaining solution resistance may be corrected using "iR compensation" features that are typically available with most potentiostats.

3.2.2 Electrochemical impedance spectroscopy

Electrochemical impedance spectroscopy (EIS) is a powerful technique that involves perturbing a system by a small amount (ideally, but not necessarily near equilibrium) and measuring the system response. Typically this is done by applying a small AC voltage ($\leq 10\text{mV}$) over a DC bias and measuring the corresponding current response as a function of perturbation frequency. (An AC current signal may also be used). Using a small perturbation amplitude ensures a linear response, which simplifies further analysis. The system impedance is related to the voltage and current response by Ohm's law

$$\tilde{Z}(\omega) = \frac{\tilde{V}(\omega)}{\tilde{I}(\omega)} \tag{3.12}$$
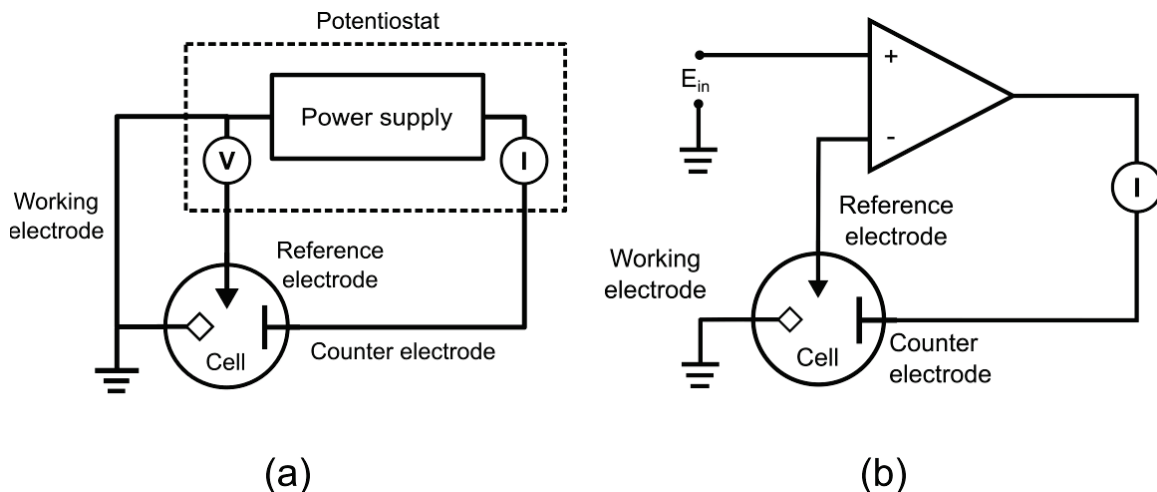
Figure 3.3: Two equivalent schematics illustrating the experimental set-up for a three-electrode measurement performed with a potentiostat. (a) The symbols V and I each represent an ideal voltmeter and ammeter, respectively; however, the true input impedance for the voltmeter is not infinite and a small amount of current flows through the reference electrode (1 pA – 1 nA). (b) The potentiostat acts as an amplifier, which outputs a current through the counter electrode when the two inputs (from the setpoint voltage (E_{in}) and reference electrode) are not equal. Current flows through the working electrode to complete the circuit until the two amplifier inputs are equal, at which point the working electrode has reached the specified setpoint with respect to the reference electrode.

where $\tilde{Z}(\omega)$, $\tilde{I}(\omega)$ and $\tilde{V}(\omega)$ are the complex impedance, current and voltage. The perturbation frequency is ω (where $\omega = 2\pi f$). EIS data is often presented in a Nyquist plot ($\text{Im}[Z]$ vs. $\text{Re}[Z]$). The real and imaginary impedance components are equivalently referred to as Z' and Z''.

Equivalent circuit analysis

A wide variety of electronic information can be extracted by fitting experimental impedance data to an equivalent circuit model, including information about: kinetic and diffusive processes, as well as inductive, resistive and capacitive elements. Simple charge-transfer at an electrode-electrolyte interface is typically modelled using a Randles circuit, which consists of a parallel RC-circuit in series with a resistor (Figure 3.4a). The total current results from charging of the electric double layer (ca-

pacitive current) in addition to the Faradaic current. These processes are modelled in the equivalent circuit using a capacitor (C_{dl}) and a resistor (R_{ct}). The charge-transfer resistance (R_{ct}) acts as a measure of how easily a reaction proceeds. A low charge-transfer resistance indicates a kinetically facile process with a high reaction rate constant; whereas, a high charge-transfer resistance indicates sluggish kinetics. An additional resistor (R_s), may account for series resistances such as solution, membrane and contact resistances. The complex impedance for a Randles circuit is given by

$$Z(\omega) = R_s + \frac{R_{ct}}{1 + (\omega R_{ct} C_{dl})^2} - i\frac{\omega R_{ct}^2 \omega C_{dl}}{1 + (R_{ct} C_{dl})^2} \tag{3.13}$$

Eliminating the frequency term from the real and imaginary components, we see that the Randles-Circuit forms a semi-circle in the complex plane (Figure 3.4b), which is described by the equation below.

$$(Z' - R_s - \frac{R_{ct}}{2})^2 + Z''^2 = (\frac{R_{ct}}{2})^2 \tag{3.14}$$
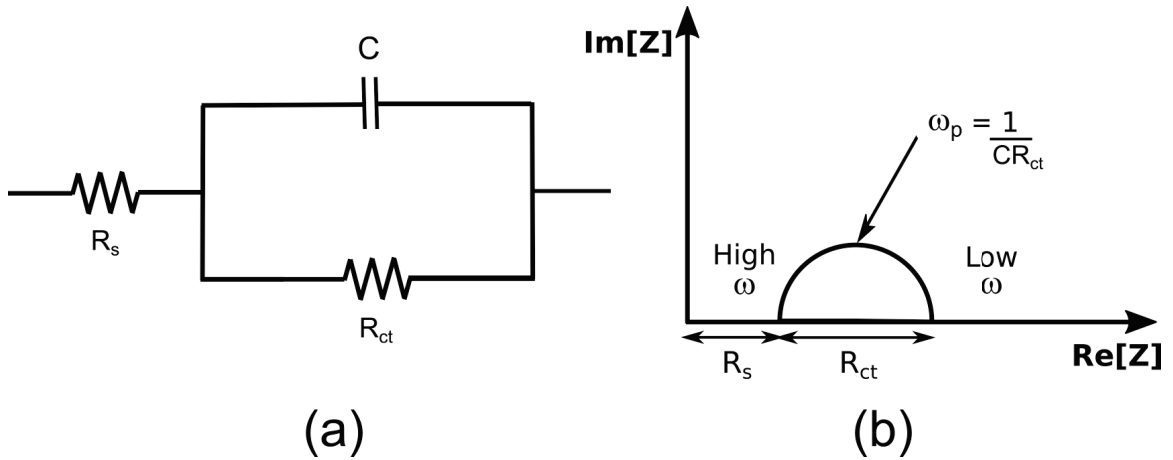
Figure 3.4: A Randles equivalent circuit (a), and a Nyquist plot for the Randles circuit (b).

In some situations, the semi-circle may be flattened. This is modelled by replacing the capacitor with a constant phase element (CPE), shown in Figure 3.5a. The CPE

accounts for a non-ideal capacitance, and is empirically modelled as

$$Z_{cpe} = \frac{1}{T(i\omega)^\alpha} \tag{3.15}$$

where T describes the magnitude of the response, and $-1 \leq \alpha \leq 1$ describes the constant phase angle in the complex plain. The impedance for a constant phase element reduces to three limiting cases: $\alpha = 1$, an ideal capacitor; $\alpha = 0$, a resistor; and $\alpha = -1$, an inductor. For the latter cases, the resistance (or inductance) is given by R or $L = \frac{1}{T}$.

(a)   (b)
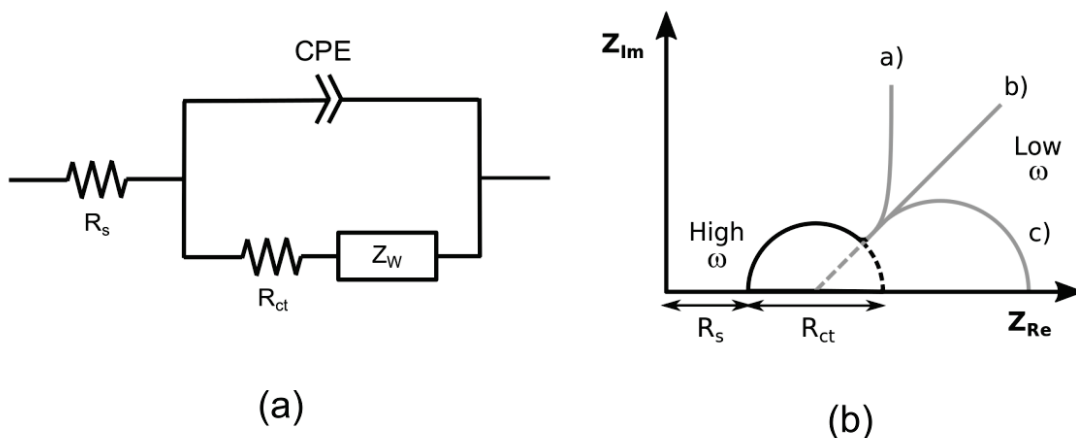
Figure 3.5: An equivalent circuit accounting for a non-ideal capacitance and diffusive processes (a). Nyquist plot for the equivalent circuit shown in (a). Three possible diffusive responses are shown at low frequency with: (a) reflective boundary conditions, (b) generalized finite diffusion, and (c) transmissive boundary conditions.

Diffusion effects can be modelled by adding a Warburg diffusion element to the Randles-Circuit (Figure 3.5). The simplest representation models semi-infinite linear diffusion in one dimension at a large planar electrode. The descriptive equation

$$Z_W = \frac{\sigma}{\omega^{1/2}} - i\frac{\sigma}{\omega^{1/2}} \tag{3.16}$$

which describes a constant phase element at an angle of 45 ° in the complex plane (Figure 3.5b, trace (b)). The quantity σ is the Warburg coefficient, which encapsulates

the effects of temperature (T), diffusion coefficients ($D_{o/r}$), and concentrations ($C_{o/r}$) of the oxidized and reduced electrolyte species.

$$\sigma = \frac{RT}{n^2 F^2 A \sqrt{2}} \left(\frac{1}{D_o^{1/2} C_o^\infty} - \frac{1}{D_r^{1/2} C_r^\infty} \right) \tag{3.17}$$

The constants R, F and A represent the universal gas constant, Faraday's constant and the geometric electrode area, respectively.

In flow batteries, electrodes are typically a porous carbon material, which also gives rise to the characteristic 45 º Warburg response. The porous electrodes are modelled using transmission line elements using methods detailed by de Levie [134]. Because the pores have a finite length, the characteristic 45 º Warburg response only exists in a specific frequency range. Treating the finite length pores can be modelled using two limiting cases: finite length ("short"), or finite space ("open") Warburg elements.

A Warburg "short" element assumes transmissive boundary conditions into the finite length elements. Physically, this may represent a response characteristic of a rotating disk electrode, or an operating flow battery where convection is used to improve transport to/from the bulk (or undepleted) electrolyte. This is described mathematically by

$$Z_{Ws} = \frac{Z_0}{(i\omega\tau)^{1/2}} \tanh(i\omega\tau)^{1/2} \tag{3.18}$$

where Z_0 and τ describe the electrode properties. At higher frequencies the behaviour approaches the characteristic 45 º response. At lower frequencies the impedance transitions into a semi-circle (Figure 3.5b, trace (c)), as though the Warburg diffusion element was "shorted" by a resistor.

A Warburg "open" element assumes reflective/blocking boundary conditions for the finite length elements, which is characteristic of solid electrodes, or unstirred solu-

tions with a thick Nernst/diffusion layer. This is similarly modelled by the following equation:

$$Z_{Wo} = \frac{Z_0}{(i\omega\tau)^{1/2}} \coth(i\omega\tau)^{1/2} \tag{3.19}$$

In the complex plane the Warburg "open" elements approach capacitive behaviour at very low frequencies (Figure 3.5b, trace (a)).

Distribution of relaxation times (DRT) analysis

Electrochemical impedance spectroscopy can be used to derive information about the kinetic and transport processes in many electrochemical systems, such as: solar cells, batteries, fuel cells, medical devices, and biological systems. As described above, this is most commonly done by fitting EIS data to an equivalent circuit model. However, many circuit models (of varying complexity) can often be used to achieve analogous fits for the same data.

Selecting a realistic equivalent circuit requires *a priori* knowledge of the physical processes governing the system being studied. This is problematic in new systems when discovering relevant kinetic and transport mechanisms becomes the question of interest. In this regard, distribution of relaxation times (DRT) can be used as a complementary analysis method.

DRT analysis determines a characteristic distribution of relaxation timescales from experimental EIS data according to the expression:

$$Z_{DRT}(f) = R_\infty + \int_0^\infty \frac{g(\tau)}{1 + i2\pi f\tau} d\tau \tag{3.20}$$

where R_∞ is represents an ohmic resistance, and $g(\tau)$ is a function describing the distribution of relaxation time constants for the system being studied. (Equation 3.20 can be modified to account for inductance by adding the term $i\omega L$). Recalling

that the characteristic relaxation time for an RC circuit element is $\tau = 1/RC$, we can see that this model represents an ohmic resistance in series with an infinite sum of parallel RC circuits. Because EIS data is typically spaced logarithmically, the model is often rewritten in terms of $\ln \tau$:

$$Z_{DRT}(f) = R_\infty + \int_{-\infty}^{\infty} \frac{\gamma(\ln \tau)}{1 + i2\pi f\tau} \, d\ln(\tau) \tag{3.21}$$

where $\gamma(\ln \tau) = \tau g(\tau)$.

The Ciucci lab at University of Hong Kong has developed open-source MatLab and Python resources to determine $\gamma(\ln \tau)$ from EIS data. The theory behind these methods is detailed in references [135–137]. A general description of the theory is given in the remainder of this section.

The Ciucci lab describes solutions for $\gamma(\ln \tau)$ using regularized regression methods. The distribution $\gamma(\ln \tau)$ can be written as a sum of Dirac distributions $\delta(\ln \tau)$ described by M characteristic relaxation times $\tau_1, \tau_2, \ldots, \tau_m$.

$$\gamma(\ln \tau) = \sum_{m=1}^{M} x_m \delta(\ln \tau - \ln \tau_m) \tag{3.22}$$

where x_m are coefficients determined by fitting. Using equation 3.22, equation 3.21 simplifies to

$$Z_{DRT}(f) = R_\infty + \sum_{m=1}^{M} \frac{x_m}{1 + i2\pi f\tau_m} \tag{3.23}$$

To modify the Dirac solution to achieve a continuous $\gamma(\ln \tau)$, equation 3.22 is instead written as

$$\gamma(\ln \tau) = \sum_{m=1}^{M} x_m \phi_\mu(|\ln \tau - \ln \tau_m|) \tag{3.24}$$

where $\phi_\mu(|\ln \tau - \ln \tau_m|)$ is a radial (symmetric and real-valued) basis function (RBF)

centered about the timescale τ_m. Commonly used RBFs include Gaussian and Matérn functions. Expanding equation 3.21 with equation 3.24 represents a sum of M generalized RC circuits that have a distribution of timescales centered at τ_m. This is represented schematically in Figure 3.6, which is adapted from Wan *et al* [135]. DRT fitting implies minimizing the sum of squares between this model and experimental data

$$S = \sum_{n=1}^{N} [w'_n[(Z'_{DRT}(f_n) - Z'_{exp})^2 + w''_n(Z''_{DRT}(f_n) - Z''_{exp}(f_n))^2] \qquad (3.25)$$

A penalty term proportional to the normalized first (or second) derivative is added to equation 3.25 to prevent over-fitting. The penalty term is scaled by the regularization parameter λ. A larger λ will result in a higher penalty, and smoother DRT profile. Typical values for Gaussian basis functions range from 5.9E-03 to 1.1E-02 [135]. Minimizing S yields the coefficients x_m, which are used to estimate $\gamma(\ln \tau)$ using relation 3.24. This process is depicted schematically in Figure 3.6, which is adapted from Wan *et al.* [135].

3.2.3 X-ray photoelectron spectroscopy

X-ray photoelectron spectroscopy (XPS) is a surface sensitive analysis technique, which can be used to identify elements and chemical bonding environments within a sample. The principle of XPS is based on the photoelectric effect. X-ray photons ($\sim 1 - 10$ keV) are focused onto a sample, liberating core level electrons from within approximately 100 Åof the surface. Electrons with sufficient energy are ejected into vacuum. The electrons have a kinetic energy (KE) equivalent to

$$KE = h\nu - BE - \Phi_S \qquad (3.26)$$

where $h\nu$ is the characteristic energy of the X-ray photon, BE is the electron binding
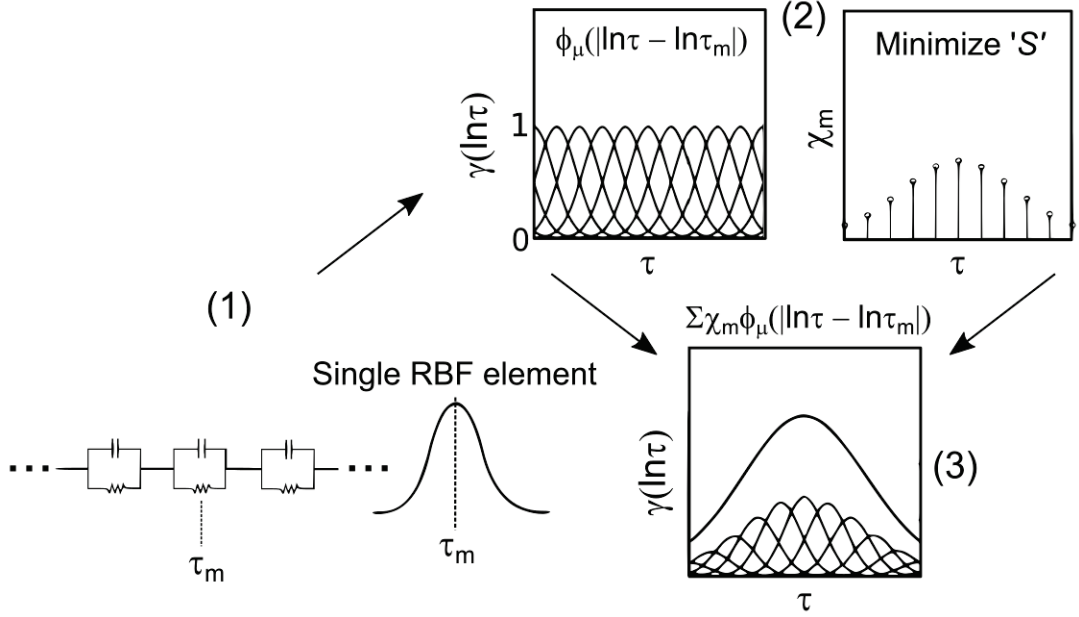
Figure 3.6: Schematic illustrating the main steps involved in distribution of relaxation times analysis. (1) Radial basis functions (RBFs) are used to represent a symmetric, real-valued distribution of relaxation times centred around a mean time-constant ($\tau_m = R_m C_m$). More than one RBF may be needed to fit experimental data. (2) Regularized regression is used to determine the coefficients (x_m) corresponding to each necessary RBF. (3) The coefficients multiplied by the respective RBFs sum to give the total distribution of relaxation times. The figure is adapted from references [135] and [137].

energy (BE), and Φ_S is the sample work function. The free electron is detected by an analyzer, with workfunction Φ_A. As a result, the kinetic energy measured by the analyzer (KE_A) is

$$KE_A = h\nu - BE - \Phi_A \tag{3.27}$$

The analyzer work function can be determined through calibration with a known standard, often a UHV-clean silver surface. Once Φ_A is known, the binding energy of the detected electron is easily determined. The relationships in equations 3.26 and 3.27 is illustrated in Figure 3.7.

The binding energy of an electron is characteristic of its atomic core level; thus, the surface composition of a sample can be determined. The bonding environment
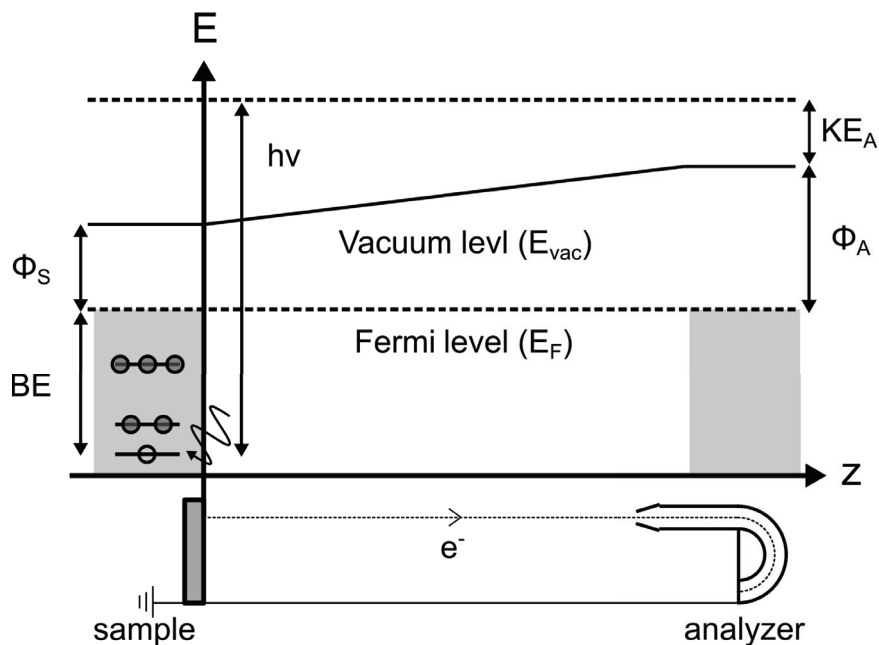
Figure 3.7: Schematic showing the working principle of XPS. All energy levels are referenced with respect to vacuum (E_{vac}).

of an electron can also affect its binding energy. Atoms bound to more electron-withdrawing neighbours will have a higher binding energy than its elemental form; meanwhile, atoms in an electron-rich environment have a lower binding energy. This effect is called a chemical shift.

XPS analysis

The percentage atomic concentration for each element (X_A) can be determined by integrating and scaling the peak intensity relative to the total (scaled) peak area for all elements. This is described mathematically in equation 3.28

$$X_A = \frac{(I_A \mathrm{KE}^a)/(R_A T(\mathrm{KE}))}{\Sigma(I_i \mathrm{KE}^a)/(R_i T(\mathrm{KE}))} \tag{3.28}$$

where I_A is the integrated peak intensity determined from least squares minimization of the root mean-squared error between a theoretical peak lineshape and the experimental data. The exponent a is given in manufacturer specifications and accounts for

the physical configuration of the analyzer relative to the sample. The relative sensitivity factor (R_A) accounts for the electron emission probability, which is dependent on the photoionization cross-section, electron inelastic mean free path and the angle between the incident X-rays and the line connecting the sample with the entrance slit to the analyzer [138]. The function $T(\mathrm{KE})$ accounts for the analyzer transmission of the intensity I_i recorded at kinetic energy KE.

3.2.4 Scanning electron microscopy

Scanning electron microscopy (SEM) uses a focused beam of electrons to measure the topography and composition of a specimen and obtain higher resolution data than allowed by the diffraction limit of light. A high energy beam of electrons (0.1 – 10's keV) is generated by thermionic emission, typically from a tungsten filament. The electron beam is focused onto the sample to produce a spot on the order of 1 nm in size. A 2D image is formed by rastering the electron beam across the sample. Each pixel in the 2D image is representative of a signal intensity at that particular location.

Interaction of the primary electrons with the sample results can produce secondary and backscattered electrons. Information about sample topography is obtained from low energy ($<$ 50 eV) secondary electrons, which are produced from inelastic collisions between the primary electrons and valence electrons near the sample surface. Backscattered electrons are produced from elastic interactions between the primary electron beam and the sample. Backscattered electrons can be used to infer information about elemental composition (and distribution), as the backscattered signal intensity scales with atomic number.
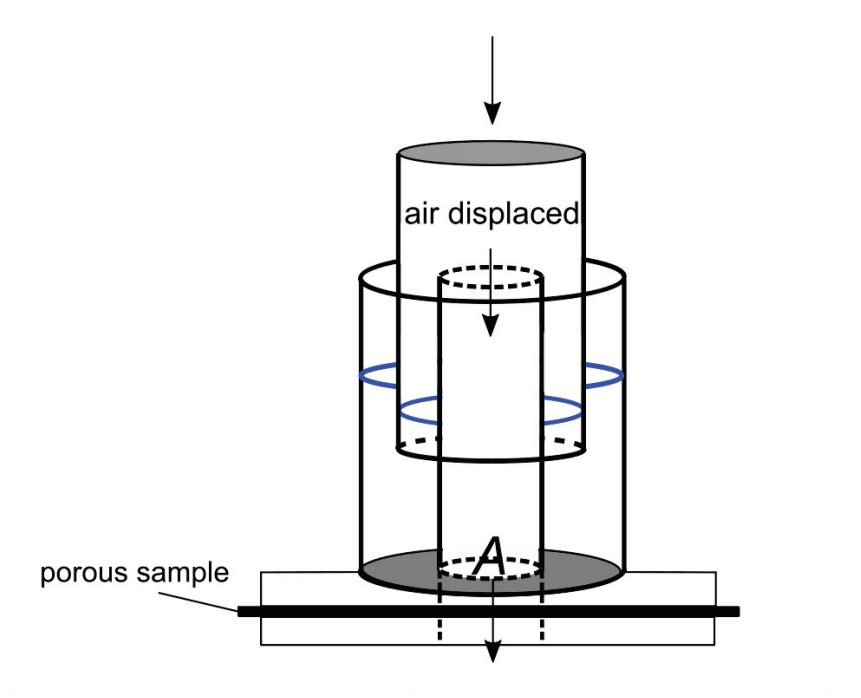
Figure 3.8: Schematic illustrating the Gurley measurement process for a porous material. The fixed inner cylinder channels air through a defined sample area. The middle cylinder floats in a liquid medium (typically oil or water), which is indicated by the blue lines contained within the fixed outer cylinder. Under standard test conditions air (volume = 100 mL) is displaced through a defined area (A = 1 square inch) of a porous sample. The differential pressure forcing the displacement is 1.2 kPa, which can be determined by adjusting the weight of the floating cylinder.

3.3   Membrane characterization methods

3.3.1   Gurley measurement

Gurley measurements are used to characterize the air permeability of a porous material. Specifically, it is the time required for 100 mL of air to pass through one square inch area of material under a differential pressure of 1.2 kPa. A typical Gurley apparatus consists of three hollow, concentric cylinders. The middle cylinder freely floats within the outer cylinder, which is fixed and filled a fluid such as oil or water. The weight of the middle cylinder defines and applies the pressure used to displace air through the fixed inner cylinder, and the sample. The sample is held between two clamping plates with a well-defined orifice area (typically defined by an elas-

tomeric gasket). A stopwatch is used to measure the displacement time. The set-up is illustrated schematically in Figure 3.8.

3.4 Electrolyte characterization methods

3.4.1 Cyclic voltammetry
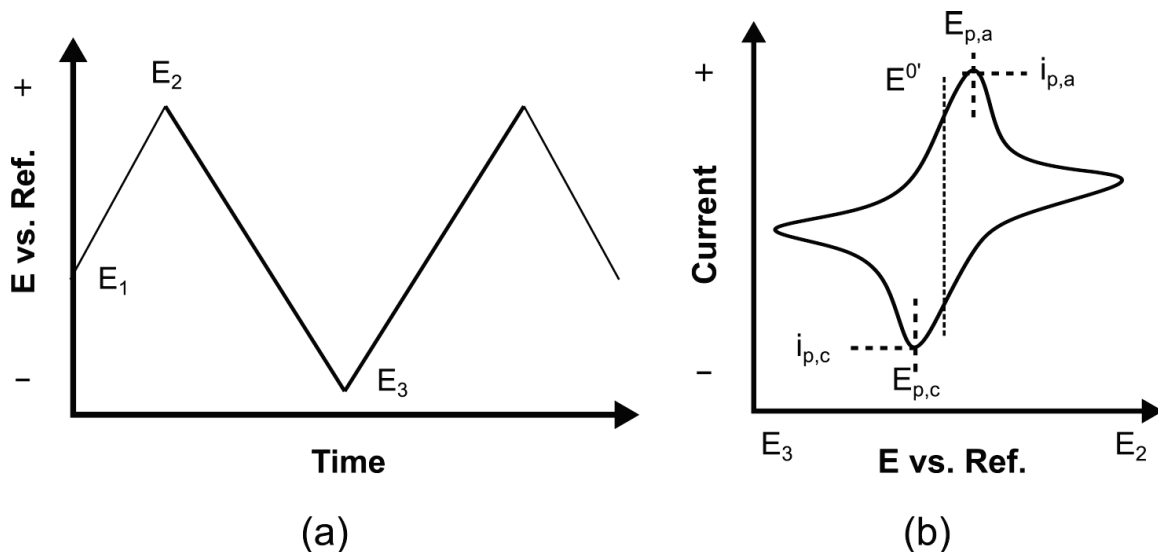
Figure 3.9: (a) A sample linear voltage sweep used in cyclic voltammetry. (b) Example current-voltage trace for an electrochemically reversible system assuming diffusion control.

Cyclic voltammetry (CV) is an electrochemical technique that can be used to study the oxidation and reduction characteristics of electrochemically active materials. CV is commonly performed in a three electrode cell. The working electrode voltage is scanned linearly and at a constant rate with respect a reference electrode. The counter electrode is used to balance current passed through the working electrode. The working electrode potential can be described by

$$E(t) = E_1 - vt \tag{3.29}$$

where v is the scan rate (V s^{-1}), t is the elapsed time (s), and E_1 is the starting

potential (V). When the voltage reaches a specified limit, the scan direction is reversed until the second limit is reached. This cycle may be repeated more than once, as illustrated in Figure 3.9a. To minimize solution resistance, CV is performed in a high concentration supporting electrolyte - a highly soluble salt that is not electrochemically active over the voltage range of interest [139]. In the following sections we examine the current resulting from these potential sweeps assuming cases of Nernstian and activation control.

Nernstian (reversible) systems

When an electrochemically active material is present at the working electrode surface, a Faradaic current is induced as the working electrode approaches the standard reduction potential of the material (E^0). (A Faradaic current results from charge-transfer between the active material and the electrode). For a chemically and electrochemically reversible system, charge-transfer is not rate-determining and the concentrations of the oxidized and reduced species are established immediately as described by the Nernst equation

$$E = E^0 + \frac{RT}{nF} \ln \frac{[Ox]}{[Red]} \tag{3.30}$$

where E is the working electrode potential (V), R is the universal gas constant (8.314 J K^{-1} mol^{-1}), T is the cell temperature (K), F is the Faraday constant (96485 C mol^{-1}) and n is the number of electrons involved in the reaction. For a reversible system, a peak Faradaic current (i_p) arises, which results from a trade-off between Nernstian and diffusion control. The peak current is described by the Randles-Sevcik equation

$$i_p = 0.466nFAC^0(\frac{nFvD_0}{RT})^{\frac{1}{2}} \tag{3.31}$$

where A is the geometric surface area of the electrode. A sample CV trace is shown

in Figure 3.9b. For electrode potentials above this corresponding point, the resulting current is limited by diffusion.

For a reversible system, the separation (ΔE_p) between the anodic $(E_{p,a})$ and cathodic $(E_{p,c})$ peak potentials is independent of scan rate. In general, the peak separation for a reversible system at 25 ^{o}C is equivalent to [140]

$$\Delta E_p = E_{p,a} - E_{p,c} = \frac{2.3RT}{nF} = \frac{59\text{mV}}{n} \tag{3.32}$$

The formal reduction potential $(E^{0'})$ of the system can be deduced from the anodic and cathodic peak potentials as described below

$$E^{0'} = \frac{E_{p,a} + E_{p,c}}{2} \tag{3.33}$$

where the formal reduction potential $(E^{0'})$ replaces the standard reduction potential and is representative of the specific experimental conditions being used.

Irreversible systems

For irreversible systems, the resulting CV current is determined by activation control (i.e. charge transfer of either an electron, or ion between the electrode surface and solution), diffusion control, or a mixture of the two. As a positive (or negative) overpotential is applied near the standard reduction potential, a net positive (or negative) current flows. As the overpotential increases, so does the resulting current until diffusion control eventually limits the maximum current. Between the regions of activation and diffusion control, a peak current occurs, which is described by

$$i_p = (2.99 \times 10^5)AC^0(\alpha D_0 \nu_0)^{\frac{1}{2}} \tag{3.34}$$

where α is a charge-transfer coefficient that encompasses information about the symmetry and stoichiometry of the reaction. For completely irreversible systems the peak

potential where i_p occurs (E_p) is a function of scan rate, which shifts by approximately 30 mV/α for every ten-fold increase in scan rate [140].

3.4.2   Infrared Raman spectroscopy

Raman spectroscopy examines the vibrational (and other) modes of molecules. The information obtained from Raman spectroscopy can often be used to identify molecular bonds, chemical structure and intermolecular properties (such as material phase and crystallinity). A monochromatic laser (typically infrared) is used to illuminate a liquid or solid sample. If Raman-active modes are present, the photons will undergo inelastic scattering, resulting in energy loss (Stokes shift) or energy gain (anti-Stokes shift). The energy shift is measured as a change in wavelength of the incident photon, so the sample emittance is typically plotted as a function of this wavelength difference (i.e. the Raman shift). Raman spectroscopy commonly employs a Michelson interferometer to identify the sample emission wavelengths. A practical interferogram detects signals for all wavelengths simultaneously and is then processed using Fourier transforms to identify the contributing frequencies.

A sample is Raman-active if it contains polarizable bonds. The signal strength depends on how easily the electron distribution may be deformed by an electromagnetic field to produce a temporary dipole. Loosely bound electrons will have an intense scattering signal; however, Raman scattering is an inherently weak process (less than 0.001 % of the source intensity is scattered). Because of this, it is common to use an infrared, or near-infrared wavelength source laser; this reduces problems with sample fluorescence washing out the Raman signal.

3.4.3   Fourier transform IR spectroscopy

Fourier transform infrared spectroscopy (FTIR) is a complementary technique to Raman measurements as modes that are not Raman-active are often infrared (IR)-

active. IR-active bonds must have a dipole moment, which changes as a function of time. Absorption occurs if the changing dipole frequency matches the frequency of incident radiation. Symmetric bonds with identical (or nearly) identical functional groups on opposite sides will not be IR-active. The IR-absorption frequency is unique to each bond and may be shifted depending on its chemical environment.

FTIR instrumentation commonly uses an attenuated total reflectance (ATR) sampling technique. A liquid/solid sample is placed on a crystal (typically germanium, zinc selenide, or diamond) and IR light is incident through the crystal such that it undergoes total internal reflection. An evanescent wave from the IR light travels into the sample where it may be absorbed. When energy is absorbed the envanescent wave returning into the crystal is attenuated, which is registered by the IR detector. An interferometer is used to collect absorption data for a range of frequencies at once, and fourier transformation is used to interpret the time-dependent intensity interferogram into a frequency dependent absorption spectrum.

3.4.4   UV-Visible absorption spectroscopy

UV-Vis absorption spectroscopy quantifies sample absorption within the ultraviolent and visible light range. A monochromator scans an incident light source through a range of wavelengths. The light is split into a reference beam, and a second beam (which travels through the sample). The incident light may be absorbed to enable electronic transitions as it passes through the sample. (The sample beam may also be attenuated due to reflection, or scattering from the sample surface). The apparent sample absorbance (A) is determined from the ratio of the light intensity transmitted through the sample (I) compared to the intensity measured from the reference beam (I_0)

$$A = \log_{10}(\frac{I}{I_0}) \tag{3.35}$$

Chapter 4

Experimental Methods

4.1 Flow cell preparation and assembly

4.1.1 Flow cell design

The low-volume flow cells used in this thesis are replicated from the "Gen 2" cell design shared by the Brushett research group at MIT. The original drawings and assembly methods are detailed in the appendix of Dr. Milshtein's PhD thesis [141]. Briefly, the endplates were machined from 0.75 inch thick polypropylene stock, which was selected for its chemical compatibility with both acetonitrile and aqueous potassium hydroxide solution (pH 9). Flow fields with either an interdigitated, or serpentine flow channel design were machined from 0.25 inch thick impervious graphite stock. It is critical to use impervious graphite (resin impregnated, or pyrolitically sealed) to prevent electrolyte loss through microscopic pores. The completed flow fields were polished with 400 grit WaterPaper to seal against the endplate o-rings and the gaskets. The endplate design was modified to reduce the o-ring groove depth by $0.1 - 0.2$ mm. This was needed to compress the endplate o-ring by $20 - 30$ %, which is recommended for static face-seals. Gaskets were punched from either EPDM or PTFE sheets to seal against the inner face of the graphite flow fields.

Electrolyte connections to the endplates were made using chemically resistant polypropylene NPT fittings, which were wrapped tightly using half-inch wide PTFE tape. In some instances a hose-barb tubing to NPT fitting was used to minimize the number of adapters and fittings required; the pump tubing (Norprene A 60 G) was connected directly to the cell. In other cases, more chemically resistant 0.125 inch outer diameter PTFE tubing (McMaster, 5239K24) was used to transport electrolyte between the pump and cell. In these cases, cell connections were made using chemically resistant polypropylene compression to NPT fittings. In early cells, the reservoirs were fashioned from 20 mL borosilicate glass vials with PTFE lined caps. Two undersized holes (less than the Norprene tubing diameter) were drilled into each cap to maintain a tight seal around the Norprene tubing and minimize solvent loss during cycling. In later cells, 22 mL and 60 mL PFA Savillex-brand impingers were used as reservoirs for better sealing. (Part numbers are given in Appendix A). A Masterflex L/S series peristaltic pump was used to circulate electrolyte between the cell and reservoirs. Figure 4.1 shows an image of the first version of our assembled cell (used in Chapter 4).

Electrical connections to the cell were also modified from the "Gen 2" design. The banana plug connections were replaced by lug terminated coaxial cables, which were connected to the potentiostat in a 4-terminal/remote sense configuration. The inner conductors were used as sense leads, and the outer conductors were used as the signal leads. A plastic bolt, a spring and some washers were used to maintain a firm connection to the graphite tab. The test leads connected to a graphite tab are pictured in Figure 4.1b. It is important to note that small stainless steel washers were used between the lug connections and the graphite tab – these were necessary to prevent corrosion of the test leads by leaked electrolyte.

Where our cell is modified slightly from the MIT design, a full parts list for each set of experiments is given in the appendix. The reader is recommended to refer to
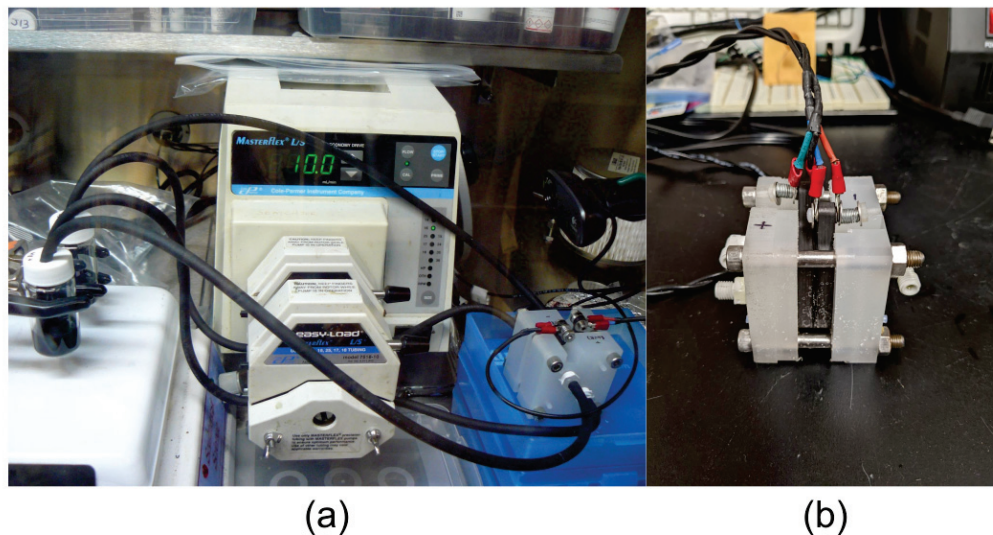
Figure 4.1: Image showing an assembled flow battery used in the vanadium (III) acetylacetonate degradation study: reservoirs (left), pump (center) and cell (right) (a). The webcam used to monitor reservoir electrolyte levels is also seen on the right. A close-up image of the electrical connections to the graphite tabs is shown in (b).

Dr. Milshtein's PhD thesis for detailed CAD drawings (recalling the o-ring groove modification noted above) [141].

4.1.2 Flow cell assembly

Prior to cycling, all cell components in direct contact with the electrolyte were thoroughly cleaned. The endplates, fittings and reservoirs were scrubbed with Sparkleen lab detergent and ultrasonicated for 10 minutes each in acetone, methanol and deionized water. As a final step, the components were rinsed three times with nanopure water (NPW). Ultrasonication is reported to damage the gaskets and flow fields; these were rinsed thoroughly with acetone, methanol and three times with NPW, but were not sonicated.

Prior to a cycling experiment, the cell was assembled (with a separator, but no electrodes) and flushed with 15 mL of clean supporting electrolyte for two hours. (The supporting electrolyte was chosen to be the same as that used during the experiment.)

The purpose of this step was to rinse the Norprene tubing and to leak test the NPT fittings and adapters, which were the most frequent source of leakage. The reservoirs were monitored with a webcam programmed for periodic image capture to ensure that no solvent loss or volume imbalance occurred, the latter of which may arise from pressure imbalances resulting from asymmetric cell/tubing arrangement. The cell was disassembled, rinsed and allowed to dry overnight before re-assembling with electrodes and a new separator for measurement.

The aqueous quinone cells in Chapter 6 were assembled using four sheets of SGL 39AA carbon electrodes (1.6 x 1.4 cm) on each side of the cell. The electrodes were pre-treated by heating at 400 °C for 8 hours in air. The electrodes were subsequently treated with UV-ozone for 10 minutes on each face. The electrodes were sealed into the cell using 0.030 inch thick gaskets (PTFE, or EPDM). A one inch square section of Fumasep E-620K membrane was used as-received. The cell components were held together using four 1/4-28 bolts tightened to 20 in lbs, using a torque wrench to maintain even compression. The final electrode compression was estimated to be approximately 75 % of its original thickness. Electrolyte preparation procedures are described in Chapter 6.

The non-aqueous cells in Chapters 7 were assembled using 2 sheets of SGL 39AA carbon electrodes (1.6 x 1.4 cm) on each side of the cell. The electrodes were used as-received, and were sealed into the cell using 0.015 inch thick EPDM gaskets. A one inch square section of Daramic 175 separator was used as-received. The cell components were held together using four 1/4-28 bolts tightened to 12 in lbs, using a torque wrench to maintain even compression. The final electrode compression was estimated to be approximately 80 % of its original thickness. Electrolyte preparation procedures are described in Chapter 7.

To minimize cell exposure to ambient oxygen (and moisture), tubing and assembled cells were stored under rough vacuum (-30 in Hg) for at least 24 hours. The

tubing and cells were back-filled with nitrogen to atmospheric pressure before transferring into the glovebox, or the nitrogen testing box described in the following section. Non-aqueous solution preparation was carried out in an N_2-filled glovebox (MBraun, Unilab), and aqueous solution preparation was performed in the nitrogen testing box using sparged NPW.

Atmospheric control

The electrolyte plumbing in RFBs is a closed system; however, sealing at the cell reservoirs and fittings is imperfect in many research-scale set-ups. As a result, ambient oxygen is known to reduce Coulombic efficiency during cycling by oxidizing reduced species in the negolyte. Ambient oxygen and moisture are also detrimental to cell stability when electrolyte degradation pathways are oxygen-mediated [2,25], or in non-aqueous cells, where the cell voltage exceeds the electrochemical stability window of water (leading to oxygen and hydrogen evolution reactions at the electrodes).

To reduce cell exposure to oxygen and moisture, a dry nitrogen testing box was built from a benchtop sandblasting cabinet (Princess Auto, 8014659). The cabinet seams were sealed with silicone caulking. Adhesive Neoprene foam (3/8" wide and 3/8" thick) and wood clamps were used to seal the viewing window; while, o-rings and grommets were used to seal the electrical and gas feedthroughs. A high purity nitrogen cylinder (Air Liquide, 99.999 %) was plumbed through a 2 stage regulator to continuously purge the box (0.05 L/min), exhausting through a check valve. Box oxygen was monitored using a handheld oxygen sensor. After purging the oxygen concentration remained below 1 – 2 % by volume while cycling under the continuous nitrogen flow. (The reliable detection limit for the oxygen sensor is 1 % by volume). Two back-up power supplies (APC Schneider electric, BR1000MS) were used: one for the potentiostat, and one for the temperature controller and pump. Using a 100 mA cm^{-2} cycling current and 60 mL min^{-1} flow rate, the power supplies are rated to last

20 - 30 minutes – enough time to softly shut-down the equipment during unplanned power outages.
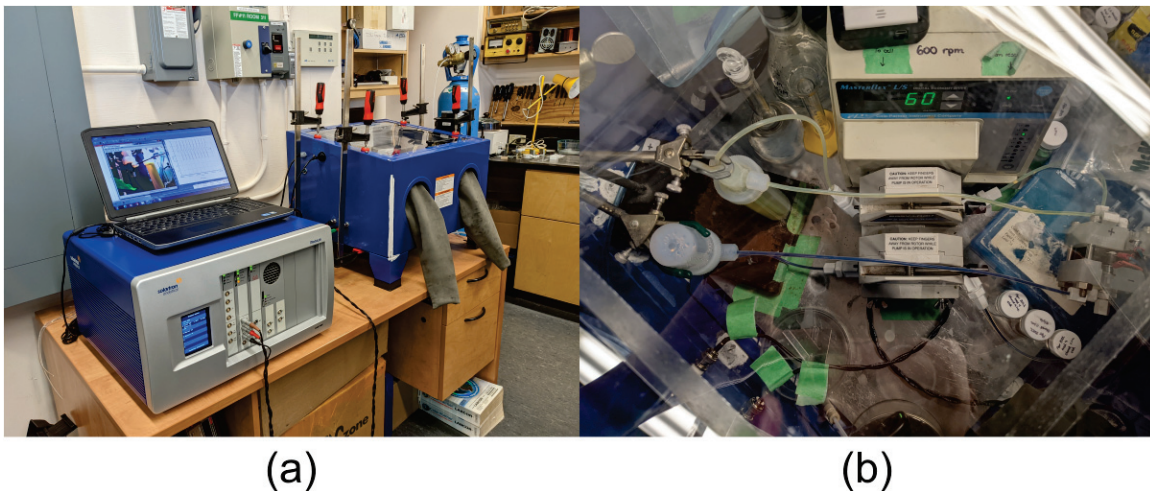
Figure 4.2: Photo of the nitrogen testing box and Modulab potentiostat (a). A bird's-eye view of the flow cell arrangement within the testing box (for the aqueous RFB) is shown in (b).

Temperature control

High-temperature measurements were performed by connecting flexible silicone heaters to an aluminium cell enclosure (Figure 4.3(a)). Clearance holes were created in the enclosure for transport tubing to connect the cell, reservoirs, and pump. The enclosure temperature was maintained at 40 °C using an Omega CN720 PID temperature controller. The cell temperature was independently monitored using a Eurotherm 2216e temperature controller, which was interfaced with the Modulab XM software to record the cell temperature while cycling.

Low-temperature measurements were performed using an Daho-80 environmental testing chamber (ETC). The cell and reservoirs were contained in the ETC, while the electrolyte was cycled using a pump outside of the ETC. The cell temperature was independently monitored using a Siglent digital multimeter, and a LabView data ac-

quisition program. An ETC setpoint of -4 ºC was used to maintain a cell temperature of 0 ºC (Figure 4.3(b)).

High-temperature (and room-temperature) cycling were performed under atmospheric control as described in section 4.1.2. Low-temperature cycling was performed under ambient atmosphere (although cells were assembled under nitrogen).

(a)   (b)
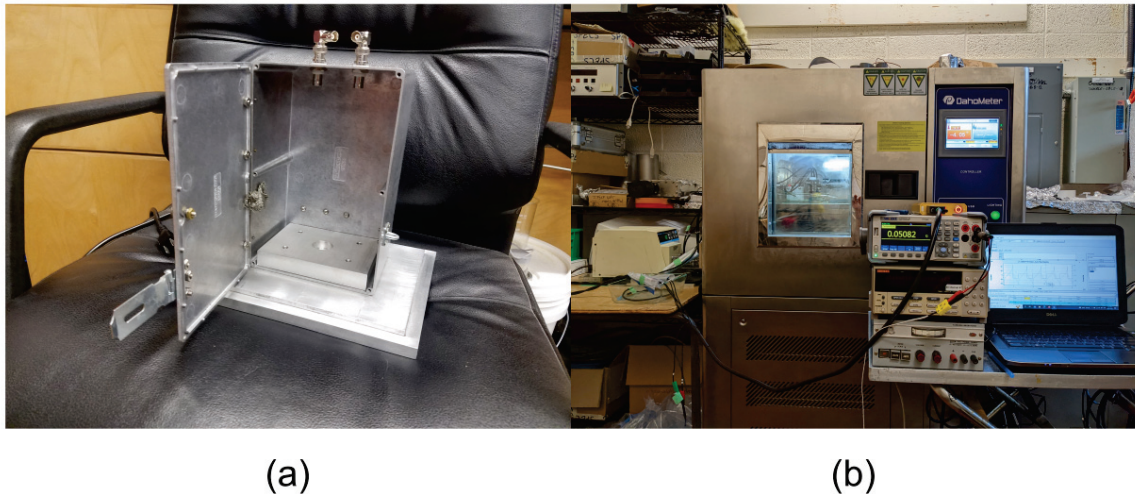
Figure 4.3: Photo of the heating box used to maintain a 40 ºC cell (a). Photo of the ETC, pump, potentiostat and multimeter set-up used for low-temperature RFB cycling (b).

4.1.3 Electrochemical (three-electrode) cell preparation

Three-electrode measurements (CV and EIS) were performed in a BaSi® VC-2 Voltammetry Cell. These borosilicate glass cells were cleaned before each experiment by ultrasonicating sequentially in acetone, methanol and NPW for 10 minutes each. When the cells were first used (i.e. the usage history was unknown), they were first scrubbed with Sparkleen detergent and de-ionized water before ultrasonicating as described above. For non-aqueous measurements, the cells was dried at 120 ºC for 2 hours prior to measurements. Preparation methods for the cell electrodes are described below.

Working electrode (glassy carbon)

A 3.0 mm diameter glassy carbon electrode (GCE) (BaSi®, MF-2012) was prepared by polishing using 15 μm, 3 μm and 1 μm diamond grit, rinsing thoroughly with methanol between each step. A slurry of 0.05 μm alumina grit was used as a final polishing treatment until a mirror-like finish was achieved. In between experiments the electrode was cleaned by rinsing with the same (clean) solvent used in the previous experiment (either de-ionized water, or acetonitrile) and wiping dry with a Kimwipe. The electrode was then rinsed and wiped with a methanol-soaked Kimwipe. The GCE was re-polished when switching between aqueous and non-aqueous electrolyte systems.

Working electrode (carbon paper and carbon felt)

Figure 4.4 shows an image of the assembly used to prepare strips of carbon paper (and felt) for use as the working electrode in three-electrode CV and EIS measurements. A 3 mm x 15 mm strip of the carbon electrode was mounted between two sheets of 0.060" PTFE. The bottom sheet contained two 4-40 tapped holes and a narrow groove (0.010") into which a 0.020" diameter 316-stainless steel wire was inserted. (The stainless steel wire served as a current collector to connect the carbon electrode to the potentiostat test leads). The carbon paper was fastened between the two sheets of PTFE using two 1/4 x 4-40 PEEK screws. The large plastic block shown was used as an alignment tool for electrode assembly to ensure that a repeatable area of carbon paper was exposed below the two PTFE sheets. The exposed area (3 mm x 3 mm) represents the geometric active area for the electrode. Figure 4.4d shows the full electrolytic cell before the carbon paper electrode was lowered into the electrolyte. The black PEEK rod was marked to ensure that the electrode was submerged to a repeatable depth such that the section of exposed carbon paper was completely wetted, but the stainless steel current collector did not contact the electrolyte.

Between experiments the PTFE sheets, PEEK screws and rod were cleaned as described in 4.1.3. Carbon paper and felt electrodes were not reused between experiments. Any pre-treatment methods for the carbon electrodes are indicated where appropriate in the thesis. When mounting between the PTFE sheets, the strips were handled to avoid contacting the active area below the PTFE sheets.

(a)   (b)   (c)   (d)
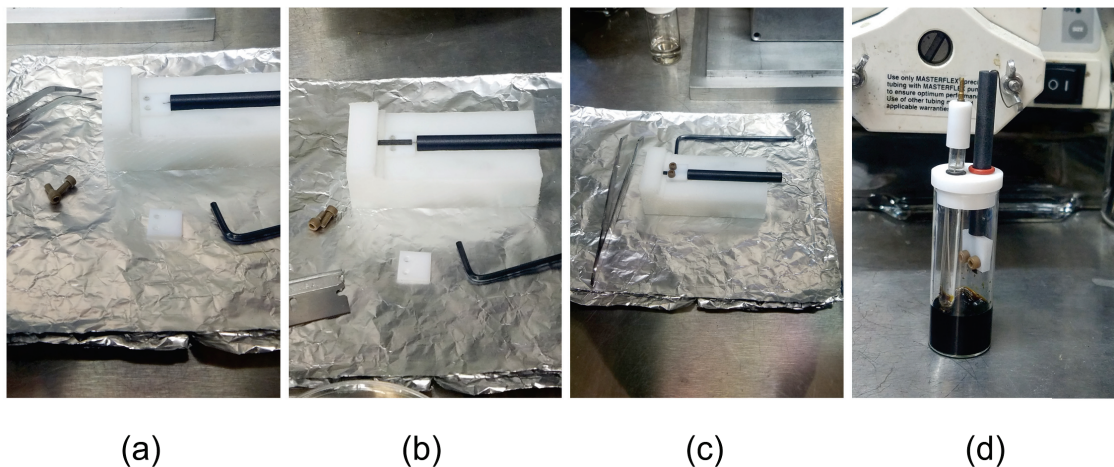
Figure 4.4: Images illustrating carbon paper preparation and mounting for three-electrode measurements. A plastic block is used as an alignment tool to hold the PEEK rod in place with a PTFE sheet (a). The alignment block is machined such that the PTFE sheet abuts a 3 mm wide ledge. A 3 x 15 mm strip of carbon paper is placed on top of the first PTFE sheet such that it contacts the stainless steel wire, and also lays over the 3 mm wide ledge, flush with the alignment block (b). A second PTFE sheet is used to secure carbon paper. It is held in place using two PEEK screws (c). The mounted carbon electrode is pictured in the three-electrode cell outside of the electrolyte (d). When measurements are performed it is lowered to just submerge the exposed 3 x 3mm square of carbon paper. (The PTFE sheets are not submerged).

Reference electrodes

The reference electrodes were prepared as described in BaSi® documentation. For non-aqueous measurements, a silver/silver ion (Ag/Ag$^+$) reference electrode was selected (BaSi®, MF-2062). The Ag/Ag$^+$ reaction proceeds as follows Ag$^+$+e$^-$ $\rightleftharpoons$ Ag and occurs at approximately 0.54 V vs SHE [142]. Prior to assembly, the glass body

and Vycor frit were dried at 120 ºC under rough vacuum to minimize moisture and oxygen exposure to the cell. The electrode was prepared in an MBraun glovebox by filling with 0.8 mL of 0.1 M electrolyte and submerging the Vycor tip in the same 0.1 M electrolyte for at least 30 minutes. (The electrolyte was selected to match the supporting electrolyte used in the experiment: in this thesis, either tetraethylammonium bis(trifluoromethanesulfonyl)imide (TEATFSI), or tetraethylammonium tetrafluoroborate (TEABF$_4$) in acetonitrile). After 30 minutes, the electrode was refilled with 0.1M electrolyte containing 0.01 M silver nitrate (AgNO$_3$). A clean silver wire was inserted into the electrode body and sealed with a PTFE cap. When preparing reference electrodes, it is important to tap the electrode after filling to remove any trapped gas bubbles attached to the frit. Between experiments, the electrode was filled and stored in a fresh solution of 0.1 M electrolyte.

For aqueous measurements, a silver/silver chloride (Ag/AgCl) reference electrode was selected (BaSi®, MF-2056). The Ag/AgCl reaction proceeds as $AgCl_{(s)} \rightleftharpoons Ag^+ + Cl^-$ and occurs at approximately 0.23 ± 0.01 V vs SHE. The electrode was prepared by filling with 3.0 M KCl solution, and was stored in 3.0 M KCl solution when not in use. The standard electrode potentials for the reference electrodes used in this thesis are stated in Table 4.1 for reference.

Table 4.1: Room temperature standard electrode potentials for reference electrodes used in this thesis (referenced to SHE).

Electrode	Electrolyte/filling solution	E^0 vs. SHE (V)
Ag/AgCl	3.0 M KCl	0.21
Ag/Ag$^+$	0.1 M TEATFSI or TEABF$_4$/ACN	0.54

Counter electrode

A 25 x 25 mm 52 mesh platinum (Pt) gauze (0.1 mm wire diameter) was used as the counter electrode. The Pt gauze was cleaned in between experiments by rinsing with the same (clean) solvent used in the previous experiment (either water, or ace-

tonitrile), then wiping gently with a methanol-soaked Kimwipe. The mesh was then ultrasonicated sequentially in acetone, methanol and NPW for 10 minutes each. The estimated surface area for the Pt wire electrode was 560 mm^2. This is approximately 80 times larger than the surface area for the GCE, and 3 times larger than the estimated surface area for the 3 x 3 mm carbon paper samples. While the surface area ratio between the platium CE and carbon paper was not ideal, it was the largest that could be feasibly achieved given the geometric constraints of our cell.

4.2 Flow cell cycling

Cell cycling was performed using a Solartron Analytical Modulab ECS, or an Ivium Vertex.C potentiostat to charge and discharge the cell. A Masterflex L/S Digital Economy Drive (07524-40, or 07524-50) was used to circulate electrolyte through the cell. Prior to charge-discharge cycling, the electrolyte was flushed through the cell for a minimum of 1 hour, periodically shifting and tapping the cell to remove trapped gas bubbles and ensure the electrodes were fully wetted. A low flow rate (8 - 10 mL min^{-1}) was used initially to avoid damaging the membrane as the cell was filled. After a few minutes, the flow rate was increased to its desired setpoint. The cycling and impedance tests performed on the full cell are described in the following subsections. All electrical measurements were performed using a 4-terminal/remote sense configuration (i.e. separate sense and current/voltage leads were connected at both the anode and cathode).

4.2.1 Stability cycling

The cells were charged and discharged using a constant current between fixed voltage limits. The measured voltage signal was averaged over a 10 mains cycle integration period. The sample rate was the lesser of 5 mV or 20 seconds (for voltage mea-

surements), and 0.1 mA or 20 seconds (for current measurements) – i.e. data was recorded when the voltage changed by $\pm$ 5 mV or 20 s, whichever occurred first. The upper voltage cutoff was selected to be within the electrochemical stability window of the supporting electrolyte and solvent, while the lower voltage cutoff was selected to correspond to approximately 1% SOC. EIS measurements were performed on the first and last cycle as described in section 4.2.2

Aqueous cell cycling

The aqueous cells examined in Chapter 6 were cycled using methods outlined by Ji *et al.* [2]. Briefly, the cells were charged and discharged using a 100 mA cm^{-2} current density with respect to the geometric membrane area (224 mA). The cells were cycled at constant-current between 0.5 – 1.5 V and 0.6 – 1.4 V charging limits. The cell was held at each voltage limit until the current density decayed to 2 mA cm^{-2} to fully charge/discharge the cell. A flow rate of 60 mL min^{-1} was used for all experiments. In addition to these cycling procedures, full cell EIS was performed periodically every 10 cycles at 50 % SOC to monitor cell impedance growth while cycling. The EIS measurements are described in section 4.2.2.

Non-aqueous cell cycling

The non-aqueous cells examined in Chapter 7 were cycled between 0.9 V and 1.3 V charging limits at constant current, while pumping electrolyte at a 10 mL min^{-1} flow rate. The optimal cycling current was first selected by examining the cell efficiency for a range of cycling currents (5 - 25 mA cm^{-2}). The current that yielded the highest energy efficiency was selected for long-term stability cycling. The optimal cycling current is a trade-off between a higher Coulombic efficiency (achieved using higher cycling currents) and a higher voltage efficiency (achieved using lower cycling currents). During long-term stability experiments the cell was charged and discharged at the

selected current between the voltage limits. Every fifth cycle, the cell was charged and discharged using the constant-current followed by constant-voltage method described in the previous section. This was used to assess the true cell capacity in the absence of impedance growth. EIS measurements were also performed at 50 % SOC every fifth cycle as described in the following section.

4.2.2 Full cell EIS

Full cell EIS measurements were performed on the first and last cycles of an experiment, and also periodically during cycling (every 5 or 10 charge-discharge cycles). Before each EIS measurement the cell was pre-conditioned to achieve 50% SOC by discharging at constant-current to the desired voltage (determined from the Nernst equation). The cell was then discharged at constant-voltage until the current density decayed to ± 2 mA cm^{-2}. This threshold was selected based on reports from the Aziz and Zawodinski research groups [2, 59]. EIS measurements were then performed at 0 V with respect to the measured open-circuit voltage of the cell. Unless otherwise noted, data were collected using a 10 mV sine wave perturbation between 1 MHz and 10 mHz with a sampling frequency of 5 points/decade. In some instances a 10 point/decade sampling frequency was used to better resolve features at higher frequencies. At the beginning and end of stability experiments, EIS measurements were performed both with and without electrolyte pumping.

4.2.3 Self-discharge measurements (OCV measurements)

Open-circuit voltage measurements were performed to assess self-discharge rates due to active species crossover through the membrane/separator. Measurements were performed by first charging the cell to its upper voltage cycling limit. Charging was performed using a constant-current, followed by a constant-voltage hold at the upper voltage limit (until the measured current density dropped to 2 mA cm^{-2}). The

potentiostat was used to record the cell OCV every five minutes for 8 to 24 hours. (The Masterflex pumps were left on to continue circulating electrolyte throughout these measurements).

4.3   Cell disassembly

After cycling, the cells were discharged to 0 V at constant-current, followed by a constant-voltage hold over several hours. The electrolyte was returned to the cell reservoirs, harvested and stored under nitrogen until *post-mortem* characterization. Clean solvent was circulated through the cell for 5 minutes to rinse the internal components, then discarded. This was repeated twice more with fresh solvent. The cell was disassembled, to harvest the electrodes and separator for *post-mortem* characterization. The harvested components were thoroughly rinsed in 2 mL of clean solvent by gently swirling for 30 seconds in a clean glass vial. The solvent was discarded and the rinse was repeated 12 times (well after the rinsed solvent appeared clear). The electrodes were dried (passively) in a nitrogen-filled glovebox, and stored in sealed glass vials until *post-mortem* characterization. The separators were stored in vials containing clean solvent in the glovebox until characterization. (Ion-exchange membranes commonly experience areal expansion under hydration, and contract when dried. To minimize further stress to the membranes they were stored in a hydrated state after cycling.)

4.4   Post-cycling electrode characterization

4.4.1   Single electrode EIS

Single electrode EIS measurements were performed in three-electrode cells (preparation described in section 4.1.3). The measurements were performed in a BaSi VC-2

Voltammetry cell filled with 5.0 mL of electrolyte. The electrolyte was prepared identically to the solutions used in full cells. The cell was pre-conditioned using a constant DC-bias for 3 minutes, or until the current density decayed to ± 2 mA cm^{-2}. EIS data were then collected under DC bias using a 10 mV sine wave perturbation between 1 MHz and 10 mHz with a sampling frequency of 5 points/decade. The bias voltage was selected from the half-cell voltage determined from the Nernst equation at the specified SOC. The rationale behind this bias and pre-conditioning treatment was to establish a local electrolyte concentration (representative of a specific SOC) at the electrode surface. Aqueous cells were prepared and measured under a blanket nitrogen set-up (described in section 4.1.2). Non-aqueous cells were assembled and measured in an oxygen- and moisture-free environment (MBraun glovebox: $O_2 \leq 0.1$ ppm and $H_2O \leq 1.2$ ppm).

EIS analysis

Equivalent circuit analysis for full cell and single electrode EIS data was performed using the Modulab XM Studio software and a Python impedance analysis package – "impedance.py", which was developed by Murbach *et al.* [143]. Selection of equivalent circuits is described in each results section. DRT analysis was performed to inform equivalent circuit selection using open-source Python software developed by the Ciucci research group [135–137].

4.4.2 X-ray photoelectron spectroscopy

XPS was used to detect insoluble degradation products on electrochemically cycled carbon electrodes. The cycled electrodes were harvested as described in Section 4.3, then stored under rough vacuum overnight. Samples were cut into 9 x 9 mm sections and mounted onto stainless steel sample pods using a 7 mm diameter aperture, machined from 0.005 inch 316 stainless steel shimstock (Figure 4.5). In early experiments,

carbon tape was used as an adhesive instead of an aperture - these experiments are appropriately indicated. Samples were mounted and transferred into the XPS chamber under blanket nitrogen to minimize surface contamination. All measurements were performed under ultra-high vacuum (UHV) using a dual-anode (Al/Mg) X-ray source and a Specs Phoibos 150 hemispherical analyzer. Survey and high-resolution spectra were collected in Fixed Analyzer Transmission mode at a base pressure of 2.0 x 10^{-10} mbar using a 1.4 x 4 mm spot size and a 2 x 2 mm spot size. Both Mg-Kα (1253.6 eV), and Al-Kα (1486.6 eV) sources were used. Whenever possible, spectra were collected on multiple samples to ensure that data were representative for each electrode.
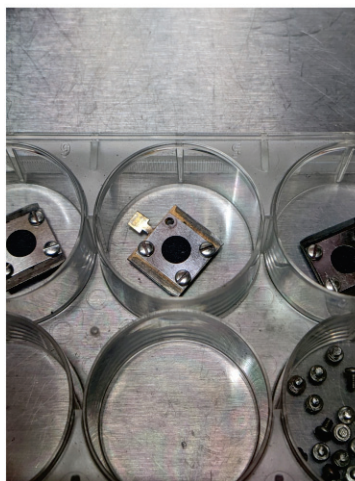
(a)   (b)

Figure 4.5: Image of the sample mount and aperture used for XPS measurements. A carbon electrode sample prepared for measurement is also shown.

XPS analysis

CasaXPS was used to analyze high-resolution XPS spectra. Fitting was performed using a Shirley background and Gaussian-Lorentzian peak shape to integrate the peak intensity. The integrated intensity was scaled with the appropriate analyzer transmis-

sion function, RSF factor and inelastic mean free path for each element (as described in 3.2.3). The scaled intensities were used to determine the relative abundance of detected elements.

4.4.3   Scanning electron microscopy

SEM was used to observe qualitative changes to the surface of electrochemically cycled carbon electrodes. A Phenom benchtop SEM was used to collect low and high magnification (500 – 10000x) images of carbon electrodes before and after cycling in the vanadium system. The Phenom benchtop SEM contains detectors that are sensitive to both secondary and backscattered electrons. For each measurement, the prepared carbon electrodes (Section 4.3) were cut into 3 x 4 mm sections and adhered to a standard electrode mount using double-sided copper tape. Images were collected in three different locations on each sample. For later experiments, a Thermo-Fisher Chem-Axia SEM was used to compare electrode samples. Images were collected between 100 – 10000 x magnification using the Everhart-Thornley detector to detect secondary electrons.

4.5   Post-cycling membrane/separator characterization

4.5.1   Impedance measurements

Membrane/separator impedance measurements were performed following a protocol described by Liang *et al.* [5]. The flow cell was assembled without carbon electrodes, using the methods described in section 4.1.2. In addition, the reservoirs were filled with only supporting electrolyte (no redox active species). Cycled separators were aligned to replace the cycled active area within the gasket window. (This was facilitated by visible separator staining, Figure 4.6c). The cell was connected to a

Modulab ECS potentiostat in a remote sense configuration, and EIS spectra were collected using a 10 mV perturbation between 1 MHz to 1 Hz (5 points/decade sampling frequency). Measurements were performed with and without the separator present. The membrane impedance was taken to be the difference in high-frequency resistance between measurements performed with and without a separator.

(a)   (b)   (c)
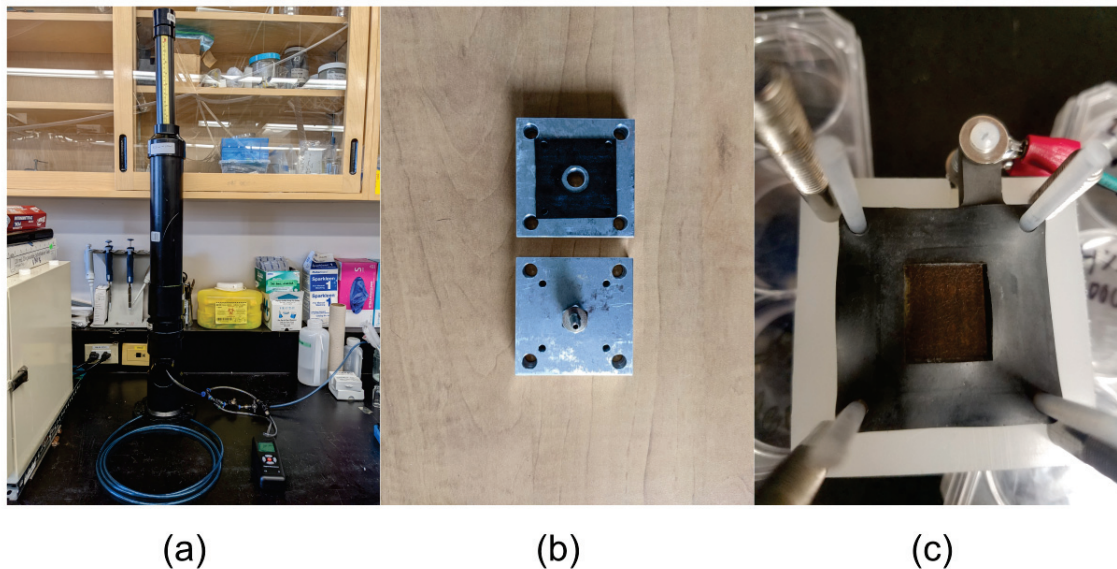
Figure 4.6: Image of Gurley measurement apparatus (a), and Gurley measurement sample holder (b). The placement of a cycled Daramic separator for membrane impedance measurements is shown in (c). The staining is clearly visible and used as a guide to align the cycled active area with the gaskets.

4.5.2 Gurley measurements

Gurley measurements were performed using a home-build apparatus pictured in Figure 4.6a. The membrane sample was sandwiched in the holder pictured in Figure 4.6b between two gaskets with a 0.2 in^2 active area. The air displacement apparatus was set to an inner column height of 13 cm. The time required to displace 100 mL of air using a 1.2 kPa pressure differential was measured by recording the time required for the inner column height to drop from 13 cm to 20.9 cm.

4.6   Post-cycling electrolyte characterization

4.6.1   Cyclic voltammetry

Cyclic voltammetry was used to detect the presence and standard reduction potential of electrochemically active materials. Measurements were conducted in a three-electrode cell using a Modulab-ECS, Metrohm Autolab, or Ivium Vertex.C potentiostat. Where indicated, iR-compensation was applied. Electrodes were prepared as described in Section 4.1.3, and mounted in a BaSi VC-2 Voltammetry cell filled with 5.0 mL of electrolyte. The electrolyte was prepared using a low concentration of active species (10 mM) in a concentrated supporting electrolyte (0.5 M $TEABF_4$, 2.0 M KCl, or 0.5 M TEATFSI). Unless otherwise stated, cells were assembled and measured in an oxygen- and moisture-free environment (either a sealed testing box filled and purged with nitrogen, or a MBraun glovebox: $O_2 \leq 0.1$ ppm and $H_2O \leq 1.2$ ppm). CV measurements were collected using 20 mV s^{-1} to 500 mV s^{-1} scan rates.

4.6.2   Raman spectroscopy

IR-Raman spectra were collected using a Nicolet NXR 9560 FT-Raman spectrometer. The spectrometer uses a 1064 nm Nd:YVO4 laser and Ge detector. 0.5 mL of electrolyte was dispensed into 5 mm NMR tubes. Spectra were collected between 50 and 4000 cm^{-1} using a 4 cm^{-1} sampling resolution, and were averaged over 128 scans.

4.6.3   Fourier transform infrared spectroscopy

FTIR spectroscopy was performed using a Cary 630 spectrometer, equipped with a diamond ATR crystal (Agilent, G8043-68310). Measurements were performed between 4000 - 600 cm^{-1} using a 4 cm^{-1} sampling resolution. $50 - 100$ μL of electrolyte was dispensed directly onto the cleaned diamond ATR crystal and the sample spectrum was averaged over 64 scans. The crystal was cleaned between measurements with a

methanol soaked Kimwipe.

4.6.4   UV-Vis absorption

Absorption measurements in the UV-Vis range were performed using a Cary 60 spectrometer. The spectrometer uses a dual-beam transmission geometry: one beam is used as a reference and the other is transmitted through the sample. A quartz cuvette was used to hold the electrolyte samples, and the absorbance was measured between 1100 and 200 nm using a 600 nm min^{-1} scan rate.

Chapter 5

Degradation in Non-Aqueous Vanadium(III) Acetylacetonate Flow Batteries

5.1   Background and motivation

Vanadium(III) acetylacetonate ($V(acac)_3$) was used as a redox active material to validate our experimental set-up against data provided by the Brushett research group. (In accordance with their data, tetrabutylammonium tetrafluoroborate ($TBABF_4$) in acetonitrile was used as the supporting electrolyte). In addition to validating our hardware and testing protocols, we examine the degradation processes affecting this system. The work from this chapter is published in J. ECS [4]. The following paragraphs provide some relevant background information introducing this non-aqueous vanadium system.

Vanadium(III) acetylacetonate exists in three reduction states, which are accessed according to the following redox reactions at -1.75 V and 0.45 V vs Ag/Ag^+, respectively:

$$[V(III)acac_3] + e^- \rightleftharpoons [V(II)acac_3]^- \tag{5.1}$$

$$[V(III)acac_3] \rightleftharpoons [V(IV)acac_3]^+ + e^- \tag{5.2}$$
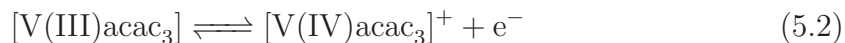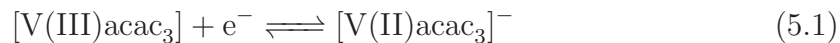
This feature enables $V(acac)_3$ to operate in a symmetric flow cell configuration, where material crossover between the two half-cells is not expected to contribute to capacity fade (section 3.1.5). A cell schematic and cyclic voltammogram for $V(acac)_3$ is illustrated in Figure 5.1. $V(acac)_3$ is soluble up to 0.6 M in acetonitrile. Combined with the increased cell potential afforded by non-aqueous solvents, the theoretical energy density for $V(acac)_3$ flow cells is 18 Wh L^{-1}. For comparison, the typical energy density for aqueous all-vanadium RFBs ranges from 20 – 33 Wh L^{-1} [11, 144, 145]. Other recent works show that solubilities up to 1.1 M are possible for $V(acac)_3$ using solvent engineering, which could increase the energy density to 27 Wh L^{-1} [146, 147].

Other studies have shown limited long-term cyclability of $V(acac)_3$ flow cells [87, 144, 148] and attribute the instability to moisture-induced degradation, which leads to the formation of $VO(acac)_2$ [87, 144]. Recently, improved cycle life was shown using graphite felt electrodes in a flow-through cell architecture under moisture-free conditions [149]. The cell was shown to exhibit stable capacity retention over 150 cycles [149]; whereas, other studies have shown that cells using carbon paper electrodes demonstrate capacity fade after 5 cycles [87]. Here we focus on further understanding the degradation mechanisms described in a previous study by Escalante-García *et al.*; but, we perform the experiments under conditions where ambient moisture is more rigorously excluded, which should inhibit the formation of $VO(acac)_2$.
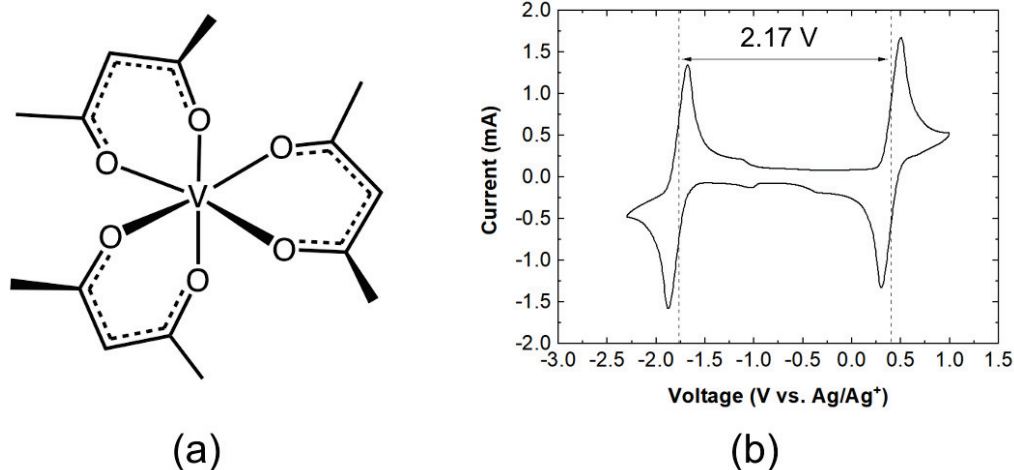
Figure 5.1: Schematic illustrating the structure of vanadium (III) acetylacetonate (a), and cyclic voltammogram of 10 mM solution highlighting the expected cell voltage (b).

5.2 Experimental methods

Cell cycling was performed using the "Gen 2" flow cell design previously described in section 4.1.1. Prior to use, all gaskets, flow fields, carbon paper electrodes and glassware were dehydrated by heating at 110 °C under rough vacuum. The Daramic 175 separator was prepared by soaking in methanol, then allowed to dry before cell assembly. Solid electrolyte reagents were also dehydrated by heating under rough vacuum prior to electrolyte preparation. The V(acac)$_3$ (Aldrich > 97.0 %) was mixed to 0.25 M in the supporting electrolyte (0.5 M tetrabutylammonium tetrafluoroborate (Aldrich > 99%) in acetonitrile (Aldrich > 99.8%; anhydrous)).

The cell was assembled using two 1.6 x 1.4 cm sheets of SGL 39 AA carbon paper (nominally 560 μm thickness total) with an interdigitated graphite plate as a flow field and current collector in each half-cell. A 0.38-mm thick PTFE gasket was used to seal the carbon papers into the cell, which compressed the electrodes to approximately 70 % of the original thickness. The two half-cells were separated by a 25 x 25 mm section of Daramic separator and bolted together between the two polypropylene end-plates.

The assembled cell was dried at 80 ºC overnight before transferring into a N$_2$-filled glovebox for testing. A peristaltic pump was used to circulate electrolyte between the cell and the reservoirs (each containing 15 mL of the vanadium electrolyte) at 10 mL min^{-1}. All solution preparation, cycling and electrochemical characterization was carried out in an N$_2$-filled glovebox (MBraun Unilab) to minimize exposure to ambient moisture and oxygen.

During one set of experiments, the cell was cycled between 1.70 V and 2.27 V using a 55 mA (25 mA cm^{-2}) charge/discharge current until complete cell failure, at which point the cell began to flip instantly between the 1.70 V and 2.27 V cycling limits due to increased internal resistance. During a second set of experiments, the cell was cycled between 1.70 V and 2.27 V using a 55 mA (25 mA cm^{-2}) charge/discharge current until the change in voltage from the end of charge to the beginning of discharge had increased by approximately 50 % compared to the first cycle. Electrochemical impedance measurements of the full cell were collected *in situ* before and after cycling. A Solartron potentiostat was used to apply a 10 mV AC perturbation to the cell and the response was measured between 100 kHz and 10 mHz using a sampling density of 10 pts/decade.

After cycling the cell was discharged to 0 % state of charge by holding at 1.7 V until the discharge current decayed to 0.25 mA cm^{-2}. The electrolyte was returned to the respective reservoirs and collected for *post-mortem* characterization, as described in Chapter 4.

5.3   Results

5.3.1   Cell cycling

Constant-current cycling data for a V(acac)$_3$ flow cell is shown in Figure 5.2a. The upper (2.27 V) and lower (1.70 V) voltage limits correspond to theoretical states

of charge (SOC) of approximately 80 % and 0.01 %, respectively (assuming no ohmic losses). The 2.27 V upper cut-off potential was selected in agreement with previous reports in order to minimize the formation of vanadyl(II) acetylacetonate (VO(acac)$_2$) [87], which is reported to occur spontaneously in the presence of moisture, or with electrochemical cycling in the positive half-cell at high potentials [144]. During the first five cycles, the average cell voltage is 2.20 V on charge, and 2.01 V on discharge. These results are consistent with estimations from cyclic voltammetry (Figure 5.1c), and with previous reports [148, 150, 151]. The measured coulombic, voltage and energy efficiencies are nominally 80 %, 90 % and 70 %, respectively. The coulombic and energy efficiencies are marginally greater than previously reported for the same electrolyte chemistry and cell architecture [87]. However, these differences may be attributed to variation in the flow field and choice of electrode supplier (Spectracarb vs. Sigracet).

The reduced duration of each successive cycle over 20 hours of cycling suggests rapid capacity loss (Figure 5.2a). However, further examination shows that the shortened cycle duration can be attributed to an increase in cell overpotential, and not electrolyte degradation. After approximately five cycles, the average charge voltage drifts towards higher potentials, while the average discharge voltage drifts to lower potentials. This effect is summarized in Figure 5.2b, which shows the change in voltage (ΔV) observed upon immediately switching current direction at the end of charge (ΔV_C) and discharge (ΔV_D). To clarify, ΔV_C for each cycle is the difference between the upper charge limit (2.27 V) and the first voltage measured on the corresponding discharge curve as indicated in Figure 5.2a (and similarly for ΔV_D). The rise in (ΔV_C) and (ΔV_D) with cycling suggests that growing cell resistance causes the upper charge limit to be exceeded before the cell can reach its desired state of charge. This behaviour is consistent with previous studies [87].

To quantify the actual capacity accessed during cycling, the upper and lower

79
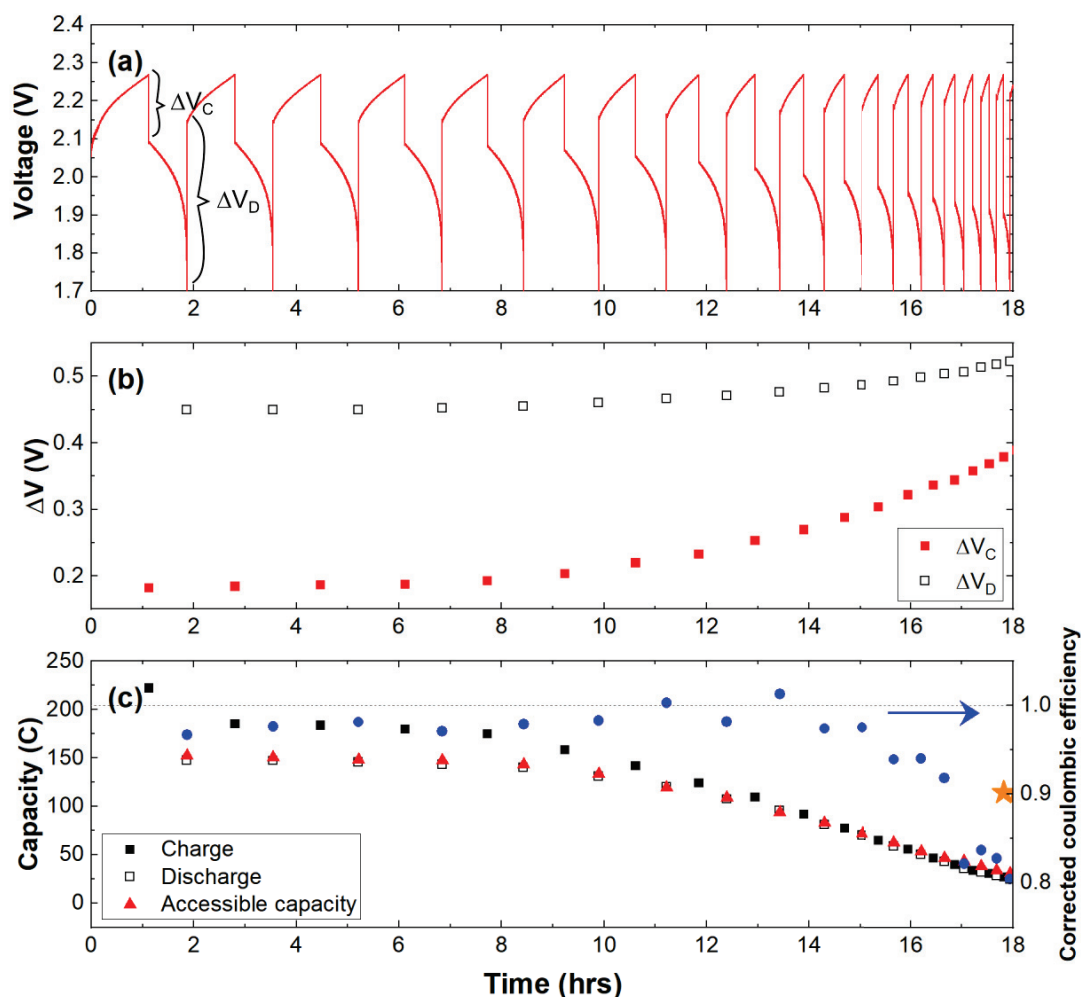
Figure 5.2: Constant current cycling data for a V(acac)$_3$ flow cell (a). The change in voltage observed upon immediately switching current direction at the end of each charge (ΔV_C) and at the end of each discharge (ΔV_D) (b). The cell capacity and estimated accessible capacity determined by subtracting ohmic losses (see main text) for each cycle are shown in (c). The capacity recovered at the end of cycling by constant-voltage (dis)charging (114.2 C) is indicated by the star at 18 hours. The corrected coulombic efficiency compares the discharge capacity to the estimated accessible capacity for each cycle and is given by the blue circles on the right axis.

cutoff potentials were corrected by one-half of (ΔV_C) and (ΔV_D) to estimate the true potential at the end of charge and discharge, respectively. From the Nernst equation, these potentials were used to calculate the SOC that was actually reached at the end of each charge and discharge stage. Multiplying by the volume and concentration of V(acac)$_3$, the accessible capacity (C_A) between the two corrected cycling limits can

be determined. To summarize:

$$C_A = 0.25\text{M} \times 0.015\text{L} \times (\text{SOC} \times (2.27 - \frac{\Delta V_C}{2}) - \text{SOC} \times (1.70 + \frac{\Delta V_D}{2})) \quad (5.3)$$

The accessible capacity is plotted as a function of time in Figure 5.2c in comparison to the measured charge and discharge capacity (C_C) and (C_D) determined from the charge and discharge duration of each cycle, i.e.

$$C_C = 0.055\text{A} \times t_C \quad (5.4)$$

$$C_D = 0.055\text{A} \times t_D \quad (5.5)$$

where $t_{C/D}$ is the charge/discharge duration for each cycle. Comparing the discharge capacity with the estimated accessible capacity in Figure 5.2c, we see that the corrected coulombic efficiency is > 95 % for the first 15 hrs. In contrast, when the discharge capacity is compared with the charge capacity, as it normally is, the coulombic efficiency is only 80 % for the first 15 hrs. For the first five cycles the charge capacity significantly exceeds the estimated accessible capacity, which suggests that parasitic reactions may be consuming excess charge. (More evidence to support this hypothesis is discussed further in this work).

After cycling for 20 cycles, the cell was charged using a constant voltage hold at 2.27 V until the current decayed to < 1.5 mA. The cell was then immediately discharged using a 55 mA current followed by a constant voltage hold at 1.70 V until the current decayed to 0.01 mA. The total charge extracted during discharge was found to be 114.2 C, indicated by the star at 18 hours in Figure 5.2c. This value represents 74.2 % of the initial capacity, indicating that the observed cell degradation is dominated by increased internal resistance, and not chemical degradation of the

electrolyte active species. To further investigate cell degradation mechanisms, the cell was discharged to 0 % SOC, and the electrolyte and electrodes were harvested for *post-mortem* characterization.

5.3.2   Post-cycling electrolyte analysis

Cycled negolyte and posolyte were diluted with supporting electrolyte for cyclic voltammetry and UV-Vis characterization. The UV-Vis spectra comparing fresh and cycled 0.1 mM $V(acac)_3$ electrolyte are shown in Figure 5.3a. The main absorption features of the neutral $V(acac)_3$ molecule are visible at 280 nm and 345 nm, in agreement with previous reports [150, 152]. The change in relative peak intensity between 280 nm and 290 nm for the positive and negative cycled electrolyte is consistent with a change in oxidation state of the neutral $V(acac)_3$ molecule. As reported by Saraidaridis *et al.*, a positive feature in the differential absorption spectrum is observed at 280 – 290 nm when $V(acac)_3$ is reduced. When $V(acac)_3$ is oxidized, a negative feature is observed in the same region, while a positive feature is observed below 275 nm [152]. The slight differences in overall absorption intensity between the four spectra may be explained by solvent loss during the cycling experiments. A common degradation product of $V(acac)_3$ is $VO(acac)_2$, which is reported to show a characteristic absorption peak at 320 nm, a shoulder at 400 nm, and broad peaks at 577 nm and 650 – 800 nm [87, 150]. These $VO(acac)_2$ features were not observed, even when the electrolyte concentration was increased to 10 mM.

Figure 5.3b compares the cyclic voltammetry of fresh and cycled electrolyte at an uncycled carbon paper working electrode. The fresh electrolyte shows the expected features for $V(acac)_3/V(acac)_3^+$ and the $V(acac)_3/V(acac)_3^-$ redox couples at 0.40 V and -1.77 V vs. Ag/Ag^+, respectively. The nominal cell voltage is 2.17 V, which is in good agreement with previous reports of 2.2 V [144, 148, 150, 151, 153]. In the fresh electrolyte one unexpected reduction peak is observed at -1.0 V vs. Ag/Ag^+. This
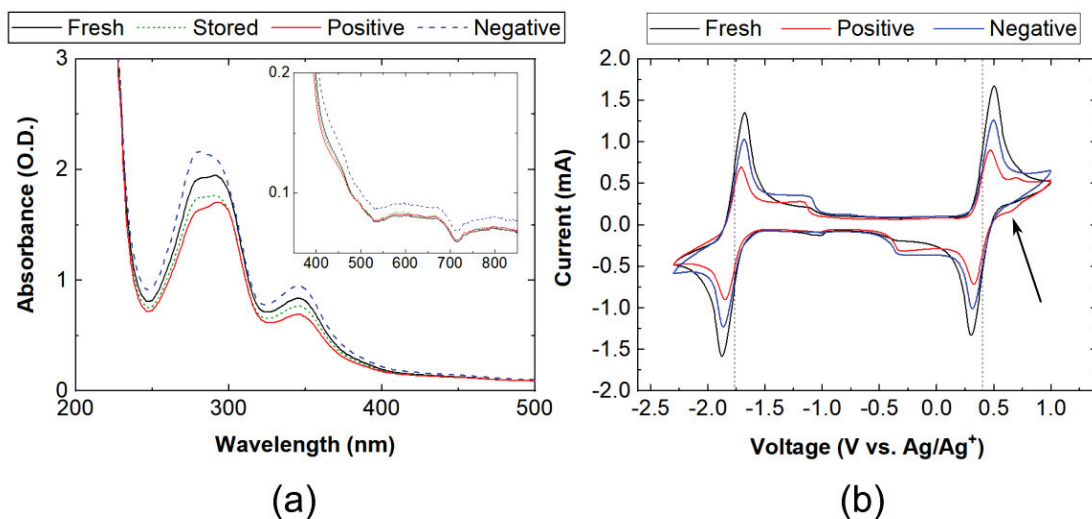
Figure 5.3: UV-Vis spectra comparing cycled and fresh V(acac)$_3$ solutions diluted to 0.1 mM (a). The inset shows the absorption spectra for the same solutions between 400 — 800 nm. Cyclic voltammograms comparing cycled and fresh V(acac)$_3$ solution using a fresh carbon paper working electrode are shown in (b). Measurements were performed using a 50 mV s^{-1} scan rate. A peak at 0.7 V vs Ag/Ag$^+$ corresponding to VO(acac)$_2$ is indicated by the black arrow.

feature was similarly observed in previous reports, but the precise reaction mechanism was not identified [87, 144, 150]. The VO(acac)$_2$ degradation product is known to undergo oxidation and reduction at +0.75 V and -2.0 V vs. Ag/Ag$^+$, respectively [144, 150]. In the cycled negolyte, no peaks are observed in these regions. In the cycled posolyte a small feature around +0.7 V is clearly visible (indicated by the black arrow). It is interesting to note that this feature is much less pronounced here than observed by Escalante-García et al.. We attribute this difference to our protocol where all steps were performed in a glovebox (MBraun, H$_2$O and O$_2$ < 1.2 ppm). Escalante-García et al. reported a higher ambient water concentration (< 250 ppm), which is consistent with a greater quantity of VO(acac)$_2$ being produced in their cell during cycling [87].

To further analyze the electrolyte degradation products, Raman spectra were collected comparing fresh and cycled electrolyte. Peaks attributed to the V(acac)$_3$

molecule (indicated by (∗) in Figure 5.4) are consistent with what has been previously reported for non-aqueous acetylacetonate anions and other metal acetylacetonate ($M(acac)_3$) molecules [154, 155]. The difference spectra between the fresh electrolyte and the cycled positive/negative electrolyte are shown in the bottom panel of Figure 5.4. Except for a small peak at 396 cm^{-1}, little change is observed in the positive electrolyte. The remaining features in the positive difference spectrum are attributed to artefacts generated by subtracting the signal of the fresh electrolyte from the cycled positive electrolyte. In contrast, several new features are observed in the negative electrolyte. Three sharp peaks can be clearly seen in the difference spectrum for the cycled negative electrolyte, as well as in the raw measurement: 1565 cm^{-1}, 672 cm^{-1} and 396 cm^{-1}. Shifts in the Raman peak position are not uncommon with variations in solvent polarity [156, 157]; therefore, an exact identification of the new modes observed in the cycled electrolyte may not be possible from literature references. However, in the discussion below we describe the most likely bonding environments based on previous reports.

Of the new modes visible in the cycled negolyte, the largest visible peak at 1565 cm^{-1} may be associated with a shift in the symmetric C-O vibrational mode (which is commonly observed at 1506 cm^{-1} and 1600 cm^{-1} in non-aqueous acetylacetonate anions, and other $M(acac)_3$ molecules [154, 155]). The peak at 672 cm^{-1} may be associated with shifts in the in-plane C-C-C bending mode or ring deformation modes, which are commonly observed in acetylacetonate anions at 634 cm^{-1} and 660 – 688 cm^{-1} respectively [155, 158]. Finally, the peak at 396 cm^{-1} could be attributed to a shift in the C-CH$_3$ bending mode, which has been previously reported at 392 and 405 cm^{-1} for acetylacetonate anions in non-aqueous solution and in vanadyl acetylacetonate ($VO(acac)_2$) [155, 158]. Vanadyl acetylacetonate is a commonly reported degradation product for $V(acac)_3$ [87, 144]. In order of decreasing intensity, $VO(acac)_2$ has been reported to produce sharp, characteristic features at 486, 1004, 1292 and 1377 cm^{-1}
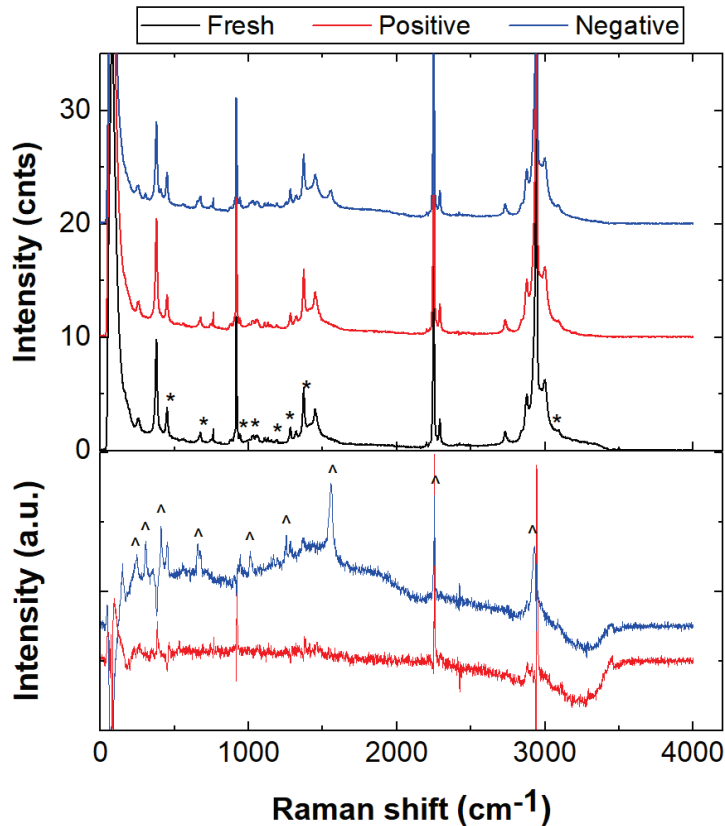
Figure 5.4: IR-Raman spectra of fresh and cycled 0.25 M V(acac)$_3$ electrolyte measured in 0.5 M TBABF$_4$ (top panel). Peaks attributed to the vanadium acetylacetonate are indicated with a ($*$). The lower panel depicts the difference spectra between the cycled and fresh vanadium electrolyte. Major peaks in the difference spectra are marked with a ($\wedge$).

when measured in chloroform [158]. However, these do not correlate with the sharpest peaks visible in the difference spectra for the cycled negative electrolyte. It is possible that trace signals of VO(acac)$_2$ are visible in the form of V=O and C-C-C vibrational modes at 1014 cm^{-1} and 1256 cm^{-1} [158]; but, clearly the majority of degradation products observed in the negative electrolyte cannot be attributed to VO(acac)$_2$. These results are contrary to previous reports that the primary source of capacity fade is caused by degradation of V(acac)$_3$ to VO(acac)$_2$ in the positive electrolyte, with little change observed in the negative electrolyte [87]. Here, under moisture-free conditions we observe significant degradation in the negative electrolyte, and only

trace evidence of VO(acac)$_2$ measured in the positive electrolyte by CV.

5.3.3 Post-cycling electrode characterization

As discussed previously, a large portion of the apparent capacity fade can be attributed to a growth in cell overpotential. Figure 5.5a compares the Nyquist plots for EIS measurements performed *in situ* before and after cell cycling. In this measurement the cell was cycled until the change in voltage at the end of charge (ΔV_C) had increased by ~ 50 % compared to ΔV_C for the first charge. Measurements were performed with pumping (10 mL min^{-1}) under bias near 50 % SOC (2.2 V). On the first cycle, the cell shows an impedance measurement characteristic of SGL carbon paper at low flow rates [43]. The impedance spectrum appears to be largely dominated by mass transfer resistance at low frequencies and exhibits a significant ohmic loss ($\sim 2.25\,\Omega\,\mathrm{cm}^2$), which is consistent with measurements reported by Escalante-García *et al.* [87]. Considerable ohmic losses are not unexpected considering the modest conductivity of non-aqueous electrolytes [17,141]. A large fraction of the ohmic losses can be attributed to the Daramic separator ($\sim 1.5\,\Omega\,\mathrm{cm}^2$), as reported in other works [87].

After cycling, the Nyquist plot is significantly changed -– three semi-circular features are evident. The large high-frequency feature is consistent with a growth in charge-transfer resistance (R$_{ct}$). Compared to the measurement before cycling, R$_{ct}$ is increased to $\sim 18.5\,\Omega\,\mathrm{cm}^2$, which is larger than the combined charge-transfer and mass-transport losses observed before cycling. The low-frequency feature may be attributed to mass-transfer limitations related to ion migration and electrolyte transport within the cell. In comparison to the other features, the relative change of the mass-transfer impedance is minimal, growing from $\sim 1\,\Omega\,\mathrm{cm}^2$ before cycling to $\sim 2\,\Omega\,\mathrm{cm}^2$ after cycling. A large feature at intermediate frequencies is observed as well. Escalante-García *et al.* also report a small feature at intermediate frequencies; however, the source of this behaviour was not identified. They speculate that the
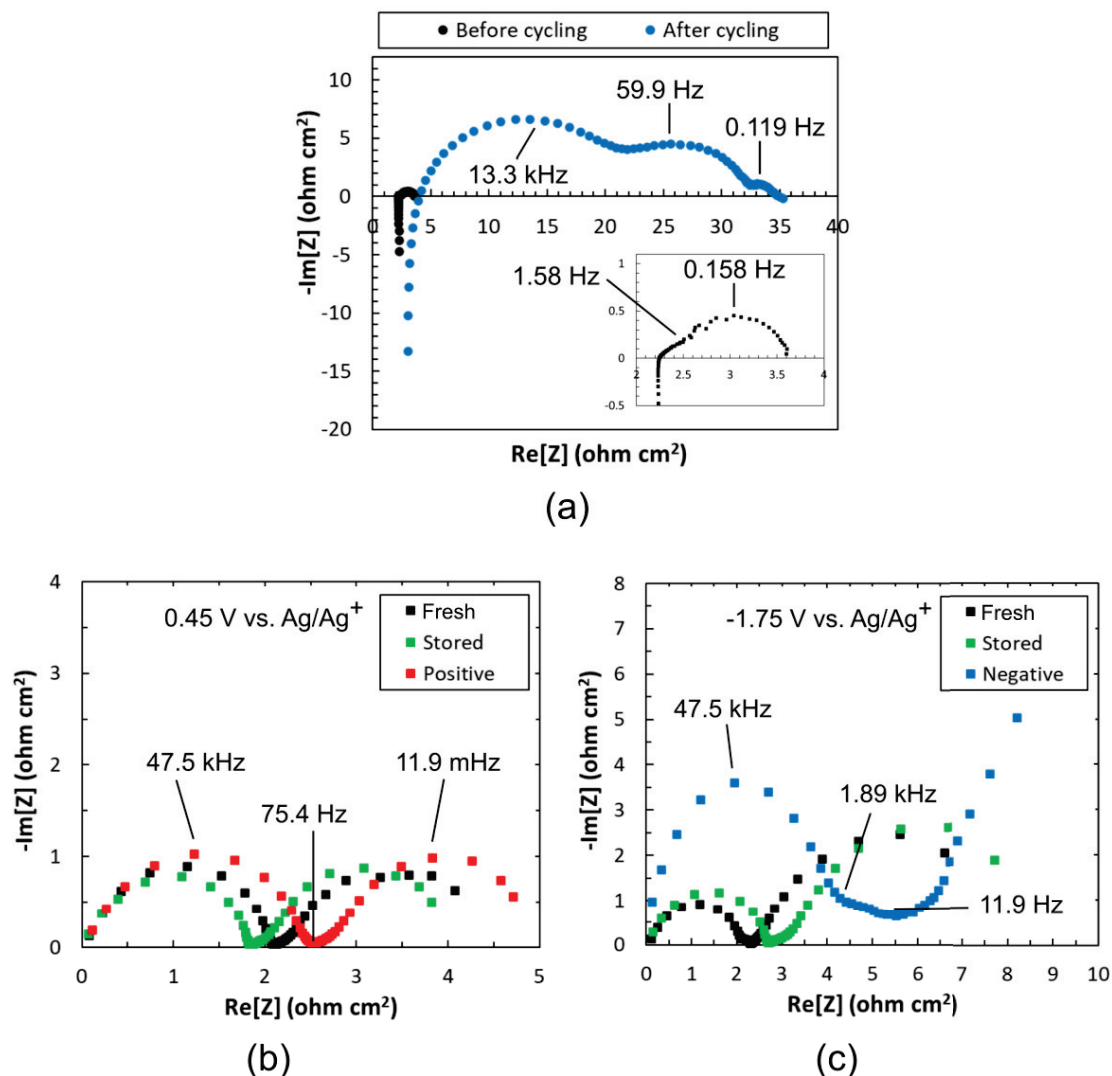
Figure 5.5: EIS measurements from a full cell before and after cycling. The cell was cycled until the change in voltage at the end of charge (ΔV_C) increased by ~ 50 % from the first cycle (a). The inset shows the first cycle spectrum on a smaller scale. Impedance spectra of cycled positive, stored and fresh electrodes measured using a DC bias at +0.45 V vs. Ag/Ag$^+$ (b). Impedance spectra of cycled negative, stored and fresh electrodes measured using a DC bias at -1.75 V vs. Ag/Ag$^+$ (c). Spectra in panels (b) and (c) were measured in a three-electrode cell. The real component of impedance is corrected to subtract the effect of solution resistance. In all panels, the area specific impedance is normalized with respect to the geometric surface area. (The true microporous area is expected to be 10 – 20 x greater).

feature may be associated with the growth of an electrode film through precipitation

of vanadium species, or decomposition of the solvent or supporting electrolyte [87].

In contrast to the observations by Escalante-García *et al.*, this feature becomes dramatically apparent with cell cycling, suggesting that it may be critically linked with the apparent capacity loss in the cell. After cycling the series resistance increased from $\sim$2.25 Ω cm^2 to $\sim$4 Ω cm^2. This may be associated with fouling of the separator during cycling, or loss of electrolyte conductivity due to degradation.

To characterize the relative contributions of the positive and negative electrodes to the total cell impedance, electrode samples were harvested from the cell *post-mortem* and further studied by EIS. Nyquist plots comparing the impedance measurements of fresh electrodes to the positive and negative cycled electrodes are shown in Figure 5.5b and c. Compared to the fresh electrode the charge transfer resistance at the cycled positive electrode is increased from 2.05 to 2.54 Ω cm^2 – a small amount, but the change is significant given the uncertainty (see below). The negative electrode shows a much greater charge-transfer resistance – 4.28 Ω cm^2. In both panels Nyquist plots for electrodes that were not cycled but stored in fresh electrolyte for the same duration as the cycling experiment (herein referred to as "stored electrodes") are also shown for reference. Although the charge-transfer resistance differs slightly from the fresh electrodes, the results indicate that the changes observed at the cycled electrodes are induced by cycling, as opposed to passive electrolyte exposure. Given the difference in measurement geometry and conditions, it is difficult to draw a direct quantitative comparison between the *ex situ* three-electrode measurements and the full cell. However, we can conclude that the majority of impedance growth in the cell occurs due to changes at the negative electrode, and that these changes are primarily induced by electrochemical cycling, and not passive electrolyte exposure.

To characterize the uncertainties inherent in our measurement protocol, impedance spectra were measured for six 3 mm x 3 mm samples of fresh carbon paper (Figure 5.6). The average charge-transfer resistance was determined to be 2.33 $\pm$ 0.08 Ω cm^2 and 2.05 $\pm$ 0.09 Ω cm^2, respectively, when the electrode was biased at -1.75V and

+0.45 V with respect to the Ag/Ag$^+$ reference. The reported uncertainties represent the standard error of the measurements. We interpret these small uncertainties to indicate the reliability of this design and the consistency with which small electrode samples with a repeatable surface area can be measured using this protocol.
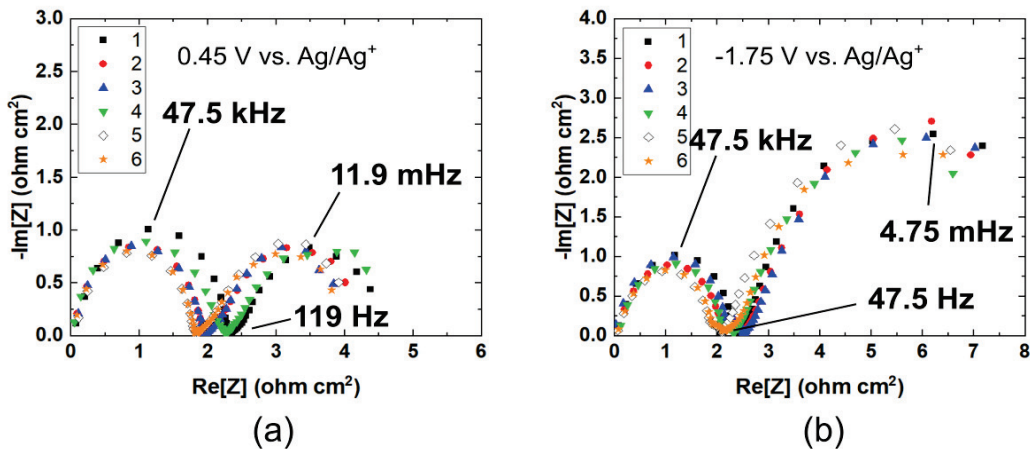
Figure 5.6: Electrochemical impedance spectra of a fresh carbon electrode measured at (a) +0.45 V vs. Ag/Ag$^+$ and (b) -1.75 V vs. Ag/Ag$^+$. Each spectrum represents an impedance measurement on a separate sample of fresh carbon paper. At +0.45 V vs. Ag/Ag$^+$ the diameter of the semi-circle ranges from 1.83 — 2.32 Ω cm^2 with an average of 2.05 $\pm$ 0.09 Ω cm^2. At -1.75 V vs. Ag/Ag$^+$ the diameter of the semi-circle ranges from 2.08 — 2.52 Ω cm^2 with an average of 2.33 $\pm$ 0.08 Ω cm^2. The uncertainties represent the standard error of the measurements.

X-ray photoelectron spectroscopy (XPS) is a powerful surface characterization technique, which has been shown in previous studies to resolve chemical changes on the surface of flow battery electrodes [42, 44, 46, 47, 52, 53, 55, 159, 160]. Figure 5.7a shows the survey spectra for the four electrode samples: uncycled (fresh), stored, cycled positive and cycled negative. The uncycled carbon electrode is mainly feature-less, but shows the expected C1s peak at 285 eV, the C KLL auger peak at 990 eV and a very weak O1s peak at 533 eV. Compared to the uncycled carbon paper, the positive cycled electrode and stored electrode show increased O1s intensity, and the appearance of the O KLL auger peak. Small quantities of fluorine and vanadium are

also visible in the close-up scans on the stored and cycled positive electrode. Peak fitting and analysis suggest that the relative quantities of these elements are small (< 1.5 % fluorine and < 0.3 % vanadium) compared to those observed on the negative cycled electrode (Figure 5.7b). The negative cycled electrode shows a much greater abundance of fluorine and vanadium on the surface (up to 9.5 % and 7 %, respectively). In addition, a nitrogen peak becomes visible at 405 eV, as well as a boron peak at 195 eV. Two unexpected elements were identified in two of the samples (Na1s and S2p). Impurities containing Na and S are known to be present in carbon tape, which was used to mount the samples for XPS. Although we cannot rule out the presence of impurities in our raw materials, we attribute the Na1s peak and S2p peak to the underlying carbon tape due to the macroscopic porosity of the samples and the unfocused nature of the X-ray source.
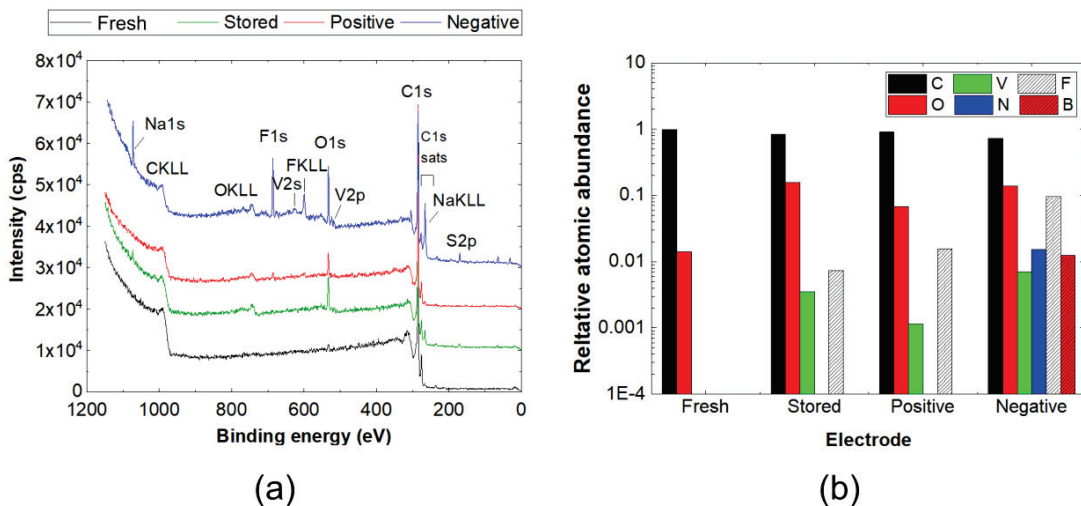
Figure 5.7: XPS survey spectra of positive and negative electrodes harvested from a cycled cell compared with uncycled and stored electrode samples (a). Relative atomic abundances for each element determined from high-resolution XPS spectra (b).

The increased abundance of XPS features not native to the uncycled carbon paper on the negative cycled electrode is consistent with fouling of the electrode, leading to the increased charge transfer resistance observed by EIS (Figure 5.5) and the appear-

ance of new Raman modes in the cycled negative electrolyte (Figure 5.4). We speculate that these changes are associated with the decomposition of electrolyte species induced during electrochemical cycling, resulting in the deposition of an insoluble surface layer on the cycled electrodes — particularly the negative electrode. The fact that such a surface layer is not observed on the surface of the stored electrode (Figure 5.7) again suggests that the degradation is likely caused by cycling-induced changes and not a result of insufficient electrode rinsing *post-mortem*. The decomposition of electrolyte at the negative electrode is also consistent with the apparent capacity fade (Figure 5.2), where a growing charge-transfer resistance causes the upper cut-off potential to be reached more rapidly during cell cycling.
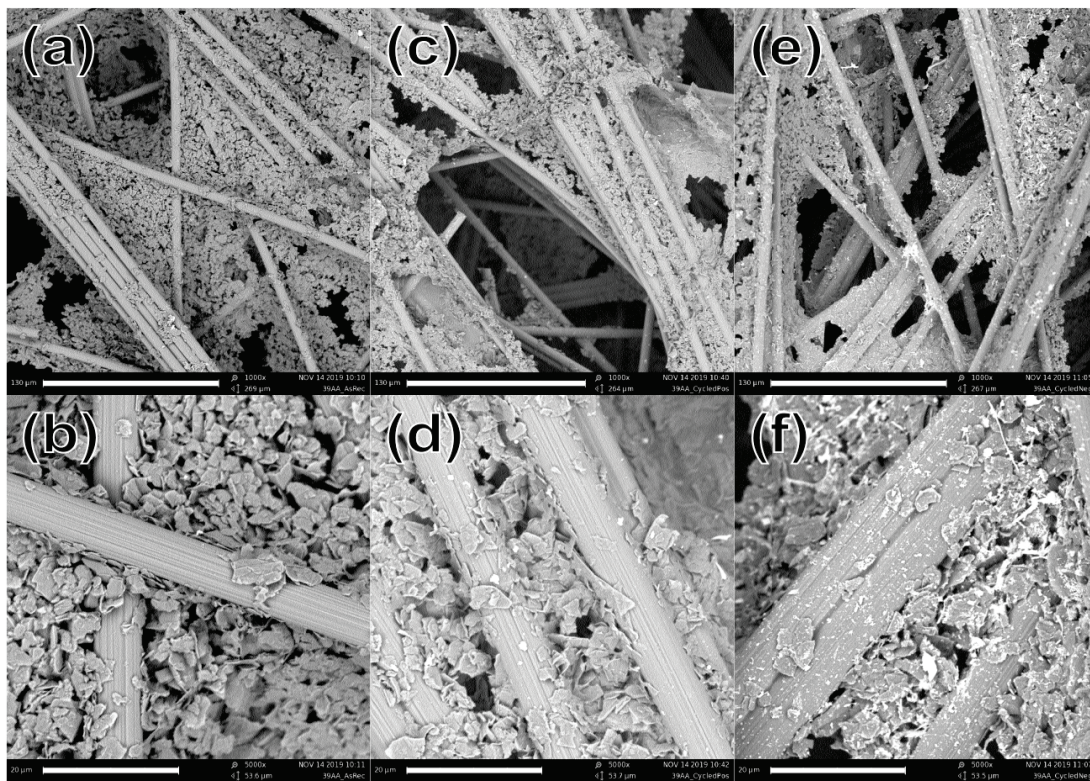
Figure 5.8: Representative SEM images of uncycled (a-b), positive cycled (c-d), and negative cycled (e-f) electrodes. Scale bars indicate 130 μm in panels (a), (c) and (e); and, 20 μm in panels (b), (d) and (f)

Scanning electron micrographs collected before and after cycling are shown in

Figure 5.8. Similar to the structure observed in other reports, the SGL carbon paper exhibits a large open pore-structure consisting of loose layers of randomly oriented carbon fibres filled with a graphitic binder [42,43]. As noted in previous studies some clear ridges, or 'edge-structures', are observed in the uncycled carbon electrodes. Other aqueous vanadium flow battery degradation studies have reported significant changes to the carbon fibre morphology after electrochemical cycling, including loss of edge-structure and peeling of the fibre surface [52–54]. Here we do not observe any significant changes to the structure of the carbon fibres. If at all, a small amount of residue appears to be present on the cycled negative electrode compared to the others.

The rate of capacity loss observed in this experiment is nearly identical to that reported by Escalante-Garcia *et al.*, despite cycling under much lower background levels of moisture (< 1 ppm vs. < 250 ppm). In both studies a clear loss of capacity relative to that observed on the first charge cycle was observed after approximately five cycles [87]. The previous authors posited that the cell lifetime is limited by the instability of $V(acac)_3$, which reacts with moisture to form $VO(acac)_2$ (a degradation pathway that has also been reported in other studies) [87,144,150]. Using CV, the previous authors identified $VO(acac)_2$ in comparable quantities to $V(acac)_3/V(acac)_3^+$ in the cycled posolyte, and lower amounts in the cycled negolyte [87]. The authors hypothesized that the $VO(acac)_2$ was formed at the positive electrode and diffused into the negative half-cell due to the poor selectivity of the Daramic separator. CV measurements conducted in the present study reveal a lower, but still appreciable, peak current of $VO(acac)_2$ relative to the $V(acac)_3/V(acac)_3^+$ couple in the cycled posolyte, despite the fact that background moisture levels were reduced by over two orders of magnitude. Although no $VO(acac)_2$ was observed in CV of the cycled negolyte, several new vibrational modes were visible in the IR-Raman spectra, indicating that other degradation products are present. In tandem with these degradation

92

products a dramatic increase in charge-transfer resistance was observed by EIS at the negative cycled electrode compared to positive, stored and uncycled electrodes. This evidence suggests that moisture-induced degradation to $VO(acac)_2$ is not necessarily the limiting source of instability in the $V(acac)_3$ electrolyte system, and that cell lifetime is limited by electrode and electrolyte degradation in the negative half-cell.

5.4 Conclusions

In this study we characterized the degradation of non-aqueous vanadium flow batteries under moisture-free conditions. Rapid cell failure was still observed within the first 20 hours of cycling at a moderate current density, even under an inert atmosphere. Constant voltage charging/discharging after perceived cell failure recovered 75 % of the initial capacity, which suggests that resistive losses masked cell capacity retention. Although no significant changes were apparent in UV-Vis absorption measurements, some electrolyte degradation was evidenced by the appearance of a $VO(acac)_2$ oxidation peak in cyclic voltammetry of the cycled posolyte, though to a much lesser extent than previous reports [87]. As well, the appearance of several new Raman modes in the cycled negolyte, but not the posolyte suggests that $V(acac)_3$ degradation to $VO(acac)_2$ is not the only source of instability.

In addition to electrolyte degradation, significant changes to the electrodes were observed post-cycling. XPS revealed the presence of vanadium, fluorine and oxygen containing compounds, as well as small quantities of nitrogen and boron on the negative cycled electrode. The appearance of these features was correlated with increased charge-transfer resistance observed *in situ* post-cycling. We have shown that even when steps are taken to minimize the impact of moisture, the stability of non-aqueous vanadium flow batteries is limited by degradation processes occurring at the negative electrode. In fact, the rate of degradation observed here was similar to that seen in experiments with much higher background levels of moisture, indicating that

this is likely not the primary source of the instability.

Chapter 6

Electrode Stability in a Near pH-Neutral Aqueous Quinone Negolyte

6.1 Background and motivation

Quinones are one of the most well-studied families of organic molecules that are being investigated for ORFB applications. While many quinone-based flow cells have been realized, most of these cells were dominated by rapid and irreversible capacity loss (on the order of a few percent per day) – making them unsuitable for commercial energy storage [25, 27, 90, 100–104]. In 2019, Ji *et al.* developed a novel quinone derivative functionalized with phosphonic acid-terminated side chains: (((9,10-dioxo-9,10-dihydroanthracene-2,6-diyl)bis(oxy)) bis(propane-3,1-diyl))bis(phosphonic acid), here referred to as 2,6-DPPEAQ. This molecule exhibits good solubility (0.75 M, or 1.5 M electrons) in nearly pH-neutral aqueous solutions (pH 9). Paired with a potassium ferro/ferricyanide posolyte, Ji *et al.* reported a 0.5 M 2,6-DPPEAQ flow cell with an OCV of 1.0 V and a record capacity fade rate of less than 0.014 %/day – a record for its time. The authors confirmed using proton nuclear magnetic resonance (NMR),

that even under accelerated degradation conditions (65 ℃, pH 14) 2,6-DPPEAQ exhibits high stability in its reduced form.

Because of its strong performance, we seek to characterize the losses and degradation that occurs at electrode interfaces during electrochemical cycling of 2,6-DPPEAQ flow cells. As described in Chapter 2, electrode morphology (microstructure, and macrostructure), precursor material, and pre-treatment methods have all been shown to influence the surface chemistry and efficiency losses at the electrode-electrolyte interface. In this study, we aim to characterize these losses in a cell that is prepared and cycled identically to that reported by Ji *et al.*. In their study, Ji *et al.* perform an excellent characterization of 2,6-DPPEAQ chemical stability, but the loss of cell voltage efficiency with electrochemical cycling was not addressed. Two observations in their study suggest either electrode or membrane fouling: (1) a gradual decline in voltage efficiency with cycling (Ji *et al.*, Figure 4); and (2), the quantity of charge recovered during voltage holds at the upper and lower charge limits increased by nearly a factor of two (Ji *et al.*, Supplementary information) [2]. Here, we characterize these voltage losses using a combination of *in situ* EIS (performed on operating cells), and post-cycling EIS and XPS measurements of cycled electrodes. We hope that understanding the origins of impedance growth will facilitate the development of cell preparation and/or cycling protocols that improve cell efficiency and extend operational lifetime.

6.2 Experimental methods

2,6-DPPEAQ/potassiumm ferrocyanide cells were assembled as described in Chapter 4. Briefly, 4 sheets of SGL 39AA carbon paper (1.6 x 1.4 cm) were sealed into each half-cell using 0.030 inch thick gaskets (PTFE or EPDM). The electrodes were pre-treated by baking at 400 ℃ for 8 hrs, followed by treating with UV-Ozone for 10 minutes on each side prior to cell assembly. The electrodes were separated using

a Fumasep E620-K potassium ion exchange membrane, which was used as-received. Impervious graphite engraved with a 1 mm deep serpentine channel were used as a flow field and current collector in each half-cell. The cells were held together using four 1/4-28 bolts, tightened to 20 in lbs. The final electrode compression using this torque setting and gasket thickness was estimated to be 75 %. The cell was assembled on the benchtop before storing under rough vacuum (-30 in Hg) to remove ambient oxygen for 24 hours. (The pump and transport tubing were also stored under rough vacuum).

The vacuum chamber was back-filled with nitrogen, and the cell, tubing and electrolyte were transferred into the nitrogen testing box (section 4.1.2) for final assembly. Conical-bottom Savillex PFA impingers were used as reservoirs. The negative reservoir was filled with 5.5 mL of 2,6-DPPEAQ tetrapotassium salt. The salt was prepared by mixing 2,6-DPPEAQ (Strem: P/N 15-8245) with four mole equivalents of potassium hydroxide to de-protonate the phosphorous side-chains. For 7.5 mL of 0.5 M electrolyte, 1.1816 g of solid 2,6-DPPEAQ was gradually stirred into 2.0 M potassium hydroxide (KOH) solution under nitrogen. For the reaction to proceed correctly, it is critical that the solution remain basic; the solid must be gradually added to the KOH solution with stirring, and not vice versa. After the reaction was complete, the solution was adjusted to pH 9 by adding 75 μL of 0.001 M KOH to the electrolyte mixture. The positive reservoir was filled with 60 mL of posolyte: a mixture of 0.4 M potassium ferrocyanide and 0.1 M potassium ferricyanide mixed in pH 9 KOH. The posolyte mixture is approximately 4.5 times in excess of the quinone to ensure that it does not become capacity limiting. (Electrolyte preparation was performed a day prior to cell assembly. The NPW was sparged for 30 minutes prior to preparing the KOH solutions. Final electrolyte solutions were stored under nitrogen until final cell assembly).

After assembly, the cell was primed with electrolyte by circulating with a gentle

flow rate (1 mL min^{-1}). After 10 minutes, the electrolyte was increased to its working flow rate (60 mL min^{-1}). The cell was tilted from side-to-side and tapped gently to remove trapped gas bubbles. The electrolyte was circulated for another hour before beginning electrochemical cycling. The purpose of this one-hour priming step was two-fold: (1) to ensure no electrolyte leakage occurred at the cell fittings, and (2) to hydrate the Fumasep membrane. (In performing membrane impedance measurements, we found that a minimum 1 hour hydration time was needed for the membrane to reach steady impedance value). The cells were (dis)charged at constant-current followed by a constant-voltage hold at the (lower) upper voltage cut-off as described by Ji *et al.* [2]. Cell impedance was monitored by performing EIS at 0 V with respect to open-circuit voltage at 50 % SOC. EIS measurements were performed at the beginning and end of cycling, as well as every 10 cycles in between. The cell was pre-conditioned for EIS measurements by performing a constant-voltage hold after discharging to 50 % SOC. A current threshold of 2 mA cm^{-2} was used to terminate the constant-voltage holds at the charge limits, and at 50 % SOC, as reported in other groups [2, 59].

Cell components were harvested and cleaned post-cycling as described in section 4.3. Electrode and electrolyte characterization measurements were performed as described in Chapter 4. Cyclic voltammetry and membrane impedance measurements were performed using 2.0 M potassium chloride (KCl) as a supporting electrolyte (adjusted to pH 9 by adding a small volume of KOH). The 2.0 M KCl was selected to maintain an equivalent potassium ion concentration as in the flow cell negolyte. CV solutions were diluted to a 10 mM active species concentration. Single electrode EIS measurements (described in section 4.4.1) were performed using 5.0 mL of full concentration electrolyte (prepared identically to the solutions used in the full cell).

6.3 Results

A total of five cells were assembled using the 2,6-DPPEAQ aqueous chemistry. Cycling data and full cell impedance analysis for the three successful trials (trials 3 – 5) are discussed in the following results sections. A description of learned failure mechanisms and cell design issues from trials 1 – 3 are listed below for the interested reader.

1. **Electrolyte mixing:** the 2,6-DPPEAQ tetrapotassium salt (negolyte) is prepared by mixing 2,6-DPPEAQ with four mole equivalents of potassium hydroxide to de-protonate the phosphorous side-chains. For the reaction to proceed correctly it is critical that the solution remain basic; the solid must be gradually added to the KOH solution with stirring, and not vice versa (trial 1).

2. **Cell priming:** electrolyte should be circulated through the cell before cycling to wet the electrodes and membrane. When priming the cell, it is important to use a low flow rate to reduce pressure differentials across the membrane as the cell is filled. Filling the cell using a high flow rate can cause physical damage (i.e. rupturing) in the thin ($< 20\mu$m) Fumasep membrane (trial 2).

3. **Cell sealing:** eliminating electrolyte leakage is critical for evaluating long-term stability. This can be achieved by: (1) selecting a (chemically resistant) compressible/conformable gasket material such as EPDM over a hard/rigid material such as PTFE; (2) using an adequate length of PTFE thread tape to seal fittings into the cell body (or by sealing fittings with epoxy when the plastic threads become worn); and, (3) ensuring that o-ring seating in the polypropylene endplates allows for 20 – 30 % compression to the original chord thickness, which is recommended for static face-seals (trial 3).

4. **Four-wire measurement:** using a four-terminal remote sense potentiostat

configuration is necessary to eliminate variable contact resistance at test leads, which can be affected by corrosion of the test leads by leaked electrolyte. Using stainless steel test leads to contact the graphite tabs can minimize unintentional corrosion. Using a plastic connection bolt (pictured in Figure 4.1b), improved our four-terminal sense configuration (as opposed to a stainless steel bolt, which shorted the source and sense leads together) (trial 3).

5. **EIS sampling density:** using a high sampling density (e.g. 10 pts/decade vs 5 pts/decade) can improve resolution of small high-frequency features in full cell EIS data. This is not a critical recommendation, but it was found to ease DRT and equivalent circuit fitting for full cell EIS data (trials 4 – 5).

6. **Cable management:** it is recommended to minimize inductive contributions (which can mask high frequency EIS features) by reducing the length of test cables, and using proper cable management practices; however, inductive contributions can be numerically subtracted from full cell data when this is not possible (trials 4 – 5).

6.3.1   Cell cycling

Capacity loss and cell efficiency

Cell efficiency and capacity data for trials 4 and 5 is shown in Figure 6.1. (Capacity loss for the trial 3 cell was dominated by electrolyte leakage, so we exclude it from this discussion. A discussion of the trial 3 results can be found in the Appendix). The trial 4 cell was cycled for a total of 160 hours and the trial 5 cell was cycled for a total of 950 hours. By applying a linear fit to the total charge capacity as a function of time (shown in the insets in Figure 6.1), the rate of capacity loss is determined to be 0.23 C day^{-1} and 0.10 C day^{-1} for trials 4 and 5, respectively. Ji *et al.* do not describe how their capacity fade rates are determined, but a commonly reported method involves
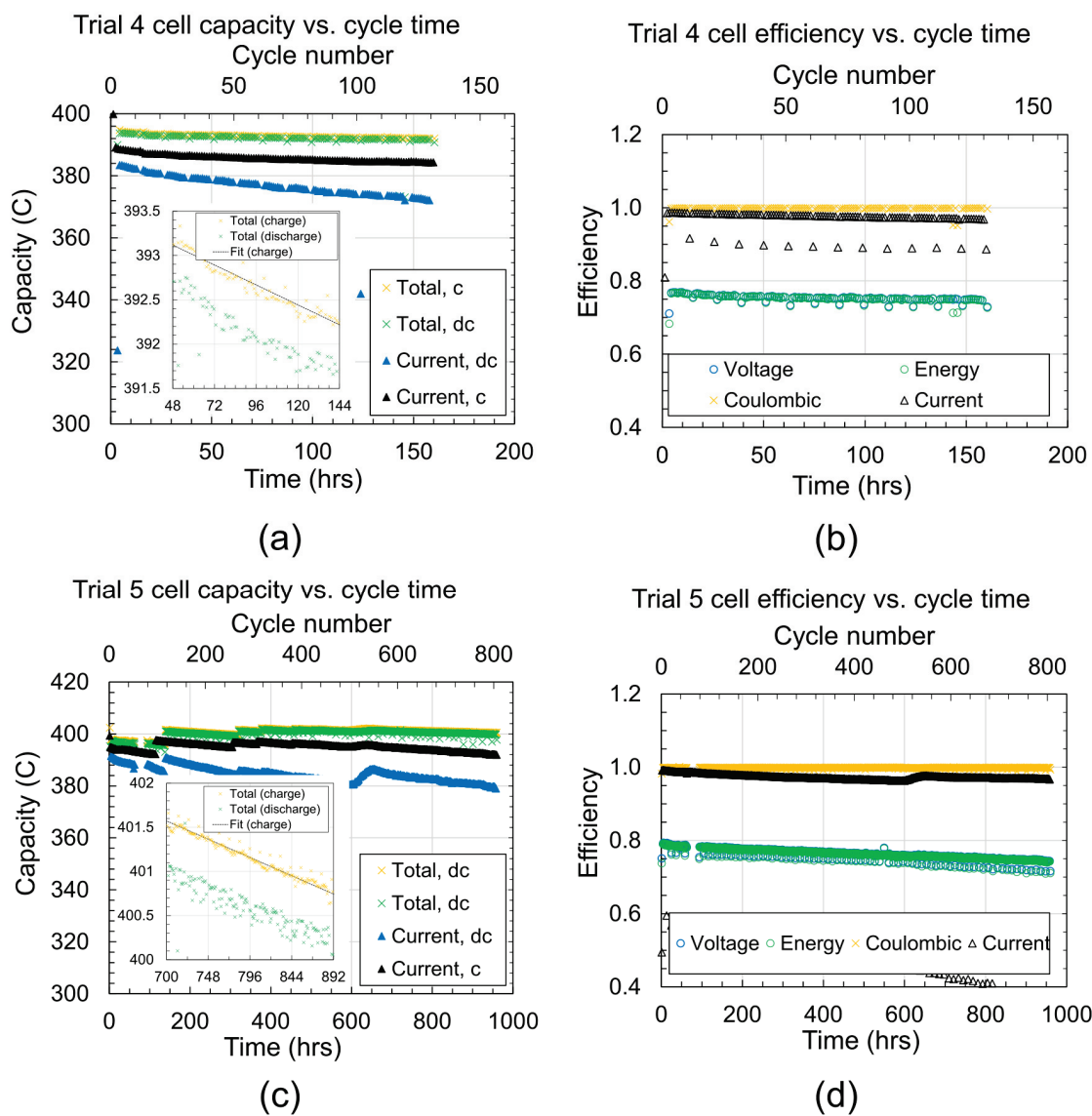
Figure 6.1: Figures illustrating the cell capacity (a) and efficiency (b) as a function of cycle time for trial 4 of a 2,6-DPPEAQ-potassium ferrocyanide flow cell. The same data for trial 5 is shown in panels (c) and (d). The "current" capacity in the capacity time plots refers to the charge integrated during the constant-current charge/discharge steps only. The "current" efficiency refers to the ratio of the discharge to charge capacity during constant-current cycling only (excluding charge during constant-voltage holds). Linear regression to the total cell capacity yields a fit characterized by y = -0.00936x + 393.6 for the inset in panel (a); and, y = -0.0043x + 404.6 for the inset in panel (c). Cells were cycled using a 100 mA cm^{-2} current density (1.6 C).

dividing the capacity-time slope by the initial cell capacity [129]. Using this method, the capacity fade rate for our cell is determined to be 0.057 % day^{-1} and 0.026 % day^{-1} for trials 4 and 5. These figures are in good agreement with that reported by Ji *et al.* (0.014 % day^{-1}) [2]. Both trials were prematurely terminated when a software error froze the cycling protocol and caused irreversible cell damage.

In both cells, we see that the ratio of charge accessed during the constant-current charging portion of cycling gradually diverges from the total cell capacity over time, which indicates that a larger fraction of charge must be accessed during the constant-voltage hold. As we reported in the previous chapter, this apparent loss of capacity during constant-current charging can be caused by growing internal resistances, which cause the cell to prematurely reach the cycling limits before the electrolyte is fully charged/discharged. Interestingly, this divergence is more apparent in the discharge phase of cycling and develops at a faster rate. In trial 4 every 10th data point falls below the main discharge capacity trend. This is an artefact of pre-conditioning the cell at 50 % SOC using a constant-voltage hold every 10th cycle on discharge (as described in the methods section: 6.2). This trend is removed in the trial 5 data. Another interesting feature in the trial 5 data is the increased constant-current discharge capacity after 625 hours. The increased capacity was correlated with increased concentration of ambient oxygen in the nitrogen testing box after a gas cylinder was exchanged. The measured oxygen concentration rose from 1 % to 8 % by volume before recovering after 24 hours.

The cell efficiency data is shown in Figure 6.1b and d. The voltage and energy efficiency for the trial 4 cell begin at approximately 77 %, decreasing to 74 % after 160 hours of cycling. In the trial 5 cell, the voltage and energy efficiency begin at 80 % and fall to approximately 73 % after 950 hours of cycling. Both of these figures exceed the efficiencies reported by Ji *et al.*. In both cases a number of voltage and energy efficiency data points fall below the main trend by 1 – 2 %. These data points coincided

102
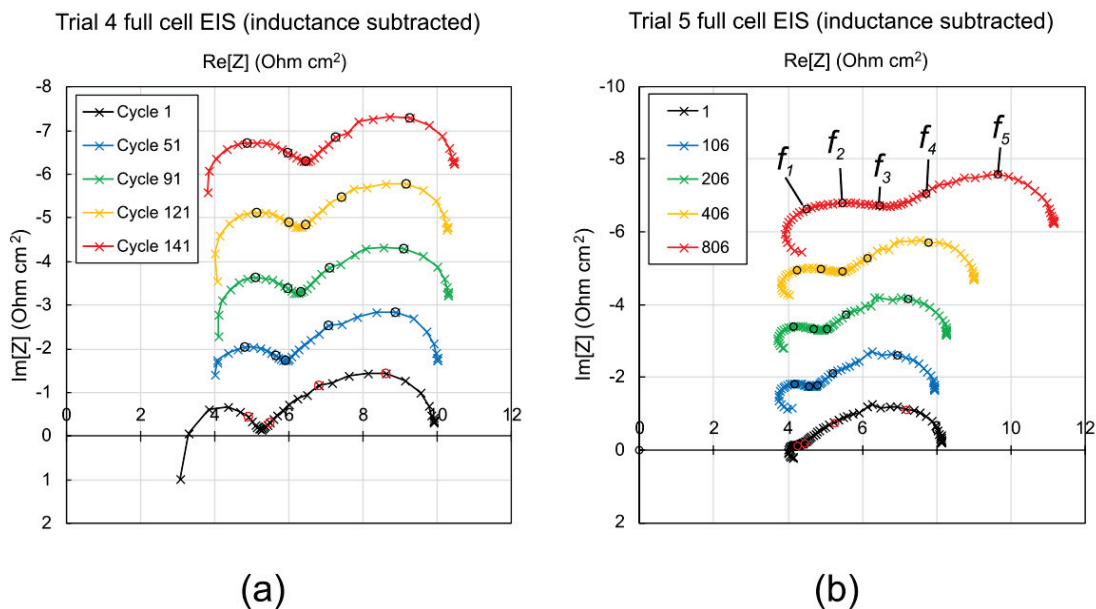
Figure 6.2: Figures illustrating the progression of full cell impedance spectra for the trial 4 (a) and trial 5 (b) 2,6-DPPEAQ/potassium ferrocyanide flow cells. The inductive contributions have been numerically subtracted from the data. The spectra are vertically offset by 1.5 Ω cm^2 for visual clarity. As in Figure B.3, the area specific resistance is reference to the total geometric area of the electrodes, though the true macroporous area is expected to be $10-20$x greater. Datapoints are spaced 5 points per decade in (a) and 10 points per decade in (b). The circular markers indicate the locations of the characteristic frequencies corresponding to the relaxation times determined through DRT analysis (as described in the following paragraphs). The values for the trial 5 dataset are listed in Table 6.1.

with the cycles in which EIS was performed (every 10 cycles). The voltage-hold used to pre-condition the cell for EIS contributed to the cell discharge, which caused the average cell voltage (determined from the constant-current charge/discharge steps) to decrease.

Full cell impedance evolution (with cycling)

The full cell EIS data for trial 4 and 5 cells is shown in Figure 6.2. The series resistance found from the high frequency intercept is stable around 4 Ω cm^2. In both cases, two main features are visible. At low-frequencies ($f_p = 0.39$ or 0.79 Hz, for trials 4 and 5, respectively), we observe a broad, asymmetric semi-circular arc which begins

103

with the characteristic 45 º Warburg response, before transitioning into a semi-circle. This behaviour is typical of a Warburg "short" element where electrolyte convection improves active material transport between the electrode pores and bulk electrolyte (section 3.2.2). The magnitude of this diffusion feature appears constant over 141 cycles in the trial 4 cell. In the trial 5 cell, the low frequency feature increases in magnitude between cycle 406 and cycle 806. Both cells also exhibit a distinct semi-circle at high frequency, which we attribute to the charge-transfer effects. We interpret this charge-transfer resistance as a measure of the activation energy required for the oxidation/reduction of posolyte/negolyte species at the electrode interface. The high-frequency feature has a characteristic peak frequency of 10 kHz between cycle 1 and cycle 141 in the trial 4 cell. In the trial 5 cell, the peak frequency shifts from 3162 Hz (cycle 1) to 630 Hz (cycle 806). The magnitude of the high frequency feature increases with cycling, and becomes more broadly distributed along the real axis. The broadening of this feature could suggest new processes beginning to dominate the impedance spectra. Evidence for this hypothesis is presented in the following paragraphs.

Equivalent circuit fitting was performed to analyze the full cell impedance data shown in Figure 6.2. To inform our equivalent circuit selection, we employed DRT analysis to understand the distribution of relaxation times that were characteristic for our data. Briefly, DRT analysis fits a distribution of relaxation timescales to experimental EIS data. Each time constant represents a relaxation time for a parallel RC (Voigt) element ($\tau = 1/RC$), and the final distribution can be used to interpret the number of Voigt elements that are characteristic for a given impedance spectrum. (Further details regarding DRT theory can be found in section 3.2.2). Figure 6.3 shows the calculated distribution of relaxation times corresponding to different cycles throughout the lifetime of the trial 5 cell. The relaxation times are shown on the x-axis and the calculated distribution ($\gamma(\tau)$) is shown on the y-axis. The solid traces

Figure 6.3: Figure illustrating the distribution of relaxation times (a) and associated EIS fits (b) for the trial 5 aqueous 2,6-DPPEAQ-potassium ferrocyanide flow cell. The relaxation times are shown on the x-axis and the calculated distribution ($\gamma(\tau)$) is shown on the y-axis. The solid traces indicate the *maximum a priori* distribution (MAP), which loosely translates to the most likely distribution of relaxation times for a given set of experimental data. The shaded regions in plot (a) indicate a 99 % confidence interval for the data. The data in panels (a) and (b) are vertically offset for visual clarity. The equivalent circuit interpreted from DRT analysis and used for further fitting is shown in (c).

indicate the *maximum a priori* distribution (MAP), which loosely translates to the

most likely distribution of relaxation times for a given set of experimental data. The

MAP is bounded in either direction by a 99 % confidence interval (indicated by the

shaded regions), which is determined through Bayesian sampling (as described by Ciucci *et al.*) [136, 137]. The distribution for cycle 1 shows 4 characteristic relaxation times, which are summarized in Table 6.1. The peak centred close to $\tau = 100$ s is an artefact of noise in the lowest-frequency data – (it disappears when the dataset is truncated a half decade before the lowest sampling frequency). After 106 cycles, a third characteristic time constant appears (τ_3) and grows in magnitude with continued cycling.

Table 6.1: Table summarizing the characteristic relaxation times for an aqueous 2,6-DPPEAQ-ferrocyanide flow cell (trial 5) determined by DRT analysis.

Cycle number	τ_1 (µs)	τ_2 (ms)	τ_3 (ms)	τ_4 (ms)	τ_5 (s)
1	64	0.77	n/a	22	0.25
21	80	1.2	n/a	20	0.20
51	50	0.47	4.2	32	0.21
106	50	0.04	2.3	17	0.18
206	40	0.29	2.3	21	0.18
406	40	0.27	2.3	27	0.21
806	50	0.35	2.7	39	0.27

Table 6.2: Table summarizing the characteristic frequencies for an aqueous 2,6-DPPEAQ-ferrocyanide flow cell (trial 5) determined by DRT analysis.

Cycle number	f_1 (Hz)	f_2 (Hz)	f_3 (Hz)	f_4 (Hz)	f_5 (Hz)
1	2501	209	n/a	7.4	0.64
21	1989	133	n/a	8.0	0.80
51	3158	338	38	5.0	0.77
106	3156	405	67	9.2	0.86
206	3982	541	68	7.7	0.85
406	3982	585	69	5.9	0.76
806	3156	450	57	4.1	0.58

The characteristic time constants and associated frequencies determined through DRT analysis are summarized in Tables 6.1 and 6.2, respectively. The datapoints approximately corresponding to each frequency are indicated by the large circles in Figure 6.2. With the exception of f_4, the location of these frequencies align with plausible features in the data. The feature at f_4/τ_4 appears to account for low-frequency

noise (in the 1 - 4 Hz region between τ_4 and τ_5). This frequency range correlates with the peristaltic pump roller frequency, which is 3.6 Hz. The pump rollers push "pulses" of electrolyte through the cell body, so it is reasonable to expect some resulting noise around the low-frequency diffusion feature. Indeed in previous studies, we have observed periodic pulses in time-domain voltage measurements during cycling at the pump roller frequency. We believe this fourth time constant (f_4/τ_4) to be an artefact of pump noise and disregard it in further analysis. Ignoring both the τ_4 peak and long time constant artefact $\tau = 100$ s from Figure 6.3a, four distinct peaks remain: τ_1, τ_2, τ_3, and τ_5. (The time-constants and their corresponding EIS frequencies are labelled in Figures 6.2 and 6.3 for clarity). Given that each peak represents a characteristic RC relaxation time constant, we suggest an equivalent circuit containing 3 RC-elements (corresponding to τ_1, τ_2 and τ_3). To capture diffusion processes, we use a Warburg "short" element in place of an RC-element for τ_5. As suggested by the DRT analysis, we assert that this is the minimum number of equivalent circuit elements required to model the EIS data without over-fitting. In early cycles, a distinct feature corresponding to τ_3 cannot be resolved in either the DRT or EIS spectra. A physical rationale for its appearance with extended cycling is discussed in the following paragraphs.

We interpret each RC-element to represent charge-transfer for a redox-active species at an electrode interface (as described for the Randles circuit in section 3.2.2). One may ask why three elements are visible, rather than two, when there are two distinct electrode environments – positive and negative. Two plausible physical origins accounting for these elements are described below. First, the additional RC elements may be needed to account for inhomogeneities in across the carbon electrode surface. The Sigracet-brand (SGL 39 AA) carbon papers used in this study are well-known to consist of at least two-carbon environments: structured PAN-based carbon fibres, and a graphitic binder derived from a proprietary resin [42, 43]. Using EDX mapping

Greco *et al.* showed the surface oxygen content to be up to a factor of four greater on the graphitic binder compared to the carbon fibre surface, and further showed strong correlation between the vanadium reduction rate constant, and surface oxygen concentration [42]. Given these observations, it would not be unreasonable to expect variations in charge-transfer kinetics resulting from electrode inhomogeneities. More specifically, the three RC elements may capture charge-transfer processes occurring at the carbon fibres, graphitic binder, and graphite current collectors. The charge-transfer resistance and capacitance for these environments may suffer unequally with cycling induced degradation, causing the corresponding RC semi-circles to become broader and more distributed in the EIS Nyquist plots (Figure 6.2).

As a second hypothesis, the three RC elements may capture charge-transfer processes occurring in the positive and negative half-cells. The two half-cells are assembled with identically prepared electrodes and are therefore expected to exhibit a similar ECSA and capacitance at the beginning of cycling. Two identical capacitors in series are represented by a single semi-circle in a Nyquist plot, but will form distinct semi-circles as the associated RC time constants become dissimilar, due to changes in either or both the capacitance and charge transfer resistance caused by degradation. This behaviour is observed in Figure 6.2b, which shows a single high-frequency semi-circle for cycle 1. As the cell is cycled, this feature becomes broader and the individual relaxation times (indicated by f_1, f_2, and f_3) become distinguishable. The appearance (and subsequent growth) of a third, distinct relaxation time after cycle 106 may indicate preferential fouling of one half-cell over the other. In fact, evidence suggesting increased fouling of the negative half-cell is observed in the single electrode EIS data, which is discussed in section 6.3.2.

We interpret the Warburg diffusion element to represent the diffusion of posolyte or negolyte species from the bulk electrolyte to the electrode surface. The series resistor (R_s) accounts for flow cell features that manifest as a pure resistance, such

as solution, membrane, electronic and contact resistances. Finally, the inductor (L) accounts for inductive contributions (mainly from the test leads). Equivalent circuit fits to the raw (no inductance subtracted) trial 5 EIS data are shown in Figure 6.3b using the suggested equivalent circuit model.
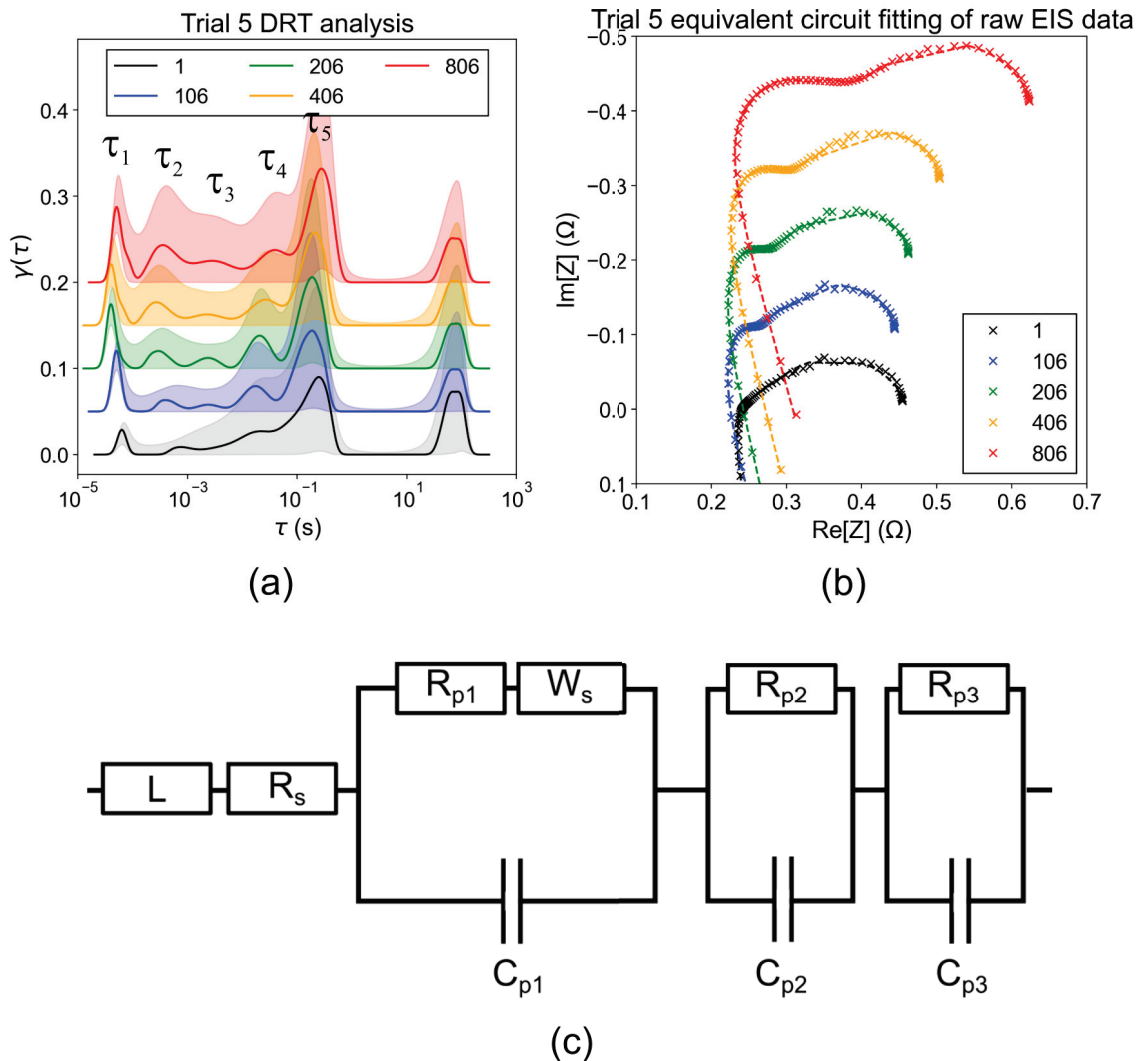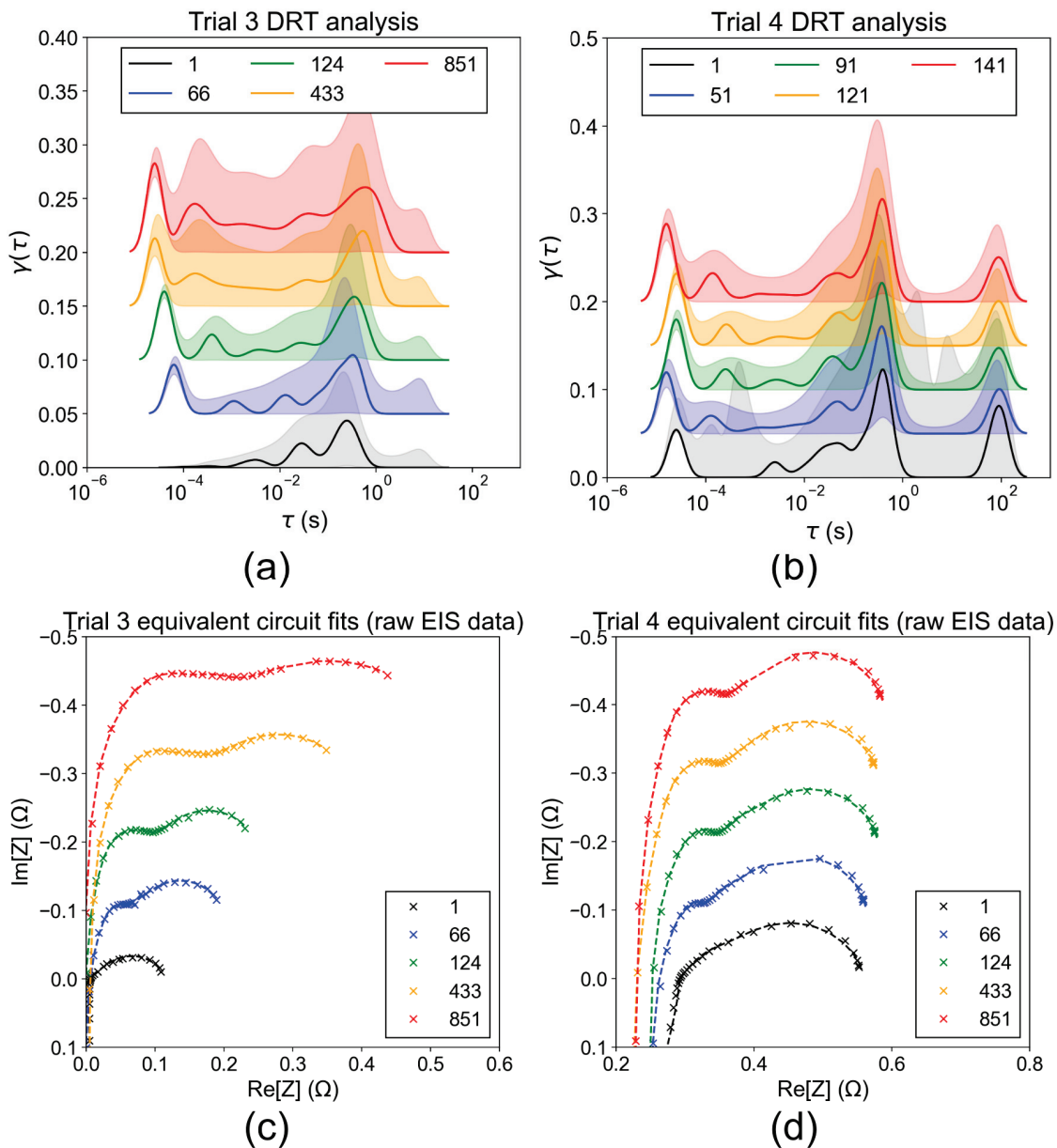

Figure 6.4: Figure illustrating the distribution of relaxation times (a) and associated fits (c) for the trial 3 aqueous 2,6-DPPEAQ-potassium ferrocyanide flow cell. Trial 4 DRT (b) and equivalent circuit fits (d) are also shown. The shaded regions in (a) and (b) indicate a 99 % confidence interval.

DRT and equivalent circuit analysis were similarly performed on the trial 4 and 3 datasets. The results are shown in Figure 6.4. (The high-frequency intercept for trial 3 data (Figure 6.4c) appears near 0 Ω on the real axis. This numerical subtraction was performed only for presentation clarity in Figure 6.4, to offset the variable contacted resistance described in Appendix B). The EIS sampling density for trials 3 and 4 was lower (5 pts/decade) compared to the trial 5 cell (10 pts/decade), which reduced the confidence with which the distribution of relaxation times can be determined. In addition, cable management was improved in the trial 5 dataset to reduce lossy inductance (which can obscure high frequency features in EIS data). Despite these experimental differences, DRT analysis revealed a similar distribution of relaxation time constants as for the trial 5 data. Five peaks can be observed in both trials after extended cycling; meanwhile, 3 – 4 peaks are visible early on in cycling (cycles 1 – 66). Again, the peak centred near $\tau = 100$ s in Figure 6.4b is attributed to noise in the lowest-frequency data. (The low frequency data was truncated in the trial 3 dataset to remove this feature). The similarity between the three datasets lends further confidence to support our equivalent circuit selection depicted in Figure 6.3c.

The parameters determined from equivalent circuit fitting are shown in Figures 6.5 and 6.6. The three resistors in parallel RC units grow monotonically with cycling. In general between the three trials: R_{p1} increases by approximately a factor of 2, R_{p2} grows by approximately a factor of 3 and R_{p3} grows by a factor of nearly 7. Meanwhile, the three capacitors decrease with cycling. A larger change appears to occur within the first 100 cycles; however, it is possible that this may be an artefact of fitting uncertainty. Data for early cycle numbers exhibits more scatter, which is attributed to the inherent difficulty in fitting the small semi-circular feature at high frequencies. In trials 3 and 4, this feature is dominated by a large inductance, which contributes to the fitting difficulty. As cycling continues the high frequency feature diameter grows, causing it to become more distinct. This uncertainty is also reflected
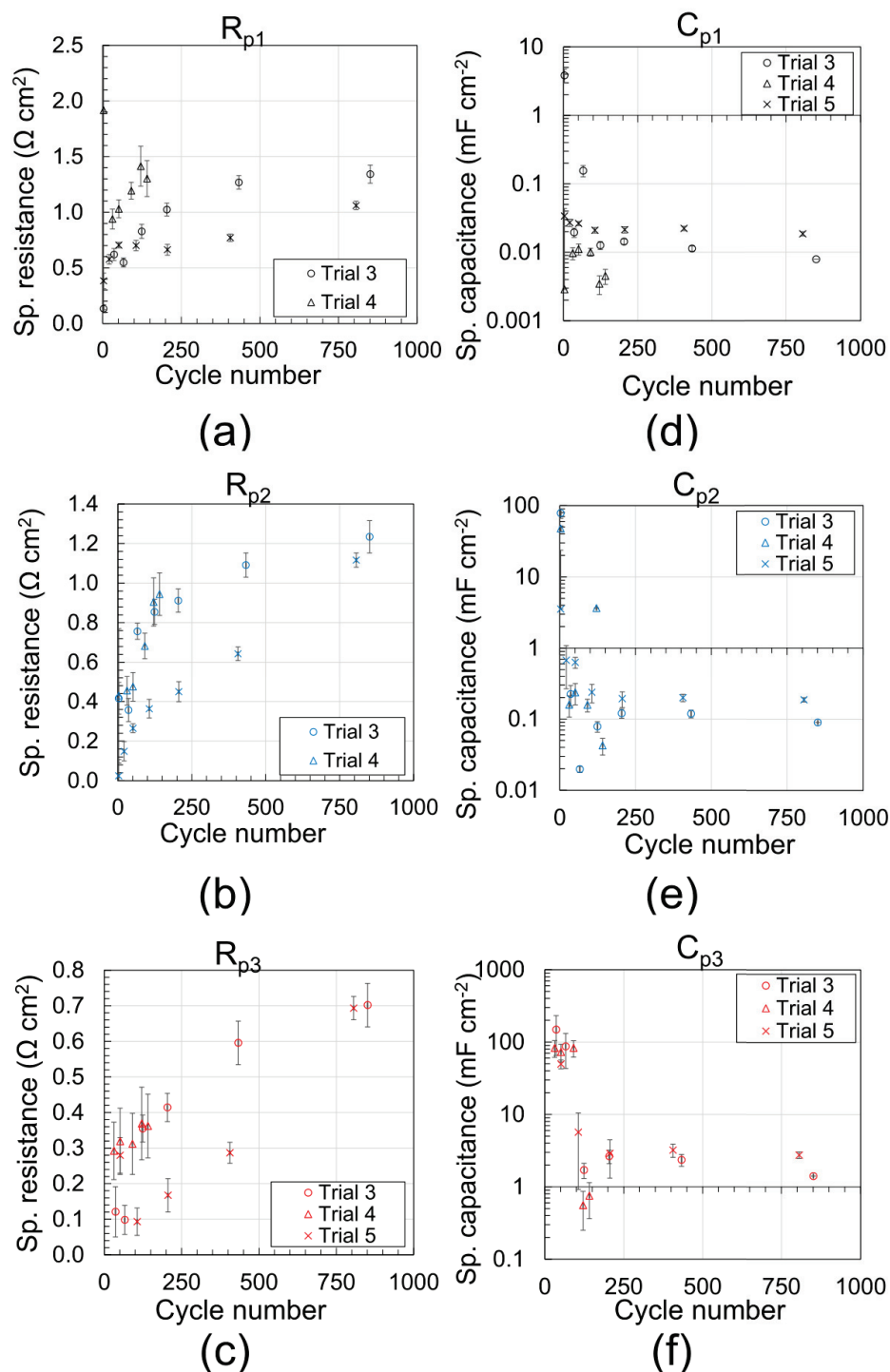
Figure 6.5: Figure illustrating the evolution of R_{p1} (a), R_{p2} (b), R_{p3} (c), C_{p1} (d), C_{p2} (e) and C_{p3} (f) with cycling for aqueous 2,6-DPPEAQ-potassium ferrocyanide flow cells. The parameters were determined using equivalent circuit fitting as described above. The area specific resistance and specific capacitance are referenced with respect to the total geometric surface area of the electrodes, though the true macroporous area is expected to be 10 - 20x greater.
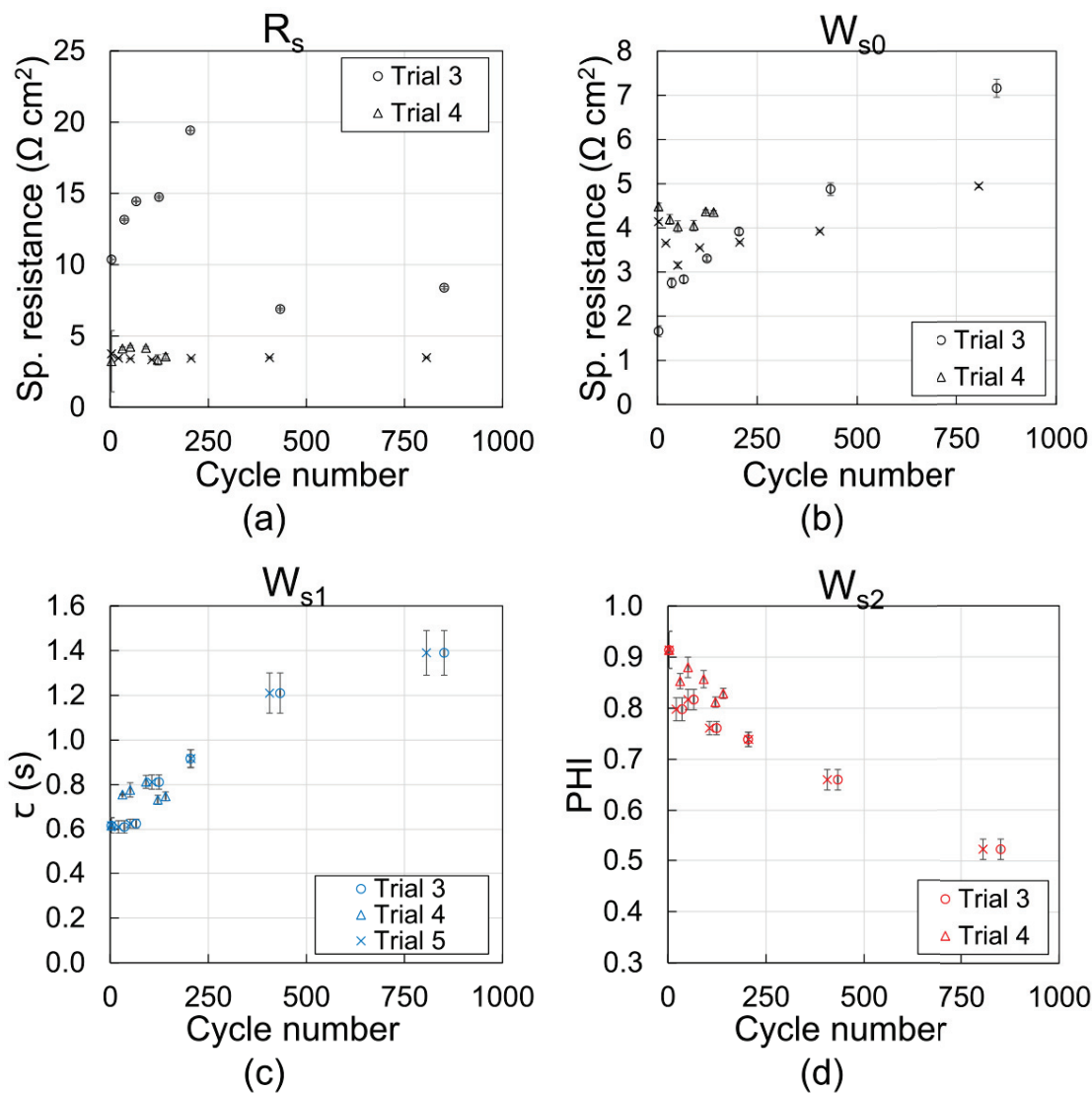
Figure 6.6: Figures illustrating the evolution of series resistance (a) and Warburg diffusion parameters (b) – (d) with cycling for aqueous 2,6-DPPEAQ/potassium ferrocyanide flow cells. The parameters were determined using equivalent circuit fitting as described above.

in the size of the error bars, which are generally larger for lower cycle numbers. The trial 4 data also shows more scatter; we attribute this to the cell inductance, which was largest for this dataset (before cable management was improved for trial 5).

The series resistance, shown in Figure 6.6a is constant within uncertainty for trials 4 and 5 (after issues with contact resistance were corrected). The Warburg impedance parameters show a noticeable change with cycling. The magnitude of the Warburg resistance increases only slightly, which is consistent with observations in the full cell EIS spectra (Figures B.3 and 6.2). The trends and magnitudes of the fitted parameters are sensible when compared to the inductance-corrected EIS data shown in Figures B.3 and 6.2.

6.3.2   Post-cycling electrode analysis

X-ray photoelectron spectroscopy

XPS measurements were performed to compare the surface composition of cycled electrodes with fresh and uncycled samples. Here, the term "uncycled" refers to electrodes that were stored in posolyte (or negolyte) solutions, but were not electro-chemically cycled. Figure 6.7a compares the survey spectra from fresh and cycled samples. Quantitative analysis of high-resolution scans reveals minor quantities of phosphorus (0.3 %) and iron (0.4 %) on the cycled electrode surface. Phosphorus and iron are present in the negolyte and posolyte (respectively) and would be expected if electrolyte residues, or degradation products were present on the electrode surface. Figures 6.7c and d show for comparison the survey spectra and surface composition of uncycled and fresh electrodes. Peak fitting of the high-resolution data suggests that no more than 0.6 % and 0.2 % of the electrode surface composition can be attributed to phosphorus and iron (respectively) in the uncycled samples. In many cases the detection limit of XPS is no better than 0.1 - 1 atomic % [138]. Taking this into consideration, the quantity of phosphorus and iron observed on the cycled elec-
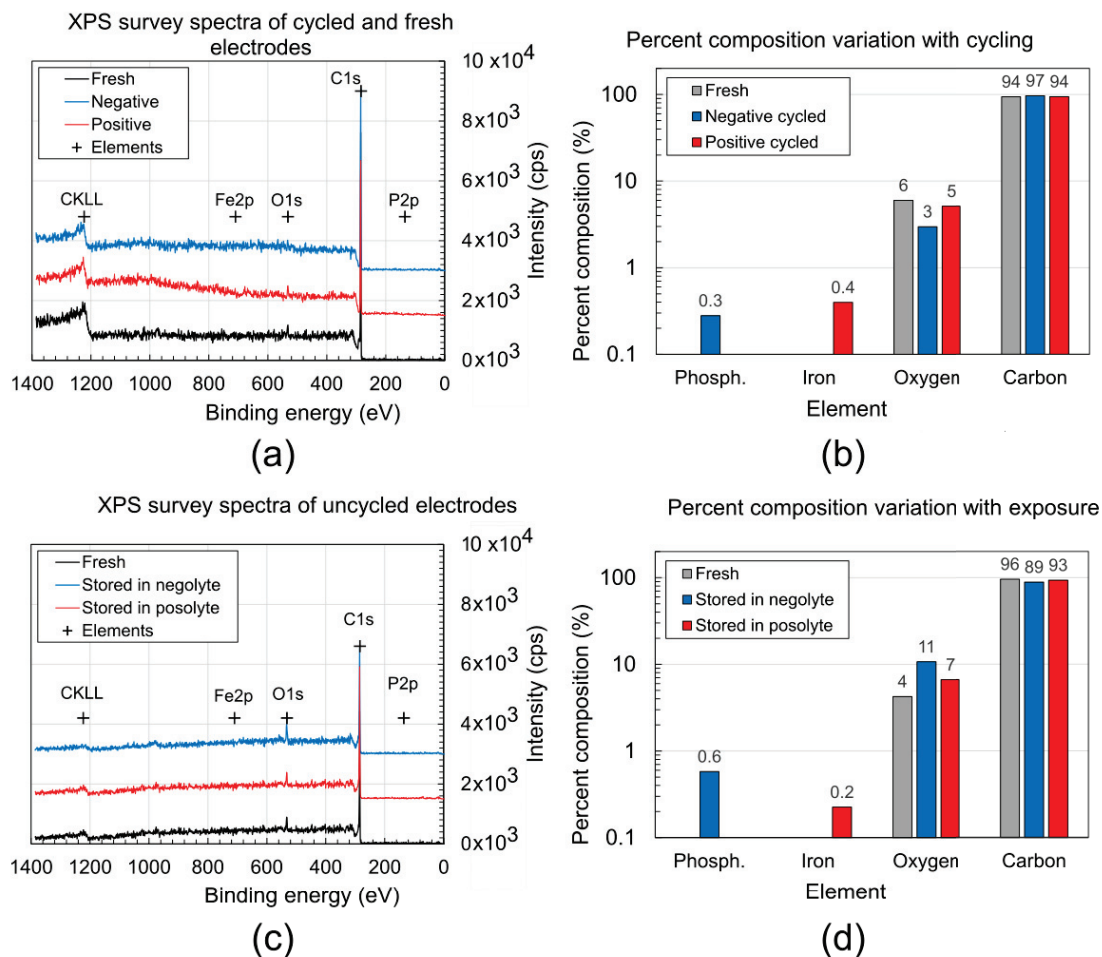
Figure 6.7: Figure showing XPS survey spectra (a) and atomic concentrations (b) for electrodes harvested from a cycled cell compared to a fresh electrode. For comparison, survey spectra for electrodes that were stored in electrolyte solution but not cycled are shown in (c). The calculated atomic surface concentrations are shown in (d). Peak positions for elements observed in high-resolution scans are indicated by black crosses in (a) and (c).

trodes is comparable to that expected from passive electrolyte exposure (i.e. residues remaining on the porous surface after cleaning).

Ideally, electrode samples from multiple cells cycled under the same conditions (and to the same state-of-health) would be analyzed to quantify the uncertainty in our compositional analysis. Two additional cells were cycled for this purpose; however, these cells were irreversibly damaged by instrumental and software errors. As a rough indicator of sample-to-sample variation, we take the difference between the fresh electrode samples analyzed in Figure (b) and (d), which show that oxygen constitutes between $4 - 6$ % of the surface composition, while carbon accounts for $94 - 96$ %. Using this 2 % range in uncertainty, we see that the total surface composition is comparable to what would be expected from passive electrolyte exposure. The oxygen content of electrodes stored/cycled in negative electrolyte may show subtle changes compared to the fresh electrode sample; however, these differences are minor in comparison to other systems we have characterized [4].
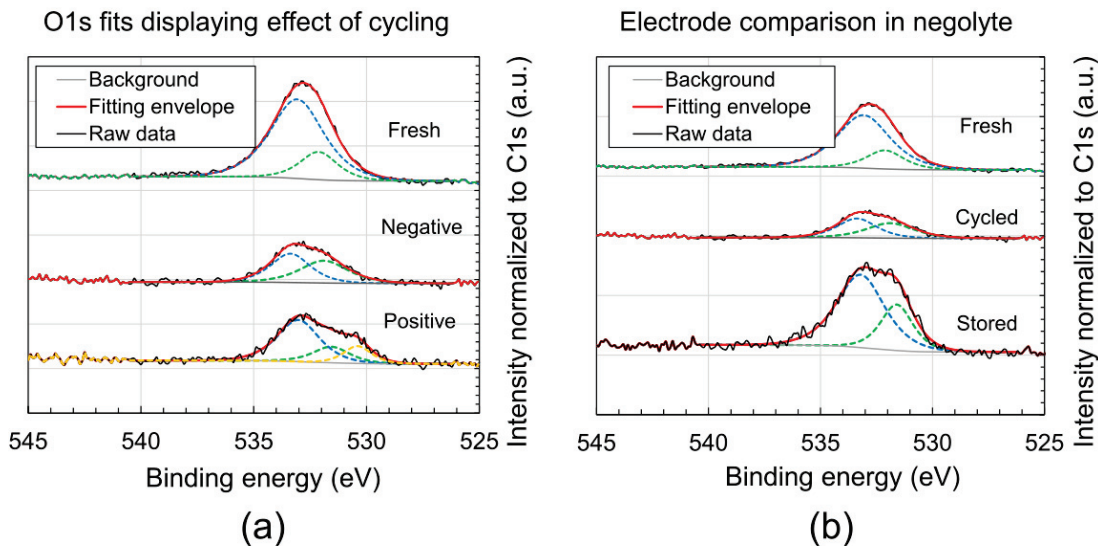
Figure 6.8: Figure showing high-resolution O1s spectra from electrodes harvested from a cycled cell in comparison to a fresh electrode (a). A comparison of the oxygen 1s transition for electrodes that were cycled and stored in negolyte is shown in (b). Spectra are normalized to the C1s peak intensity, and vertically offset for clarity.

Figure 6.8 shows the high-resolution oxygen 1s (O1s) data and fits for cycled (a) and uncycled (b) electrodes in comparison to a fresh sample. Oxygen has a high electronegativity, and does not exhibit a significant chemical shift (in XPS) when different bonding environments are present. As a result, the individual peaks contributing to the O1s environment in these samples cannot be individually resolved. To handle this, we constrain two peaks to each spectrum to represent the low ($\sim$ 531.5 eV), and high ($\sim$ 533.2 eV) binding energy environments. In the positive cycled sample, a pronounced shoulder is visible at low binding energy, which we treat with a third environment at $\sim$ 530.5 eV. The fractional peak intensity attributed to the high binding energy environment decreases from 81 % in the fresh electrode to 70 % and 52 % in the uncycled and cycled electrodes respectively.

Scanning electron microscopy

Figure 6.9 compares some representative scanning electron images of a fresh electrode ((a) and (d)) to cycled negative ((b) and (e)) and positive ((c) and (f)) electrode samples. Each image shows a mat of carbon fibers (nominal diameter $\sim$ 10 μm) adhered together with a graphitic binder. Images of the fresh electrode show clean carbon fibers and graphitic binder. No structural changes to the fiber mat are apparent after cycling. Some authors have reported peeling and/or pitting of cycled carbon electrodes in vanadium RFBs [52]; however, the electrodes from this quinone/ferrocyanide flow cell show no observable changes to the carbon fibers. Some small particles may be observed on the cycled positive electrode fibers (if at all); however, these could equally be attributed to the graphitic binder. Physical changes were also not observed for electrode samples stored in negolyte and posolyte without electrochemical cycling (B.5).
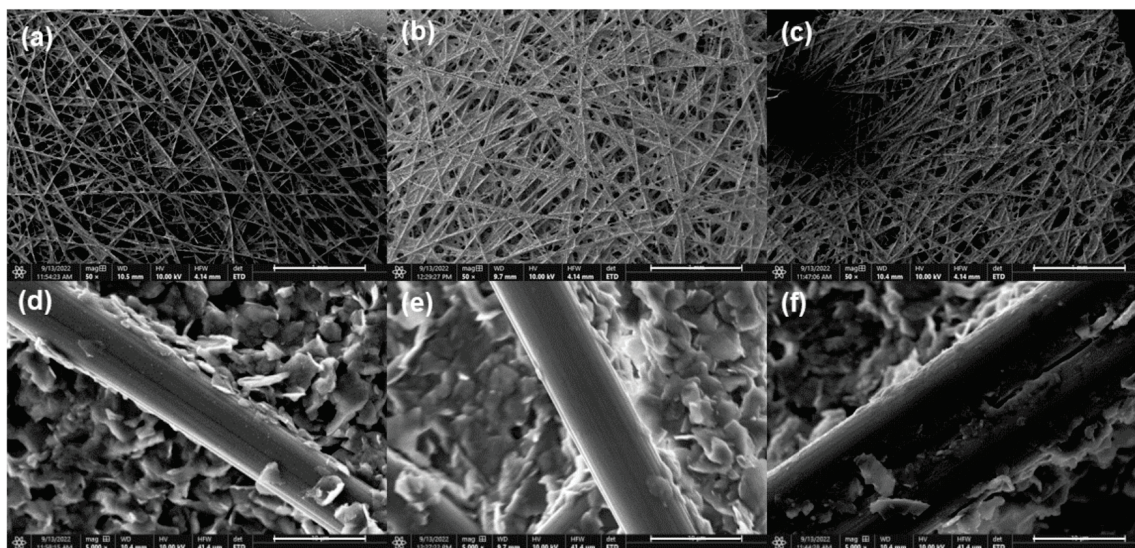
Figure 6.9: SEM images of fresh (a,d), cycled negative (b/e) and cycled positive (c/f) carbon electrodes at two different magnifications. The scale bars in the top row represent 1 mm, while the scale bars in the bottom row represent 10 μm.

Single electrode EIS

Single-electrode EIS was performed on the cycled electrodes (*ex situ*) in a three-electrode cell. The results are summarized in Figure 6.10. The spectra show a large sample-to-sample variance, which we attribute to the uncertainty involved in preparing a reproducible electrode area (3 x 3 mm). Qualitatively we observe that the positive cycled electrode exhibits a comparable spectrum to the fresh and stored electrode samples. In contrast the negative cycled electrode shows a larger diameter high-frequency feature (which we attribute to increased charge-transfer resistance); the cycled spectrum shape also differs from the uncycled samples.

It is difficult to extract a meaningful quantitative comparison between this data and the full cell EIS spectra shown in Figure 6.2. The measurement geometry differs significantly between the two experiments, and the full cell impedance spectra sample a much larger electrode area (896 mm^2) that is exposed to a much higher concentration (0.5 M) of pumped electrolyte. In comparison, the single electrode EIS measurements were performed in a three electrode cell using 10 mM quiescent
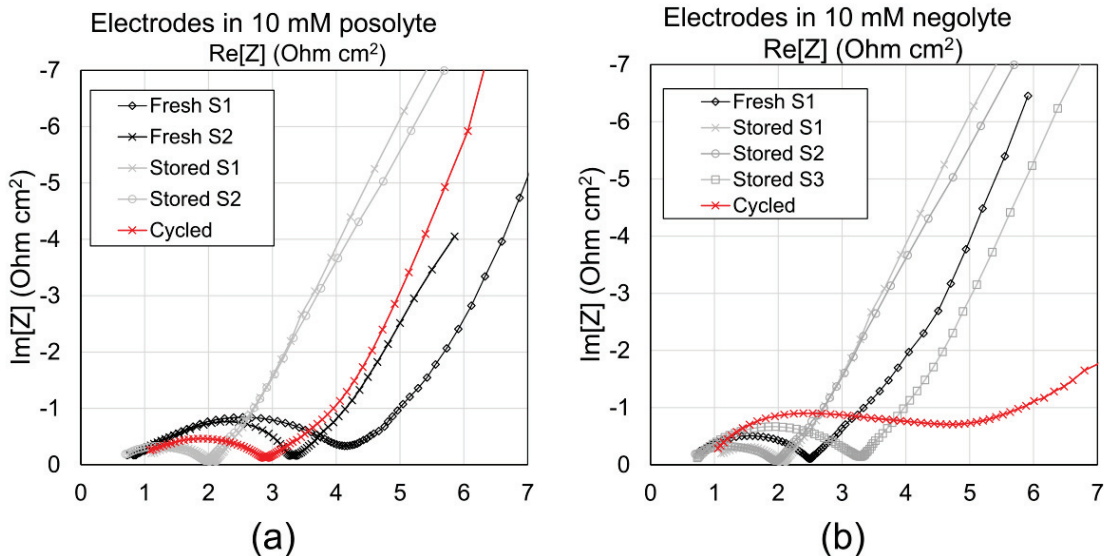
Figure 6.10: Single electrode Nyquist plots for a cycled positive (a), and negative electrode (b), compared to a fresh sample. Spectra for electrodes that were stored in electrolyte (but not cycled) are also shown. The area specific resistance is given with respect to the total geometric surface area of the carbon paper sample (3 x 3 mm); however, the true macroporous surface area is expected to be 10 – 20x greater.

electrolyte. The electrolyte concentration was lowered to better resolved the high-frequency charge-transfer feature (which was small in 0.5 M electrolyte). Attempts to stir the solution (to mimic electrolyte convection in the full cell) resulted in noisy EIS data. Qualitatively we conclude that the only statistically significant increase in charge-transfer resistance is observed at the negative electrode (through single electrode EIS). Therefore, we expect the changes observed in full cell EIS spectra (Figure 6.2) to originate primarily at the negative electrode.

6.3.3 Post-cycling membrane analysis

Electrochemical impedance spectroscopy was used to quantify changes in the membrane through-plane resistance. The mean high-frequency resistance was found to be $2.1 \pm 0.1\Omega$ cm^2 for cells assembled with fresh membrane samples. The uncertainty represents the standard error in high frequency resistance for four cells, each assem-

bled with a different sample of fresh membrane. The high-frequency resistance for cells assembled with a cycled membrane was 1.9 Ω cm^2. In both cases, the area specific resistance is quoted with respect to the geometric area of membrane between the two half-cells (2.24 cm^2). The measured series resistance for the cells assembled with each membrane are equivalent within uncertainty, so membrane fouling is not expected to contribute significantly to cell impedance growth.
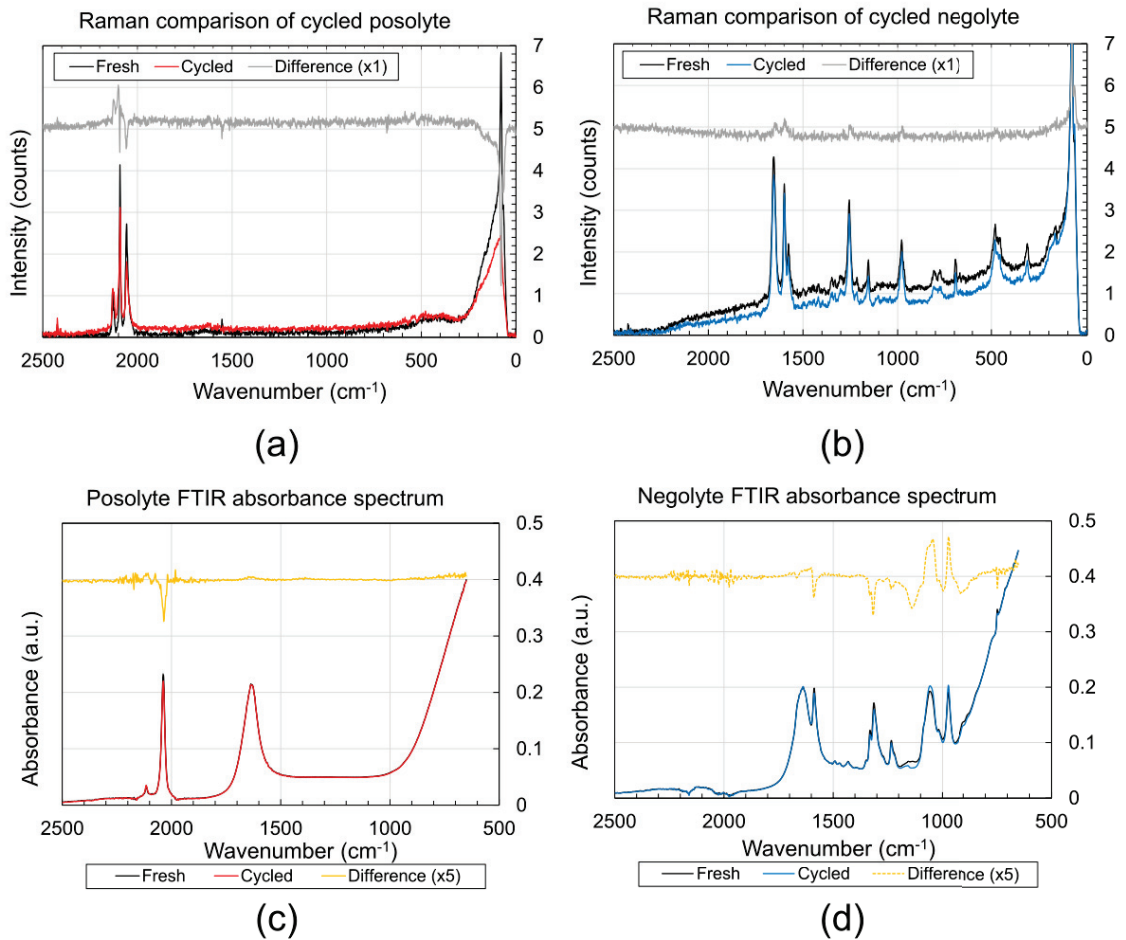
Figure 6.11: Raman spectra comparing cycled and fresh posolyte (a), and negolyte (b) solutions. FTIR absorption spectra comparing cycling and fresh posolyte (c), and negolyte (d) solutions.
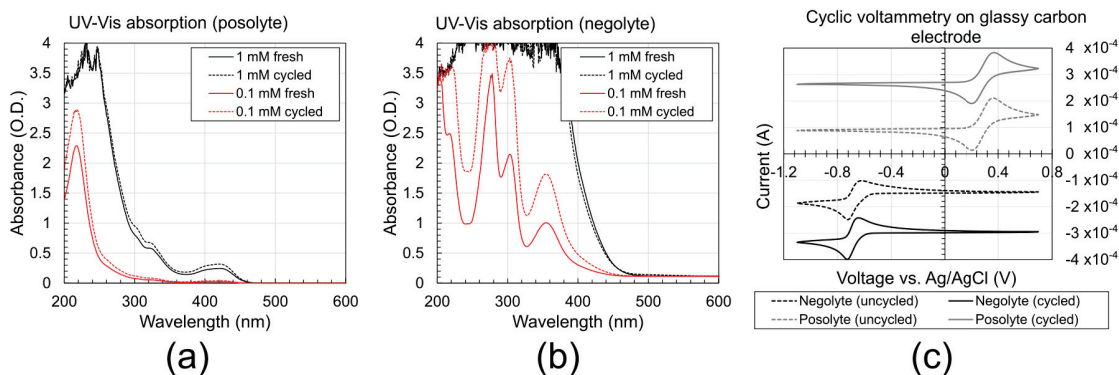
Figure 6.12: UV-Vis absorption spectra comparing cycled and fresh posolyte (a) and negolyte solutions (b). Cyclic voltammograms of cycled and fresh electrolyte are shown in (c). Electrolyte was diluted to 10 mM concentration in a supporting electrolyte of 2.0 M KCl (adjusted to pH 9).

6.3.4 Post-cycling electrolyte analysis

Analysis of cycled electrolyte samples suggests that there are negligible differences compared to the uncycled electrolyte controls. Raman and FTIR spectroscopy (Figure 6.11) show no new vibrational modes. No outstanding peaks are visible in the difference spectra (between fresh and cycled electrolyte) outside of minor changes in peak intensity. We attribute these differences to small variations in concentration caused by solvent evaporation during cycling, and residual species that were not fully discharged. This is supported by differences in UV-Vis absorption intensity observed in Figures 6.12a and b. We conclude that chemical degradation does not account for a significant portion of capacity loss, which is not surprising given the high stability reported for 2,6-DPPEAQ and potassium ferrocyanide. Figure 6.11(c) also shows that crossover of active electrolyte species through the membrane does not occur in detectable quantities and therefore also cannot account for capacity loss.

6.4   Discussion and conclusions

The 2,6-DPPEAQ-potassium ferrocyanide flow cells examined in this study are characterized by very low capacity fade rates. After correcting for cell design issues, we determined the average capacity fade rates to be 0.026 % day^{-1} and 0.057 % day^{-1} in two separate longevity trials. The excellent capacity retention is consistent with our expectations from the literature: 2,6-DPPEAQ is reported to exhibit robust chemical stability, even under accelerated stress conditions (pH 14 and elevated temperature) [2]. Potassium ferrocyanide is similarly reported to exhibit high chemical stability [28,95,97]. Characterization of our cycled electrolytes by Raman, FTIR and UV-Vis spectroscopy confirms that negligible differences are observed compared to fresh electrolyte. If at all, only minor differences in some peak intensity are observed – consistent with changes to electrolyte concentration during characterization.

While the cell exhibits strong capacity retention, we observe a loss in voltage and energy efficiency with continued cycling (Figure 6.1). The trial 4 cell shows a loss of 3 % energy efficiency after 160 hours of cycling; meanwhile, the trial 5 cell shows a loss of 7 % energy efficiency after 950 hours. We correlate this loss with increased cell impedance, which evolves gradually with cycling (Figure 6.2). Visual inspection and equivalent circuit fitting of the datasets confirms that the cell series resistance (taken from the high-frequency intercept with the real axis in a Nyquist plot) does not change appreciably with cycling. As a result, changes to the solution conductivity and membrane through-plane impedance (which manifest as a series resistance) are not expected after cycling. Post-cycling membrane analysis confirms that the high frequency resistance for cells assembled with fresh and cycled membrane samples are equivalent within uncertainty, which is consistent with the stable series resistance for the cell. We conclude that membrane fouling does not contribute to the decreased cell performance after cycling.

DRT analysis of the full cell impedance spectra suggests that the EIS data is most

appropriately modelled using an equivalent circuit containing 3 parallel RC elements in series, and a Warburg "short" diffusion element. The Warburg diffusion element is used to capture the longest relaxation time (low frequency), which is indicated in the EIS data in Figure 6.2. We interpret it to signify the diffusion of posolyte/negolyte species from the bulk solution to the electrode interface. While this diffusion resistance grows with cycling, visual inspection and equivalent circuit fitting show that this change is comparatively small in relation to other changes. The most significant changes appear at the shortest three relaxation times (which are represented by the 3 RC-elements), also indicated in Figure 6.2. We associate these features with charge-transfer at the electrode interface, where each RC-element may represent a different electrode environment (either the positive and negative half-cells; or, inhomogeneities across the electrode surface). These changes in the charge-transfer features are characterized by increased area specific resistance (associated with each relaxation time), and a decreased specific capacitance. The third RC element shows the largest fractional changes of the three relaxation times: R_{p3} increases by a factor of seven, while C_{p3} decreases by approximately two orders of magnitude.

Post-cycling electrode characterization was performed on the cycled positive and negative electrodes to help determine the origin for these changes. SEM images do not show significant changes to the morphology of cycled electrodes in comparison to fresh electrode samples. Single electrode EIS measurements show that the diameter of the high-frequency semi-circle (which we associate with charge-transfer resistance) is approximately 50 % larger for both the cycled positive and negative electrodes in comparison to a fresh electrode sample. Interestingly the changes observed through impedance spectroscopy do not manifest as dramatic changes in XPS measurements. Very few foreign elements are detected on the cycled electrode surfaces in comparison to electrodes that were stored (but not cycled) in electrolyte. These results are not consistent with electrochemical deposition of an insoluble overlayer on the electrode

(which could inhibit charge-transfer at the solution interface). If any differences in electrode surface composition are present, we see a minor reduction in oxygen concentration on the negative cycled electrode surface.

Considered with the changes in full cell impedance spectra, these post-cycling electrode characterization results suggest that more subtle changes in the electrode surface may be responsible for the increased cell impedance and loss of voltage/energy efficiency with cycling. As discussed in Chapter 2, changes in oxygen surface functional groups have been correlated with improved cell efficiency. Sun *et al.* suggest a mechanism whereby certain OSFs act as active sites to facilitate charge-transfer to the vanadium electrolyte [50, 51]. It is unknown whether OSFs function similarly in organic electrolytes; however, the trends in oxygen concentration reported by Sun *et al.* are consistent with the diminished O1s peak intensity in cycled electrodes (relative to the C1s transition). In addition, we see that the fraction of oxygen present in a high binding energy environment is diminished in cycled electrodes. Higher binding energy oxygen ($\sim$ 533 eV) has been associated with nominally phenolic C–O bonds [50, 51]. Sun *et al.* report that thermal activation of carbon electrodes (by heating at 400 °C), and chemical activation (by treating with acid) increases the surface concentration of oxygen (relative to C1s) and also increases the fraction of high binding energy C–O groups relative to low binding energy C $=$ O groups. These changes were associated with an improvement in cell energy efficiency by more than 10 % [50, 51]. Given these reports it is not unreasonable to suggest that similar subtle changes could be responsible for the loss in 2,6-DPPEAQ cell performance with cycling. For future work, repeatability studies will be instrumental to assess the validity of this hypothesis. Characterizing the change in cell impedance and O1s environment for cells that are cycled to different states of health will also be informative for establishing trends and/or correlation between impedance growth and changes to the O1s chemical environment.

Chapter 7

Electrode Stability in a Non-Aqueous Viologen and Phenothiazine Electrolyte

7.1 Background and motivation

Starting in 2015, the Odom research group at University of Kentucky pioneered development of stable, non-aqueous electrolyte molecules. In 2015, a high-solubility phenothiazine-based posolyte material was developed – 10-[2-(2-methoxyethoxy)-ethyl]-10H-phenothiazine (MEEPT). This material was shown to exhibit no capacity loss after cycling at high current-density for 100 cycles using a symmetric cell configuration [6]. This was a significant advancement in the non-aqueous ORFB field, which still lags aqueous ORFB performance. MEEPT is now commercially available from TCI (M3068) to use as a standard non-aqueous electrolyte. In 2020 Attanayake *et al.* reported on (2-(2-methoxyethoxy)ethyl)viologen bis(bis(trifluoro methanesulfonyl)imide (MEEV-TFSI$_2$), a novel two-electron receptor with high solubility. Liang *et al.* and Attanayake *et al.* reported negligible degradation products for full cells assembled using these materials; however, issues with capacity loss have yet to be

fully understood [5, 126].

Electrode and separator fouling have not been evaluated for cells assembled with MEEPT and MEEV molecules. As described in Chapter 2, electrode properties strongly affect cell efficiency and losses at the electrode-electrolyte interface. In this study we characterize electrode and separator degradation in MEEPT/MEEV-TFSI$_2$ flow cells that are prepared as reported by Liang *et al.* [5]. We perform a combination of EIS (*in situ* and post-cycling) and XPS measurements to understand the origins of impedance growth after cycling. It is our hope that developing this understanding will help to improve cell efficiency for longer duration cycling. In addition, we repeat these measurements under a range of anticipated application temperatures: 0, 24 and 40 °C. With the exception of a handful of works this question is largely unexplored in ORFB literature at this time [127, 161–164].

7.2   Experimental methods

MEEPT/MEEV(TFSI)$_2$ flow cells were assembled as described in Chapter 4. Briefly, 2 sheets of SGL 39 AA carbon paper (1.6 x 1.4 cm) were sealed into each half-cell using 0.015 inch thick EPDM gaskets. The electrodes were separated using a one inch square section of Daramic 175. Both electrodes and separator were used as-received from their respective manufacturers. The cells were held together using four 1/4-28 bolts tightened to 12 in lbs to compress the electrodes to $\sim 80\%$ of their original thickness. Cell assembly was performed on the benchtop before storing under rough vacuum (-30 in Hg) to remove ambient oxygen and moisture for 48 hours. (The pump and transport tubings were likewise stored under rough vacuum). The vacuum chamber was back-filled with nitrogen, and the cell components were transferred into a nitrogen glovebox to connect the cell, tubing and reservoirs. Room temperature and high temperature cells were filled with 7 mL of 0.5 M electrolyte; however, the low temperature cells required longer tubing lengths to transport electrolyte between the

pump and cell (in the Environmental Test Chamber (ETC)), so these were filled with 8.5 mL of electrolyte. Cells for room temperature and high temperature experiments were transported into a continuous-flow nitrogen testing box (section 4.1.2), which was sealed and flushed with nitrogen for testing ($O_2 < 2\%$ vol). The low temperature cells were sealed and then transported into the ETC, where they were cycled under ambient atmosphere.

The electrolyte was prepared in a LCTech glovebox (H_2O and $O_2 < 1$ ppm). Tetraethylammonium bis(trifluoromethylsulfonyl)imide (TEATFSI, Iolitec: IL-0335-HP) was used as a supporting electrolyte. It was dehydrated under rough vacuum for 24 hrs, then mixed with dry acetonitrile to produce a 0.5 M solution. The negolyte ((2-(2-methoxyethoxy)ethyl)viologen bis(bis(trifluoro methanesulfonyl)imide ($MEEV$-$TFSI_2$)) was synthesized by Dr. Odom's research group. This was mixed in equal molar ratios with 10-[2-(2-methoxyethoxy)- ethyl]-10H-phenothiazine (MEEPT, TCI: M3068) to produce a final active electrolyte concentration of 0.5 M each in 0.5 M TEATFSI in dry acetonitrile. As described in section 2.3.2, the same pre-mixed electrolyte was used to fill both half-cells to create a cell with symmetric electrolyte configuration. This was done to minimize separator crossover, which can be driven by concentration gradients across the cell.

The electrolyte was pumped through the cell at 1 mL/min for 10 minutes to wet the electrodes and separator before the electrolyte flow-rate was increased to 10 mL/min. The electrolyte was then flushed through the cell for 30 minutes prior to cycling to ensure that the separator and electrodes were fully wetted. For each temperature (24, 40 and 0 °C), a cycle rate experiment was performed before stability cycling to identify an optimal cycle rate. As described in section 2.2, this optimal cycling current results from a trade-off between high voltage efficiency (low cycling currents), and a high Coulombic efficiency at (fast cycling currents).

During the cycle rate experiment, the cell was cycled at constant current between

0.9 V and 1.3 V limits. The charge/discharge current was incremented every 5 cycles. On the fifth cycle at each current level, the cell was charged and discharged using a constant-current, followed by a constant-voltage hold at the upper/lower voltage limit. This was done to estimate the true capacity of the cell (without resistive losses) before the current was incremented. Full cell EIS data was also collected every fifth cycle at 50 % SOC (1.1 V), as described in section 4.2.2. The following current densities were tested in sequence: 5, 10, 15, 20, 25, 40, and 5 mA cm^{-2}.

Following the cycle rate experiment the cell was also cycled at constant current to evaluate its long-term cycling stability. Again, EIS and constant-current/constant-voltage charging was used every fifth cycled to monitor cell capacity and impedance growth. In addition, full cell EIS was performed on the first and last cell cycles along with OCV self-discharge measurements (which are described in section 4.2.3). After cycling the cells were discharged to 0 % state-of-charge by holding at 0.9 V until the discharge current decayed to 2 mA cm^{-2}. The electrolyte was returned to the respective reservoirs and the electrodes, electrolyte and separator were collected for *post-mortem* characterization as described in Chapter 4.

7.3   Results

7.3.1   Cell cycling

While MEEPT is a commercially available molecule, the MEEV-TFSI$_2$ negolyte was synthesized by a previous graduate student in Dr. Odom's research group. A total of five cells were cycled (two each at 0 and 40ºC, and one at room temperature) – the maximum allowable from the quantity of negolyte material.
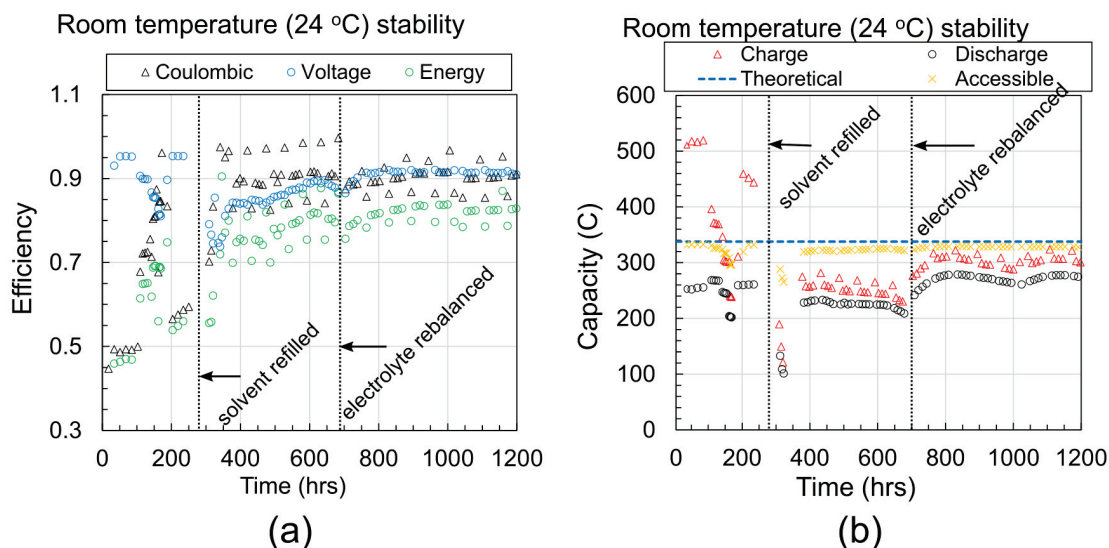
Figure 7.1: Figure illustrating the cell efficiency (a) and capacity (b) for a MEEPT-MEEV flow cell cycled at 24 °C as a function of time. After the cycle rate study (0 – 260 hrs), the reservoirs were topped up with solvent and the cell was cycled using a constant current density (5 mA cm^{-2}, C-rate = 0.12C). At 675 hours, the electrolyte was rebalanced between the two half-cells. A total of 127 charge-discharge cycles are shown in this figure.

Room temperature cycling

Room-temperature cell cycling was performed at 24 °C under nitrogen in a dry testing box (section 4.1.2). The cycling data is shown in Figure 7.1. Data shown for the first 260 hours of cycling corresponds to the cycle rate experiment, which was used to identify an optimal cycling current. (The tested currents and cell efficiency data are more clearly indicated in the Appendix (Figure C.1)). As described in section 2.2, the energy efficiency for RFBs using non-selective microporous separators is a trade-off between achieving high voltage or coulombic efficiency. These cells are expected to show higher voltage efficiency for lower cycling currents due to reduced ohmic losses. However, longer charge/discharge durations will allow additional time for charged electrolyte species to diffuse across the non-selective microporous separator (which results in reduced coulombic efficiency). A 15 mA cm^{-2} current density was found to produce the highest energy efficiency (68 %). (By convention the current density is

referenced with respect to the geometric area of the separator (1.6 cm x 1.4 cm)).

After the cycle rate experiment, the cell was cycled for an additional month. While 15 mA cm^{-2} yielded the best energy efficiency during the cycle rate study, increased cell impedance required a lower current density (5 mA cm^{-2}) for further long-term cycling. Again, constant-voltage holds were performed at the voltage limits every fifth cycle to estimate the true cell capacity (without ohmic losses). The voltage holds are responsible for the increased charge and discharge capacity observed at regular intervals (Figure 7.1b). Outside of these periodic changes, the cell capacity was observed to exhibit reversible losses during long-term cycling, which was attributed both to solvent loss and electrolyte imbalancing. After the cycle rate experiment, the volume of electrolyte decreased by over 50 % in the negative reservoir (only). No leakage points were identified in the cell, so the volume loss was attributed to solvent evaporation resulting from imperfect sealing at the reservoir fittings; this was observed to cause precipitation of active species in the negative reservoir and a qualitatively higher solution viscosity (compared to fresh electrolyte samples). The inaccessible material was redissolved by adding 2 mL of dry acetonitrile, which returned the reservoir fluid height to its original level. After a few cycles, the cell capacity almost completely recovered to its original value (on discharge). With continued cycling, a net migration of electrolyte from the negative to positive reservoir was observed. The volume difference caused the negative half-cell to become capacity-limiting. After 25 cycles, the electrolyte was manually redistributed between the two reservoirs (in a discharged state), and the cell capacity recovered. These solvent loss and imbalancing features have been reported in previous studies [5,126], and are not unexpected in this system given the high vapour pressure for acetonitrile (at room temperature), and the non-selective microporous structure of the Daramic separator. After the solvent was refilled, the accessible capacity was not observed to change for the remainder of the experiment. An interesting feature in the capacity data is that the charge

capacity during the first 260 hours greatly exceeds the theoretical and accessible cell capacity (which was determined by applying ohmic corrections to the charging limits as described in Chapter 5). Possible explanations for this behaviour include: coulombic inefficiency (resulting from crossover of charged active species through the microporous separator); and/or, parasitic reactions (occurring during the first few cycles). More evidence to support these explanations is discussed in the following sections.

As previously mentioned, the cycling data showed 15 mA cm^{-2} to yield the highest energy efficiency (68 %, Figure C.1). Interestingly, after performing further long-term cycling at 5 mA cm^{-2} (post-260 hours), the energy efficiency was observed to exceed this value. Immediately after the cycle rate experiment, the coulombic and energy efficiency were 60 % and 58 %, respectively. These figures rose to nearly 90 % and 84 % at the end of cycling. For comparison, the coulombic and energy efficiency were only 50 % and 48 % for the first five cycles at 5 mA cm^{-2} (0 – 100 hours).

Periodic fluctuations in coulombic efficiency are present in our dataset. The regular increases in coulombic efficiency correspond to cycles where constant-voltage holds were performed at the charging limits, and a 1.1 V hold is performed (on discharge) to pre-condition the cell for EIS. Charge passed during the constant-voltage holds is included in our calculation of coulombic efficiency. The 1.1 V hold increases the discharge capacity extracted (before crossover/self-discharge of charged species can occur), thereby increasing the coulombic efficiency. The coulombic efficiency for the following cycle (after constant-voltage holds) falls below the average trend. Because the cell was previously discharged using a combination of constant-current and constant-voltage holds, more time is required during the subsequent constant-current charge to reach the upper voltage cut-off. Since the subsequent discharge is also performed only using constant-current, the coulombic efficiency appears reduced.

High temperature cycling

High-temperature cell cycling was performed at 40 °C in the same nitrogen testing box (section 4.1.2). Temperature control methods are described in section 4.1.2.

The cell capacity and efficiency data for the high temperature cells are presented in Figure 7.2. Cycle rate experiments (Figure C.2, Appendix) found that a 10 mA cm^{-2} current density yielded the highest energy efficiency and cell capacity. Following the cycle rate experiment, the cell was cycled for an additional 100 hours at 10 mA cm^{-2} (which is indicated after the vertical line at 430 hours in Figures 7.2a and b). During constant-current cycling the discharge capacity was observed to fade at a rate of approximately 0.44 C day $^{-1}$, or 0.1 % (of the theoretical cell capacity) day $^{-1}$.

A second cell was assembled and cycled using only a 10 mA cm^{-2} current density (Figure 7.2c and d). This cell is referred to as HT2 and the first cell as HT, herein. The average charge and discharge capacity for the HT2 cell is approximately 350 C and 250 C at the beginning of cycling, respectively. This is similar to the 10 mA cm^{-2} current density data for the HT cell (Figure 7.2 and C.2). After about 200 hours of cycling, the HT2 cell capacity begins to rapidly decline at a rate of approximately 1.0 C day $^{-1}$, or 0.3 % (of the theoretical cell capacity) day $^{-1}$. This is mirrored by a loss in accessible capacity (which was determined by applying ohmic corrections to the charging limits as described in Chapter 5). The electrolyte fluid level in the negative reservoir (for the HT2 cell) was observed to decrease with cycling time. We again suspected that the resulting precipitation of active electrolyte species contributed to the lost cell capacity; so, 2 mL of dry acetonitrile was added to the negative reservoir (at 330 hours) to return the negolyte fluid line to its original height. This only resulted in a 50 % recovery of the lost capacity.

Similar to the room temperature study, the high-temperature cells show a steady increase in coulombic efficiency with cycling. This is most visible in the HT2 trial, where the coulombic efficiency begins at 50 %, and rises to 90 % at the end of cycling.
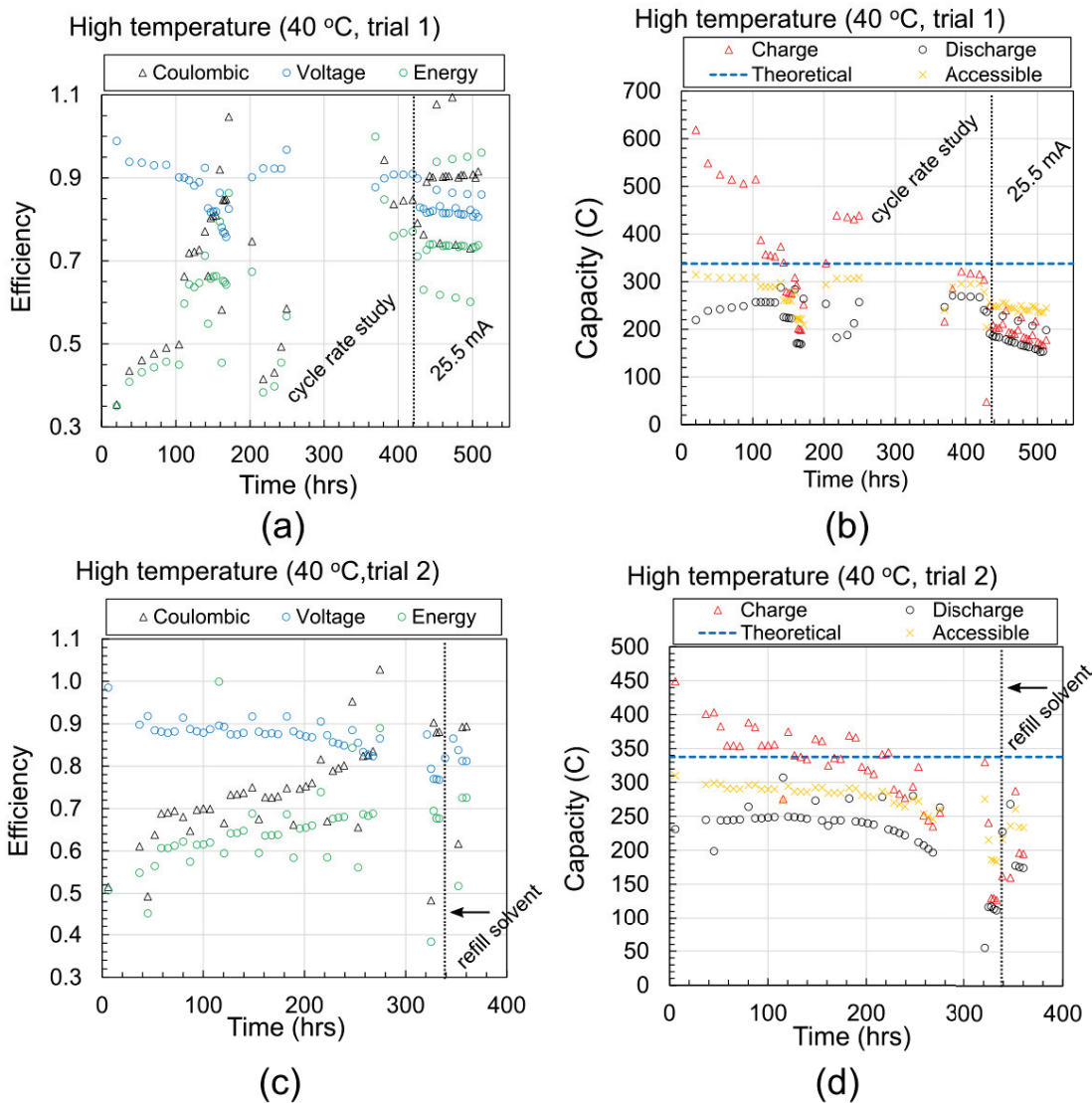
Figure 7.2: Figure illustrating the cell efficiency (a/c) and capacity (b/d) for two MEEPT-MEEV flow cells as a function of cycle time. Data from the first trial (a/b) includes data from the cycle rate study. After 430 hours, the cell was cycled using a constant current density (10 mA cm^{-2}, C-rate = 0.24C). The trial 2 cell (c/d) was cycled at a constant current density (10 mA cm^{-2}). Solvent was refilled after 340 hours. The stability experiment (trial 2) was cycled a total of 50 times.

Neglecting time when the cell was not cycled, the time scale for capacity loss (and onset of capacity loss) is comparable for both high-temperature cells. Compared to the room temperature cell, the capacity retention is much lower. A loss of over 50 % of the theoretical cell capacity is observed for the high-temperature cells after approximately 300 – 400 hours of cycle time. In contrast the cell capacity for the room temperature cell remains close to the theoretical capacity after 1200 hours of nearly continuous cycling. Reversible capacity changes are observed; however, these are easily corrected by refilling lost solvent and redistributing imbalanced electrolyte between the cell reservoirs. Although these corrections are qualitative, we do not expect them to introduce significant uncertainty in the final cycling results. We address this in the following paragraphs.

In these studies, volume loss observed in the cell reservoirs was attributed to solvent evaporation (through imperfect sealing of the cell reservoirs). Given the impermeability of our other cell materials, this is not an unreasonable assumption when no physical electrolyte leakage is observed – especially given the high vapour pressure for acetonitrile above room temperature. At 0, 24 and 40 °C, the vapour pressure for acetonitrile is reported to be 3, 12 and 22 kPa, respectively [165]. Solvent loss can cause precipitation of active material species (especially less soluble charged species [6]), which results in a loss of cell capacity. Solvent refilling was performed by eye, adding anhydrous acetonitrile to the depleted reservoir(s) to return the electrolyte fluid level to its original height. (This was referenced in comparison to photos of the reservoirs taken during the first hours of cycling). A difference in 1 mL of solvent clearly changes the fluid height in our low-volume reservoirs, so we take 1 mL as an upper limit on the uncertainty of the correct volume to return to depleted reservoirs. In our cells a 1 mL volume uncertainty would correspond to a change of electrolyte concentration by 0.063 M. We do not expect this to significantly affect the accessed cell capacity, as we do not operate this close to the solubility limit for negolyte/posolyte species.

It is possible that the addition of incorrect volumes of solvent could affect chemical decomposition rates if they are bimolecular, or mediated by chemical impurities in acetonitrile as suggested by some authors [113]; however, these effects are beyond the scope of our investigation.

Rebalancing electrolyte is performed to balance net migration of electrolyte from one half-cell to the other. The imbalancing is caused by a pressure differential across the separator, and results in one half-cell becoming capacity-limiting. Electrolyte rebalancing involves fully discharging the cell and returning excess electrolyte from one half-cell to the capacity-limiting side. Because our active posolyte and negolyte are pre-mixed (and used in both reservoirs) this process is not detrimental to cell operation. Furthermore, we show in later sections that the average self-discharge time for newly-assembled cells is on the order of 24 – 48 hrs, so any material that is originally native to one reservoir can be expected to diffuse to the other half-cell within the time duration required for two cycles. Likewise, any material that forms in one half-cell (e.g. degradation products) can be expected in the opposite half-cell within two cycles. Because of this, we do not expect any negative side-effects from electrolyte rebalancing that are not already characteristic to the cell.

Low temperature cycling

Low-temperature cell cycling was performed at 0 °C in an Environmental Testing Chamber (section 4.1.2). (We originally intended to cycle cells at -20 °C; however, the charged MEEPT cation was found to become insoluble at such low temperatures. The cell temperature was increased until the charged electrolytes remained soluble.)

Cell stability data is shown in Figure 7.3 for a cell that was cycled under ambient atmosphere. The cell shows a steady decline in capacity after the first cycle; nearly 50 % of the original capacity is lost after 150 hours. Compared to the room temperature and high-temperature studies, the cell coulombic efficiency begins at a
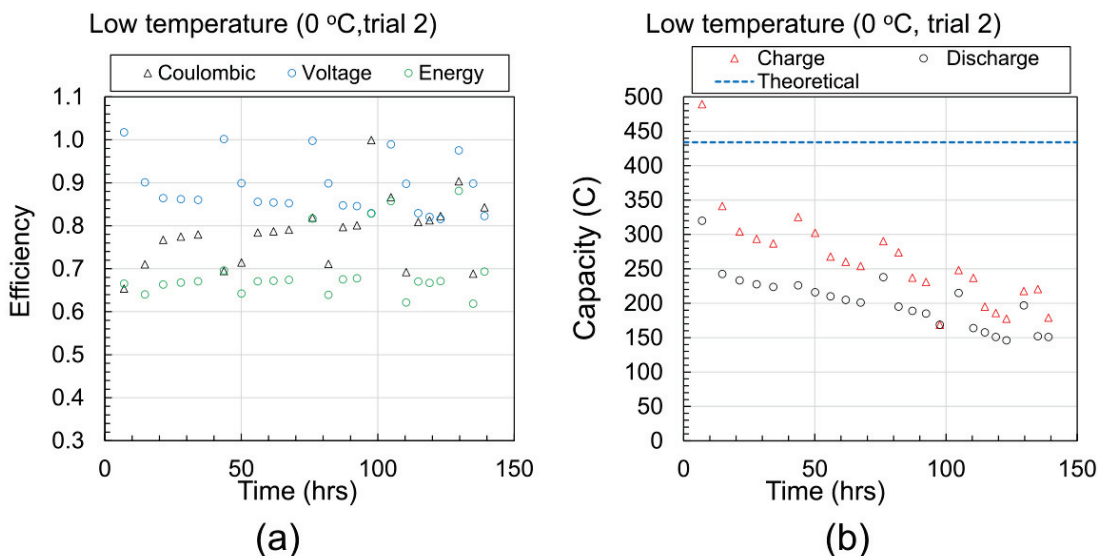
Figure 7.3: Figure illustrating the cell efficiency (a) and capacity (b) for a MEEPT-MEEV flow cell cycled at 0 °C under ambient atmosphere. A 10 mA cm⁻² current density was used for charge-discharge cycling, which corresponds to a C-rate of 0.19 C for this cell. A total of 25 cycles are shown in this data.

significantly higher value (∼ 70 %). This may result from increased solution viscosity at low-temperature, and/or reduced diffusion of charged active species through the separator (lower self-discharge). As in the previous MEEPT-MEEV cells, the coulombic efficiency rises gradually with cycling, reaching up to 85 % after 140 hours. This behaviour is discussed further in section 7.3.4.

7.3.2 Full cell impedance evolution

The evolution of full-cell impedance spectra for MEEPT-MEEV flow cells cycled at room temperature and high temperature are shown in Figure 7.4(d, e and f). The spectra are numerically corrected to remove inductive contributions, which can obscure, or exaggerate high-frequency features such as charge-transfer resistance. In all cells, we observe the evolution of a distinct semi-circle at high frequency, which we attribute to the charge-transfer effects. The charge-transfer resistance is negligible for early cycles, but grows with cycling and becomes more broadly distributed along
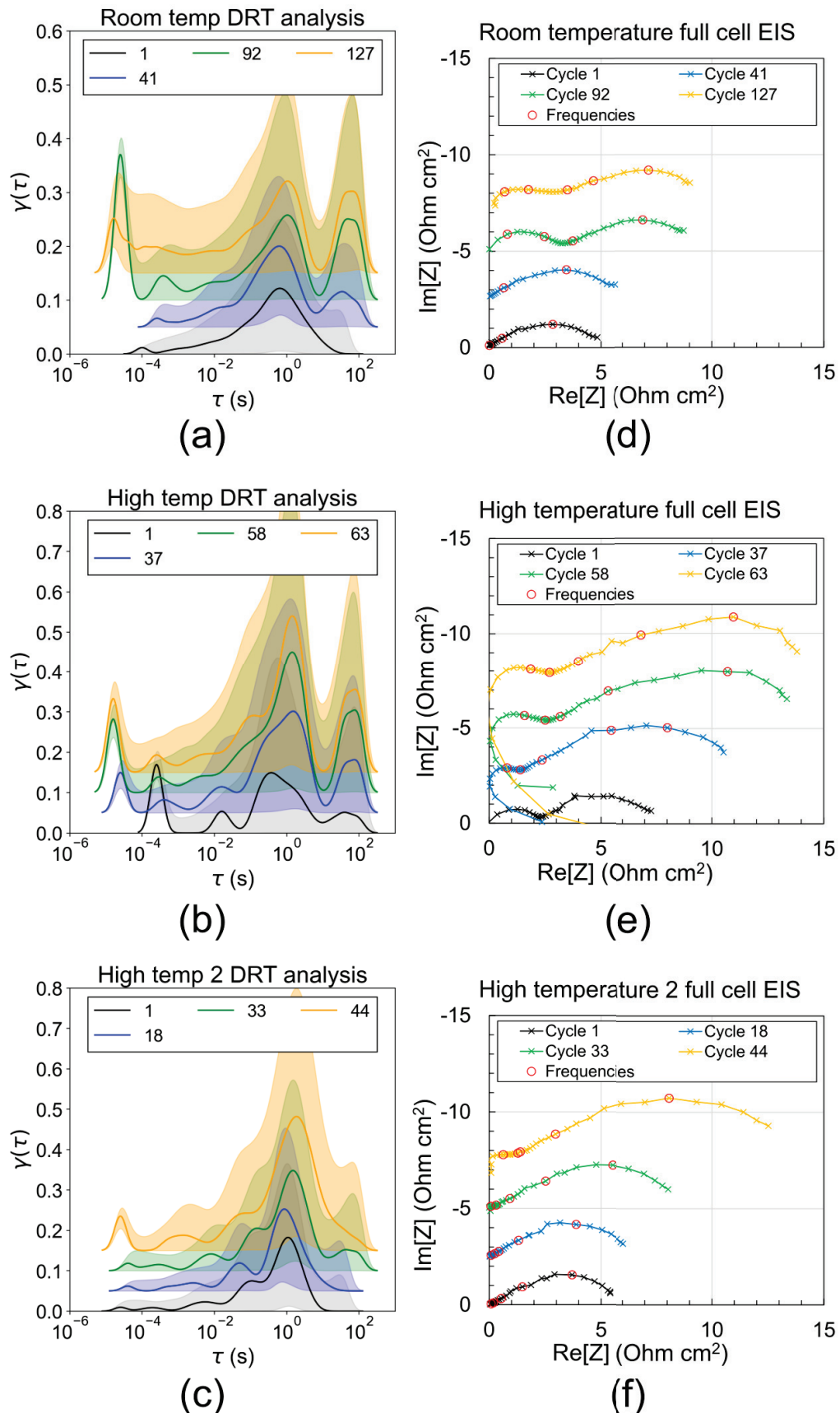
Figure 7.4: Figures illustrating the distribution of relaxation times and locations of corresponding frequencies in EIS spectra measured for MEEPT-MEEV flow cells at room temperature (a/d) high temperature (b,c,e,f). Inductive contributions were

Table 7.1: Table summarizing the characteristic frequencies determined by DRT analysis for a MEEPT-MEEV flow cell cycled at high temperature (HT2).

Cycle number	f_1 (Hz)	f_2 (Hz)	f_3 (Hz)	f_4 (Hz)	f_5 (Hz)
1	6391	842	30	1.5	0.15
18	4008	266	68	3.0	0.18
33	3844	564	19	1.0	0.1
44	6443	202	115	2.4	0.08

the real axis. The growth in charge transfer resistance appears to occur more rapidly in the first high temperature cell. As an aside, the room temperature and first high temperature cells exhibited a large non-ideal inductance, which we believe is responsible for the anomalously large high-frequency features observed on cycle 92 (room temperature) and cycle 1 (high temperature). The lossy inductance was reduced for the second high-temperature trial by reducing the length of test leads, and improving cable management.

In addition to charge-transfer resistance, each cell exhibits a broad, asymmetric semi-circular arc at low frequencies (f $\sim$ 0.1 Hz), which begins with the characteristic 45 $^\circ$ Warburg response, before transitioning into a semi-circle. This behaviour is typical of a Warburg "short" element where electrolyte convection improves active material transport between the electrode pores and bulk electrolyte (section 3.2.2). The magnitude of this diffusion feature appears relatively constant in the room temperature cell. In the high temperature cells it grows gradually with cycling. The high-temperature cells also show increased noise at low frequencies, despite using an almost identical experimental set-up. We suspect the noise may originate from the PID-controlled flexible heaters used to maintain the cell temperature.

As in the previous chapter, DRT analysis was used to develop an informed equivalent circuit model to analyze EIS data. The distributions for each cycle are plotted above the corresponding panels in Figure 7.4. The frequencies determined from the characteristic time constants identified through DRT analysis are summarized in Table 7.1 for the second high temperature cell. The datapoints roughly corresponding to

each frequency are indicated by the large red circles in Figure 7.4. With the exception of f_4, the location of these frequencies align with plausible features in later cycles. The feature at f_4/τ_4 appears to account for noise in the low-frequency feature. We believe this fourth time constant (f_4/τ_4) to be an artefact and disregard it in further analysis. From our DRT fitting we conclude that 3 parallel RC-elements (corresponding to τ_1, τ_2 and τ_3) and a Warburg diffusion element (corresponding to τ_5) are needed to model data in later cycles. In early cycles, the characteristic frequencies appear to converge, and the equivalent circuit may be better modelled with fewer RC-elements.

Figures 7.5 and 7.6 show the results from equivalent circuit fitting for the presented data. The fitted spectra are shown in the Appendix (Figure C.4) for reference. The data are largely scattered, but appear to show a general increase in R_{p2} and R_{p3} with cycling. In contrast the parallel capacitance elements decrease with cycling. These changes may occur at a faster rate in high temperature cells, although statistically this is difficult to verify given the scatter and uncertainty. We interpret the scatter and large error bars to reflect the inherent uncertainty in fitting the small charge-transfer features with a low measured point density (5 points/decade). In the previous chapter these features were larger due to extended cycling times (and more easily fit); trends were also more easily discerned over a longer cycle duration.

The specific series resistance shows a much clearer trend. Figure 7.6a shows a nearly linear increase with cycling. The Warburg diffusion resistance (W_{s0}) also clearly increases – more rapidly at high temperatures (Figure 7.6b), which is consistent with visual inspection of the EIS spectra in Figure 7.4.
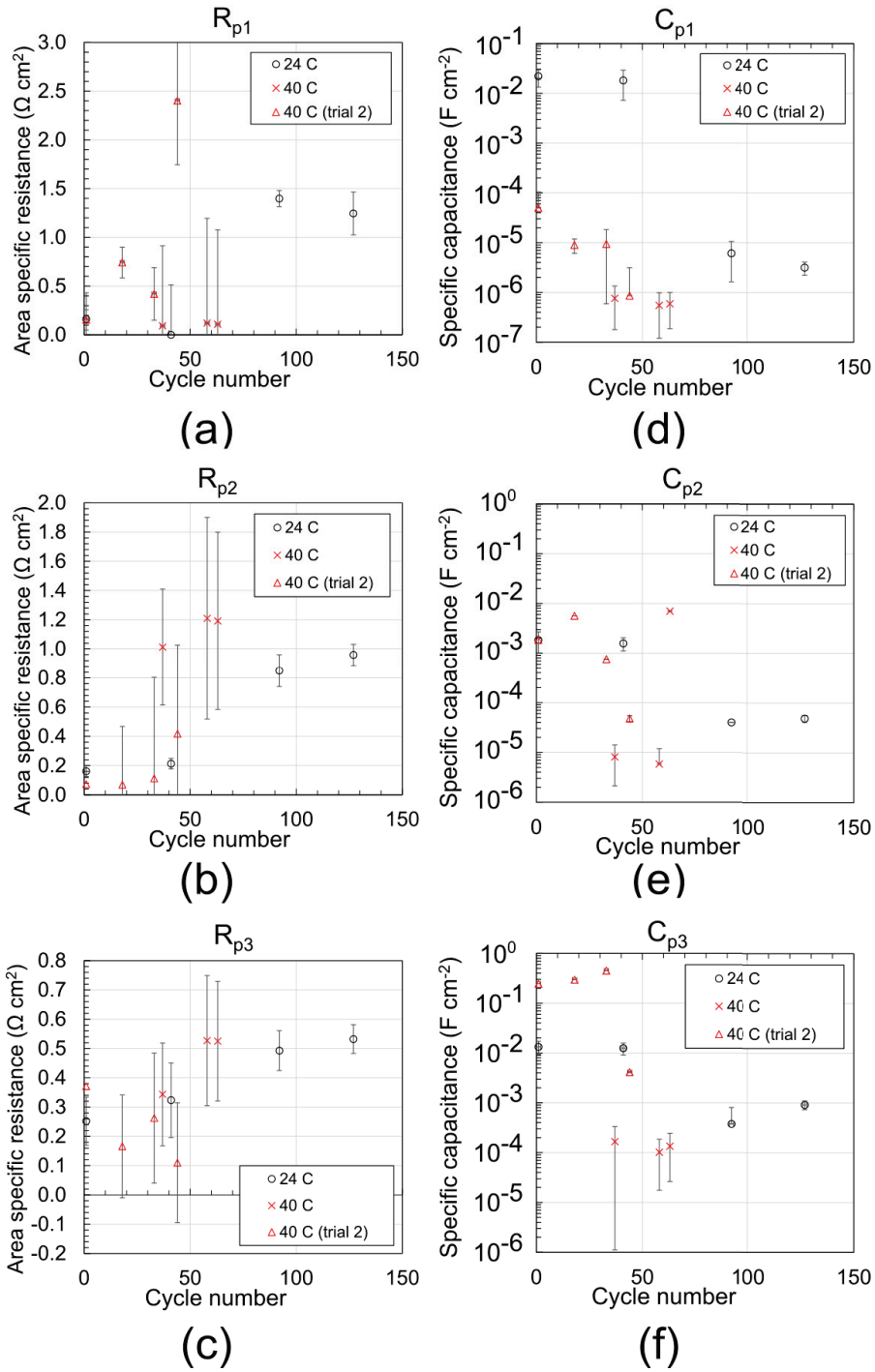
Figure 7.5: Figures illustrating the evolution of R_{p1} (a), R_{p2} (b), R_{p3} (c), C_{p1} (d), C_{p2} (e) and C_{p3} (f) with cycling for MEEPT-MEEV flow cells. The parameters were determined using equivalent circuit fitting as described above. The area specific resistance and specific capacitance are referenced with respect to the total geometric surface area of the electrodes, though the true macroporous area is expected to be 10 - 20x greater.
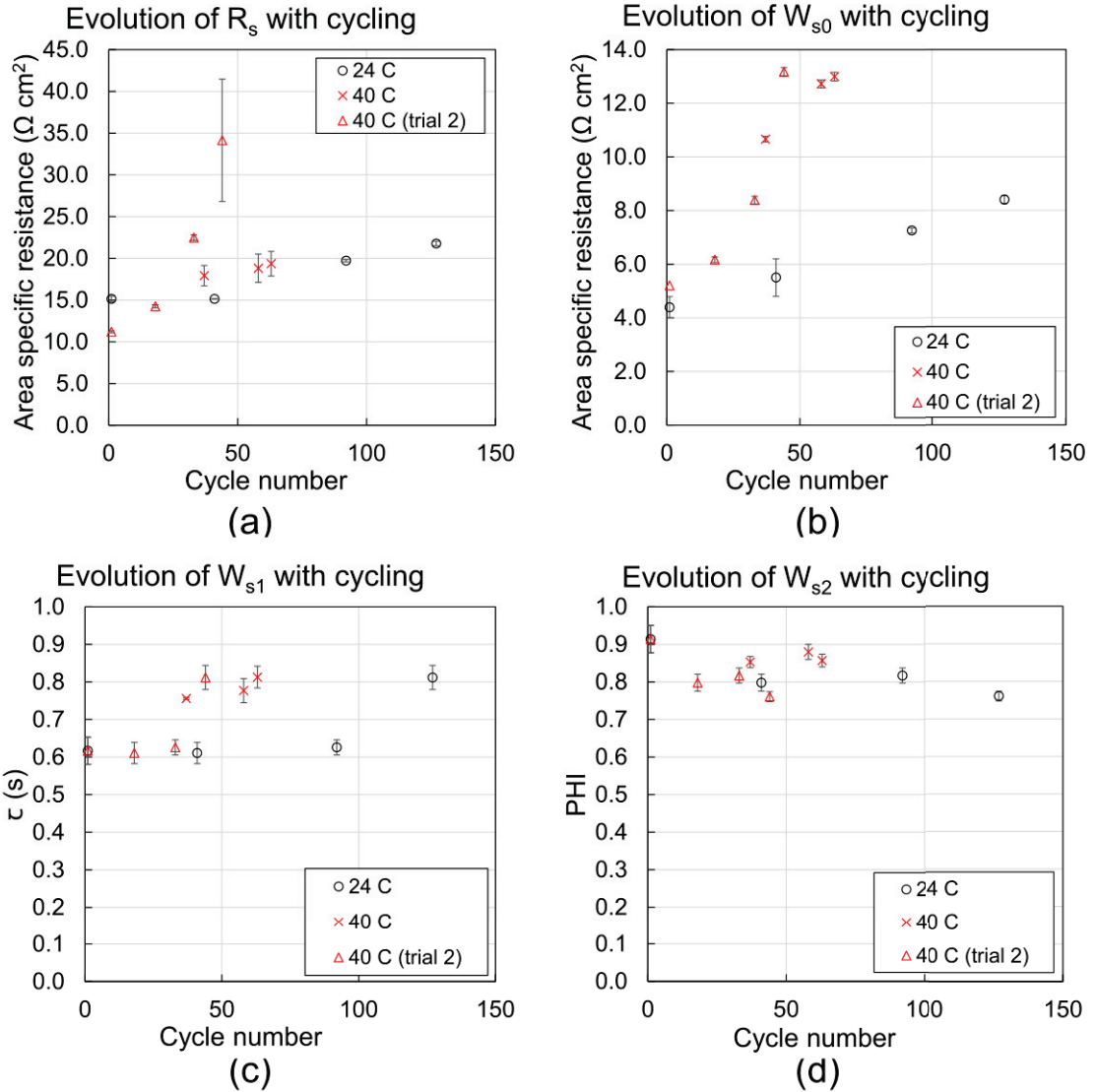
Figure 7.6: Figures illustrating the evolution of series resistance (a) and Warburg diffusion parameters (b) – (d) with cycling for MEEPT-MEEV flow cells. The parameters were determined using equivalent circuit fitting as described above.
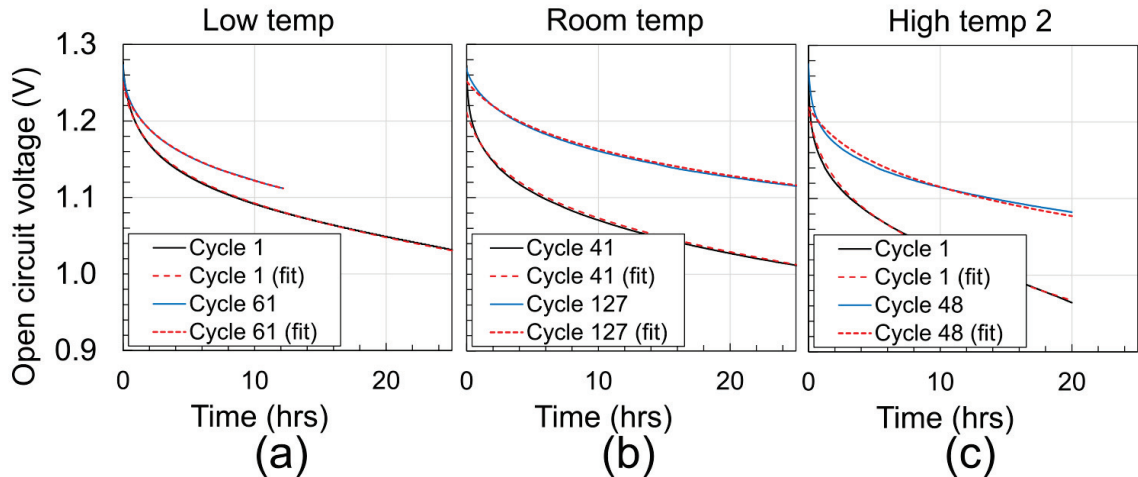
Figure 7.7: Open-circuit voltage measurements for MEEPT-MEEV cells at different states of health. Measurements were performed at 0 °C (a), 24 °C (b), and 40 °C (c). The y-scale shows 0.9 V to 1.3 V for each panel.

Due to electrical noise, we were not able to rigorously analyse EIS data from the low-temperature cell. Vibrations and electrical noise from the ETC caused significant noise at high frequencies in EIS spectra (coinciding with the expected location for the charge-transfer resistance). Very large inductive contributions were also present (despite attempts to shield test leads and minimize cable lengths). The large inductance (and noise) is suspected to originate from the ETC and nearby turbo pumps.

7.3.3 Self-discharge measurements

As described in section 4.2.3, OCV measurements were performed on fully charged cells (1.3 V) to estimate the self-discharge rate for cells after cycling (compared to early in cycling). Figure 7.7 shows these OCV measurements for cells cycled at 0, 24 and 40 °C. Two measurements are shown in each panel: one taken before cycling (or early in the cycling history), and one taken after cycling. Under open-circuit conditions (with electrolyte pumping), the cell voltage is observed to drop more quickly at the beginning of cycling. Near the end of cycling, the open-circuit voltage decreases more slowly. The cell temperature also affects the OCV, which

decreases faster under higher temperatures than lower temperatures.

The cell voltage is a reflection of the charged electrolyte concentration in each half-cell, so the change in OCV mirrors the change in charged species concentration over time. The cells were (reasonably) well-sealed, and (except for the low-temperature cells) were cycled under blanket nitrogen (oxygen $< 2.0\,\%$ vol), so we assume that the change in charged species concentration occurs primarily from internal self-discharge (i.e. membrane crossover). Starting from the Nernst equation, we can develop an expression for the change in OCV with charged species concentration.

$$V = E_{cell}^0 + \frac{2RT}{nF} \ln \left(\frac{\text{SOC}}{1 - \text{SOC}} \right) = E_{cell}^0 + \frac{2RT}{nF} \ln \left(\frac{x}{0.5 - x} \right)$$

$$\frac{dV}{dx} = \frac{2RT}{nF} \left(\frac{0.5}{x(0.5 - x)} \right)$$

(7.1)

Here '0.5 (M)' is the starting electrolyte concentration for our system, and x is the concentration of charged electrolyte species. The change in OCV with time becomes

$$\frac{dV}{dt} = \frac{dV}{dx} \frac{dx}{dt}$$

$$= \frac{2RT}{nF} \left(\frac{0.5}{x(0.5 - x)} \right) \frac{dx}{dt}$$

(7.2)

Assuming diffusion-based membrane crossover, the change in electrolyte concentration is expected to be proportional to the charged species concentration, which suggests a solution with an exponential form. Using $x = A \exp(-kt)$ gives:

$$V(t) = \frac{2RT}{nF} \ln \left(\frac{\exp(-kt)}{0.5 - A\exp(-kt)} \right) + C_1$$

(7.3)

The self-discharge current can be calculated from the solutions for x using
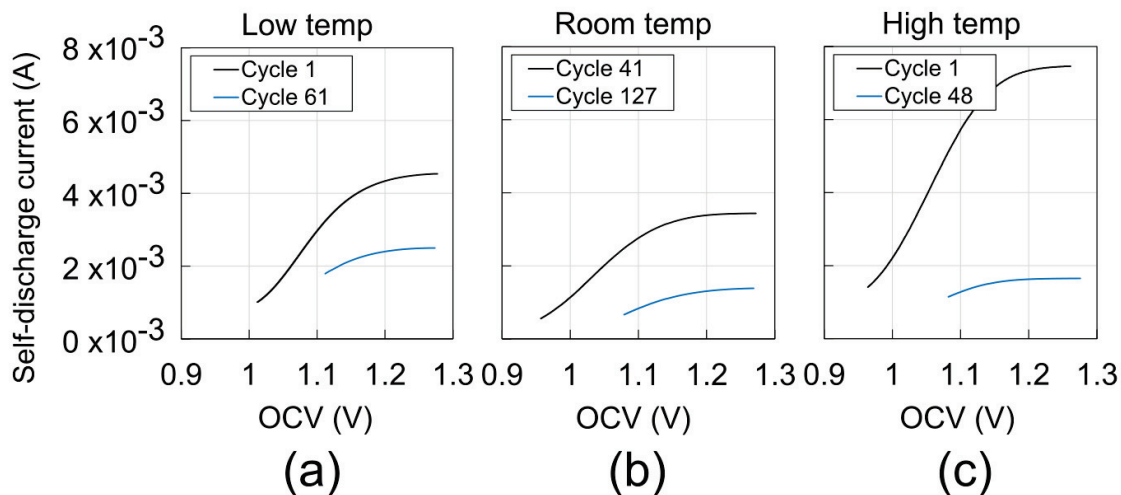
Figure 7.8: Self-discharge current for MEEPT-MEEV flow cells plotted as a function of OCV. The self-discharge currents are calculated from the OCV measurements shown in Figure 7.7 at 0 °C (a), 24 °C (b), and 40 °C (c).

$$i = \frac{dx}{dt} \times v \times F \qquad (7.4)$$

where v is the electrolyte volume and F is Faraday's constant. This model appears to fit the cell data well at low temperatures (Figure 7.7a/b), but not at high temperature. It is possible that additional processes may contribute more to self-discharge at higher temperature such that our basic model no longer holds.

The self-discharge currents estimated from fitting the OCV data are shown in Figure 7.8 as a function of cell voltage. In each panel the self-discharge current is lower after cycling (consistent with expectations from OCV vs time data). The 40 °C cell shows the highest self-discharge currents at each voltage, and the largest decrease in self-discharge current after cycling. The low-temperature cell shows higher self-discharge currents compared to the room temperature cell, which would not be expected if the discharge was entirely diffusion-based. Two possibilities could account for this. First, the low-temperature cell was cycled under ambient atmosphere. Oxygen may have permeated into the cell, which would cause external oxidation of

143

charged negolyte. Second, longer tubing was required to transport electrolyte between the reservoirs and cell; longer tubing makes it more difficult to balance unwanted pressure differentials across the cell, which would increase self-discharge. It is also worth noting that the self-discharge currents for the room-temperature cell are not directly comparable to the other cells for two reasons. First, the room temperature cell was cycled 3 times longer than the high-temperature cell, and 5 times longer than the low-temperature cell (so the cell was not in a comparable state-of-health) when performing the end-of-life self-discharge measurements. Second, we did not perform self-discharge measurements before cycling for the room-temperature cell, so the early cycle data are also not comparable to the other two cells.

7.3.4 Post-cycling membrane analysis

Qualitative inspection

Cell disassembly and component harvesting (for *post-mortem* characterization) was performed as previously described (section 4.3). The cycled Daramic separators showed significant staining on the negative facing side (Figure 7.9); meanwhile, the positive face was unchanged. Rinsing and soaking in fresh solvent did not remove any staining from the samples, which suggests that the changes are due to the deposition of some insoluble species. The effects of these changes are characterized in the following sections.

SEM images comparing the HT cycled and fresh Daramic separators are shown in Figure 7.10. The fresh separator (Figure 7.10c and d) appears featureless with the exception of a few surface particles, which we believe to be dust. The cycled separators appear coated with an inhomogeneous residue, which even appears to be crystalline in some locations (Figure 7.10b). In addition, some linear features ~ 10 µm in width appear on the surface. This size is consistent with the nominal diameter of the carbon fibres $(5 - 10$ µm$)$, which we believe imprinted on the separator surface.
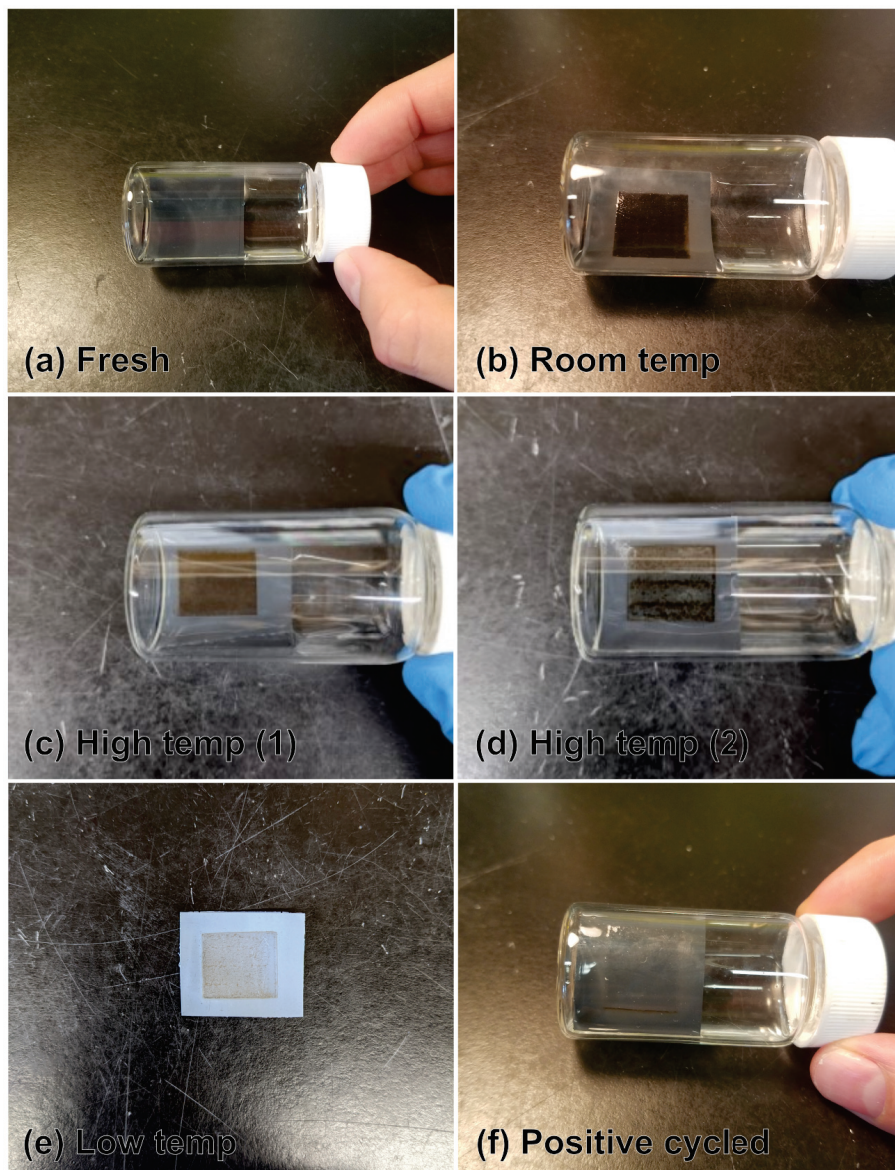
Figure 7.9: Images of a fresh Daramic separator (a), and cycled Daramic separators harvested from a room temperature cell (b), the first high temperature cell (c), the second high temperature cell (d), and the low temperature cell (e). The positive face of a cycled separator is also shown for comparison. The image is representative for all the samples.
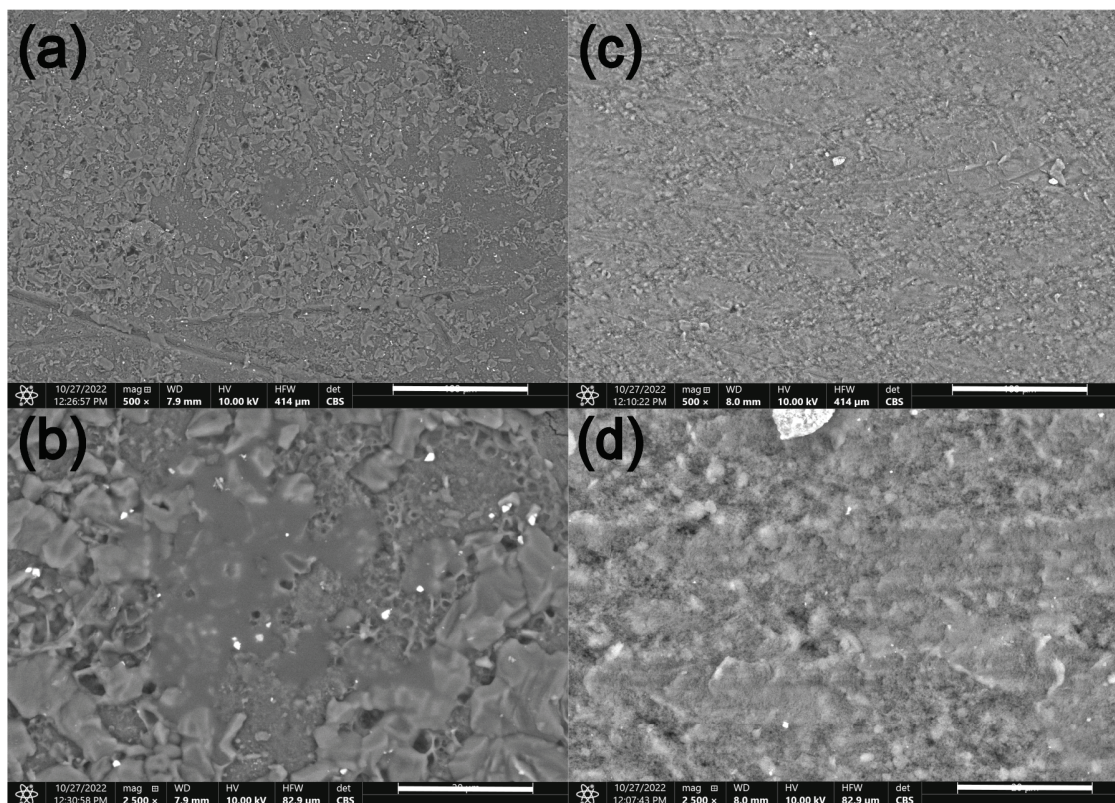
Figure 7.10: Figure showing SEM images comparing the negative face of HT cycled (a/b), and fresh (c/d) Daramic separators. The scale bars in figures (a and c) represent 100 µm, and the scale bars in figures (b and d) represent 20 µm. Measurements were performed using an environmental imaging mode (0.3 mbar vapour pressure).

Membrane impedance measurements

Separator impedance was evaluated as described in section 4.5.1. Measurements performed on cells assembled with 0.5 M TEATFSI in acetonitrile show a significant increase in the high-frequency intercept (with the real axis) when samples of fresh separator are exchanged for cycled samples (Table 7.2). The increase is nearly 50 % of the original impedance. These results are significant given our estimates of measurement uncertainty, which we take to be $\pm$ 0.2 - 0.3 Ω. This uncertainty was determined from the standard error of the high-frequency cell impedance measured for three identical samples of fresh Daramic separator ($\sigma/\sqrt{3}$). The uncertainty for cycled separators is expected to be higher, and dominated by the repeatability with which the separator may be replaced within the gasket window. Replacing the cycled separator in the gasket window is not difficult given the bold staining, but even minor misalignment could expose separator regions that were not exposed to electrolyte, or cycling. Given this, the values reported for cycled separators in Table 7.2 likely underestimate the true impedance, though they are expected to show a higher uncertainty.

Table 7.2: High-frequency impedance for cells assembled with different samples of Daramic separator. The uncertainties represent the standard error of the high-frequency impedance measured from three identical samples of fresh separator.

	Measured at 25 °C	Measured at 40 °C
Fresh	1.6 $\pm$ 0.3	1.5 $\pm$ 0.2
Cycled (room temp)	2.2	2.2
Cycled (HT1)	-	1.9
Cycled (HT2)	-	2.2

Gurley measurements

As described in section 4.5.2, an apparatus was constructed to perform Gurley measurements on cycled separators. The Gurley unit is defined as the time (s) required to displace 100 mL of air through a 1 square inch sample of porous material under

147

a differential pressure of 1.2 kPa. Measurements performed on standard samples of Celgard 3501 yield an average displacement time of 410 ± 10 s using this apparatus – twice what was expected from manufacturer specifications. While this result suggests that our apparatus may not represent standard test conditions, we expect any trends determined from these measurements to hold. We refer to the following data as "effective Gurley" measurements to indicate this distinction.

Table 7.3 summarizes the recorded times required to displace 100 mL of air through cycled and fresh samples of Daramic separator. The mean time required to displace 100 mL of air through a 1 square inch section of fresh Daramic separator is 980 ± 60 seconds. The uncertainty represents the standard error for measurements performed on three identical samples ($\sigma/\sqrt{3}$). In comparison, the average time for a separator that was cycled at 40 °C is 3000 ± 300 s. Here the uncertainty represents the standard error for three measurements repeated on the same sample, which was replaced to measure a different section of the cycled area each time. The higher uncertainty may capture areal variation across the separator, which may not foul uniformly across the surface. All cycled separators show a larger effective Gurley measurement compared to measurements performed on fresh separators. The difference is significant within uncertainty. The effective Gurley measurements appear to be correlated with physical staining on the separator surface. This is especially apparent for the low-temperature separator, which shows the least visible staining and has a recorded displacement time of 1400 ± 100 s. (The separator that was cycled in the room temperature cell was unfortunately misplaced, so this measurement is lacking).

The changes described here and in the sections above are significant. The effective Gurley measurements are a direct indicator of sample porosity. We speculate that the observed separator changes contribute to the increased coulombic efficiency seen in the room temperature and 40 °C stability studies by reducing the rate of active species crossover through the separator. This could occur if separator fouling occurred, which

Table 7.3: Effective Gurley measurements for different samples of Daramic separator. The uncertainties represent the standard error of three measurements.

Sample ID	Time to displace 100 mL air (s)	Range of measurements (s)
Fresh	980 ± 60	$850 - 1050$
Uncycled	980	–
RT cycled	lost	–
HT cycled	3000 ± 300	$2700 - 3500$
HT2 cycled	4800 ± 200	$4500 - 5200$
LT cycled	1400 ± 100	$1200 - 1700$

resulted in pore-blocking. As insoluble species are deposited on the membrane surface, the separator porosity becomes reduced, and passage of material through micropores would become restricted. This would result in reduced ionic conductivity through the separator in impedance measurements and reduced crossover of active species (leading to a higher Coulombic efficiency, but at the cost of a reduced voltage efficiency due to increased series resistance). This is also consistent with the self-discharge measurements reported earlier (section 7.3.3), which show slower crossover of active species through the separator after cycling compared to before (or earlier on) in cycling.

Table 7.4: Ratios of cycled to fresh Gurley measurements (inverse), and self-discharge currents. The error in the Gurley ratios captures the root mean squared error for the trials performed in Table 7.3, and an additional 2 % error corresponding to the uncertainty in measuring the volume displacement. The largest uncertainty in the self-discharge current ratios involves the assumption that the OCV vs. time measurements reflect self-discharge (and not other voltage relaxation processes). However, we are not able to numerically quantify this uncertainty, and therefore do not report errors in column three.

Sample ID	Inverse Gurley measurement ratio	Self-discharge current ratio
LT/fresh	0.68 ± 0.08	0.552
RT/fresh	lost	0.33
HT/fresh	0.204 ± 0.01	0.221

Table 7.4 compares the ratios of cycled to fresh separator porosity and self-discharge current for each cell temperature. The separator porosities are inversely related to the Gurley displacement times reported in Table 7.3; their ratio is listed in

the second column. The third column reports the mean self-discharge current ratio between cycled to fresh cells (i.e. the mean ratio for each cell voltage). The trends in each column agree with each other, and there is strong agreement between the porosity ratio and self-discharge ratio for the high-temperature cell. These observations further support our theory of pore-blocking reducing self-discharge, thereby increasing Coulombic efficiency.

It is important to note that cell capacity loss can also contribute to increases in coulombic efficiency. Charging limits are reached more rapidly at lower cell capacity, which reduces the available self-discharge time. While capacity loss occurs in some of our MEEPT-MEEV flow cells, we note that the observed increase in coulombic efficiency is also observed when the cell capacity is stable (Figures 7.2c/d and 7.1). Because of this we assert that while capacity loss may contribute to the increased coulombic efficiency, it is not the only contributing factor. Separator fouling is believed to be the dominant mechanism. The insoluble species deposited on the separator surface are currently unknown; however, EDS measurements of the cycled separator indicate the composition to primarily consist of fluorine and sulfur, which are both present in the electrolyte (Appendix, Figure C.5). (Silicon, aluminum and copper are also detected; however, we attribute these signals to the underlying copper tape and sample stub, which are visible due to the large sampling depth reported for EDS).

7.3.5 Post-cycling electrode analysis

X-ray photoelectron spectroscopy

Figure 7.11 summarizes the results for XPS measurements performed on carbon electrodes cycled in a MEEPT-MEEV flow cell at room temperature. The survey spectra are shown in Figure 7.11b; elements that are visible in high-resolution scans are labelled as indicated. Compared to the fresh and uncycled electrodes, the cycled

Figure 7.11: XPS survey spectra comparing a fresh electrode with cycled samples harvested from a MEEPT-MEEV flow cell cycled at room temperature (b). The relative abundance of detected elements is shown in (a).

samples show additional material on the sample surface. High-resolution scans show that the peaks corresponding to F1s, N1s, S2s and S2p transitions are characteristic for our expected electrolyte components. Both the S2s and S2p signals show two different bonding environments, shifted by 5.2 ± 0.2 eV from each other (Figure C.6, Appendix). Based on external references, the higher binding energy peak can be attributed to sulfur bonded in a sulfone chemical environment (present in the TFSI anion), while the lower binding energy peak can be attributed to sulfur in a thiophene environment (present in MEEPT) [166]. A larger proportion of sulfur is present in the sulfone environment on the negative electrode, while a higher proportion of thiophene-like sulfur is visible on the positive electrode. Both cycled electrodes show a similar N1s intensity, while no N1s signal is observed on the uncycled electrode. The negative electrode exhibits a small N1s signal at higher binding energies, which is associated with ammonium salts [166] (Figure C.6, Appendix). (The F1s and O1s transitions do not show strong chemical shifts, so we do not discuss the bonding environments here.)

An additional (and unexpected) peak is visible in high-resolution scans of the

negative electrode, which we attribute to the Cl2p transition. Figure 7.11a shows that significant quantities of chlorine are present on the negative electrode. Meanwhile, a negligible amount (if any) is present on the positive cycled electrode. Compositional analysis shows that chlorine constitutes up to 54 % of the fluorine abundance on the negative electrode surface. This is a significant and surprising quantity given that the amount of halide impurities specified in the Iolitec TEATFSI is reported to be less than 100 ppm. This would translate to 0.0002 % surface abundance — less than the resolution achievable by XPS. (A second sample of the cycled negative electrode was also measured, which confirmed the presence of chlorine on the negative electrode. Analysis of the second sample places the relative quantity of chlorine at about 40 % compared to fluorine). The difference between the two samples may result from regional variations in our flow cell, and places an upper limit on the uncertainty of using XPS for compositional analysis in these studies. The electrode sample stored (but not cycled) in MEEPT-MEEV electrolyte shows some evidence of F1s and Cl2p transitions, but in smaller quantities than observed on the cycled electrodes. The presence of chlorine on the stored electrode sample indicates that the impurity does not originate from any of the cell components, and is inherent to one of the electrolyte materials.

Figure 7.12 summarizes the XPS measurements performed on the electrodes cycled at high temperature. As observed in the room-temperature study, the cycled electrodes show a higher surface concentration of elements not native to the carbon paper (with a higher concentration occurring on the cycled negative electrode). The first high temperature cell shows a large abundance of oxygen and fluorine on the negative electrode and a diminished carbon peak intensity. These changes are much greater compared to the room temperature study. In contrast, the HT2 cell shows a lower concentration of non-native elements detected on the negative electrode surface. Cell assembly methods were improved for the HT2 trial to reduce oxygen exposure,
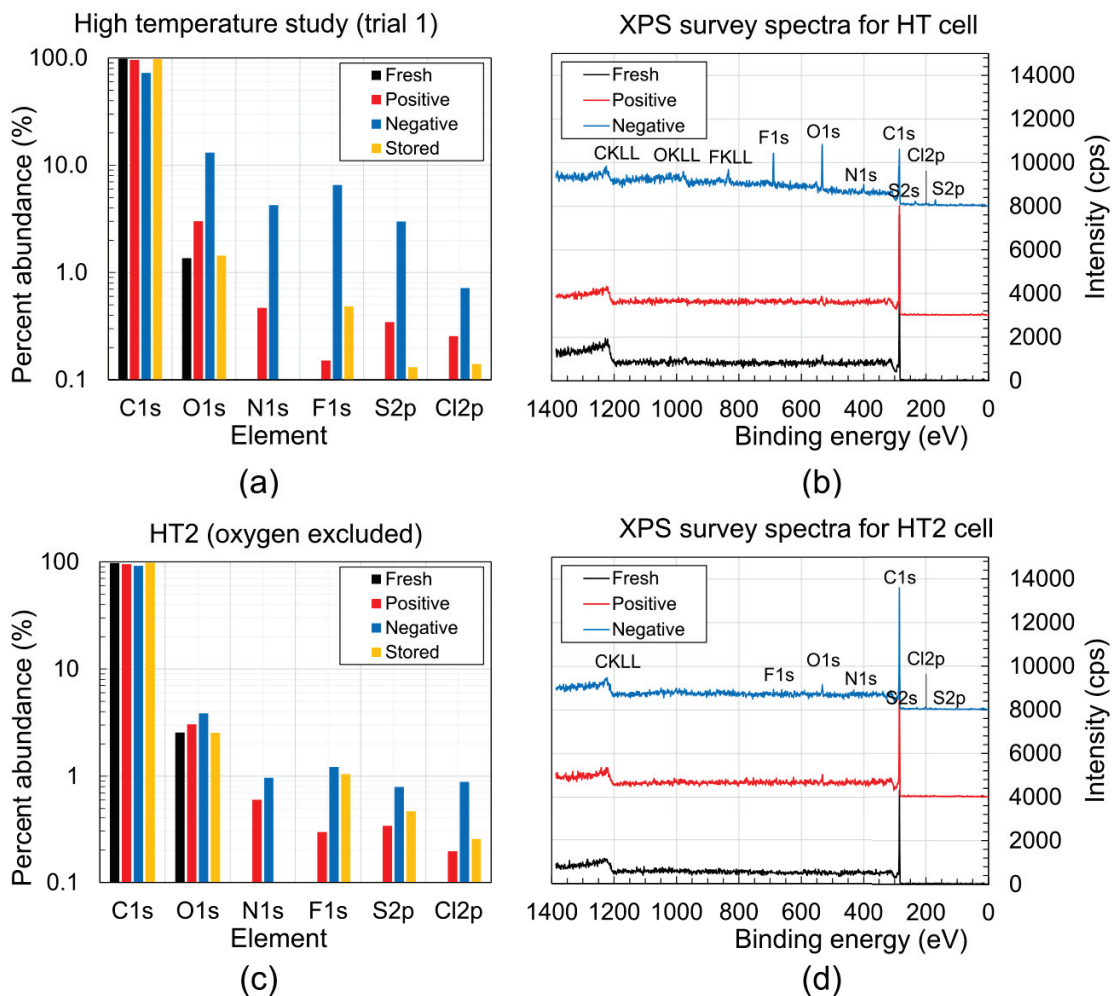
Figure 7.12: XPS survey spectra comparing a fresh electrode with cycled samples harvested from the first high temperature cell (b). The relative abundance of detected elements is shown in (a). Survey spectra for the second high temperature cell (HT2) are shown in (d), and the relative abundance of detected elements in (c).
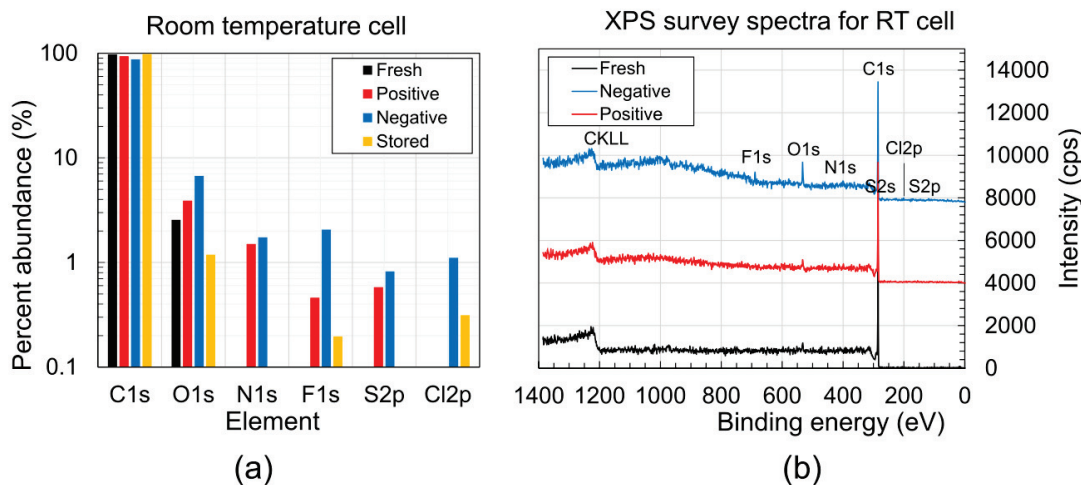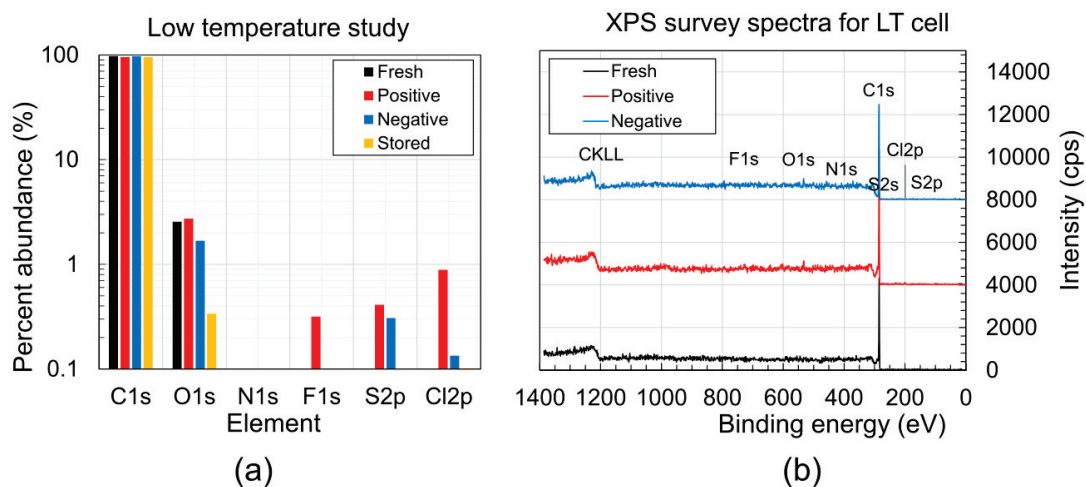
Figure 7.13: XPS survey spectra comparing a fresh electrode with cycled samples harvested from a MEEPT-MEEV flow cell cycled at low temperature (b). The relative abundance of detected elements is shown in (a).

which could contribute to the reduced changes observed at the electrode surface.

The same characteristic sulfur and nitrogen bonding environments are observed in high-resolution scans as described for the room-temperature cell. In addition, we see a similar concentration of chlorine on the high-temperature cycled electrodes as in the room-temperature study. The increased material concentration and diminished C1s intensity observed on cycled electrodes (in both studies) would be consistent with an overlayer of insoluble material on the electrode surface. A surface overlayer could contribute to the increased charge-transfer resistance that is observed in electrochemical impedance spectra after cycling. Interestingly, the samples of electrodes stored in electrolyte (but not cycled) show a comparable abundance of F1s, S2p and Cl2p to the cycled electrode samples. No N1s peaks were observed in high-resolution scans of the stored electrodes despite the fact that nitrogen is present in every electrolyte component.

The atomic abundances and survey spectra for electrodes that were cycled in a low-temperature MEEPT-MEEV flow cell are shown in Figure 7.13. The atomic abundances are comparable to the room-temperature cycled cell, which is interesting

154

considering that the low-temperature cell was cycled for only a quarter of the total time that the room-temperature cell was cycled; yet, it exhibited a greater total capacity loss. It is possible that these accelerated changes may be linked to cycling under an ambient atmosphere. Interestingly, no N1s signal was observed in any high-resolution scans on the low-temperature cycled electrodes.

Inspecting all XPS spectra, we see that the chlorine contamination persists in non-trivial quantities on all electrodes that were exposed to electrolyte (even without cycling). Because the Cl2p signature was also observed in all uncycled samples, we can conclude that the contamination did not arise inadvertently from any of the cell components. Chlorine also does not arise from sample mishandling during XPS preparation, as it was never observed in the several fresh electrode samples that were measured. The most plausible explanation appears to be that the chlorine is an impurity in one (or more) of the electrolyte materials: MEEPT, MEEV, TEATFSI, or acetonitrile. The comparable abundance of chlorine to fluorine, sulphur and nitrogen suggests that it may be present in significant quantities in the electrolyte. Understanding the source of this impurity (and possibly other impurities containing non-unique elements) may be useful for improving cell stability under cycling conditions.

Scanning electron microscopy

SEM images comparing a fresh (as-received) electrode with samples of negative and positive electrodes cycled at room temperature are shown in Figure 7.14. Images comparing electrodes that were cycled at high temperature and low temperature are also shown in Figures 7.15 and 7.16. The images show a standard mat of carbon fibers (nominally 10 μm diameter) expected for SGL 39 AA carbon papers [43,52]. The carbon fibers are adhered together with a graphitic binder. Cycling does not appear to elicit any structural changes to the macroporous structure of the mat, nor
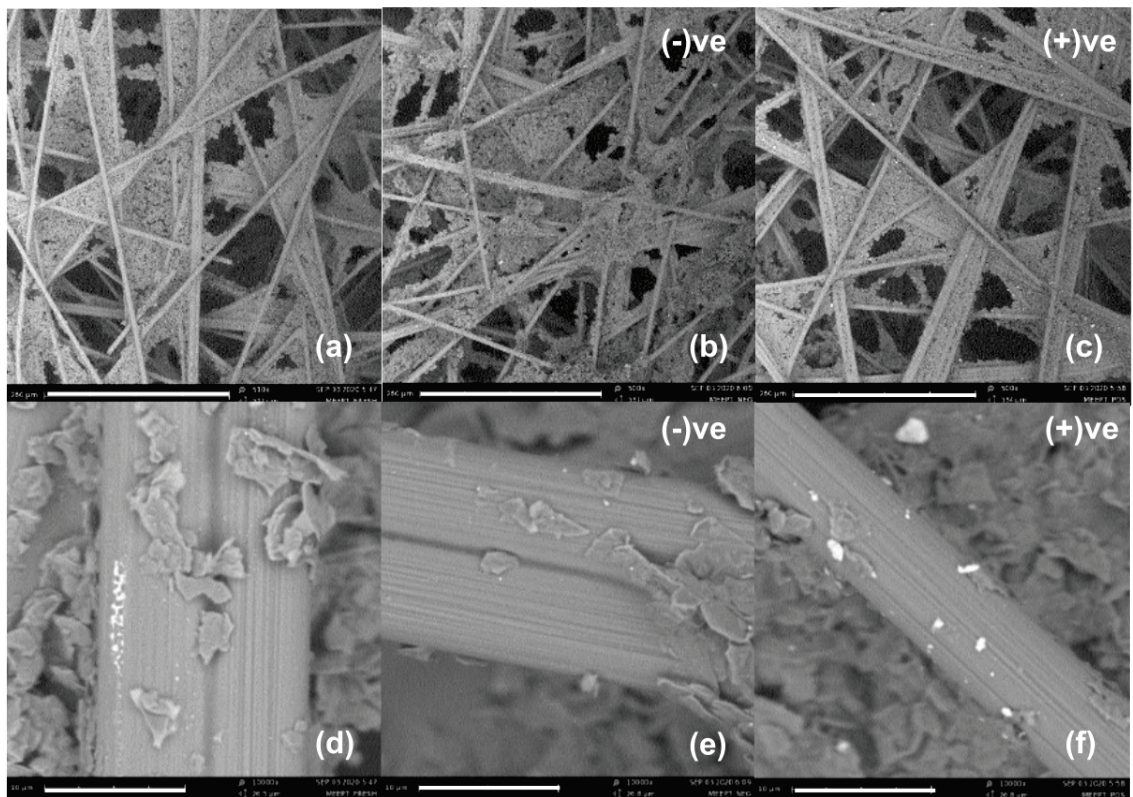
Figure 7.14: SEM images of a fresh electrode (a/d) compared to cycled negative (b/e), and positive (c/f) electrodes harvested from a room-temperature cell. The scale bars represent 250 μm in the top row, and 10 μm in the bottom row.
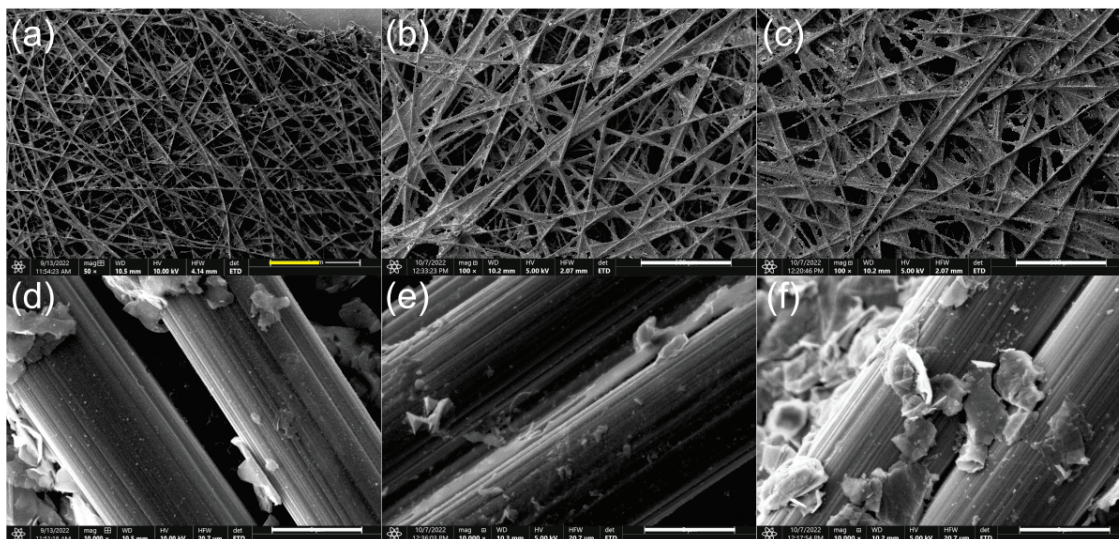
Figure 7.15: SEM images of a fresh electrode (a/d) compared to cycled negative (b/e), and positive (c/f) electrodes harvested from a high-temperature cell. The scale bars represent 500 μm in the top row, and 5 μm in the bottom row.

the fibers themselves. Other authors have reported peeling and/or pitting of cycled carbon electrodes harvested from vanadium RFBs [52]; however, the electrodes from this cell show no observable changes to the fiber structure. Some small particles (if any) may be adhered to the positive electrode after cycling at room temperature.

Electrodes that were stored in electrolyte (at 24, 40 and 0 °C) without cycling were also characterized with SEM. These samples also did not show any observable differences to the as-received carbon paper. We include them for reference in Figure C.7, Appendix.

A qualitative observation made when preparing samples for post-cycling analysis was that the negative cycled electrodes were (almost universally) more fragile to handle. In some cases thin layers of carbon fibers delaminated from the main electrode sample, despite using careful handling practices. This was not captured in the sub-millimetre SEM images, but is worth noting. Similar behaviour was not observed for the cycled positive, stored, or fresh electrodes.
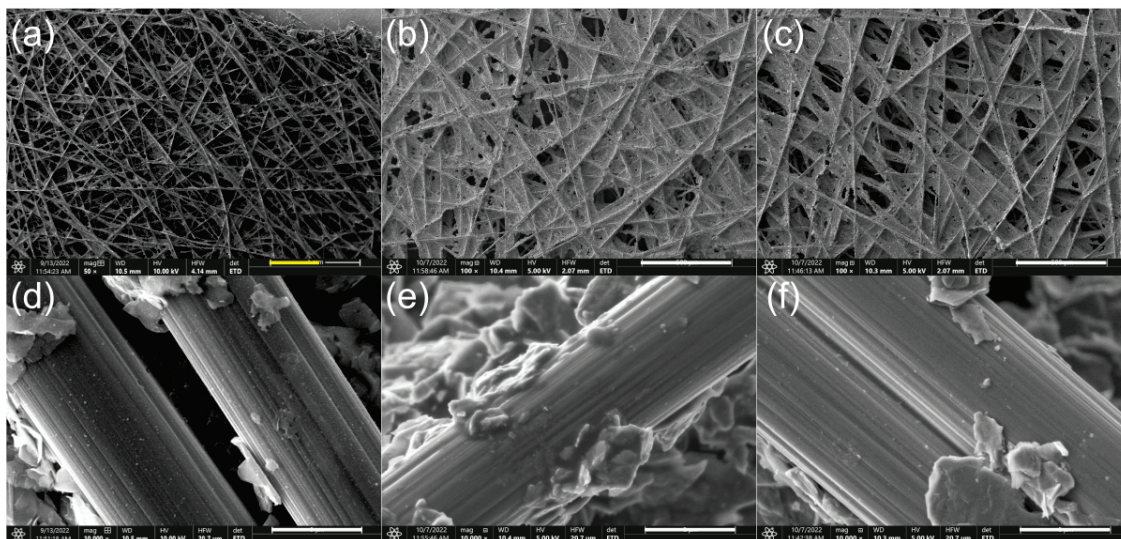
Figure 7.16: SEM images of a fresh electrode (a/d) compared to cycled negative (b/e), and positive (c/f) electrodes harvested from a low-temperature cell. The scale bars represent 500 μm in the top row, and 5 μm in the bottom row.

7.3.6 Post-cycling electrolyte analysis

Characterization of (discharged) cycled electrolyte from MEEPT-MEEV flow cells cycled at 24 °C, 40 °C and 0 °C suggests only minor electrolyte degradation. Figure 7.17 compares FTIR spectra of cycled electrolyte with fresh electrolyte samples. All cells show similar changes in the difference spectra, which is plotted above (scaled by a factor of 2x). Two distinct peaks are visible in the cycled solutions at 750 and 1640 cm^{-1}. These circled peaks occur in a frequency range that is commonly reported for C $\equiv$ N (positive difference spectrum) and aromatic bending modes (negative difference spectrum). It is difficult to determine the specific cause for these changes, but we are confident that these are not signatures from residual charged species. (FTIR measurements comparing charged solutions only show notable differences in the 1200 cm^{-1} region – Figure C.8, Appendix). Some increases in peak intensity are observed between 1100 and 1200 cm^{-1} for cycled solutions in each cell. It is possible that these could be attributed to residual charged species. (Additional evidence suggesting that these features correlate with residual charged species is observed in
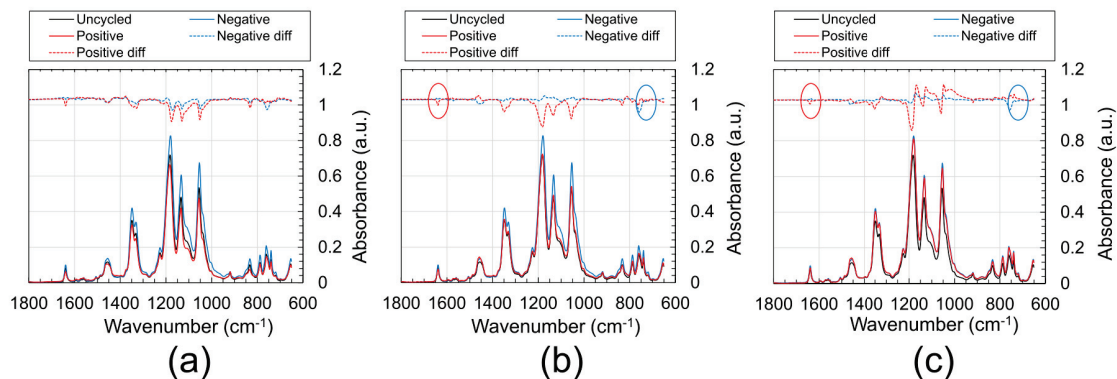
Figure 7.17: FTIR spectra comparing cycled and fresh electrolyte from MEEPT-MEEV flow cells cycled at 0 °C (a), 24 °C (b), and 40 °C . The difference spectra (between the cycled and fresh electrolyte) are plotted on a unitless scale above the raw data, scaled by a factor of 2x. Cycled solutions were discharged before removing from the cell.

UV-Vis spectroscopy, discussed below). Some differences in peak intensity are also expected to arise from variations in electrolyte concentration, which is expected to change after cycling – especially given the issues with evaporation and electrolyte imbalancing that were previously discussed (section 7.3.1).

Raman spectroscopy is a natural complement to FTIR; however, measurements revealed an overwhelming background signal in cycled solutions (which overshadowed the main spectral features). These issues were suspected to originate from particulates in solution, which could cause light scattering. Particles could originate from sloughing of the pump tubing, or damage to the carbon electrodes. (For each cell the negative cycled electrodes were found to be more fragile to handle after cycling.) After filtering solutions through a 0.45 µm pore syringe filter, the data was not noticeably improved. We do not discuss these spectra here, but the data are available in (Figures C.10 – C.11, Appendix C).

Figure 7.18 shows UV-Vis spectra comparing fresh and cycled electrolyte collected from cells cycled at 24 °C, 40 °C and 0 °C. The cycled electrolytes strongly resemble fresh (and stored, but uncycled) solutions. New peaks are not visible after cycling;
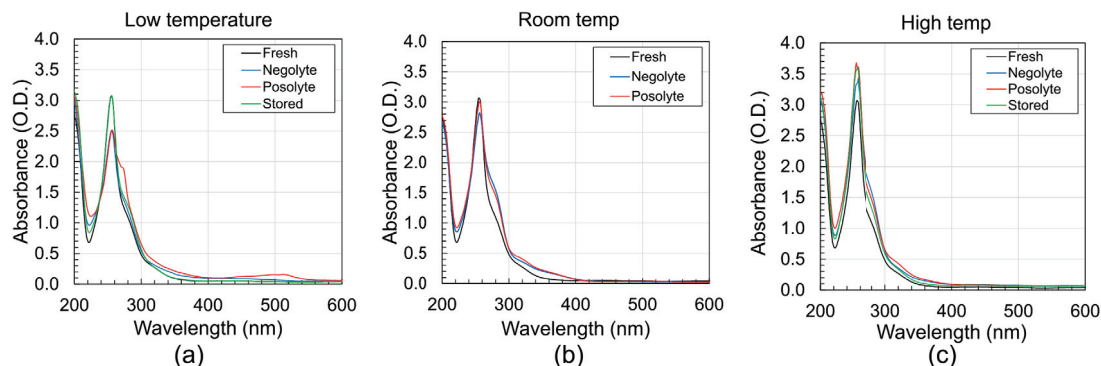
Figure 7.18: UV-Vis spectra comparing cycled and fresh electrolyte from MEEPT-MEEV flow cells cycled at 0 ºC (a), 24 ºC (b) and 40 ºC (c). Cycled solutions were discharged before removing from the cell. All solutions were diluted to 0.05 mM concentration (from 0.5 M) in dry acetonitrile.

however, additional absorption intensity is seen at 280 nm and 320 nm in cycled solutions. These shoulders align with characteristic peak positions for uncharged MEEV and MEEPT, respectively (Figure C.12a). Charged MEEV also exhibits a sharp peak around 270 nm (Figure C.12b), which could account for the shoulder observed at 270 nm. Minor differences in electrolyte concentration (for cycled solutions) are also expected given the issues with solvent evaporation (and uncertainty and solvent refilling) that were previously described. Changed electrolyte concentration most likely accounts for the changes observed in the high-temperature spectra, given that increased absorption intensity is also observed at 260 nm for these solutions. The broad peak at 500 nm in the low temperature spectrum is characteristic for the charged MEEPT cation (Figure 7.19a).

Figure 7.19b shows UV-Vis spectra of 5 mM charged negolyte collected every 15 seconds under ambient conditions. The feature centred at 600 nm is attributed to the charged MEEV species. (The uncharged solution is clear, only absorbing in the UV-region, Figure C.12a). After only a few minutes the absorption intensity at 600 nm decays by 50 % (pressumably due to moisture and/or oxygen exposure). This loss of absorption intensity is not fully reversible on recharging. While recharging
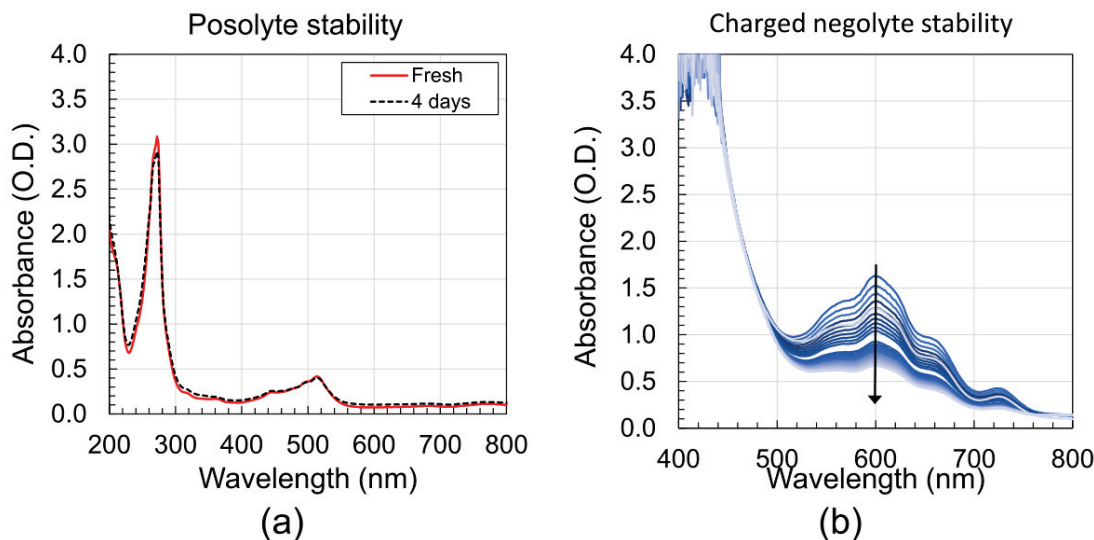
Figure 7.19: UV-Vis spectra illustrating the benchtop stability of charged posolyte (a) and negolyte solutions (b). The posolyte shows good long-term stability after 4 days, and the negolyte peak at 600 nm decays within minutes. Spectra in panel (b) were collected every 15 seconds.

was visually observed to recover some negolyte pigmentation, subsequent charges appeared progressively less pigmented (Figure C.13). No degradation in the charged posolyte was observed on this timescale, or even after 4 days (Figure 7.19a).

Figure 7.20 shows the CV scans for cycled electrolyte that was harvested from cells cycled at 24, 40 and 0 °C. Minor differences in peak current are observed compared to samples of uncycled electrolyte. These could easily originate from changes in species concentration due to solvent loss during cycling, or species crossover through the non-selective Daramic separator, and therefore cannot conclusively indicate a loss of active species due to degradation. Interestingly, the cycled solutions from the high temperature cell show a loss in peak current for the first MEEV reduction event after only five cycles. In contrast, the stored (uncycled) solution does not show this same effect, even with further cycling. Electrolyte harvested from cells cycled at room temperature and 0 °C also do not display this effect.

We investigate this behaviour further in Figure 7.21. Panel (a) shows that the
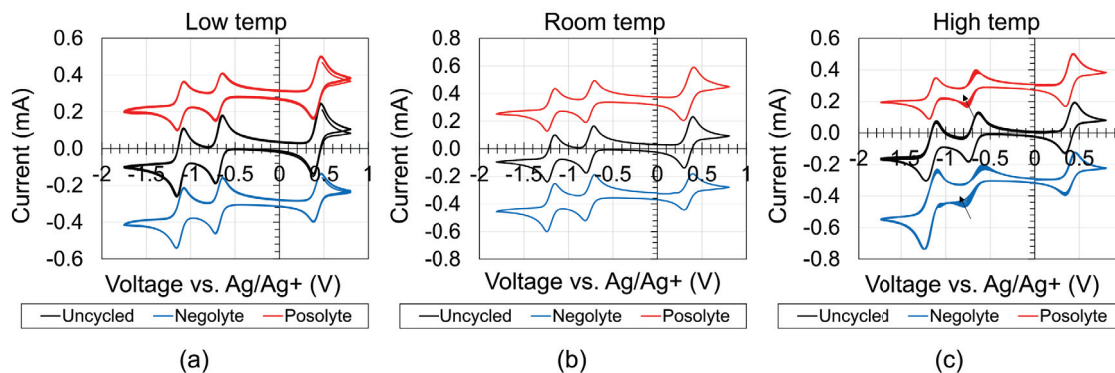
Figure 7.20: Cyclic voltammetry of cycled electrolyte harvested from low-temperature (a), room-temperature (b), and high-temperature (c) cells in comparison to uncycled electrolyte that was stored (but not cycled) under the same conditions. All measurements were performed under nitrogen at room temperature. Electrolyte was diluted to 10 mM in 0.5 M TEATFSI in acetonitrile to maintain solution conductivity. Measurements were performed using a 100 mV/s scan rate with 100 % iR-compensation.

diminished peak current is reversed by wiping the glassy carbon electrode (GCE) with a methanol-soaked Kimwipe, which suggests that the behaviour may be due to fouling of the GCE during cycling. To investigate whether this effect is induced by exposure to trace oxygen and/or moisture, the measurements were repeated in a glovebox (at room temperature). Figure 7.21(b) reveals that even under inert conditions, a loss of peak current in a sample of cycled posolyte is still observed after repeated cycling. Narrowing the CV scan range was found to eliminate the loss of peak current over the same timescale (Figure 7.21(c)).

7.4   Discussion and conclusions

In this study we examine the cycling stability for non-aqueous MEEPT-MEEV flow cells that are cycled under a range of operating temperatures: 24, 40 and 0 ^{0}C. The room temperature cell shows strong cycling performance with reversible losses in capacity. The high-temperature cells, exhibit more rapid capacity loss, which begins after $200 - 300$ hours of cycling. The low-temperature cell also shows rapid capacity loss (roughly 50 % loss after cycling for 150 hours), which may result from cycling
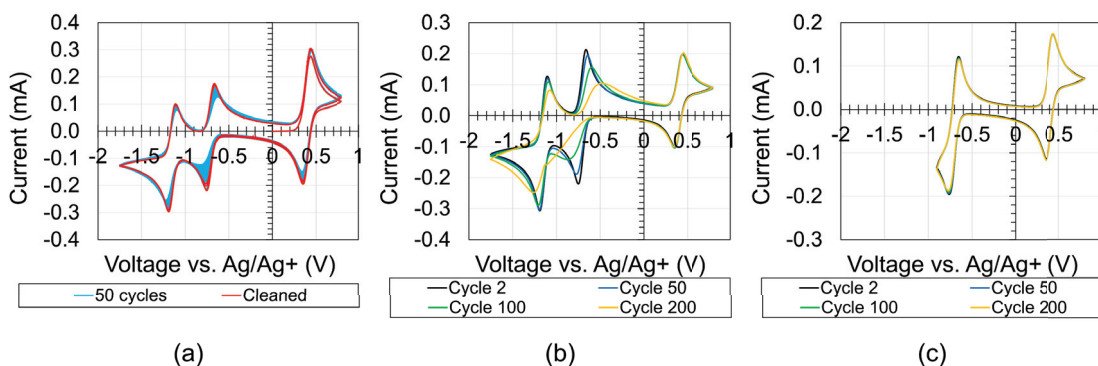
Figure 7.21: CV illustrating the fouling behaviour of a glassy carbon electrode to the first MEEV reduction event. The effect of electrode cleaning after repeated cycling is shown in (a). Repeated cycling in an oxygen- and moisture-free environment (glovebox) is shown in (b). Repeated cycling using a smaller voltage window in an oxygen- and moisture-free environment is shown in (c). Measurements were performed at 100 mV/s scan rate with 100 % iR-compensation.

under an ambient atmosphere. While the flow cell itself is a closed system, imperfect sealing at the reservoirs and fittings may allow gradual permeation of oxygen and/or moisture into the cell.

Interestingly, all cells exhibit a steady increase in coulombic efficiency with cycling. In the high temperature cells, the coulombic efficiency is approximately 50 % at the beginning of cycling, and 90 % at the end of cycling (using the same current). Three processes may lend to increased coulombic efficiency with cycling: reduced cycle time (that can result from capacity loss), parasitic reactions (that disappear with cycling), and/or reduced separator permeability (that results in lower self-discharge). In our data the growth in coulombic efficiency persists when the cell capacity (and therefore constant-current cycle time) is stable, which suggests that this is not the dominant factor contributing to this trend. Parasitic reactions are a plausible possibility. Post-cycling XPS measurements unanimously show an increased concentration of new elements on cycled carbon electrodes compared to fresh electrode samples. The elements are mainly expected based on the electrolyte components, with the exception of chlorine. Significant concentrations of chlorine are visible on the surfaces

of all electrodes that are cycled, or passively exposed to electrolyte. This suggests that one (or more) of the electrolyte components contains chlorine-containing impurities. The fact that chlorine is observed in comparable quantities to other elements suggests that it is present in significant quantities in the electrolyte; and/or, that it preferentially forms reaction products on the electrodes. If these impurities undergo irreversible parasitic reactions this would present as increased coulombic efficiency as the reactants are consumed. Qualitative evidence for parasitic reactions is also seen on the cycled separators, which show irreversible staining on the negative face.

Post-cycling membrane characterization suggests that reduced permeability may also contribute to increased coulombic efficiency. The microporous Daramic separator is known to be highly permeable to the active electrolyte materials [5,126], which can lead to coulombic inefficiency resulting from crossover of charged species. Reducing charged species crossover would improve coulombic efficiency. Gurley measurements show that significantly greater times are required to displace 100 mL of air through cycled Daramic separators compared to fresh samples. This suggests that the Daramic porosity is reduced with cycling, which lends itself to a theory involving membrane fouling. It is possible that parasitic reactions during cycling may deposit insoluble products on the separator, which restricts material transport between the half-cells. This would lead to a higher coulombic efficiency with cycling. Through-plane ionic conductivity through the separator would also be reduced, which is consistent with our observations of increased cell impedance and reduced voltage efficiency observed with cycling. Self-discharge measurements also show slower crossover of active species through the separator after cycling, which supports this theory.

In situ EIS performed on operating cells shows a gradual increase in cell impedance with cycling. The cell impedance is dominated by increased series and diffusion resistance with cycling. An increased charge-transfer resistance is also observed. However, this change is small in comparison to other systems that we have characterized. This

may result from good charge-transfer kinetics, which are reported to be inherently strong in non-aqueous organic electrolytes; however, these cells were only cycled up to a maximum of 130 cycles. This system could stand to benefit from additional trials and extended cycling at room temperature to better understand the evolution of cell impedance. This may not be practical under high- and low-temperature conditions, however, where the cell performance is dominated by rapid capacity loss. Performing low-temperature cycling under an inert atmosphere will also be useful to determine if the observed capacity loss results from temperature, or atmospheric effects.

The FTIR, CV and UV-Vis measurements performed in this study do not reveal significant changes between cycled and fresh samples of electrolyte (to an extent that can account for the observed capacity loss). UV-Vis spectroscopy, however, shows that the charged MEEV negolyte is very unstable under ambient atmosphere (likely resulting from oxygen exposure). By comparison, the charged MEEPT posolyte was stable under the timescales investigated. Instability of the charged MEEV negolyte may limit capacity retention in these cells; however, chemical characterization methods with higher sensitivity may be required to discern the electrolyte degradation products (and mechanism).

Chapter 8

Conclusions and Future Work

8.1 Summary of work

Redox flow batteries are a prospective technology for grid-scale electrochemical energy storage. Current state-of-the-art flow batteries employ an aqueous vanadium electrolyte; however, organic redox flow batteries (ORFBs) have become a recent focus, as a possible means to circumvent the high and volatile cost of vanadium. In this study, we characterized cycling-induced impedance growth and changes to cell components for a vanadium-based flow cell and two promising ORFB systems. Impedance growth and electrode properties have been studied for aqueous vanadium RFBs with long-term cycling [52–54]; however, this topic was unexplored in ORFBs at this time. Recent improvements in organic electrolytes have enabled long lifetime flow cells with strong performance under relevant cycling conditions [2, 3, 91, 124]. Given these advancements, characterizing impedance growth and electrode changes will become important to understand and reduce performance loss in new ORFBs.

In this thesis we characterize degradation in cell performance for three different RFB systems by applying a combination of electrochemical methods and spectroscopic techniques. Cell components (electrolyte, membrane, and electrodes) are compared before and after cycling; and, *in situ* EIS is used to monitor the evolution in

cell impedance with cycling. Equivalent circuit fitting is also used to quantify changes in resistance and capacitance when possible.

In the first study we examined degradation in non-aqueous vanadium (III) acetylacetonate ($V(acac)_3$) flow cells. $V(acac)_3$ was shown by other authors to undergo rapid degradation to $VO(acac)_2$ in the presence of moisture [87, 144]. We cycled $V(acac)_3$ flow cells under moisture-free conditions (Mbraun glovebox, H_2O < 1.2 ppm), but continued to observe rapid cell failure on the order of 20 hours. Electrolyte degradation was confirmed in cyclic voltammetry and Raman spectroscopy, but not in quantities that would account for the magnitude of capacity loss. A significant portion of the apparent capacity loss was found to originate from increased cell resistance, which caused the cell to exceed charging limits before the electrolyte was fully charged/discharged. EIS confirmed a dramatic growth in cell impedance after cycling. Post-cycling XPS revealed significant quantities of material deposited on the negative cycled electrode surface compared to other electrode samples, which we correlate with greater charge-transfer resistance observed on the cycled negative electrode.

In the second study, we examined degradation in a nearly pH-neutral (aqueous) 2,6-DPPEAQ/potassium ferrocyanide flow cells. This electrolyte system was reported to exhibit outstanding calendar lifetimes by previous authors [2]; however, changes in cell impedance were not characterized. We characterized the performance and impedance growth for three 2,6-DPPEAQ/potassium ferrocyanide flow cells throughout long-term cycling. Our cells exhibited comparable capacity fade rates to previous reports [2], and a loss of $\sim 5\%$ energy efficiency after 1000 hours of cycling. *In situ* EIS performed on operating cells revealed a steady impedance growth with cycling. The change in EIS spectra suggested increased charge-transfer and mass-transfer resistance after cycling. DRT analysis of impedance spectra revealed three characteristic (RC) time constants at mid- and high- frequencies, and a low time constant

feature associated with mass-transfer resistance. Equivalent circuit fitting with this knowledge indicated a growth in these resistances, and a loss of specific capacitance. Fitting the mass-transfer feature revealed a steady growth in Warburg impedance. The series resistance did not change with cycling. In agreement with expectations from literature, post-cycling electrolyte analysis did not reveal significant chemical changes. XPS analysis did not reveal significant quantities of new material deposited on the cycled electrodes, especially when compared with electrodes that were stored (but not cycled) in electrolyte. This was surprising given the notable changes observed in full cell impedance spectroscopy. The minimal chemical changes observed by XPS could result from a lack of sampling statistics. It is also possible that more subtle changes in surface chemistry (e.g. changes in oxygen chemical environment observed on the negative electrode) could be responsible for the degradation in cell performance. Repeated trials would be necessary to validate this theory.

In the final study, we examined degradation in non-aqueous flow cells employing a MEEPT/MEEV electrolyte under different ambient temperatures. Room-temperature cycling revealed strong capacity retention (with some reversible changes) over 1200 hours. At 40 °C cells showed rapid capacity fade after $200 - 300$ hours of cycling. The low-temperature (0 °C) cell (which was cycled under ambient atmosphere) also showed rapid capacity loss. Interestingly, all cells exhibited a growth in coulombic efficiency with cycling. This change was most notable for the cells cycled at 40 °C, which diplayed a coulombic efficiency of 50 % at the beginning, and 90 % at the end of cycling. We attributed the increased coulombic efficiency to two processes: (1) parasitic reactions early in cycling (that decrease as reactant is consumed) and/or (2) fouling of the Daramic separator, which reduced crossover of charged active species between the two half-cells. Evidence for separator fouling was observed as irreversible staining on the negative separator face. Gurley measurements also suggested reduced porosity for cycled separator samples. Post-cycling electrolyte analysis did not reveal

obvious degradation of cycled electrolyte; however, the charged MEEV negolyte was observed to be unstable in the presence of oxygen. (The instability was not fully reversible). XPS measurements revealed significant quantities of new material deposited on cycled electrode surfaces. Large concentrations of chlorine were also detected on electrodes that were exposed to electrolyte, which suggests that chlorine-containing impurities are present in the electrolyte. Understanding the source of chlorine contamination, and whether it contributes to degradation in cell performance will be important for this system moving forward.

8.2 Future work and recommendations

As discussed in the paragraphs above, the quinone/ferrocyanide flow cells show large changes in the full-cell EIS spectra that do not immediately correlate with chemical changes detected by XPS, or single electrode EIS. More trials would be beneficial to elucidate statistically significant XPS trends. As mentioned previously, it is also possible that the full-cell impedance growth may result from more subtle changes in electrode surface chemistry. In this case, cycling to a very poor state-of-health could help to amplify features in post-cycling analysis. Repeated measurements would also be beneficial.

Understanding electrode degradation and impedance growth in both studies could benefit greatly from improved *ex situ* impedance spectroscopy post-cycling. In the quinone study, single electrode impedance measurements were performed using small samples of cycled carbon paper as a working electrode. However, the resulting charge-transfer feature was very small (likely due to the small electrode size). To better resolve this feature, we diluted the concentration of active electrolyte species from 0.5 M to 10 mM in the three-electrode cell. However, these conditions (and the conditions in a three-electrode cell) are not representative of full-cell operation, which makes it difficult to draw meaningful quantitative comparisons between these measurements

and the full cell. This is a significant drawback as the original intention of these measurements was to understand the origin of new features in full-cell impedance spectra, and characterize the relative contribution of the negative and positive electrodes to these changes. The three electrode cell set-up was also limited by an inherent uncertainty in the accuracy with which repeatable and known sample sizes (3 x 3 mm working area) can be prepared. Some areal variation, even in fresh electrodes received from the manufacturer may even be expected on these lengthscales. These factors are reflected by the visible scatter in impedance spectra for otherwise identical samples.

One option to improve the *ex situ* impedance measurements could involve constructing a new symmetric flow cell using cycled electrodes harvested from each half-cell – similar (but not identical) to Figure 3.2b. The new cell would contain cycled negative (or positive) electrodes in both half-cells and the electrolyte would consist of fresh negolyte (or posolyte) at 50 % SOC. The electrolyte would be circulated between the two half-cells such that is it charged on one side, then discharged on the other side (to maintain the 50 % SOC). These results would be compared to cells constructed using fresh electrodes on both sides. Similar cells have been developed by Darling *et al.*, and other authors to perform polarization measurements, or EIS measurements on fresh electrodes [43, 167]. This was not practical in our studies, as we required the cycled electrodes for other characterization techniques as well (SEM, XPS and single electrode EIS). Electrodes aged in repeated trials were unfortunately damaged by instrumentation/software errors as previously mentioned.

A significant drawback in our analysis of impedance growth in the non-aqueous MEEPT/MEEV cells was the inherent uncertainty attributed to fitting small high-frequency features associated with charge-transfer effects. We believe the uncertainty in trends determined through equivalent-circuit fitting may be reduced by performing EIS measurements over a much greater range of cycles (as in the quinone study). This may not be practical under high- and low-temperature conditions (which show

rapid capacity loss); however, long-term cycling at room temperature under blanket nitrogen should be possible. Obtaining high-quality EIS data can help simplify DRT and equivalent circuit analysis. Some lessons learned from this work include: using a high sample density (10 pts/decade, if feasible), minimizing inductive contributions (which may mask, or sometimes exaggerate apparent charge-transfer features), reducing sources of electrical noise as much as possible, and selecting fast current/voltage ranging setting for relevant instrumentation. When inductive contributions cannot be reduced, selecting a high upper frequency limit is recommended to characterize inductance. The high frequency data can be fit to quantify the inductance and numerically "correct" raw data.

The low-temperature cycling data collected for the non-aqueous MEEPT/MEEV flow cells was not ideal in this study. Cycling was performed under ambient atmosphere after preliminary characterization (by cyclic voltammetry) suggested that the MEEPT/MEEV electrolyte was insensitive to oxygen and moisture. Based on the rapid capacity fade observed in this study, this may not be true under relevant operating conditions. It is recommended that repeated low-temperature cycling for this system be performed under nitrogen, if possible.

Finally, while appreciable capacity loss was observed after high-temperature and low-temperature cycling, the characterization methods used in this study did not reveal significant changes in the cycled electrolyte. Chemical characterization methods with higher sensitivity, such as H NMR, or mass spectroscopy are recommended if possible.

8.3 Future work for RFBs

Organic RFBs are still a nascent technology (particularly those using non-aqueous electrolytes). However, organic redox materials have recently shown significant improvements in material lifetime, and should not be discounted as a potential energy

storage technology [133]. Electrolyte stability and materials costs are currently well-studied in ORFB literature, but two common themes appear to be lacking: (1) full-cell operation under commercially relevant cycling conditions (i.e. high active materials concentration, and high currents); and, (2) development of standardized lifetime testing protocols and benchmarks. (The latter will become increasingly important as the organic RFBs develop into a mature technology.) In addition, ion-selective membranes still constitute a significant fraction of capital investment costs aqueous ORFBs [16,168]; and, this cell component is currently underdeveloped in non-aqueous counterparts.

One significant shortcoming in current RFB literature is the lack of studies characterizing the performance of high-concentration electrolytes. Technoeconomic analyses recommend high concentrations of redox-active species to offset materials and balance-of-plant costs over projected operational lifetimes [16, 17]. In non-aqueous systems this equates to an upper window of 3-5 M (dissolved electron equivalence), or 1-2 M in aqueous systems. (However, improvements to other systems components may eventually necessitate lower species concentrations). Many non-aqueous RFBs do not reach this benchmark (nor do they operate at the concentration limit for a given electrolyte species). In aqueous ORFB literature, some recent materials have reached these concentration targets; however, long-term cell cycling has not been reported at these upper concentration targets [2,3,91,105].

Beyond improving energy density, increased solute concentrations can significantly affect the physical and chemical properties of electrolytes, and therefore cell performance [169, 170]. At high concentrations, solution behaviour can change in non-intuitive ways [170]. For example, increasing supporting electrolyte concentrations improves solution conductivity; however, at high concentrations there are diminishing returns as solution viscosity begins to limit redox species mobility. Higher flow rates can be used to encourage material transport, but pumping efficiency is typi-

cally diminished for high solution viscosity. In addition, high solute concentrations can favour non-Newtonian behaviours and intermolecular interactions such as dimerization, oligomerization and contact networks [132, 171–175]. Understanding the cumulative effect of these behaviours will be instrumental to the commercialization of ORFBs. Characterization of high concentration electrolytes will present unique challenges that necessitate the use of modified measurements techniques. For example, higher concentrations of active species will result in larger currents, and therefore larger ohmic losses. Fenton *et al.* suggest a number of spectroscopic and electrochemical methods to address these challenges, such as the use of microelectrodes and microfluidic cells [169].

Improving the performance and manufacturing of membranes and separators will also be important for both reducing materials costs, and improving cell performance and capacity retention – particularly in non-aqueous systems. RFB membranes both keep redox active materials separate; and, allow passage of supporting ions to charge-balance the cell – two critical functions. Aqueous flow batteries have benefited from earlier fuel cell developments; Nafion membranes are still the most common ion-selective separators in the more developed acidic aqueous electrolyte systems (despite their high areal costs) [168]. Cheaper, non-fluorinated options (such as Fumatech® brand materials) are also available, and have been shown to function well in alkaline electrolyte [2, 3]. While these ion-selective separators have also been used in non-aqueous systems, the low intrinsic conductivity of non-aqueous electrolytes exacerbates voltage losses due membrane resistance under relevant operating currents [176]. Microporous separators (such as Daramic and Celgard membranes) are often used as an alternative to achieve high-current density cycling; however, these materials exhibit poor-selectivity and lead to significant capacity fade in under 100 cycles unless electrolyte pre-mixing (as described in this thesis and other works) is performed [5].

Some common suggestions for non-aqueous separators involve working around

porosity limitations through the rational design of long-chain oligomers as redox-active materials. The resulting size-exclusion is reported to eliminate active material crossover in organic electrolytes [173, 177–179]. However, technoeconomic analyses, suggests that low-molecular weight materials are necessary to maintain low capital investment costs, so it is unclear how successful this strategy will be in the long-term [16, 17]. Chemical surface modifications and pore-filling are being explored as possible techniques to impart ion-selective characteristics on microporous separators [176]. Some chemical surface treatments have shown improved coulombic efficiency compared to untreated controls [180–182]; however, higher coulombic efficiencies and selectivity will still be needed for long-term cycling. In addition, understanding the chemical and cycling stability of surface-modified separators will become important. (Currently, these investigations only report datasets with limited cycle numbers [176].)

In addition to materials and process developments, understanding the performance and longevity of flow batteries under different temperatures will be critical to their intended application. Surprisingly, this topic is under-explored in organic RFB literature. High-temperatures are often used to evaluate the chemical of novel organic molecules under storage [2, 3, 91, 105]; however, cell cycling under temperatures outside of 25 °C have only been explicitly examined in a handful of studies [128, 161–164]. Temperature is expected to impact the rate of parasitic reactions and cell degradation.

Beyond impacting cell performance and longevity, elevated temperatures could be used to implement accelerated stress testing protocols to extrapolate lifetime limitations for promising and stable organic electrolytes. Accelerated stress testing (under elevated temperature and humidity, for example) is a common lifetime assessment method in the organic photovoltaic research [183–185]. In the lithium-ion field, temperature studies are also used to evaluate cell lifetimes [39, 186]. More importantly, high-precision coulometry and impedance measurements have been shown to provide accurate indications of lifetime trends in lithium-ion batteries, which eliminates the

174

need to rely exclusively on slow, long-duration cycling tests [187,188]. Along this same vein, the ORFB field could benefit from developing standardized testing protocols to evaluate and/or extrapolate cell lifetimes from high-precision and/or aggressive testing protocols. Establishing benchmark performance standards (as in the lithium-ion battery community) [39], will also be useful – especially given the diversity of organic electrolyte systems. Standardized cycling protocols and reliable methods for accelerated lifetime testing will become increasingly important as organic electrolyte lifetimes continue to improve and ORFBs develop into a mature technology.

Bibliography

[1] D Rastler. Electricity energy storage technology options a white paper primer on applications, costs, and benefits. *Electric Power Research Institute, Technical Update*, 2010.

[2] Yunlong Ji, Marc-Antoni Goulet, Daniel A Pollack, David G Kwabi, Shijian Jin, Diana De Porcellinis, Emily F Kerr, Roy G Gordon, and Michael J Aziz. A phosphonate-functionalized quinone redox flow battery at near-neutral pH with record capacity retention rate. *Advanced Energy Materials*, 9(12):1900039, 2019.

[3] David G Kwabi, Kaixiang Lin, Yunlong Ji, Emily F Kerr, Marc-Antoni Goulet, Diana De Porcellinis, Daniel P Tabor, Daniel A Pollack, Alán Aspuru-Guzik, Roy G Gordon, et al. Alkaline quinone flow battery with long lifetime at pH 12. *Joule*, 2(9):1894–1906, 2018.

[4] Charlotte Clegg and Ian G Hill. Characterizing degradation in non-aqueous vanadium (III) acetylacetonate redox flow batteries. *Journal of The Electrochemical Society*, 167(12):120510, 2020.

[5] Zhiming Liang, N Harsha Attanayake, Katharine V Greco, Bertrand J Neyhouse, John L Barton, Aman Preet Kaur, William L Eubanks, Fikile R Brushett, James Landon, and Susan A Odom. Comparison of separators vs membranes in nonaqueous redox flow battery electrolytes containing small molecule active materials. *ACS Applied Energy Materials*, 4(6):5443–5451, 2021.

[6] Jarrod D Milshtein, Aman Preet Kaur, Matthew D Casselman, Jeffrey A Kowalski, Subrahmanyam Modekrutti, Peter L Zhang, N Harsha Attanayake, Corrine F Elliott, Sean R Parkin, Chad Risko, et al. High current density, long duration cycling of soluble organic active species for non-aqueous redox flow batteries. *Energy & Environmental Science*, 9(11):3531–3543, 2016.

[7] PR Shukla, J Skea, R Slade, A Al Khourdajie, R van Diemen, D McCollum, M Pathak, S Some, P Vyas, R Fradera, M Belkacemi, A Hasija, G Lisboa, S Luz, and J Malley. IPCC, 2022: Summary for policymakers. *Climate Change 2022: Mitigation of Climate Change. Contribution of Working Group III to the Sixth Assessment Report of the Intergovernmental Panel on Climate Change*, 2022.

[8] J Lelieveld, K Klingmüller, A Pozzer, RT Burnett, A Haines, and V Ramanathan. Effects of fossil fuel and total anthropogenic emission removal on public health and climate. *Proceedings of the National Academy of Sciences*, 116(15):7192–7197, 2019.

[9] Max Roser Hannah Ritchie and Pablo Rosado. Energy, 2020. https://ourworldindata.org/energy.

[10] Natural Resources Canada. Energy fact book 2019–2020, 2019.

[11] Maria Skyllas-Kazacos, George Kazacos, Grace Poon, and Hugh Verseema. Recent advances with UNSW vanadium-based redox flow batteries. *International Journal of Energy Research*, 34(2):182–189, 2010.

[12] Maria Skyllas-Kazacos, MH Chakrabarti, SA Hajimolana, FS Mjalli, and M Saleem. Progress in flow battery research and development. *Journal of the electrochemical society*, 158(8):R55, 2011.

[13] Sumitomo Electric Group. Sumitomo electric redox flow battery brochure, 2022. https://sumitomoelectric.com/products/redox.

[14] S Djunisic. Sumitomo electric awarded contract to supply, install redox battery system, 2020. https://renewablesnow.com/news/sumitomo-electric-awarded-contract-to-supply-install-redox-battery-system-709459/.

[15] Binqi Guo, Meng Niu, Xiaokang Lai, and Liquan Chen. Application research on large-scale battery energy storage system under global energy interconnection framework. *Global Energy Interconnection*, 1(1):79–86, 2018.

[16] Robert M Darling, Kevin G Gallagher, Jeffrey A Kowalski, Seungbum Ha, and Fikile R Brushett. Pathways to low-cost electrochemical energy storage: a comparison of aqueous and nonaqueous flow batteries. *Energy & Environmental Science*, 7(11):3459–3477, 2014.

[17] Rylan Dmello, Jarrod D Milshtein, Fikile R Brushett, and Kyle C Smith. Cost-driven materials selection criteria for redox flow battery electrolytes. *Journal of Power Sources*, 330:261–272, 2016.

[18] Yan Huang, Shuang Gu, Yushan Yan, and Sam Fong Yau Li. Nonaqueous redox-flow batteries: features, challenges, and prospects. *Current Opinion in Chemical Engineering*, 8:105–113, 2015.

[19] Jan Winsberg, Tino Hagemann, Tobias Janoschka, Martin D Hager, and Ulrich S Schubert. Redox-flow batteries: from metals to organic redox-active materials. *Angewandte Chemie International Edition*, 56(3):686–711, 2017.

[20] John B Goodenough and Youngsik Kim. Challenges for rechargeable batteries. *Journal of Power Sources*, 196(16):6688–6694, 2011.

[21] C-N Sun, MM Mench, and TA Zawodzinski. High performance redox flow batteries: an analysis of the upper performance limits of flow batteries using non-aqueous solvents. *Electrochimica Acta*, 237:199–206, 2017.

[22] D Rastler. Market driven distributed energy storage system requirements for load management applications. *Electric Power Research Institute, Palo Alto, CA*, 2007.

[23] Bin Li and Jun Liu. Progress and directions in low-cost redox-flow batteries for large-scale energy storage. *National Science Review*, 4(1):91–105, 2017.

[24] Sydney M Laramie, Jarrod D Milshtein, Tanya M Breault, Fikile R Brushett, and Levi T Thompson. Performance and cost characteristics of multi-electron transfer, common ion exchange non-aqueous redox flow batteries. *Journal of Power Sources*, 327:681–692, 2016.

[25] Kristina Wedege, Emil Draževic, Denes Konya, and Anders Bentien. Organic redox species in aqueous flow batteries: redox potentials, chemical stability and solubility. *Scientific reports*, 6(1):1–13, 2016.

[26] Jian Luo, Bo Hu, Camden Debruler, Yujing Bi, Yu Zhao, Bing Yuan, Maowei Hu, Wenda Wu, and T Leo Liu. Unprecedented capacity and stability of ammonium ferrocyanide catholyte in pH neutral aqueous redox flow batteries. *Joule*, 3(1):149–163, 2019.

[27] Zhengjin Yang, Liuchuan Tong, Daniel P Tabor, Eugene S Beh, Marc-Antoni Goulet, Diana De Porcellinis, Alán Aspuru-Guzik, Roy G Gordon, and Michael J Aziz. Alkaline benzoquinone aqueous flow battery for large-scale storage of electrical energy. *Advanced Energy Materials*, 8(8):1702056, 2018.

[28] Marc-Antoni Goulet and Michael J Aziz. Flow battery molecular reactant stability determined by symmetric cell cycling methods. *Journal of The Electrochemical Society*, 165(7):A1466, 2018.

[29] Jian Luo, Alyssa Sam, Bo Hu, Camden DeBruler, Xiaoliang Wei, Wei Wang, and T Leo Liu. Unraveling pH dependent cycling stability of ferricyanide/ferrocyanide in redox flow batteries. *Nano Energy*, 42:215–221, 2017.

[30] Advaith Murali, Archith Nirmalchandar, Sankarganesh Krishnamoorthy, Lena Hoober-Burkhardt, Bo Yang, Grigorii Soloveichik, GK Surya Prakash, and SR Narayanan. Understanding and mitigating capacity fade in aqueous organic redox flow batteries. *Journal of The Electrochemical Society*, 165(7):A1193, 2018.

[31] Min Li, Susan A Odom, Adam R Pancoast, Lily A Robertson, Thomas P Vaid, Garvit Agarwal, Hieu A Doan, Yilin Wang, T Malsha Suduwella, Sambasiva R Bheemireddy, et al. Experimental protocols for studying organic non-aqueous redox flow batteries, 2021.

[32] Marc-Antoni Goulet, Liuchuan Tong, Daniel A Pollack, Daniel P Tabor, Susan A Odom, Alán Aspuru-Guzik, Eugene E Kwan, Roy G Gordon, and Michael J Aziz. Extending the lifetime of organic flow batteries via redox state management. *Journal of the American Chemical Society*, 141(20):8014–8019, 2019.

[33] Zhijiang Tang, Aman Preet Kaur, Alan Pezeshki, Subrahmanyam Modekrutti, Frank Delnick, Thomas Zawodzinski, Gabriel Veith, and Susan Odom. Determining performance limits for non-aqueous redox flow batteries. *ChemRxiv (unpublished)*, 2021.

[34] Daniel P Tabor, Rafael Gómez-Bombarelli, Liuchuan Tong, Roy G Gordon, Michael J Aziz, and Alán Aspuru-Guzik. Mapping the frontiers of quinone stability in aqueous media: implications for organic aqueous redox flow batteries. *Journal of Materials Chemistry A*, 7(20):12833–12841, 2019.

[35] P Leung, AA Shah, L Sanz, C Flox, JR Morante, Q Xu, MR Mohamed, C Ponce De León, and FC Walsh. Recent developments in organic redox flow batteries: a critical review. *Journal of Power Sources*, 360:243–283, 2017.

[36] Kendall Mongird, Vilayanur Viswanathan, Jan Alam, Charlie Vartanian, Vincent Sprenkle, and Richard Baxter. 2020 grid energy storage technology cost and performance assessment. *US Department of Energy: Energy Storage Grand Challenge Cost and Performance Assessment 2020*, 2020, 2020.

[37] A Saiyid. Grid storage systems unlikely to see price declines until 2024, 2022. https://cleanenergynews.ihsmarkit.com/research-analysis/grid-storage-systems-unlikely-to-see-price-declines-until-2024.html.

[38] KM Abraham. How comparable are sodium-ion batteries to lithium-ion counterparts? *ACS Energy Letters*, 5(11):3544–3547, 2020.

[39] Jessie E Harlow, Xiaowei Ma, Jing Li, Eric Logan, Yulong Liu, Ning Zhang, Lin Ma, Stephen L Glazier, Marc ME Cormier, Matthew Genovese, et al. A wide range of testing results on an excellent lithium-ion cell chemistry to be used as benchmarks for new battery technologies. *Journal of The Electrochemical Society*, 166(13):A3031, 2019.

[40] Che-Nan Sun, Frank M Delnick, DS Aaron, AB Papandrew, Matthew M Mench, and Thomas A Zawodzinski. Probing electrode losses in all-vanadium redox flow batteries with impedance spectroscopy. *ECS Electrochemistry Letters*, 2(5):A43, 2013.

[41] Che-Nan Sun, Frank M Delnick, Douglas S Aaron, Alexander B Papandrew, Matthew M Mench, and Thomas A Zawodzinski. Resolving losses at the negative electrode in all-vanadium redox flow batteries using EIS. *Journal of The Electrochemical Society*, 161(6):A981, 2014.

[42] Katharine V Greco, Antoni Forner-Cuenca, Adrian Mularczyk, Jens Eller, and Fikile R Brushett. Elucidating the nuanced effects of thermal pretreatment on carbon paper electrodes for vanadium redox flow batteries. *ACS applied materials & interfaces*, 10(51):44430–44442, 2018.

[43] Antoni Forner-Cuenca, Emily E Penn, Alexandra M Oliveira, and Fikile R Brushett. Exploring the role of electrode microstructure on the performance of non-aqueous redox flow batteries. *Journal of The Electrochemical Society*, 166(10):A2230, 2019.

[44] Holger Fink, Jochen Friedl, and Ulrich Stimming. Composition of the electrode determines which half-cell's rate constant is higher in a vanadium flow battery. *The Journal of Physical Chemistry C*, 120(29):15893–15901, 2016.

[45] Alan M Pezeshki, Jason T Clement, Gabriel M Veith, Thomas A Zawodzinski, and Matthew M Mench. High performance electrodes in vanadium redox flow batteries through oxygen-enriched thermal activation. *Journal of Power Sources*, 294:333–338, 2015.

[46] Joachim Langner, Michael Bruns, Ditty Dixon, A Nefedov, Ch Wöll, Frieder Scheiba, Helmut Ehrenberg, Christina Roth, and Julia Melke. Surface properties and graphitization of polyacrylonitrile based fiber electrodes affecting the negative half-cell reaction in vanadium redox flow batteries. *Journal of Power Sources*, 321:210–218, 2016.

[47] MA Miller, A Bourke, N Quill, JS Wainright, RP Lynch, DN Buckley, and RF Savinell. Kinetic study of electrochemical treatment of carbon fiber microelectrodes leading to in situ enhancement of vanadium flow battery efficiency. *Journal of The Electrochemical Society*, 163(9):A2095, 2016.

[48] Che-Nan Sun, Frank M Delnick, Loïc Baggetto, Gabriel M Veith, and Thomas A Zawodzinski Jr. Hydrogen evolution at the negative electrode of the all-vanadium redox flow batteries. *Journal of Power Sources*, 248:560–564, 2014.

[49] Graziela C Sedenho, Diana De Porcellinis, Yan Jing, Emily Kerr, Luis Martin Mejia-Mendoza, Álvaro Vazquez-Mayagoitia, Alan Aspuru-Guzik, Roy G Gordon, Frank N Crespilho, and Michael J Aziz. Effect of molecular structure of quinones and carbon electrode surfaces on the interfacial electron transfer process. *ACS Applied Energy Materials*, 3(2):1933–1943, 2020.

[50] Bianting Sun and Maria Skyllas-Kazacos. Chemical modification of graphite electrode materials for vanadium redox flow battery application—part I. Thermal treatment. *Electrochimica Acta*, 37(7):1253–1260, 1992.

[51] Bianting Sun and Maria Skyllas-Kazacos. Chemical modification of graphite electrode materials for vanadium redox flow battery application—part II. Acid treatments. *Electrochimica Acta*, 37(13):2459–2465, 1992.

[52] Olga Nibel, Susan M Taylor, Alexandra Pătru, Emiliana Fabbri, Lorenz Gubler, and Thomas J Schmidt. Performance of different carbon electrode materials: insights into stability and degradation under real VRFB operating conditions. *Journal of The Electrochemical Society*, 164(7):A1608, 2017.

[53] Igor Derr, Michael Bruns, Joachim Langner, Abdulmonem Fetyan, Julia Melke, and Christina Roth. Degradation of all-vanadium redox flow batteries (VRFB) investigated by electrochemical impedance and X-ray photoelectron spectroscopy: Part 2 electrochemical degradation. *Journal of Power Sources*, 325:351–359, 2016.

[54] Igor Derr, Daniel Przyrembel, Jakob Schweer, Abdulmonem Fetyan, Joachim Langner, Julia Melke, Martin Weinelt, and Christina Roth. Electroless chemical aging of carbon felt electrodes for the all-vanadium redox flow battery (VRFB) investigated by electrochemical impedance and x-ray photoelectron spectroscopy. *Electrochimica Acta*, 246:783–793, 2017.

[55] Alan M Pezeshki, Robert L Sacci, Gabriel M Veith, Thomas A Zawodzinski, and Matthew M Mench. The cell-in-series method: A technique for accelerated electrode degradation in redox flow batteries. *Journal of The Electrochemical Society*, 163(1):A5202, 2015.

[56] Chanyong Choi, Soohyun Kim, Riyul Kim, Juhyuk Lee, Jiyun Heo, and Hee-Tak Kim. In-situ observation of the degradation of all-vanadium redox flow batteries with dynamic hydrogen reference electrode under real operation conditions. *Journal of Industrial and Engineering Chemistry*, 70:355–362, 2019.

[57] XL Zhou, TS Zhao, Liang An, YK Zeng, and Lei Wei. Critical transport issues for improving the performance of aqueous redox flow batteries. *Journal of Power Sources*, 339:1–12, 2017.

[58] Mike L Perry, Kara E Rodby, and Fikile R Brushett. Untapped potential: The need and opportunity for high-voltage aqueous redox flow batteries. *ACS Energy Letters*, 7(2):659–667, 2022.

[59] Doug Aaron, Zhijiang Tang, Alexander B Papandrew, and Thomas A Zawodzinski. Polarization curve analysis of all-vanadium redox flow batteries. *Journal of Applied Electrochemistry*, 41(10):1175–1182, 2011.

[60] Kevin M Tenny, Antoni Forner-Cuenca, Yet-Ming Chiang, and Fikile R Brushett. Comparing physical and electrochemical properties of different weave patterns for carbon cloth electrodes in redox flow batteries. *Journal of Electrochemical Energy Conversion and Storage*, 17(4):041010, 2020.

[61] Andrew A Wong and Michael J Aziz. Method for comparing porous carbon electrode performance in redox flow batteries. *Journal of The Electrochemical Society*, 167(11):110542, 2020.

[62] Tao Liu, Xianfeng Li, Chi Xu, and Huamin Zhang. Activated carbon fiber paper based electrodes with high electrocatalytic activity for vanadium flow batteries with improved power density. *ACS applied materials & interfaces*, 9(5):4626–4633, 2017.

[63] Donghyun Kil, Hyo June Lee, Sangki Park, Sangkyun Kim, and Hansung Kim. Synthesis of activated graphite felts using short-term ozone/heat treatment for vanadium redox flow batteries. *Journal of The Electrochemical Society*, 164(13):A3011, 2017.

[64] Daniel Manaye Kabtamu, Jian-Yu Chen, Yu-Chung Chang, and Chen-Hao Wang. Water-activated graphite felt as a high-performance electrode for vanadium redox flow batteries. *Journal of Power Sources*, 341:270–279, 2017.

[65] Cristina Flox, Javier Rubio-García, Marcel Skoumal, Teresa Andreu, and Juan Ramón Morante. Thermo–chemical treatments based on NH3/O2 for improved graphite-based fiber electrodes in vanadium redox flow batteries. *Carbon*, 60:280–288, 2013.

[66] Nir Pour, David G Kwabi, Thomas Carney, Robert M Darling, Michael L Perry, and Yang Shao-Horn. Influence of edge-and basal-plane sites on the vanadium redox kinetics for flow batteries. *The Journal of Physical Chemistry C*, 119(10):5311–5318, 2015.

[67] Guanjie Wei, Wei Su, Zengfu Wei, Xinzhuang Fan, Jianguo Liu, and Chuanwei Yan. Electrocatalytic effect of the edge planes sites at graphite electrode on the vanadium redox couples. *Electrochimica Acta*, 204:263–269, 2016.

[68] Thomas J Rabbow, Markus Trampert, Peter Pokorny, Paul Binder, and Adam H Whitehead. Variability within a single type of polyacrylonitrile-based graphite felt after thermal treatment. part I: physical properties. *Electrochimica Acta*, 173:17–23, 2015.

[69] CR Dennison, Ertan Agar, Bilen Akuzum, and EC Kumbur. Enhancing mass transport in redox flow batteries by tailoring flow field and electrode design. *Journal of The Electrochemical Society*, 163(1):A5163, 2015.

[70] Jarrod D Milshtein, Kevin M Tenny, John L Barton, Javit Drake, Robert M Darling, and Fikile R Brushett. Quantifying mass transfer rates in redox flow batteries. *Journal of The Electrochemical Society*, 164(11):E3265, 2017.

[71] Alan M Pezeshki, Robert L Sacci, Frank M Delnick, Douglas S Aaron, and Matthew M Mench. Elucidating effects of cell architecture, electrode material, and solution composition on overpotentials in redox flow batteries. *Electrochimica Acta*, 229:261–270, 2017.

[72] Benedict A Simon, Andrea Gayon-Lombardo, Catalina A Pino-Muñoz, Charles E Wood, Kevin M Tenny, Katharine V Greco, Samuel J Cooper, Antoni Forner-Cuenca, Fikile R Brushett, Anthony R Kucernak, et al. Combining electrochemical and imaging analyses to understand the effect of electrode microstructure and electrolyte properties on redox flow batteries. *Applied Energy*, 306:117678, 2022.

[73] Simone Dussi and Chris H Rycroft. Less can be more: Insights on the role of electrode microstructure in redox flow batteries from 2D direct numerical simulations. *arXiv preprint arXiv:2201.00423*, 2022.

[74] Immanuel Mayrhuber, Christopher R Dennison, Vibha Kalra, and Emin Caglan Kumbur. Laser-perforated carbon paper electrodes for high-power vanadium redox flow batteries. In *ECS Meeting Abstracts*, number 4, page 372. IOP Publishing, 2014.

[75] XL Zhou, YK Zeng, XB Zhu, Lei Wei, and TS Zhao. A high-performance dual-scale porous electrode for vanadium redox flow batteries. *Journal of Power Sources*, 325:329–336, 2016.

[76] XL Zhou, TS Zhao, YK Zeng, Liang An, and Lei Wei. A highly permeable and enhanced surface area carbon-cloth electrode for vanadium redox flow batteries. *Journal of Power Sources*, 329:247–254, 2016.

[77] Kevin M Tenny, Katharine V Greco, Maxime van der Heijden, Tommaso Pini, Adrian Mularczyk, Alexandru-Petru Vasile, Jens Eller, Antoni Forner-Cuenca, Yet-Ming Chiang, and Fikile R Brushett. A comparative study of compressive effects on the morphology and performance of carbon paper and cloth electrodes in redox flow batteries. *Energy Technology*, 10(8):2101162, 2022.

[78] S Zhong, C Padeste, M Kazacos, and M Skyllas-Kazacos. Comparison of the physical, chemical and electrochemical properties of rayon-and polyacrylonitrile-based graphite felt electrodes. *Journal of Power sources*, 45(1):29–41, 1993.

[79] Ruediger Schweiss, Alexander Pritzl, and Christian Meiser. Parasitic hydrogen evolution at different carbon fiber electrodes in vanadium redox flow batteries. *Journal of The Electrochemical Society*, 163(9):A2089, 2016.

[80] Susan M Taylor, Alexandra Patru, Daniele Perego, Emiliana Fabbri, and Thomas J Schmidt. Influence of carbon material properties on activity and stability of the negative electrode in vanadium redox flow batteries: a model electrode study. *ACS Applied Energy Materials*, 1(3):1166–1174, 2018.

[81] Petr Mazúr, J Mrlik, J Pocedic, Jiří Vrána, Jan Dundálek, Juraj Kosek, and T Bystron. Effect of graphite felt properties on the long-term durability of negative electrode in vanadium redox flow battery. *Journal of Power Sources*, 414:354–365, 2019.

[82] Lei Wei, TS Zhao, Qian Xu, XL Zhou, and ZH Zhang. In-situ investigation of hydrogen evolution behavior in vanadium redox flow batteries. *Applied Energy*, 190:1112–1118, 2017.

[83] S Rudolph, U Schröder, and IM Bayanov. On-line controlled state of charge rebalancing in vanadium redox flow battery. *Journal of Electroanalytical Chemistry*, 703:29–37, 2013.

[84] S Rudolph, U Schröder, IM Bayanov, and D Hage. Measurement, simulation and in situ regeneration of energy efficiency in vanadium redox flow battery. *Journal of Electroanalytical Chemistry*, 728:72–80, 2014.

[85] Bhuvaneswari M Sivakumar, Venkateshkumar Prabhakaran, Kaining Duanmu, Edwin Thomsen, Brian Berland, Nicholas Gomez, David Reed, and Vijayakumar Murugesan. Long-term structural and chemical stability of carbon electrodes in vanadium redox flow battery. *ACS Applied Energy Materials*, 4(6):6074–6081, 2021.

[86] Lorenz Gubler. Membranes and separators for redox flow batteries. *Current Opinion in Electrochemistry*, 18:31–36, 2019.

[87] Ismailia L Escalante-García, Jesse S Wainright, Levi T Thompson, and Robert F Savinell. Performance of a non-aqueous vanadium acetylacetonate prototype redox flow battery: examination of separators and capacity decay. *Journal of The Electrochemical Society*, 162(3):A363, 2014.

[88] Ganesh Venugopal, John Moore, Jason Howard, and Shekhar Pendalwar. Characterization of microporous separators for lithium-ion batteries. *Journal of power sources*, 77(1):34–41, 1999.

[89] Carlos Antonio Pineda Arellano and Susana Silva Martínez. Effects of pH on the degradation of aqueous ferricyanide by photolysis and photocatalysis under solar radiation. *Solar Energy Materials and Solar Cells*, 94(2):327–332, 2010.

[90] Kaixiang Lin, Qing Chen, Michael R Gerhardt, Liuchuan Tong, Sang Bok Kim, Louise Eisenach, Alvaro W Valle, David Hardee, Roy G Gordon, Michael J Aziz, et al. Alkaline quinone flow battery. *Science*, 349(6255):1529–1532, 2015.

[91] Min Wu, Meisam Bahari, Eric M Fell, Roy G Gordon, and Michael J Aziz. High-performance anthraquinone with potentially low cost for aqueous redox flow batteries. *Journal of Materials Chemistry A*, 9(47):26709–26716, 2021.

[92] S Ašpergĕr. Kinetics of the decomposition of potassium ferrocyanide in ultraviolet light. *Transactions of the Faraday Society*, 48:617–624, 1952.

[93] M Reinhard, TJ Penfold, FA Lima, J Rittmann, MH Rittmann-Frank, R Abela, I Tavernelli, U Rothlisberger, CJ Milne, and M Chergui. Photooxidation and photoaquation of iron hexacyanide in aqueous solution: A picosecond X-ray absorption study. *Structural Dynamics*, 1(2):024901, 2014.

[94] IM Kolthoff and EA Pearson. Stability of potassium ferrocyanide solutions. *Industrial & Engineering Chemistry Analytical Edition*, 3(4):381–382, 1931.

[95] Teresa Páez, Alberto Martínez-Cuezva, Jesús Palma, and Edgar Ventosa. Revisiting the cycling stability of ferrocyanide in alkaline media for redox flow batteries. *Journal of Power Sources*, 471:228453, 2020.

[96] Mathilde Cazot, Gaël Maranzana, Jérôme Dillet, Florent Beille, Thibault Godet-Bar, and Sophie Didierjean. Symmetric-cell characterization of the redox flow battery system: Application to the detection of degradations. *Electrochimica Acta*, 321:134705, 2019.

[97] Eric Fell, Diana De Porcellinis, Yan Jing, Valeria Gutierrez-Venegas, Roy Gordon, Sergio Granados-Focil, and Michael Aziz. Long-term stability of ferri-/ferrocyanide as an electroactive component for redox flow battery applications: On the origin of apparent capacity fade. *Under review*, 2022.

[98] Christopher Batchelor-McAuley, Qian Li, Sophie M Dapin, and Richard G Compton. Voltammetric characterization of DNA intercalators across the full pH range: Anthraquinone-2, 6-disulfonate and anthraquinone-2-sulfonate. *The Journal of Physical Chemistry B*, 114(11):4094–4100, 2010.

[99] Partha Sarathi Guin, Saurabh Das, and PC Mandal. Electrochemical reduction of quinones in different media: a review. *International Journal of Electrochemistry*, 2011, 2011.

[100] Michael R Gerhardt, Liuchuan Tong, Rafael Gómez-Bombarelli, Qing Chen, Michael P Marshak, Cooper J Galvin, Alán Aspuru-Guzik, Roy G Gordon, and Michael J Aziz. Anthraquinone derivatives in aqueous flow batteries. *Advanced energy materials*, 7(8):1601488, 2017.

[101] Liuchuan Tong, Yan Jing, Roy G Gordon, and Michael J Aziz. Symmetric all-quinone aqueous battery. *ACS Applied Energy Materials*, 2(6):4016–4021, 2019.

[102] Qing Chen, Michael R Gerhardt, Lauren Hartle, and Michael J Aziz. A quinone-bromide flow battery with 1 W/cm2 power density. *Journal of the Electrochemical Society*, 163(1):A5010, 2015.

[103] Michael R Gerhardt, Eugene S Beh, Liuchuan Tong, Roy G Gordon, and Michael J Aziz. Comparison of capacity retention rates during cycling of quinone-bromide flow batteries. *MRS Advances*, 2(8):431–438, 2017.

[104] Shijian Jin, Yan Jing, David G Kwabi, Yunlong Ji, Liuchuan Tong, Diana De Porcellinis, Marc-Antoni Goulet, Daniel A Pollack, Roy G Gordon, and Michael J Aziz. A water-miscible quinone flow battery with high volumetric capacity and energy density. *ACS Energy Letters*, 4(6):1342–1348, 2019.

[105] Min Wu, Yan Jing, Andrew A Wong, Eric M Fell, Shijian Jin, Zhijiang Tang, Roy G Gordon, and Michael J Aziz. Extremely stable anthraquinone negolytes synthesized from common precursors. *Chem*, 6(6):1432–1442, 2020.

[106] Susan A Odom. Mitigating chemical paths to capacity fade in organic flow batteries. *Chem*, 6(6):1207–1209, 2020.

[107] Yan Jing, Evan Wenbo Zhao, Marc-Antoni Goulet, Meisam Bahari, Eric M Fell, Shijian Jin, Ali Davoodi, Erlendur Jónsson, Min Wu, Clare P Grey, et al. In situ electrochemical recomposition of decomposed redox-active species in aqueous organic flow batteries. *Nature chemistry*, 14(10):1103–1109, 2022.

[108] E Bellini. Quinone flow battery for grid-scale renewables storage now close to commercial viability, 2022. https://www.pv-magazine.com/2022/10/20/quinone-flow-battery-for-grid-scale-renewables-storage-now-close-to-commercial-viability/.

[109] Changkun Zhang, Zhihui Niu, Sangshan Peng, Yu Ding, Leyuan Zhang, Xuelin Guo, Yu Zhao, and Guihua Yu. Phenothiazine-based organic catholyte for high-capacity and long-life aqueous redox flow batteries. *Advanced Materials*, 31(24):1901052, 2019.

[110] Aman Preet Kaur, Nicolas E Holubowitch, Selin Ergun, Corrine F Elliott, and Susan A Odom. A highly soluble organic catholyte for non-aqueous redox flow batteries. *Energy Technology*, 3(5):476–480, 2015.

[111] N Harsha Attanayake, Jeffrey A Kowalski, Katharine V Greco, Matthew D Casselman, Jarrod D Milshtein, Steven J Chapman, Sean R Parkin, Fikile R Brushett, and Susan A Odom. Tailoring two-electron-donating phenothiazines to enable high-concentration redox electrolytes for use in nonaqueous redox flow batteries. *Chemistry of Materials*, 31(12):4353–4363, 2019.

[112] Jeffrey A Kowalski, Matthew D Casselman, Aman Preet Kaur, Jarrod D Milshtein, Corrine F Elliott, Subrahmanyam Modekrutti, N Harsha Attanayake, Naijao Zhang, Sean R Parkin, Chad Risko, et al. A stable two-electron-donating phenothiazine for application in nonaqueous redox flow batteries. *Journal of Materials Chemistry A*, 5(46):24371–24379, 2017.

[113] Aman Preet Kaur, Oliver C Harris, N Harsha Attanayake, Zhiming Liang, Sean R Parkin, Maureen H Tang, and Susan A Odom. Quantifying environmental effects on the solution and solid-state stability of a phenothiazine radical cation. *Chemistry of Materials*, 32(7):3007–3017, 2020.

[114] CL Bird and AT Kuhn. Electrochemistry of the viologens. *Chemical Society Reviews*, 10(1):49–82, 1981.

[115] Eugene S Beh, Diana De Porcellinis, Rebecca L Gracia, Kay T Xia, Roy G Gordon, and Michael J Aziz. A neutral pH aqueous organic–organometallic redox flow battery with extremely high capacity retention. *ACS Energy Letters*, 2(3):639–644, 2017.

[116] Bo Hu, Camden DeBruler, Zayn Rhodes, and T Leo Liu. Long-cycling aqueous organic redox flow battery (AORFB) toward sustainable and safe energy storage. *Journal of the American Chemical Society*, 139(3):1207–1214, 2017.

[117] Jian Luo, Wenda Wu, Camden Debruler, Bo Hu, Maowei Hu, and T Leo Liu. A 1.51 V pH neutral redox flow battery towards scalable energy storage. *Journal of Materials Chemistry A*, 7(15):9130–9136, 2019.

[118] Camden DeBruler, Bo Hu, Jared Moss, Jian Luo, and T Leo Liu. A sulfonate-functionalized viologen enabling neutral cation exchange, aqueous organic redox flow batteries toward renewable energy storage. *ACS Energy Letters*, 3(3):663–668, 2018.

[119] Bo Hu, Yijie Tang, Jian Luo, Grant Grove, Yisong Guo, and T Leo Liu. Improved radical stability of viologen anolytes in aqueous organic redox flow batteries. *Chemical communications*, 54(50):6871–6874, 2018.

[120] Camden DeBruler, Bo Hu, Jared Moss, Xuan Liu, Jian Luo, Yujie Sun, and T Leo Liu. Designer two-electron storage viologen anolyte materials for neutral aqueous organic redox flow batteries. *Chem*, 3(6):961–978, 2017.

[121] Lei Liu, Yanxin Yao, Zengyue Wang, and Yi-Chun Lu. Viologen radical stabilization by molecular spectators for aqueous organic redox flow batteries. *Nano Energy*, 84:105897, 2021.

[122] Margarita R Geraskina, Andrew S Dutton, Mark J Juetten, Samuel A Wood, and Arthur H Winter. The viologen cation radical pimer: A case of dispersion-driven bonding. *Angewandte Chemie*, 129(32):9563–9567, 2017.

[123] Margherita Venturi, Quinto G Mulazzani, and Morton Z Hoffman. Radiolytically-induced one-electron reduction of methyl viologen in aqueous solution: Stability of the radical cation in acidic and highly alkaline media (1). *Radiation Physics and Chemistry (1977)*, 23(1-2):229–236, 1984.

[124] Shijian Jin, Eric M Fell, Lucia Vina-Lopez, Yan Jing, P Winston Michalak, Roy G Gordon, and Michael J Aziz. Near neutral pH redox flow battery with low permeability and long-lifetime phosphonated viologen active species. *Advanced Energy Materials*, 10(20):2000100, 2020.

[125] Anne L Rieger and John O Edwards. Methyl viologen reactions. 5. rates and mechanism of cation-radical formation in aqueous base. *The Journal of Organic Chemistry*, 53(7):1481–1485, 1988.

[126] N Harsha Attanayake, Zhiming Liang, Yilin Wang, Aman Preet Kaur, Sean R Parkin, Justin K Mobley, Randy H Ewoldt, James Landon, and Susan A Odom. Dual function organic active materials for nonaqueous redox flow batteries. *Materials Advances*, 2(4):1390–1401, 2021.

[127] Zhiming Liang, Thilini M. Suduwella, N. Harsha Attanayake, Aman Preet Kaur, James Landon, and Susan A. Odom. A high energy density organic redox flow battery operated at -40C. *unpublished*, pages 5443–5451, 2020.

[128] Zhiming Liang, Rahul Kant Jha, Thilini Malsha Suduwella, N Harsha Attanayake, Yangyang Wang, Wei Zhang, Chuntian Cao, Aman Preet Kaur, James Landon, and Susan A Odom. A prototype of high-performance two-electron non-aqueous organic redox flow battery operated at-40° c. *Journal of Materials Chemistry A*, 2022.

[129] Yanxin Yao, Jiafeng Lei, Yang Shi, Fei Ai, and Yi-Chun Lu. Assessment methods and performance metrics for redox flow batteries. *Nature Energy*, 6(6):582–588, 2021.

[130] DS Aaron, Q Liu, Z Tang, GM Grim, AB Papandrew, A Turhan, TA Zawodzinski, and MM Mench. Dramatic performance gains in vanadium redox flow batteries through modified cell architecture. *Journal of Power sources*, 206:450–453, 2012.

[131] Jeffrey A Kowalski, Bertrand J Neyhouse, and Fikile R Brushett. The impact of bulk electrolysis cycling conditions on the perceived stability of redox active materials. *Electrochemistry Communications*, 111:106625, 2020.

[132] Cedrik Wiberg, Thomas J Carney, Fikile Brushett, Elisabet Ahlberg, and Ergang Wang. Dimerization of 9, 10-anthraquinone-2, 7-disulfonic acid (AQDS). *Electrochimica Acta*, 317:478–485, 2019.

[133] David G Kwabi, Yunlong Ji, and Michael J Aziz. Electrolyte lifetime in aqueous organic redox flow batteries: a critical review. *Chemical Reviews*, 120(14):6467–6489, 2020.

[134] Robert De Levie. On porous electrodes in electrolyte solutions: I. capacitance effects. *Electrochimica Acta*, 8(10):751–780, 1963.

[135] Ting Hei Wan, Mattia Saccoccio, Chi Chen, and Francesco Ciucci. Influence of the discretization methods on the distribution of relaxation times deconvolution: implementing radial basis functions with drttools. *Electrochimica Acta*, 184:483–499, 2015.

[136] Francesco Ciucci and Chi Chen. Analysis of electrochemical impedance spectroscopy data using the distribution of relaxation times: A bayesian and hierarchical bayesian approach. *Electrochimica Acta*, 167:439–454, 2015.

[137] Mohammed B Effat and Francesco Ciucci. Bayesian and hierarchical bayesian based regularization for deconvolving the distribution of relaxation times from electrochemical impedance spectroscopy data. *Electrochimica Acta*, 247:1117–1129, 2017.

[138] Grzegorz Greczynski and Lars Hultman. A step-by-step guide to perform x-ray photoelectron spectroscopy. *Journal of Applied Physics*, 132(1):011101, 2022.

[139] Noémie Elgrishi, Kelley J Rountree, Brian D McCarthy, Eric S Rountree, Thomas T Eisenhart, and Jillian L Dempsey. A practical beginner's guide to cyclic voltammetry. *Journal of Chemical Education*, 95(2):197–206, 2018.

[140] Allen J Bard, Larry R Faulkner, Johna Leddy, and Cynthia G Zoski. *Electrochemical methods: fundamentals and applications*, volume 2. wiley New York, 1980.

[141] Jarrod David Milshtein. *Electrochemical engineering of low-cost and high-power redox flow batteries*. PhD thesis, Massachusetts Institute of Technology, 2017.

[142] Vitaly V Pavlishchuk and Anthony W Addison. Conversion constants for redox potentials measured versus different reference electrodes in acetonitrile solutions at 25 c. *Inorganica Chimica Acta*, 298(1):97–102, 2000.

[143] Matthew D Murbach, Brian Gerwe, Neal Dawson-Elli, and Lok-kun Tsui. impedance. py: A python package for electrochemical impedance analysis. *Journal of Open Source Software*, 5(52):2349, 2020.

[144] Aaron A Shinkle, Alice ES Sleightholme, Lucas D Griffith, Levi T Thompson, and Charles W Monroe. Degradation mechanisms in the non-aqueous vanadium acetylacetonate redox flow battery. *Journal of Power Sources*, 206:490–496, 2012.

[145] Aaron A Shinkle, Timothy J Pomaville, Alice ES Sleightholme, Levi T Thompson, and Charles W Monroe. Solvents and supporting electrolytes for vanadium acetylacetonate flow batteries. *Journal of Power Sources*, 248:1299–1305, 2014.

[146] T Herr, J Noack, P Fischer, and J Tübke. 1, 3-dioxolane, tetrahydrofuran, acetylacetone and dimethyl sulfoxide as solvents for non-aqueous vanadium acetylacetonate redox-flow-batteries. *Electrochimica Acta*, 113:127–133, 2013.

[147] T Herr, P Fischer, J Tübke, K Pinkwart, and P Elsner. Increasing the energy density of the non-aqueous vanadium redox flow battery with the acetonitrile-1, 3-dioxolane–dimethyl sulfoxide solvent mixture. *Journal of Power Sources*, 265:317–324, 2014.

[148] Qinghua Liu, Alice ES Sleightholme, Aaron A Shinkle, Yongdan Li, and Levi T Thompson. Non-aqueous vanadium acetylacetonate electrolyte for redox flow batteries. *Electrochemistry Communications*, 11(12):2312–2315, 2009.

[149] James D Saraidaridis and Charles W Monroe. Nonaqueous vanadium disproportionation flow batteries with porous separators cycle stably and tolerate high current density. *Journal of Power Sources*, 412:384–390, 2019.

[150] M Asri Nawi and Thomas L Riechel. Electrochemical studies of vanadium (III) and vanadium (IV) acetylacetonate complexes in dimethylsulfoxide. *Inorganic Chemistry*, 20(7):1974–1978, 1981.

[151] Aaron A Shinkle, Alice ES Sleightholme, Levi T Thompson, and Charles W Monroe. Electrode kinetics in non-aqueous vanadium acetylacetonate redox flow batteries. *Journal of Applied Electrochemistry*, 41(10):1191–1199, 2011.

[152] James D Saraidaridis, Bart M Bartlett, and Charles W Monroe. Spectroelectrochemistry of vanadium acetylacetonate and chromium acetylacetonate for symmetric nonaqueous flow batteries. *Journal of The Electrochemical Society*, 163(7):A1239, 2016.

[153] Mitsutaka Kitamura, Kazuo Yamashita, and Hideo Imai. Studies on the electrode processes of oxovanadium (IV). II. electrolytic reduction of vanadyl acetylacetonate in acetonitrile solution at mercury electrode. *Bulletin of the Chemical Society of Japan*, 49(1):97–100, 1976.

[154] Ronald E Hester and Robert A Plane. Metal-oxygen bonds in complexes: Raman spectra of trisacetylacetonato and trisoxalato complexes of aluminum, gallium, and indium. *Inorganic Chemistry*, 3(4):513–517, 1964.

[155] EE Ernstbrunner. Vibrational spectra of acetylacetone and its anion. *Journal of the Chemical Society A: Inorganic, Physical, Theoretical*, pages 1558–1561, 1970.

[156] Enrique Ortí, Pedro M Viruela, Rafael Viruela, Franz Effenberger, Víctor Hernández, and Juan T López Navarrete. Raman and theoretical study of the solvent effects on the sizable intramolecular charge transfer in the pushpull 5-(dimethylamino)-5 '-nitro-2, 2 '-bithiophene. *The Journal of Physical Chemistry A*, 109(39):8724–8731, 2005.

[157] ERE Mojica, N Abbas, LO Wyan, J Vedad, and RZB Desamero. Raman spectroscopy in the undergraduate curriculum. *American Chemical Society*, 1305:181–197, 2018.

[158] Blanka Vlčková, Bohuslav Strauch, and Milan Horák. Measurement and interpretation of infrared and Raman spectra of vanadyl acetylacetonate. *Collection of Czechoslovak chemical communications*, 52(3):686–695, 1987.

[159] Jens Noack, Nataliya Roznyatovskaya, Jessica Kunzendorf, Maria SkyllasKazacos, Chris Menictas, and Jens Tübke. The influence of electrochemical treatment on electrode reactions for vanadium redox-flow batteries. *Journal of energy chemistry*, 27(5):1341–1352, 2018.

[160] Susan M Taylor, Alexandra Pătru, Daniel Streich, Mario El Kazzi, Emiliana Fabbri, and Thomas J Schmidt. Vanadium (V) reduction reaction on modified glassy carbon electrodes–role of oxygen functionalities and microstructure. *Carbon*, 109:472–478, 2016.

[161] Philipp S Borchers, Maria Strumpf, Christian Friebe, Ivo Nischang, Martin D Hager, Johannes Elbert, and Ulrich S Schubert. Aqueous redox flow battery suitable for high temperature applications based on a tailor-made ferrocene copolymer. *Advanced Energy Materials*, 10(41):2001825, 2020.

[162] Dandan Chu, Xin Li, and Shu Zhang. A non-isothermal transient model for a metal-free quinone–bromide flow battery. *Electrochimica Acta*, 190:434–445, 2016.

[163] Cheunho Chu, Byeong Wan Kwon, Wonmi Lee, and Yongchai Kwon. Effect of temperature on the performance of aqueous redox flow battery using carboxylic acid functionalized alloxazine and ferrocyanide redox couple. *Korean Journal of Chemical Engineering*, 36(10):1732–1739, 2019.

[164] Jiancong Xu, Shuai Pang, Xinyi Wang, Pan Wang, and Yunlong Ji. Ultrastable aqueous phenazine flow batteries with high capacity operated at elevated temperatures. *Joule*, 5(9):2437–2449, 2021.

[165] G Heim. Tensions de vapeur et chaleurs latentes des vaporisation de quelques nitriles normaux. *Bull. Soc. Chim. Belg*, 42:467–482, 1933.

[166] Jill Chastain and Roger C King Jr. Handbook of X-ray photoelectron spectroscopy. *Perkin-Elmer Corporation*, 40:221, 1992.

[167] Robert M Darling and Mike L Perry. The influence of electrode and channel configurations on flow battery performance. *Journal of The Electrochemical Society*, 161(9):A1381, 2014.

[168] Robert M Darling. Techno-economic analyses of several redox flow batteries using levelized cost of energy storage. *Current Opinion in Chemical Engineering*, 37:100855, 2022.

[169] Alexis M Fenton, Rahul Kant Jha, Bertrand J Neyhouse, Aman Preet Kaur, Daniel A Dailey, Susan A Odom, and Fikile R Brushett. On the challenges of materials and electrochemical characterization of concentrated electrolytes for redox flow batteries. *Journal of Materials Chemistry A*, 10(35):17988–17999, 2022.

[170] Ilya A Shkrob, Lily A Robertson, Zhou Yu, Rajeev S Assary, Lei Cheng, Lu Zhang, Erik Sarnello, Xinyi Liu, Tao Li, Aman Preet Kaur, et al. Crowded electrolytes containing redoxmers in different states of charge: Solution structure, properties, and fundamental limits on energy density. *Journal of Molecular Liquids*, 334:116533, 2021.

[171] Thomas J Carney, Steven J Collins, Jeffrey S Moore, and Fikile R Brushett. Concentration-dependent dimerization of anthraquinone disulfonic acid and its impact on charge storage. *Chemistry of Materials*, 29(11):4801–4810, 2017.

[172] Ilya A Shkrob, Tao Li, Erik Sarnello, Lily A Robertson, Yuyue Zhao, Hossam Farag, Zhou Yu, Jingjing Zhang, Sambasiva R Bheemireddy, Rajeev S Assary, et al. Self-assembled solute networks in crowded electrolyte solutions and nanoconfinement of charged redoxmer molecules. *The Journal of Physical Chemistry B*, 124(45):10226–10236, 2020.

[173] Gavvalapalli Nagarjuna, Jingshu Hui, Kevin J Cheng, Timothy Lichtenstein, Mei Shen, Jeffrey S Moore, and Joaquín Rodríguez-López. Impact of redox-active polymer molecular weight on the electrochemical properties and transport across porous separators in nonaqueous solvents. *Journal of the American Chemical Society*, 136(46):16309–16316, 2014.

[174] Elena C Montoto, Gavvalapalli Nagarjuna, Jingshu Hui, Mark Burgess, Nina M Sekerak, Kenneth Hernández-Burgos, Teng-Sing Wei, Marissa Kneer, Joshua Grolman, Kevin J Cheng, et al. Redox active colloids as discrete energy storage carriers. *Journal of the American Chemical Society*, 138(40):13230–13237, 2016.

[175] Mark Burgess, Etienne Chénard, Kenneth Hernández-Burgos, Gavvalapalli Nagarjuna, Rajeev S Assary, Jingshu Hui, Jeffrey S Moore, and Joaquín Rodríguez-López. Impact of backbone tether length and structure on the electrochemical performance of viologen redox active polymers. *Chemistry of Materials*, 28(20):7362–7374, 2016.

[176] Jiashu Yuan, Zheng-Ze Pan, Yun Jin, Qianyuan Qiu, Cuijuan Zhang, Yicheng Zhao, Yongdan Li, et al. Membranes in non-aqueous redox flow battery. 2021.

[177] Susan Odom. Preventing crossover in redox flow batteries through active material oligomerization, 2018.

[178] Koen H Hendriks, Sophia G Robinson, Miles N Braten, Christo S Sevov, Brett A Helms, Matthew S Sigman, Shelley D Minteer, and Melanie S Sanford. High-performance oligomeric catholytes for effective macromolecular separation in nonaqueous redox flow batteries. *ACS central science*, 4(2):189–196, 2018.

[179] Sean E Doris, Ashleigh L Ward, Artem Baskin, Peter D Frischmann, Nagarjuna Gavvalapalli, Etienne Chénard, Christo S Sevov, David Prendergast, Jeffrey S Moore, and Brett A Helms. Macromolecular design strategies for preventing active-material crossover in non-aqueous all-organic redox-flow batteries. *Angewandte Chemie*, 129(6):1617–1621, 2017.

[180] Eunhae Cho and Jongok Won. Novel composite membrane coated with a poly (diallyldimethylammonium chloride)/urushi semi-interpenetrating polymer network for non-aqueous redox flow battery application. *Journal of Power Sources*, 335:12–19, 2016.

[181] Sung-Jun Gong, Dongyoung Kim, Eunhae Cho, Seung Sang Hwang, and Jongok Won. A chitosan/urushi anion exchange membrane for a non–aqueous redox flow battery. *ChemistrySelect*, 2(5):1843–1849, 2017.

[182] Dongyoung Kim, Jungho Song, and Jongok Won. Structural effects of anion exchange composite membranes in non-aqueous redox flow batteries. *Journal of Membrane Science*, 564:523–531, 2018.

[183] Sergiu Spataru, Peter Hacke, and Michael Owen-Bellini. Combined-accelerated stress testing system for photovoltaic modules. In *2018 IEEE 7th World Conference on Photovoltaic Energy Conversion (WCPEC)(A Joint Conference of 45th IEEE PVSC, 28th PVSEC & 34th EU PVSEC)*, pages 3943–3948. IEEE, 2018.

[184] Peter L Hacke. Development of combined and sequential accelerated stress testing for derisking photovoltaic modules. Technical report, National Renewable Energy Lab.(NREL), Golden, CO (United States), 2019.

[185] Olivier Haillant. Accelerated weathering testing principles to estimate the service life of organic pv modules. *Solar Energy Materials and Solar Cells*, 95(5):1284–1292, 2011.

[186] Feng Leng, Cher Ming Tan, and Michael Pecht. Effect of temperature on the aging rate of li ion battery operating above room temperature. *Scientific reports*, 5(1):1–12, 2015.

[187] AJ Smith, JC Burns, and JR Dahn. A high precision study of the coulombic efficiency of li-ion batteries. *Electrochemical and Solid-State Letters*, 13(12):A177, 2010.

[188] JC Burns, Adil Kassam, NN Sinha, LE Downie, Lucie Solnickova, BM Way, and JR Dahn. Predicting and extending the lifetime of li-ion batteries. *Journal of The Electrochemical Society*, 160(9):A1451, 2013.

Appendix A

Parts lists for each RFB system

Table A.1: List of parts used in vanadium acetylacetonate flow batteries

Part	Vendor	Item description	Part number	Quantity
Endplate	McMaster-Carr	Milled from 3/4" thick polypropylene sheets	8742K144	2
O-ring	McMaster-Carr	Extreme-chemical Kalrez 4079 o-ring, dash number 014	9568K19	4
Flow field/current collector	GraphiteStore	Milled from impervious bipolar graphite plates, 1/4" thick	MW001198	2
Gaskets	McMaster-Carr	Punched from Teflon PTFE film, 0.015" thick	8569K21	2
Electrodes	Fuel cell store	SGL 39AA carbon electrodes, $280\mu m$ thick, 1.4 x 1.6 cm	1592017	4
Separator	Daramic	PET based microporous separator, 175 μm thick	Daramic 175	1 sq-inch
Cell fittings	McMaster-Carr	Polypropylene straight adapter (1/8" male NPT to 1/8" hose barb)	5121K371	4
Cell fastenings	n/a	Flat/cap socked 1/4 - 28 bolts (3 inches long) and nuts	n/a	4
Alignment pins	McMaster-Carr	FEP Rod 1/8" diameter	85325K14	4

Pump tubing	Cole Parmer	Masterflex Norprene tubing (A-60-G), L/S 16	06404-16	16 inches
Transport tubing	Cole parmer	Masterflex Norprene tubing (A-60-G), L/S 16	06404-16	16 inches
Reservoirs	VWR	20 mL borosilicate glass vials with PTFE lined caps	66065-602	2
Peristaltic pump	Cole-parmer	Masterflex Digital economy drive (10 - 600 rpm)	7524-40	1
Pump heads	Cole-parmer	Masterflex Easy load pump heads	7518-10	2
Thread sealant tape	McMaster-Carr	Pipe Thread Sealant Tape, 0.0028" thick x 1/2" wide	4591K12	40 cm

Table A.2: List of parts used in aqueous 2,6-DPPEAQ flow batteries

Part	Vendor	Item description	Part number	Quantity
Endplate	McMaster-Carr	Milled from 3/4" thick polypropylene sheets	8742K144	2
O-ring	McMaster-Carr	Extreme-chemical Kalrez 4079 o-ring, dash number 014	9568K19	4

Flow field/current collector	GraphiteStore	Milled from impervious bipolar graphite plates, 1/4" thick	MW001198	2
Gaskets (trial 3)	McMaster-Carr	Punched from Teflon PTFE film, 0.03" thick	8569K21	2
Gaskets (trial 4-5)	Fuel cell store	Punched from EPDM film, 0.03" thick	590763	2
Electrodes	Fuel cell store	SGL 39AA carbon electrodes, $280\mu m$ thick, 1.4 x 1.6 cm	1592017	8
Separator	fumatech	Potassium ion exchange membrane, 20 μm thick, not reinforced	Fumasep E-620 (K)	1 sq-inch
Cell fittings	Cole Parmer	Polypropylene straight and elbow adapter (1/8" compression to 1/8" NPT)	RK-06386-05 and RK-06385-05	4
Cell fastenings	n/a	Flat/cap socked 1/4 - 28 bolts (3 inches long) and nuts	n/a	4
Alignment pins	McMaster-Carr	FEP Rod 1/8" diameter	85325K14	4
Pump tubing	Cole Parmer	Masterflex Norprene tubing (A-60-G), L/S 16	06404-16	16 inches
Transport tubing	McMaster-Carr	Teflon PTFE semi-clear tubing for chemicals	5239K24	60 inches
Reducers	Cole Parmer	Polypropylene compression reducer (1/4" to 1/8")	RK-06381-05	4

Reservoirs	Savillex from Delta Scientific	22 and 60 mL PFA impingers	200-022-20, 200-060-20 and 600-033-26	2
Peristaltic pump	Cole-parmer	Masterflex Digital economy drive (10 - 600 rpm)	7524-40	1
Pump heads	Cole-parmer	Masterflex Easy load pump heads	7518-10	2
Thread sealant tape	McMaster-Carr	Pipe Thread Sealant Tape, 0.0028" thick x 1/2" wide	4591K12	40 cm

Table A.3: List of parts used in non-aqueous MEEPT-MEEV flow batteries (room temperature and high temperature)

Part	Vendor	Item description	Part number	Quantity
Endplate	McMaster-Carr	Milled from 3/4" thick polypropylene sheets	8742K144	2
O-ring	McMaster-Carr	Extreme-chemical Kalrez 4079 o-ring, dash number 014	9568K19	4
Flow field/current collector	GraphiteStore	Milled from impervious bipolar graphite plates, 1/4" thick	MW001198	2
Gaskets	McMaster-Carr	Punched from EPDM rubber sheet, 0.015" thick	8610K61	2

Electrodes	Fuel cell store	SGL 39AA carbon electrodes, 280μm thick, 1.4 x 1.6 cm	1592017	4
Separator	Daramic	PET based microporous separator, 175 μm thick	Daramic 175	1 sq-inch
Cell fittings	Cole Parmer	Polypropylene straight and elbow adapter (1/8" compression to 1/8" NPT)	RK-06386-05 and RK-06385-05	4
Cell fastenings	n/a	Flat/cap socked 1/4 - 28 bolts (3 inches long) and nuts	n/a	4
Alignment pins	McMaster-Carr	FEP Rod 1/8" diameter	85325K14	4
Pump tubing	Cole Parmer	Masterflex Norprene tubing (A-60-G), L/S 16	06404-16	16 inches
Transport tubing	McMaster-Carr	Teflon PTFE semi-clear tubing for chemicals	5239K24	60 inches
Reducers	Cole Parmer	Polypropylene compression reducer (1/4" to 1/8")	RK-06381-05	4
Reservoirs	Savillex from Delta Scientific	22 mL PFA impingers	200-022-20 and 600-033-26	2
Peristaltic pump	Cole-parmer	Masterflex Digital economy drive (10 - 600 rpm)	7524-40	1
Pump heads	Cole-parmer	Masterflex Easy load pump heads	7518-10	2

Thread sealant tape	McMaster-Carr	Pipe Thread Sealant Tape, 0.0028" thick x 1/2" wide	4591K12	40 cm
Heaters	Omega	10 W and 40 W flexible silicone adhesive heaters	SRMU100101-P and SRMU100202-P	1

Table A.4: List of parts used in low temperature MEEPT-MEEV flow batteries

Part	Vendor	Item description	Part number	Quantity
Endplate	McMaster-Carr	Milled from 3/4" thick polypropylene sheets	8742K144	2
O-ring	McMaster-Carr	Extreme-chemical Kalrez 4079 o-ring, dash number 014	9568K19	4
Flow field/current collector	GraphiteStore	Milled from impervious bipolar graphite plates, 1/4" thick	MW001198	2
Gaskets	McMaster-Carr	Punched from EPDM rubber sheet, 0.015" thick	8610K61	2
Electrodes	Fuel cell store	SGL 39AA carbon electrodes, 280μm thick, 1.4 x 1.6 cm	1592017	4

Separator	Daramic	PET based microporous separator, 175 μm thick	Daramic 175	1 sq-inch
Cell fittings	McMaster-Carr	Polypropylene straight adapter (1/16" male NPT to 1/16" hose barb)	53415K261	4
Cell fastenings	n/a	Flat/cap socked 1/4 - 28 bolts (3 inches long) and nuts	n/a	4
Alignment pins	McMaster-Carr	FEP Rod 1/8" diameter	85325K14	4
Pump tubing	McMaster-Carr	Tygon abrasion-resistant tubing for chemicals (A-60-G), 1/16" ID and 3/6" OD	51075K21	32 inches
Transport tubing	McMaster-Carr	Tygon abrasion-resistant tubing for chemicals (A-60-G), 1/16" ID and 3/6" OD	51075K21	60 inches
Connectors	McMaster-Carr	Polypropylene straight tubing connectors, 1/16"	5121K191	4
Reservoirs	VWR	20 mL borosilicate glass vials with PTFE lined caps	66065-602	2
Peristaltic pump	Cole-parmer	Masterflex Digital economy drive (10 - 600 rpm)	7524-40	1
Pump heads	Cole-parmer	Masterflex standard pump head for precision tubing, L/S 14	07014-20	2

Thread sealant tape	McMaster-Carr	Pipe Thread Sealant Tape, 0.0028" thick x 1/2" wide	4591K12	40 cm

Appendix B

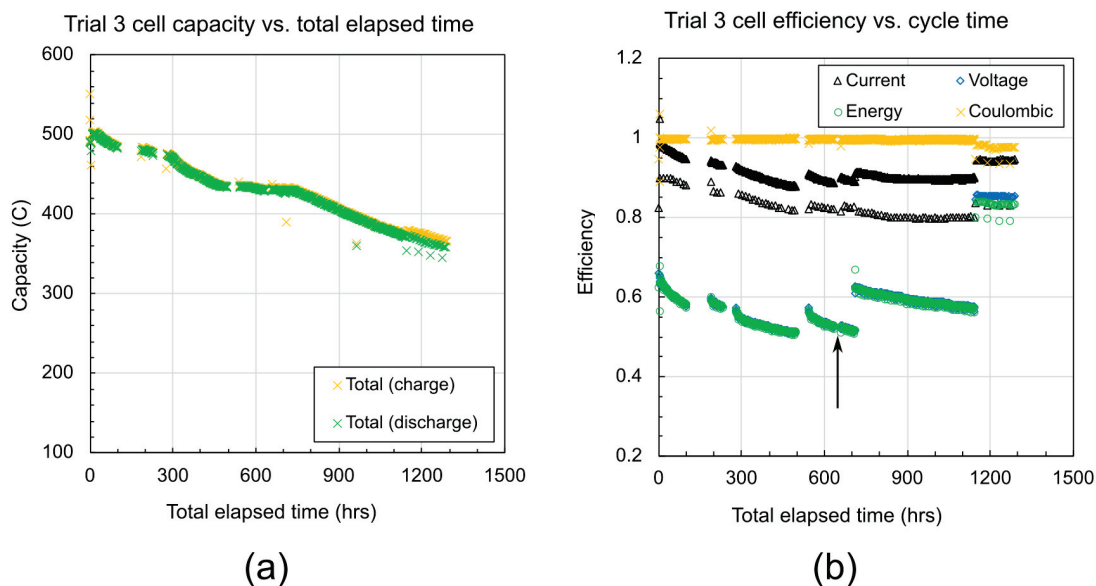# Chapter 6 Supplementary Figures

B.1 Trial 3 cycling data

Figure B.1: Figure illustrating the capacity loss (a) and cell efficiency (b) for a 2,6-DPPEAQ/ferrocyanide flow cell as a function of total elapsed time. Capacity loss in this trial was dominated by electrolyte leakage from o-rings, gaskets and fittings. The discontinuities in voltage efficiency occurred due to corrosion of test leads and issues with the 4-wire measurement set-up. After each power outage the test leads were cleaned before cycling resumed. The arrow indicates a brief power outage where the test leads were not cleaned before resuming cycling.

Figure B.1 shows the cell capacity (a) and efficiency for the trial 3 cell as a function of time (b). Over the course of 60 days the total cell capacity dropped from 518 C to 366 C – a loss of about 29 %. After 1 – 2 weeks of cycling, it became apparent that the capacity loss was attributed to electrolyte leakage. Figure B.2a gives an image of the external cell body (after cycling for nearly 2 months), showing significant accumulation of leaked electrolyte on the graphite plates and tabs (where test connections were made). Figure B.2b compares the negolyte volume harvested from the cell (left) with 5.5 mL (the original volume) of uncycled electrolyte on the right. This image qualitatively shows that approximately 20 –25 % of the negolyte volume was lost to leakage, which would account for a significant portion of the capacity loss. Electrolyte leakage issues were rectified by improving o-ring seating in the cell endplates (as described in sections 4.1.2 and 6.3) and by replacing the PTFE gaskets with EPDM, which conforms better to surface textures than PTFE. The issues with contact resistance (described in the following section) were fixed by using stainless steel washers (to contact the graphite tabs) and using an insulating plastic screw to connect the source and sense leads to the graphite tabs (as depicted in Figure 4.1).

The cell efficiency data in Figure B.1b exhibits several discontinuities in voltage and energy efficiency, which coincide with recorded power outages. The test leads were cleaned before cycling was restarted to remove residue from leaked electrolyte (which wicked up under the test leads). In contrast, when the test leads were not cleaned (indicated by the arrow in Figure B.1b), the voltage/energy efficiency continued to drop. This variable contact resistance is a significant source of error in cell efficiency data, and is likely responsible for the lower voltage/energy efficiency compared to published reports [2].

The cell efficiency data for the trial 3 cell is shown in Figure B.1(b). Accounting for the charge accessed during the constant voltage holds, the coulombic efficiency
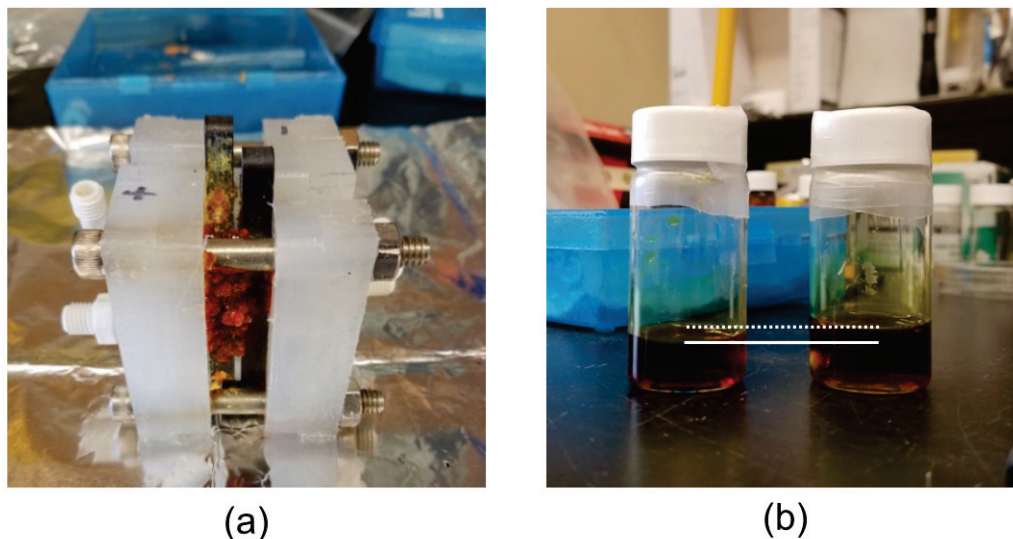
Figure B.2: Image depicting leaked electrolyte dried on the outside of the cell body (a). The image in (b) compares the volume loss between the cycled electrolyte (left) and an equivalent volume to the original electrolyte (right).

for the cell exceeds 99 % (when cycling at 100 mA cm^{-2}). However, the percentage of charge accessed during the constant-current phase of cycling only (here termed current efficiency) falls from 100 % to roughly 90 %. Meanwhile, the voltage efficiency decreases from about 66 % to 57 %. Taken together, the drop in current and voltage efficiency suggests that increased overpotential during cycling may prevent the full cell capacity from being accessed before the voltage limits are reached. (More evidence to support this hypothesis is presented in the discussion of electrochemical impedance data below and in the main chapter body). The current efficiency data falling below 90 % is an artefact of the EIS measurements, which were performed every 10th cycle. (To pre-condition the cell for each EIS measurement, the cell was held at 50 % SOC at constant-voltage as described in 4.2.2. The charge passed during this step is not accounted for in the current efficiency.)

After a total cycle duration of 1100 hours, the cell was cycled at 20 mA cm^{-2} to examine the effects of cycling rate. The coulombic efficiency dropped (to 97.5 %), which was consistent with expectations. At 20 mA cm^{-2} the cell takes five times more

slowly, which allows more time for self-discharge reactions such as membrane-crossover or oxidation of the reduced negolyte by ambient oxygen to occur. Meanwhile, the voltage efficiency increased from 57 % to 85 % as a result of reduced ohmic losses. The total energy efficiency for the cell cycling at 20 mA cm^{-2} was 83 %.
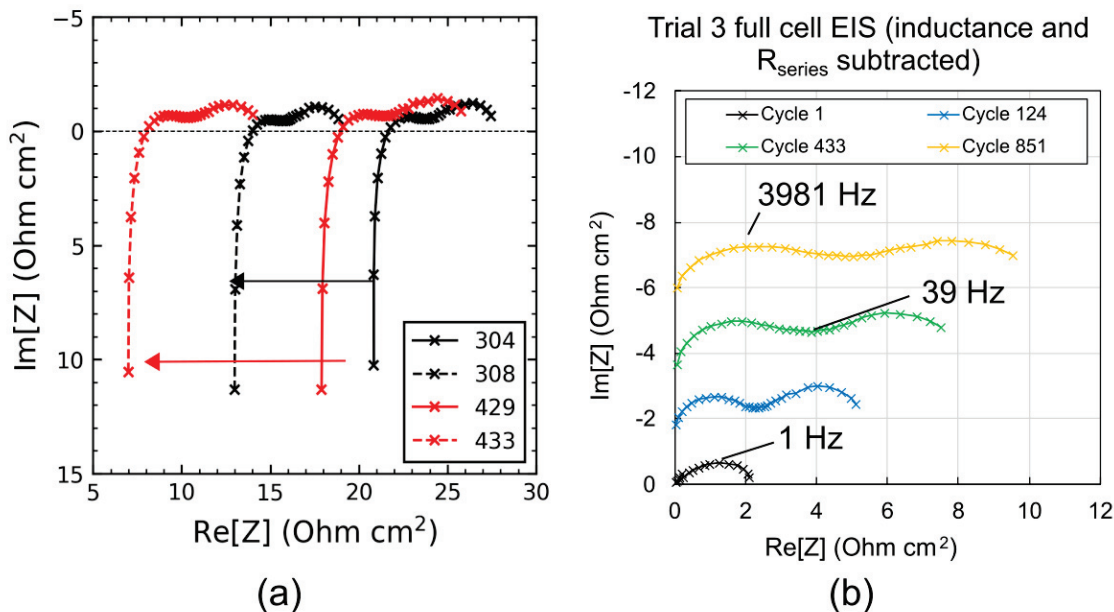

Figure B.3: Figure illustrating the effect of changing contact resistance on the full cell EIS spectra (a). The test leads were cleaned between cycles 304 and 308, as well as between 429 and 433. These cycles correspond to the discontinuities observed at 500 hrs and 700 hrs in Figure B.1b. The test leads were not cleaned between cycle 308 and 429. Nyquist plots for the full cell EIS measurements at different stages in cycling are shown in (b). The series resistance and inductance contributions to these spectra were subtracted. The cycle number for each spectrum is indicated in the legend. The area specific impedance labelled on the axes represent the total geometric area of the electrodes. The effective macroporous area is estimated to be 10 - 20x larger (based on geometric arguments involving the electrode mass, carbon fibre diameter, and density of graphite).

B.2 Preliminary EIS analysis

The variable contact resistance described in the previous section manifests as a shift in the high frequency intercept with the real impedance axis (Figure B.3(a)). This series resistance can easily be neglected while interpreting the following features.

206

Figure B.3(b) shows four impedance spectra where the series resistance and inductive contributions are subtracted from the data. The first cycle data shows very few visible features beyond a low frequency arc (fp = 1.0 Hz), which is attributed to mass-transfer effects. As described in section 3.2.2, this feature is consistent with a Warburg "short" behaviour, where electrolyte convection (in this case by pumping) is used to improve active species transport to/from the bulk electrolyte to a porous electrode surface. As the cell is cycled, a semi-circular feature appears at high frequencies (fp = 3981 Hz). We attribute this feature to charge-transfer effects. With continued cycling, the diameter of this feature grows, suggesting a growth in charge-transfer resistance. With continued cycling an additional feature also appears at mid-frequencies (39 Hz), and continues to grow in magnitude with cycling. The physical origin of the mid-frequency feature is still undetermined.
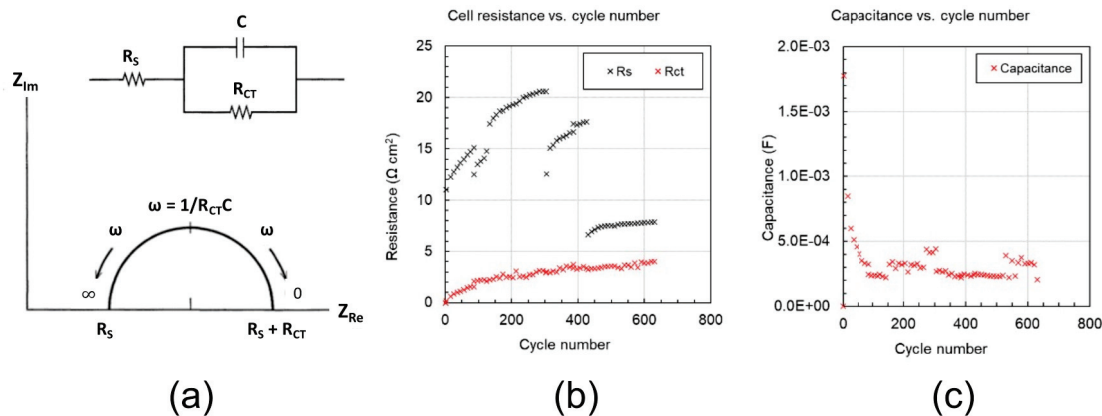

(a) (b) (c)

Figure B.4: A schematic of a Randles equivalent circuit and theoretical Nyquist plot is shown in (a). The area specific charge-transfer and series resistance determined from fitting the high-frequency feature in the full cell EIS data is shown in (b), and the capacitance is shown in (c). The area specific resistance is related to the total geometric area of the electrodes (20.4 cm^2), though the effective microporous area is estimated to by 10 - 20x larger.

Equivalent circuit fitting is a common method for extracting additional information from EIS data. One of the simplest circuits for modelling the electrode-solution interface is a Randles circuit (Figure B.4a), which appears as a semi-circle in the com-

plex impedance plane. The semi-circle diameter is indicative of the charge-transfer resistance to Faradaic processes (R_{ct}), and the peak frequency can be used to deduce the electrode capacitance. The equivalent circuit describes how the total current passing through the interface is a sum of the Faradaic (R_{ct}) and capacitive currents (C). The series resistance (R_s) encompasses factors such as electrode, contact and solution resistance. Fitting the high-frequency feature for our cell data, we see a monotonic growth in charge-transfer resistance by nearly 5 Ω cm^2 over the course of cycling. This is consistent with the magnitude of the high frequency feature observed in Figure B.3. Meanwhile, the cell capacitance appears to drop rapidly over the first 100 cycles, plateauing at approximately 20 µF after 200 cycles. The series resistance is variable, which results from the contact issues that were previously described.

It is important to recall that a Randles circuit models behaviour at a simplified electrolyte-solution interface, i.e. a single heterogeneous reaction at a planar electrode. In an operating flow cell a minimum of two charge-transfer reactions occur simultaneously (in different half-cells). Furthermore, a planar electrode model does not capture the macroscopic (and microscopic) porosity of the carbon paper electrodes, so we should not expect a single Randles element to capture all of the processes in an operating cell. In section 6.3.1 we present the framework for a more rigorous and physically informative analysis of impedance spectra for an operating RFB.

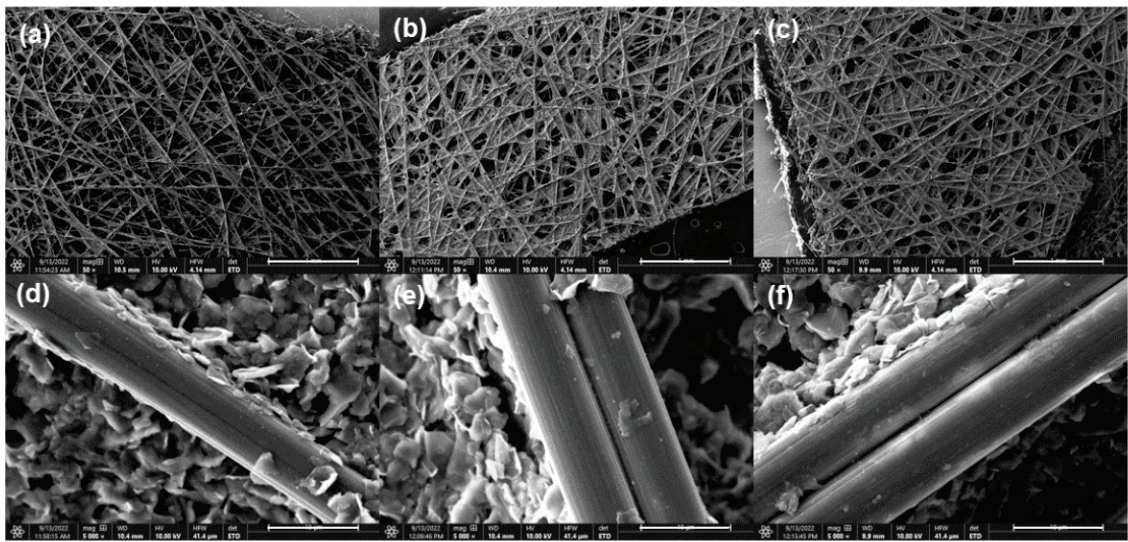## B.3   Post-cycling characterization

Figure B.5: SEM images of fresh electrodes (a,d), and electrodes stored in negolyte (b/e) and posolyte (c/f). The scale bars in the top row represent 1 mm, while the scale bars in the bottom row represent 10 μm.

Appendix C

Chapter 7 Supplementary Figures

Figure C.1: Figure illustrating the cell efficiency for a MEEPT-MEEV flow cell cycled at 24 °C. By convention, the current density (labelled) is referenced to the geometric area of the separator (2.24 cm^2). The current density was incremented every five cycles. Data for current densities ≥ 25 mA cm^{-2} are not shown as the cell immediately switched between charged and discharged states.
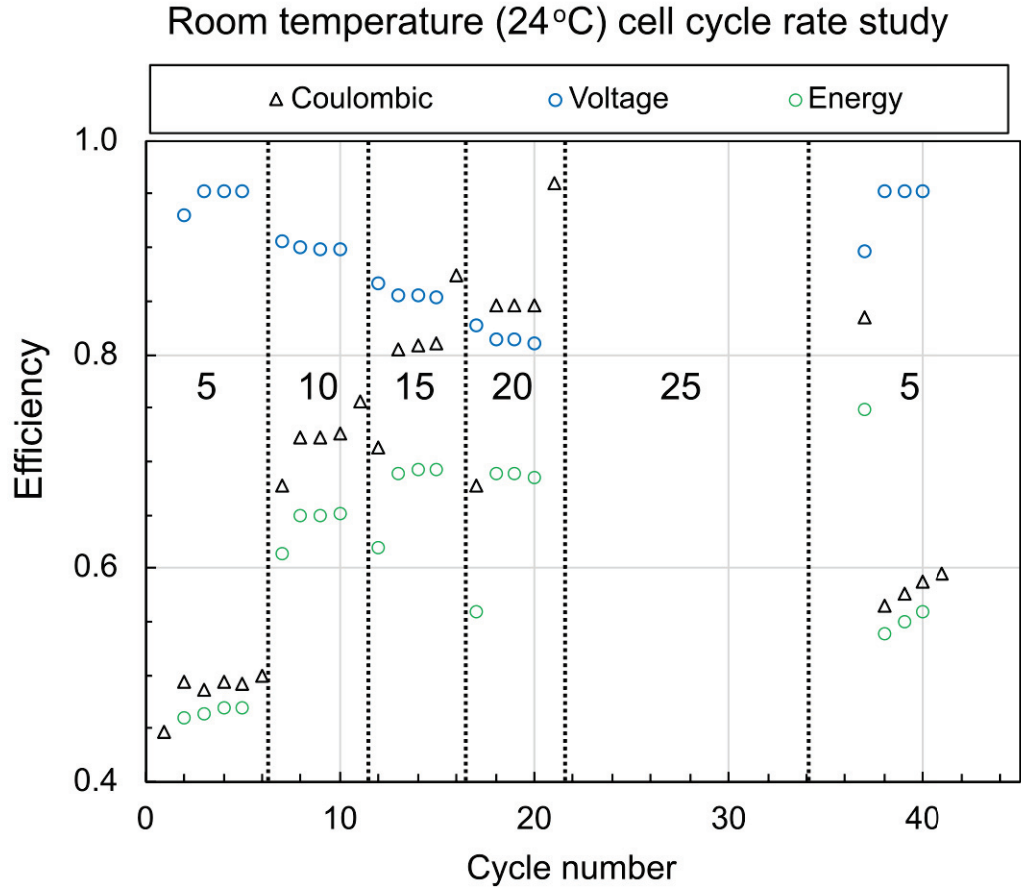
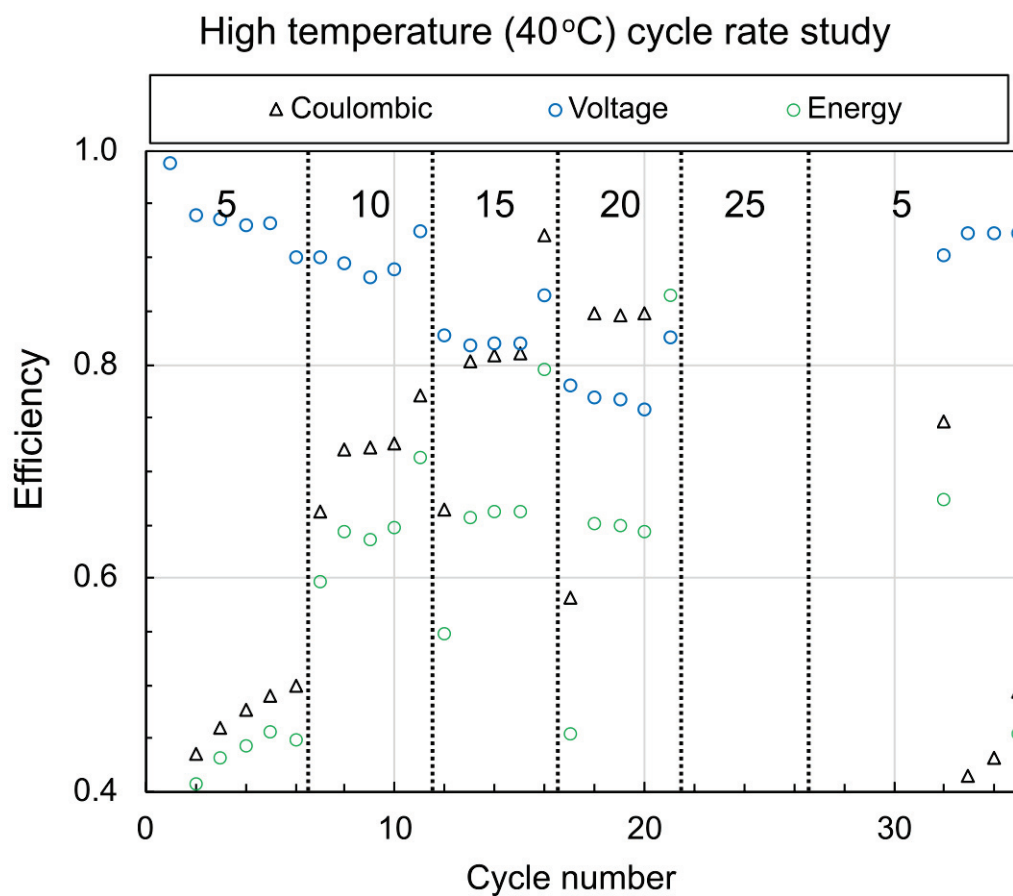Figure C.2: Figure illustrating the cell efficiency for a MEEPT-MEEV flow cell cycled at 40 °C. By convention, the current density (labelled) is referenced to the geometric area of the separator (2.24 cm^2). The current density was incremented every five cycles. Data for current densities $\geq$ 25 mA cm^{-2} are not shown as the cell immediately switched between charged and discharged states.
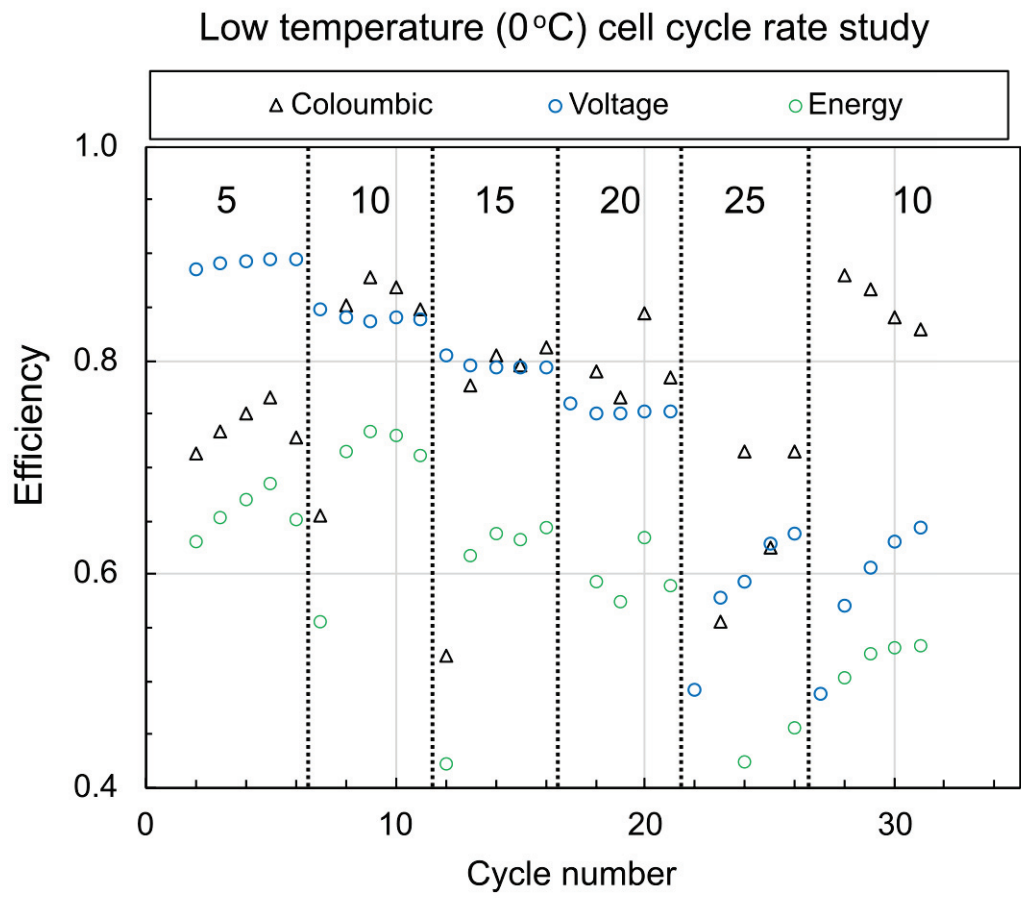
Figure C.3: Figure illustrating the cell efficiency for a MEEPT-MEEV flow cell cycled at 0 °C. The current density (labelled) was switched every five cycles.

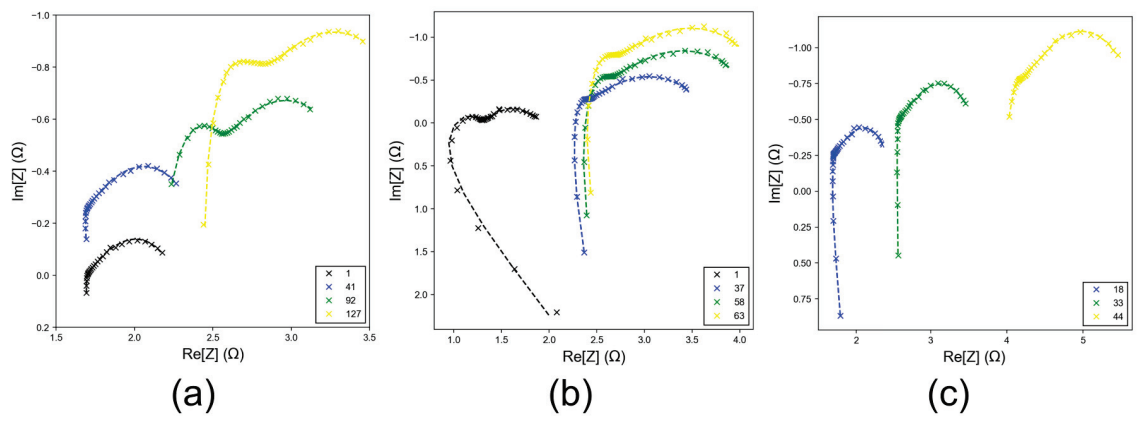Figure C.4: Equivalent circuit fits for MEEPT-MEEV cells cycled at room temperature (a) and high temperature (b) and (c).
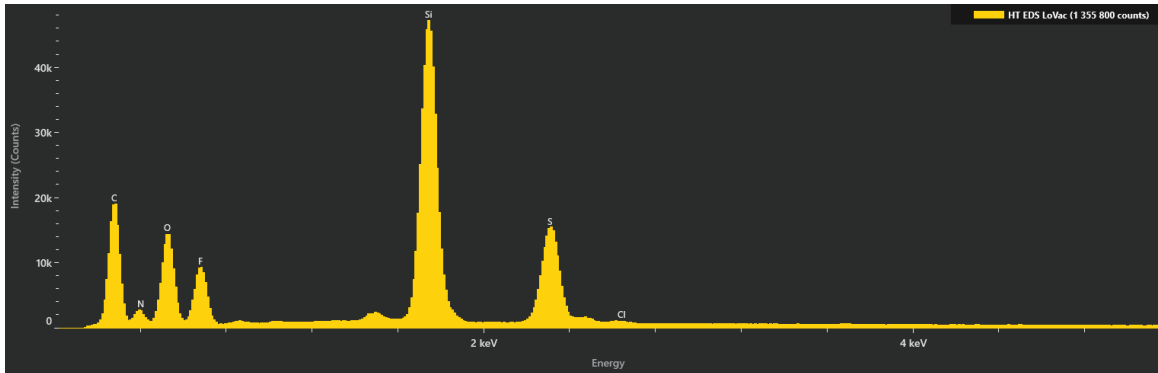
Figure C.5: Energy dispersive X-ray spectroscopy measured on the negative face of a separator cycled at high temperature.
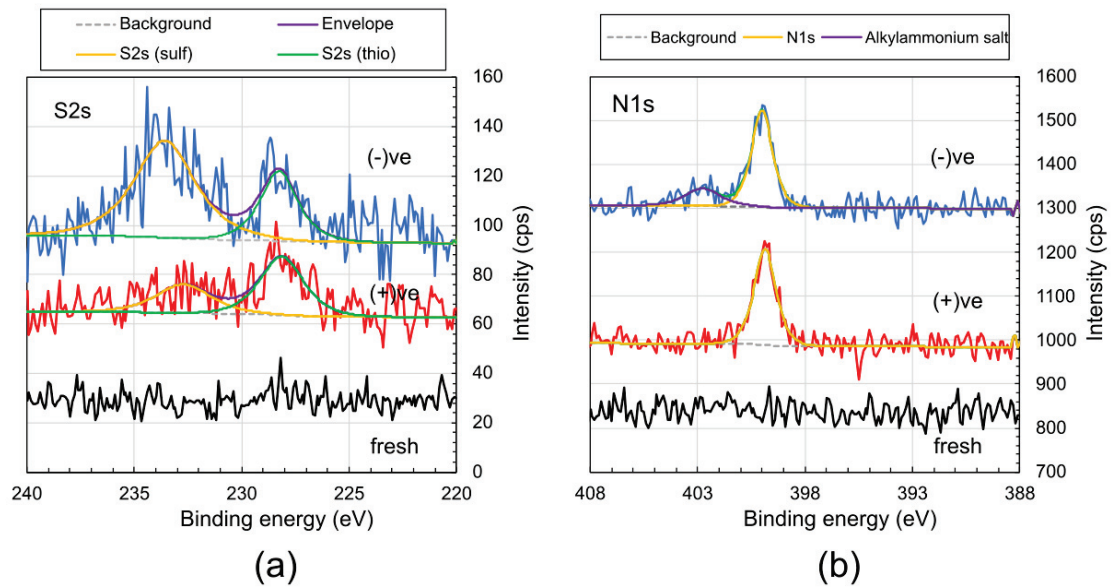
Figure C.6: High-resolution XPS spectra for S2s (a) and N1s (b) transitions observed on electrodes harvested from a MEEPT-MEEV flow cell that was cycled at room temperature.
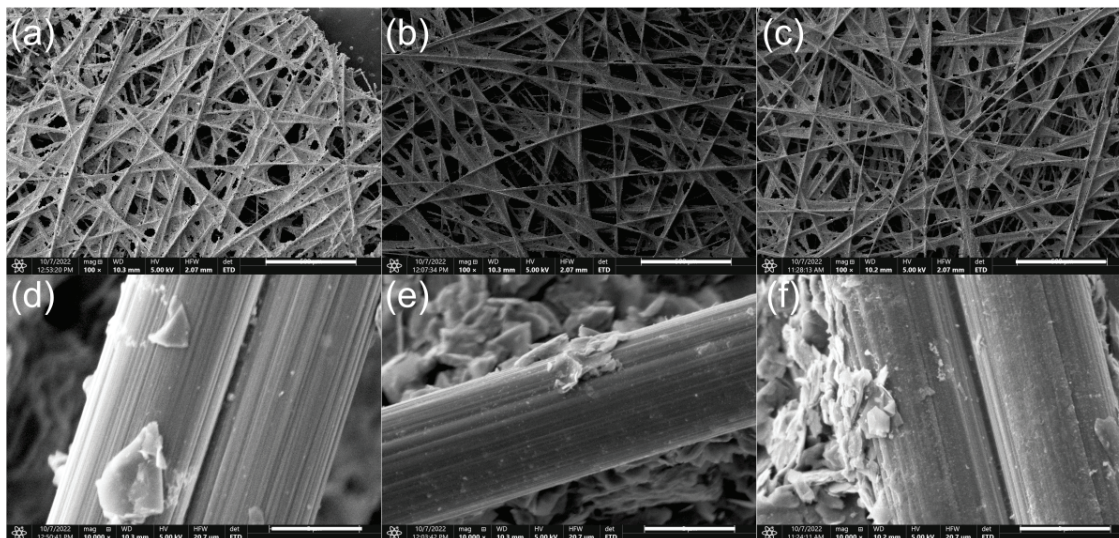
Figure C.7: SEM images of a carbon electrodes stored in MEEPT-MEEV electrolyte at room temperature (a/d), high temperature (b/e), and low temperature (c/f). The scale bars represent 500 μm in the top row, and 5 μm in the bottom row.
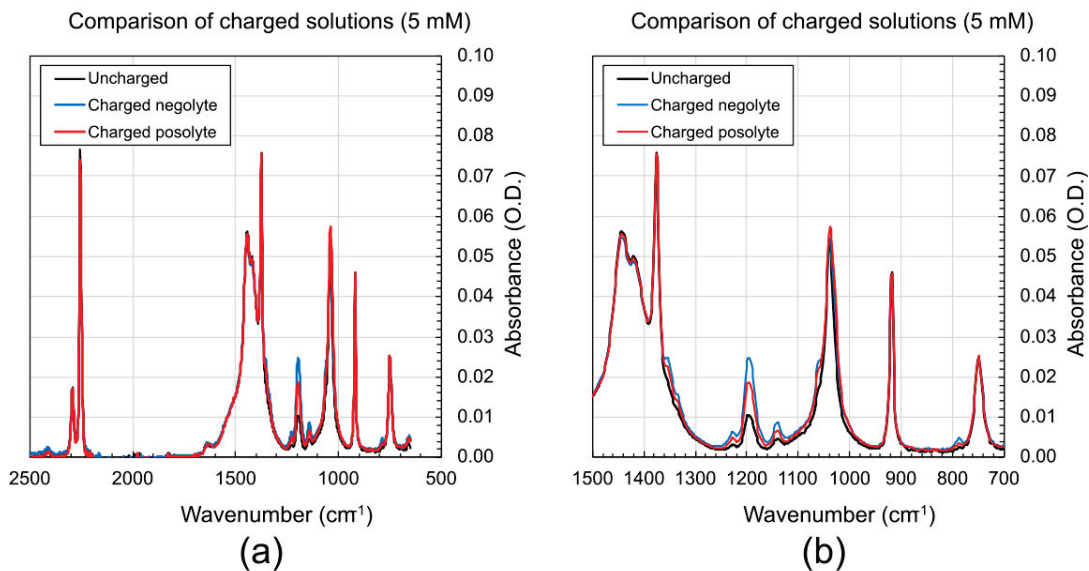
Figure C.8: FTIR spectra comparing charged and uncharged MEEPT-MEEV solutions. Both panels are identical, but the scale is altered in (b).
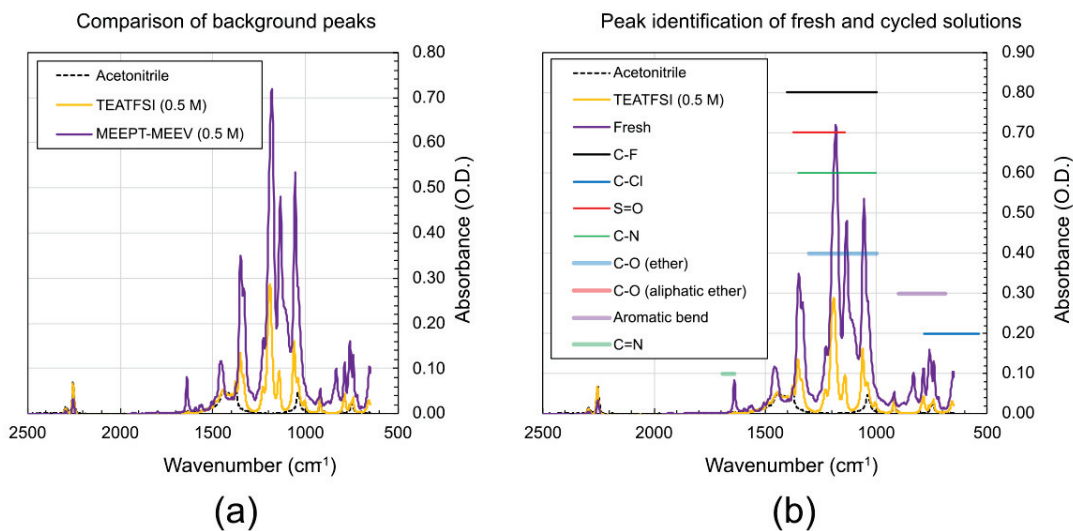
Figure C.9: FTIR spectra comparing background contributions of supporting electrolyte and solvent to an uncharged electrolyte spectrum. Commonly reported locations/ranges for listed vibrational modes are indicated in (b).
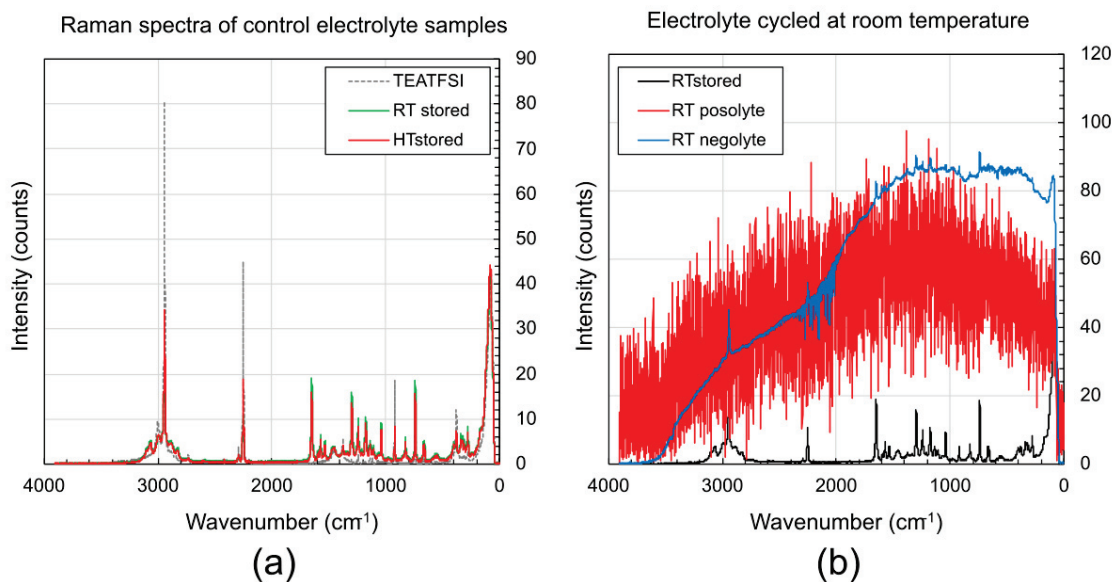
Figure C.10: Raman spectra for uncycled electrolyte samples (a), and electrolyte cycled at room temperature (b). All electrolyte solutions were discharged before harvesting.
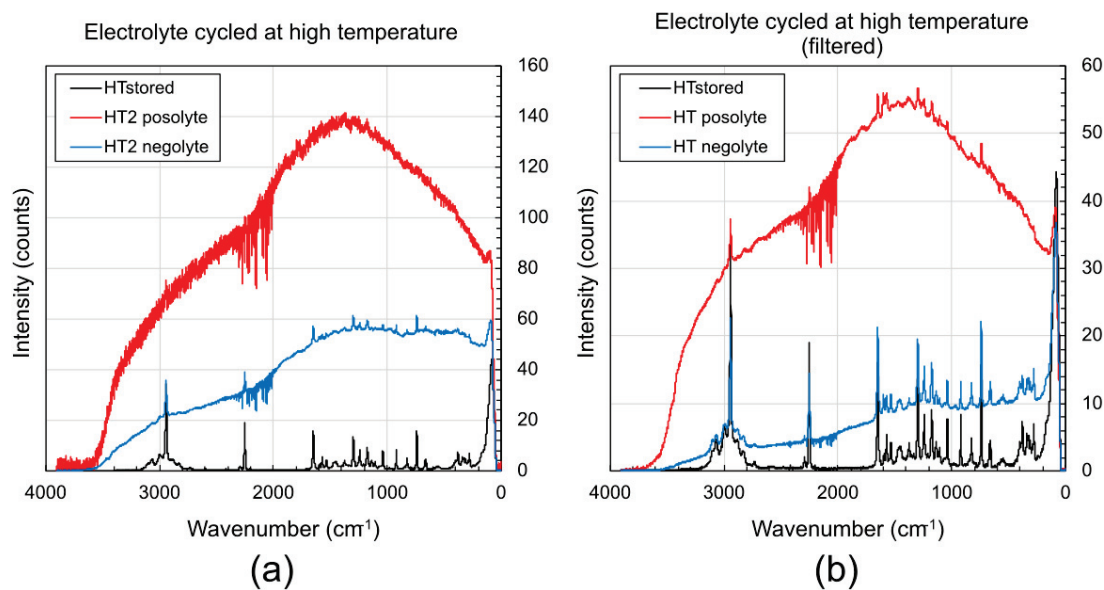
Figure C.11: Raman spectra comparing electrolyte cycled at high temperature with uncycled samples. The spectra in panel (a) are taken from electrolyte harvested directly from the cell. The spectra in panel (b) are taken from filtered electrolyte. All electrolyte solutions were discharged before harvesting.
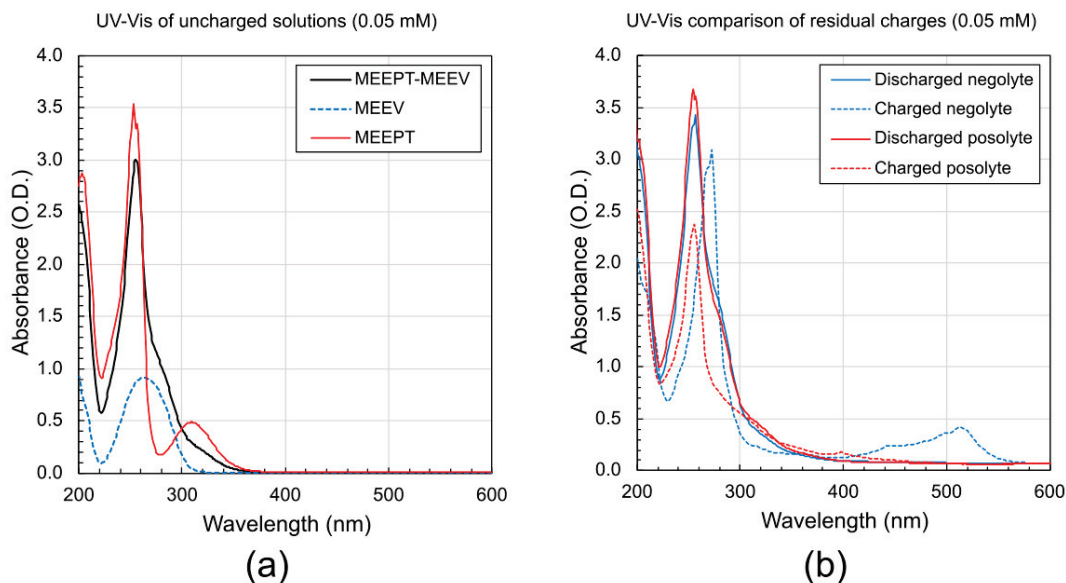
Figure C.12: UV-Vis spectra comparing uncharged electrolyte components used in MEEPT-MEEV flow cells (a). A comparison between charged, and uncharged negolyte/posolyte is shown in (b).
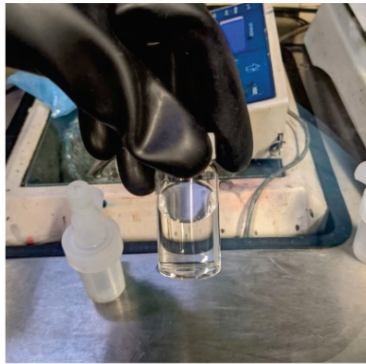
Uncharged 5 mM MEEPT-MEEV: faint
purple/weakly absorbing in visible

Charged 1x:negolyte (MEEV) is
blue/green, posolyte (MEEPT) is red
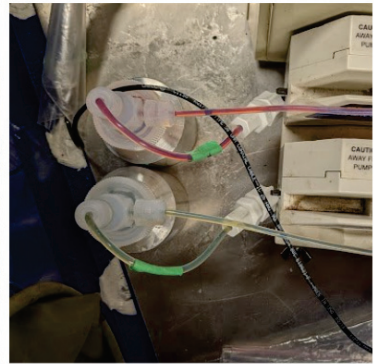
Charged4x: negolyte (MEEV) is less
saturated, posolyte (MEEPT) remains red

Figure C.13: Photographs of uncharged electrolyte, and electrolyte charged under ambient conditions.

Appendix D

Copyright Permissions

CCC Marketplace™

This is a License Agreement between Charlotte Clegg / Dalhousie University ("User") and Copyright Clearance Center, Inc. ("CCC") on behalf of the Rightsholder identified in the order details below. The license consists of the order details, the Marketplace Order General Terms and Conditions below, and any Rightsholder Terms and Conditions which are included below.

All payments must be made in full to CCC in accordance with the Marketplace Order General Terms and Conditions below.

Order Date	03-Oct-2022	Type of Use	Republish in a thesis/dissertation
Order License ID	1275139-1		
ISSN	1945-7111	Publisher	IOP Publishing
		Portion	Chapter/article

LICENSED CONTENT

Publication Title	Journal of the Electrochemical Society	Country	United States of America
		Rightsholder	IOP Publishing, Ltd
Author/Editor	Electrochemical Society.	Publication Type	e-Journal
Date	01/01/1948	URL	http://www.scitation.org/JES
Language	English		

REQUEST DETAILS

Portion Type	Chapter/article	Rights Requested	Main product and any product related to main product
Page range(s)	1-9		
Total number of pages	9		
Format (select all that apply)	Electronic	Distribution	Canada
		Translation	Original language of publication
Who will republish the content?	Academic institution	Copies for the disabled?	No
Duration of Use	Life of current edition	Minor editing privileges?	Yes
Lifetime Unit Quantity	Up to 499	Incidental promotional use?	No
		Currency	CAD

NEW WORK DETAILS

Title	Chapter title: Degradation in non-aqueous vanadium (III) acetylacetonate flow batteries	Institution name	Dalhousie University
		Expected presentation date	2022-12-01
Instructor name	Author: Charlotte Clegg		

ADDITIONAL DETAILS

Order reference number	N/A	The requesting person / organization to appear on the license	Charlotte Clegg / Dalhousie University

REUSE CONTENT DETAILS

Title, description or numeric reference of the portion(s)	Journal of the Electrochemical Society: Characterizing Degradation in Non-aqueous Vanadium(III) Acetylacetonate Redox Flow Batteries	Title of the article/chapter the portion is from	Characterizing Degradation in Non-aqueous Vanadium(III) Acetylacetonate Redox Flow Batteries
		Author of portion(s)	Electrochemical Society.
Editor of portion(s)	n/a	Issue, if republishing an article from a serial	12
Volume of serial or monograph	167	Publication date of portion	2020-08-07
Page or page range of portion	1-9		

RIGHTSHOLDER TERMS AND CONDITIONS

These special terms and conditions are in addition to the standard terms and conditions for CCC's Republication Service and, together with those standard terms and conditions, govern the use of the Works. As the User you will make all reasonable efforts to contact the author(s) of the article which the Work is to be reused from, to seek consent for your intended use. Contacting one author who is acting expressly as authorised agent for their co-author(s) is acceptable. User will reproduce the following wording prominently alongside the Work: the source of the Work, including author, article title, title of journal, volume number, issue number (if relevant), page range (or first page if this is the only information available) and date of first publication; and a link back to the article (via DOI); and if practicable, and IN ALL CASES for new works published under any of the Creative Commons licences, the words "© The Electrochemical Society. Reproduced by permission of IOP Publishing Ltd. All rights reserved" Without the express permission of the author(s) and the Rightsholder of the article from which the Work is to be reused, User shall not use it in any way which, in the opinion of IOP Publishing Ltd, could: (i) distort or alter the author(s)' original intention(s) and meaning; (ii) be prejudicial to the honour or reputation of the author(s); and/or (iii) imply endorsement by the author(s) and/or the Rightsholder and/or IOP Publishing Ltd. This licence does not apply to any article which is credited to another source and which does not have the copyright line '© The Electrochemical Society'. User must check the copyright line of the article from which the Work is to be reused to check that the Electrochemical Society and IOP Publishing Ltd has all the necessary rights to be able to grant permission. User is solely responsible for identifying and obtaining separate licences and permissions from the copyright owner for reuse of any such third party material/figures which the Rightsholder is not the copyright owner of. The Rightsholder shall not reimburse any fees which User pays for a republication license for such third party content. This licence does not apply to any material/figure which is credited to another source in the Rightsholder's publication or has been obtained from a third party. User must check the Version of Record of the article from which the Work is to be reused, to check whether any of the material in the Work is third party material. Third party citations and/or copyright notices and/or permissions statements may not be included in any other version of the article from which the Work is to be reused and so cannot be relied upon by the User. User is solely responsible for identifying and obtaining separate licences and permissions from the copyright owner for reuse of any such third party material/figures where the Rightsholder is not the copyright owner. The Rightsholder shall not reimburse any fees which User pays for a republication license for such third party content. User and CCC acknowledge that IOP Publishing Ltd and/or the Rightsholder may, from time to time, make changes or additions to these special terms and conditions without express notification, provided that these shall not apply to permissions already secured and paid for by User prior to such change or addition. User acknowledges that the Rightsholder and IOP Publishing Ltd (which includes companies within its group and third parties for whom it publishes its titles) may make use of personal data collected through the service in the course of their business. If User is the author of the Work, User may automatically have the right to reuse it under the rights granted back when User transferred the copyright in the article to the Rightsholder. User should check the copyright form and the relevant author rights policy to check whether permission is required. If User is the author of the Work and does require permission for proposed reuse of the Work, User should select 'Author of requested content' as the Requestor Type. The Rightsholder shall not reimburse any fees which User pays for a republication license. If User is the author of the article which User wishes to reuse in User's thesis or dissertation, the republication licence covers the right to include the Version of Record of the article, provided it is not then published commercially. User must include citation details and, for online use, a link to the Version of Record of the article on the IOPscience website. User may need to obtain separate permission for any third party content included within the article. User must check this with the copyright owner of such third party content. User may not include the article in a thesis or dissertation which is published by ProQuest. Any other commercial use of User's thesis or dissertation containing the article would also need to be expressly notified in writing to the Rightsholder at the time of request and would require separate written permission from the Rightsholder. As well as CCC, the Rightsholder and IOP Publishing Ltd shall have the right to bring any legal action that they deem necessary to enforce their rights should they consider that the Work infringes those rights in any way. For content reuse requests that qualify for permission under the STM Permissions

Guidelines, which may be updated from time to time, the STM Permissions Guidelines supplement the terms and conditions contained in this license.

SPECIAL RIGHTSHOLDER TERMS AND CONDITIONS

When you transferred the copyright in your article to The Electrochemical Society you were granted back certain rights, including the right to include the Final Published Version of the article within any thesis or dissertation. Please note you may need to obtain separate permission for any third party content you included within your article. Please include citation details, "© The Electrochemical Society. Reproduced with permission. All rights reserved" and for online use, a link to the Version of Record. The only restriction is that if, at a later date, you wanted your thesis/dissertation to be published commercially, further permission would be required.

Marketplace Order General Terms and Conditions

The following terms and conditions ("General Terms"), together with any applicable Publisher Terms and Conditions, govern User's use of Works pursuant to the Licenses granted by Copyright Clearance Center, Inc. ("CCC") on behalf of the applicable Rightsholders of such Works through CCC's applicable Marketplace transactional licensing services (each, a "Service").

1) Definitions. For purposes of these General Terms, the following definitions apply:

"License" is the licensed use the User obtains via the Marketplace platform in a particular licensing transaction, as set forth in the Order Confirmation.

"Order Confirmation" is the confirmation CCC provides to the User at the conclusion of each Marketplace transaction. "Order Confirmation Terms" are additional terms set forth on specific Order Confirmations not set forth in the General Terms that can include terms applicable to a particular CCC transactional licensing service and/or any Rightsholder-specific terms.

"Rightsholder(s)" are the holders of copyright rights in the Works for which a User obtains licenses via the Marketplace platform, which are displayed on specific Order Confirmations.

"Terms" means the terms and conditions set forth in these General Terms and any additional Order Confirmation Terms collectively.

"User" or "you" is the person or entity making the use granted under the relevant License. Where the person accepting the Terms on behalf of a User is a freelancer or other third party who the User authorized to accept the General Terms on the User's behalf, such person shall be deemed jointly a User for purposes of such Terms.

"Work(s)" are the copyright protected works described in relevant Order Confirmations.

2) Description of Service. CCC's Marketplace enables Users to obtain Licenses to use one or more Works in accordance with all relevant Terms. CCC grants Licenses as an agent on behalf of the copyright rightsholder identified in the relevant Order Confirmation.

3) Applicability of Terms. The Terms govern User's use of Works in connection with the relevant License. In the event of any conflict between General Terms and Order Confirmation Terms, the latter shall govern. User acknowledges that Rightsholders have complete discretion whether to grant any permission, and whether to place any limitations on any grant, and that CCC has no right to supersede or to modify any such discretionary act by a Rightsholder.

4) Representations; Acceptance. By using the Service, User represents and warrants that User has been duly authorized by the User to accept, and hereby does accept, all Terms.

5) Scope of License; Limitations and Obligations. All Works and all rights therein, including copyright rights, remain the sole and exclusive property of the Rightsholder. The License provides only those rights expressly set forth in the terms and conveys no other rights in any Works

6) General Payment Terms. User may pay at time of checkout by credit card or choose to be invoiced. If the User chooses to be invoiced, the User shall: (i) remit payments in the manner identified on specific invoices, (ii) unless otherwise specifically stated in an Order Confirmation or separate written agreement, Users shall remit payments upon receipt of the relevant invoice from CCC, either by delivery or notification of availability of the invoice via the Marketplace platform, and (iii) if the User does not pay the invoice within 30 days of receipt, the User may incur a service charge of 1.5% per

month or the maximum rate allowed by applicable law, whichever is less. While User may exercise the rights in the License immediately upon receiving the Order Confirmation, the License is automatically revoked and is null and void, as if it had never been issued, if CCC does not receive complete payment on a timely basis.

7) General Limits on Use. Unless otherwise provided in the Order Confirmation, any grant of rights to User (i) involves only the rights set forth in the Terms and does not include subsequent or additional uses, (ii) is non-exclusive and non-transferable, and (iii) is subject to any and all limitations and restrictions (such as, but not limited to, limitations on duration of use or circulation) included in the Terms. Upon completion of the licensed use as set forth in the Order Confirmation, User shall either secure a new permission for further use of the Work(s) or immediately cease any new use of the Work(s) and shall render inaccessible (such as by deleting or by removing or severing links or other locators) any further copies of the Work. User may only make alterations to the Work if and as expressly set forth in the Order Confirmation. No Work may be used in any way that is defamatory, violates the rights of third parties (including such third parties' rights of copyright, privacy, publicity, or other tangible or intangible property), or is otherwise illegal, sexually explicit, or obscene. In addition, User may not conjoin a Work with any other material that may result in damage to the reputation of the Rightsholder. User agrees to inform CCC if it becomes aware of any infringement of any rights in a Work and to cooperate with any reasonable request of CCC or the Rightsholder in connection therewith.

8) Third Party Materials. In the event that the material for which a License is sought includes third party materials (such as photographs, illustrations, graphs, inserts and similar materials) that are identified in such material as having been used by permission (or a similar indicator), User is responsible for identifying, and seeking separate licenses (under this Service, if available, or otherwise) for any of such third party materials; without a separate license, User may not use such third party materials via the License.

9) Copyright Notice. Use of proper copyright notice for a Work is required as a condition of any License granted under the Service. Unless otherwise provided in the Order Confirmation, a proper copyright notice will read substantially as follows: "Used with permission of [Rightsholder's name], from [Work's title, author, volume, edition number and year of copyright]; permission conveyed through Copyright Clearance Center, Inc." Such notice must be provided in a reasonably legible font size and must be placed either on a cover page or in another location that any person, upon gaining access to the material which is the subject of a permission, shall see, or in the case of republication Licenses, immediately adjacent to the Work as used (for example, as part of a by-line or footnote) or in the place where substantially all other credits or notices for the new work containing the republished Work are located. Failure to include the required notice results in loss to the Rightsholder and CCC, and the User shall be liable to pay liquidated damages for each such failure equal to twice the use fee specified in the Order Confirmation, in addition to the use fee itself and any other fees and charges specified.

10) Indemnity. User hereby indemnifies and agrees to defend the Rightsholder and CCC, and their respective employees and directors, against all claims, liability, damages, costs, and expenses, including legal fees and expenses, arising out of any use of a Work beyond the scope of the rights granted herein and in the Order Confirmation, or any use of a Work which has been altered in any unauthorized way by User, including claims of defamation or infringement of rights of copyright, publicity, privacy, or other tangible or intangible property.

11) Limitation of Liability. UNDER NO CIRCUMSTANCES WILL CCC OR THE RIGHTSHOLDER BE LIABLE FOR ANY DIRECT, INDIRECT, CONSEQUENTIAL, OR INCIDENTAL DAMAGES (INCLUDING WITHOUT LIMITATION DAMAGES FOR LOSS OF BUSINESS PROFITS OR INFORMATION, OR FOR BUSINESS INTERRUPTION) ARISING OUT OF THE USE OR INABILITY TO USE A WORK, EVEN IF ONE OR BOTH OF THEM HAS BEEN ADVISED OF THE POSSIBILITY OF SUCH DAMAGES. In any event, the total liability of the Rightsholder and CCC (including their respective employees and directors) shall not exceed the total amount actually paid by User for the relevant License. User assumes full liability for the actions and omissions of its principals, employees, agents, affiliates, successors, and assigns.

12) Limited Warranties. THE WORK(S) AND RIGHT(S) ARE PROVIDED "AS IS." CCC HAS THE RIGHT TO GRANT TO USER THE RIGHTS GRANTED IN THE ORDER CONFIRMATION DOCUMENT. CCC AND THE RIGHTSHOLDER DISCLAIM ALL OTHER WARRANTIES RELATING TO THE WORK(S) AND RIGHT(S), EITHER EXPRESS OR IMPLIED, INCLUDING WITHOUT LIMITATION IMPLIED WARRANTIES OF MERCHANTABILITY OR FITNESS FOR A PARTICULAR PURPOSE. ADDITIONAL RIGHTS MAY BE REQUIRED TO USE ILLUSTRATIONS, GRAPHS, PHOTOGRAPHS, ABSTRACTS, INSERTS, OR OTHER PORTIONS OF THE WORK (AS OPPOSED TO THE ENTIRE WORK) IN A MANNER CONTEMPLATED BY USER; USER UNDERSTANDS AND AGREES THAT NEITHER CCC NOR THE RIGHTSHOLDER MAY HAVE SUCH ADDITIONAL RIGHTS TO GRANT.

13) Effect of Breach. Any failure by User to pay any amount when due, or any use by User of a Work beyond the scope of the License set forth in the Order Confirmation and/or the Terms, shall be a material breach of such License. Any breach not cured within 10 days of written notice thereof shall result in immediate termination of such License without further notice. Any unauthorized (but licensable) use of a Work that is terminated immediately upon notice thereof may be

liquidated by payment of the Rightsholder's ordinary license price therefor; any unauthorized (and unlicensable) use that is not terminated immediately for any reason (including, for example, because materials containing the Work cannot reasonably be recalled) will be subject to all remedies available at law or in equity, but in no event to a payment of less than three times the Rightsholder's ordinary license price for the most closely analogous licensable use plus Rightsholder's and/or CCC's costs and expenses incurred in collecting such payment.

14) Additional Terms for Specific Products and Services. If a User is making one of the uses described in this Section 14, the additional terms and conditions apply:

a) *Print Uses of Academic Course Content and Materials (photocopies for academic coursepacks or classroom handouts).* For photocopies for academic coursepacks or classroom handouts the following additional terms apply:

i) The copies and anthologies created under this License may be made and assembled by faculty members individually or at their request by on-campus bookstores or copy centers, or by off-campus copy shops and other similar entities.

ii) No License granted shall in any way: (i) include any right by User to create a substantively non-identical copy of the Work or to edit or in any other way modify the Work (except by means of deleting material immediately preceding or following the entire portion of the Work copied) (ii) permit "publishing ventures" where any particular anthology would be systematically marketed at multiple institutions.

iii) Subject to any Publisher Terms (and notwithstanding any apparent contradiction in the Order Confirmation arising from data provided by User), any use authorized under the academic pay-per-use service is limited as follows:

A) any License granted shall apply to only one class (bearing a unique identifier as assigned by the institution, and thereby including all sections or other subparts of the class) at one institution;

B) use is limited to not more than 25% of the text of a book or of the items in a published collection of essays, poems or articles;

C) use is limited to no more than the greater of (a) 25% of the text of an issue of a journal or other periodical or (b) two articles from such an issue;

D) no User may sell or distribute any particular anthology, whether photocopied or electronic, at more than one institution of learning;

E) in the case of a photocopy permission, no materials may be entered into electronic memory by User except in order to produce an identical copy of a Work before or during the academic term (or analogous period) as to which any particular permission is granted. In the event that User shall choose to retain materials that are the subject of a photocopy permission in electronic memory for purposes of producing identical copies more than one day after such retention (but still within the scope of any permission granted), User must notify CCC of such fact in the applicable permission request and such retention shall constitute one copy actually sold for purposes of calculating permission fees due; and

F) any permission granted shall expire at the end of the class. No permission granted shall in any way include any right by User to create a substantively non-identical copy of the Work or to edit or in any other way modify the Work (except by means of deleting material immediately preceding or following the entire portion of the Work copied).

iv) Books and Records; Right to Audit. As to each permission granted under the academic pay-per-use Service, User shall maintain for at least four full calendar years books and records sufficient for CCC to determine the numbers of copies made by User under such permission. CCC and any representatives it may designate shall have the right to audit such books and records at any time during User's ordinary business hours, upon two days' prior notice. If any such audit shall determine that User shall have underpaid for, or underreported, any photocopies sold or by three percent (3%) or more, then User shall bear all the costs of any such audit; otherwise, CCC shall bear the costs of any such audit. Any amount determined by such audit to have been underpaid by User shall immediately be paid to CCC by User, together with interest thereon at the rate of 10% per annum from the date such amount was originally due. The provisions of this paragraph shall survive the termination of this License for any reason.

b) *Digital Pay-Per-Uses of Academic Course Content and Materials (e-coursepacks, electronic reserves, learning management systems, academic institution intranets).* For uses in e-coursepacks, posts in electronic reserves, posts

in learning management systems, or posts on academic institution intranets, the following additional terms apply:

i) The pay-per-uses subject to this Section 14(b) include:

A) Posting e-reserves, course management systems, e-coursepacks for text-based content, which grants authorizations to import requested material in electronic format, and allows electronic access to this material to members of a designated college or university class, under the direction of an instructor designated by the college or university, accessible only under appropriate electronic controls (e.g., password);

B) Posting e-reserves, course management systems, e-coursepacks for material consisting of photographs or other still images not embedded in text, which grants not only the authorizations described in Section 14(b)(i)(A) above, but also the following authorization: to include the requested material in course materials for use consistent with Section 14(b)(i)(A) above, including any necessary resizing, reformatting or modification of the resolution of such requested material (provided that such modification does not alter the underlying editorial content or meaning of the requested material, and provided that the resulting modified content is used solely within the scope of, and in a manner consistent with, the particular authorization described in the Order Confirmation and the Terms), but not including any other form of manipulation, alteration or editing of the requested material;

C) Posting e-reserves, course management systems, e-coursepacks or other academic distribution for audiovisual content, which grants not only the authorizations described in Section 14(b)(i)(A) above, but also the following authorizations: (i) to include the requested material in course materials for use consistent with Section 14(b)(i)(A) above; (ii) to display and perform the requested material to such members of such class in the physical classroom or remotely by means of streaming media or other video formats; and (iii) to "clip" or reformat the requested material for purposes of time or content management or ease of delivery, provided that such "clipping" or reformatting does not alter the underlying editorial content or meaning of the requested material and that the resulting material is used solely within the scope of, and in a manner consistent with, the particular authorization described in the Order Confirmation and the Terms. Unless expressly set forth in the relevant Order Conformation, the License does not authorize any other form of manipulation, alteration or editing of the requested material.

ii) Unless expressly set forth in the relevant Order Confirmation, no License granted shall in any way: (i) include any right by User to create a substantively non-identical copy of the Work or to edit or in any other way modify the Work (except by means of deleting material immediately preceding or following the entire portion of the Work copied or, in the case of Works subject to Sections 14(b)(1)(B) or (C) above, as described in such Sections) (ii) permit "publishing ventures" where any particular course materials would be systematically marketed at multiple institutions.

iii) Subject to any further limitations determined in the Rightsholder Terms (and notwithstanding any apparent contradiction in the Order Confirmation arising from data provided by User), any use authorized under the electronic course content pay-per-use service is limited as follows:

A) any License granted shall apply to only one class (bearing a unique identifier as assigned by the institution, and thereby including all sections or other subparts of the class) at one institution;

B) use is limited to not more than 25% of the text of a book or of the items in a published collection of essays, poems or articles;

C) use is limited to not more than the greater of (a) 25% of the text of an issue of a journal or other periodical or (b) two articles from such an issue;

D) no User may sell or distribute any particular materials, whether photocopied or electronic, at more than one institution of learning;

E) electronic access to material which is the subject of an electronic-use permission must be limited by means of electronic password, student identification or other control permitting access solely to students and instructors in the class;

F) User must ensure (through use of an electronic cover page or other appropriate means) that any person, upon gaining electronic access to the material, which is the subject of a permission, shall see:

○ a proper copyright notice, identifying the Rightsholder in whose name CCC has granted permission,

- a statement to the effect that such copy was made pursuant to permission,

- a statement identifying the class to which the material applies and notifying the reader that the material has been made available electronically solely for use in the class, and

- a statement to the effect that the material may not be further distributed to any person outside the class, whether by copying or by transmission and whether electronically or in paper form, and User must also ensure that such cover page or other means will print out in the event that the person accessing the material chooses to print out the material or any part thereof.

G) any permission granted shall expire at the end of the class and, absent some other form of authorization, User is thereupon required to delete the applicable material from any electronic storage or to block electronic access to the applicable material.

iv) Uses of separate portions of a Work, even if they are to be included in the same course material or the same university or college class, require separate permissions under the electronic course content pay-per-use Service. Unless otherwise provided in the Order Confirmation, any grant of rights to User is limited to use completed no later than the end of the academic term (or analogous period) as to which any particular permission is granted.

v) Books and Records; Right to Audit. As to each permission granted under the electronic course content Service, User shall maintain for at least four full calendar years books and records sufficient for CCC to determine the numbers of copies made by User under such permission. CCC and any representatives it may designate shall have the right to audit such books and records at any time during User's ordinary business hours, upon two days' prior notice. If any such audit shall determine that User shall have underpaid for, or underreported, any electronic copies used by three percent (3%) or more, then User shall bear all the costs of any such audit; otherwise, CCC shall bear the costs of any such audit. Any amount determined by such audit to have been underpaid by User shall immediately be paid to CCC by User, together with interest thereon at the rate of 10% per annum from the date such amount was originally due. The provisions of this paragraph shall survive the termination of this license for any reason.

c) *Pay-Per-Use Permissions for Certain Reproductions (Academic photocopies for library reserves and interlibrary loan reporting) (Non-academic internal/external business uses and commercial document delivery).* The License expressly excludes the uses listed in Section (c)(i)-(v) below (which must be subject to separate license from the applicable Rightsholder) for: academic photocopies for library reserves and interlibrary loan reporting; and non-academic internal/external business uses and commercial document delivery.

i) electronic storage of any reproduction (whether in plain-text, PDF, or any other format) other than on a transitory basis;

ii) the input of Works or reproductions thereof into any computerized database;

iii) reproduction of an entire Work (cover-to-cover copying) except where the Work is a single article;

iv) reproduction for resale to anyone other than a specific customer of User;

v) republication in any different form. Please obtain authorizations for these uses through other CCC services or directly from the rightsholder.

Any license granted is further limited as set forth in any restrictions included in the Order Confirmation and/or in these Terms.

d) *Electronic Reproductions in Online Environments (Non-Academic-email, intranet, internet and extranet).* For "electronic reproductions", which generally includes e-mail use (including instant messaging or other electronic transmission to a defined group of recipients) or posting on an intranet, extranet or Intranet site (including any display or performance incidental thereto), the following additional terms apply:

i) Unless otherwise set forth in the Order Confirmation, the License is limited to use completed within 30 days for any use on the Internet, 60 days for any use on an intranet or extranet and one year for any other use, all as measured from the "republication date" as identified in the Order Confirmation, if any, and otherwise from the date of the Order Confirmation.

ii) User may not make or permit any alterations to the Work, unless expressly set forth in the Order Confirmation

(after request by User and approval by Rightsholder); provided, however, that a Work consisting of photographs or other still images not embedded in text may, if necessary, be resized, reformatted or have its resolution modified without additional express permission, and a Work consisting of audiovisual content may, if necessary, be "clipped" or reformatted for purposes of time or content management or ease of delivery (provided that any such resizing, reformatting, resolution modification or "clipping" does not alter the underlying editorial content or meaning of the Work used, and that the resulting material is used solely within the scope of, and in a manner consistent with, the particular License described in the Order Confirmation and the Terms.

15) Miscellaneous.

a) User acknowledges that CCC may, from time to time, make changes or additions to the Service or to the Terms, and that Rightsholder may make changes or additions to the Rightsholder Terms. Such updated Terms will replace the prior terms and conditions in the order workflow and shall be effective as to any subsequent Licenses but shall not apply to Licenses already granted and paid for under a prior set of terms.

b) Use of User-related information collected through the Service is governed by CCC's privacy policy, available online at www.copyright.com/about/privacy-policy/.

c) The License is personal to User. Therefore, User may not assign or transfer to any other person (whether a natural person or an organization of any kind) the License or any rights granted thereunder; provided, however, that, where applicable, User may assign such License in its entirety on written notice to CCC in the event of a transfer of all or substantially all of User's rights in any new material which includes the Work(s) licensed under this Service.

d) No amendment or waiver of any Terms is binding unless set forth in writing and signed by the appropriate parties, including, where applicable, the Rightsholder. The Rightsholder and CCC hereby object to any terms contained in any writing prepared by or on behalf of the User or its principals, employees, agents or affiliates and purporting to govern or otherwise relate to the License described in the Order Confirmation, which terms are in any way inconsistent with any Terms set forth in the Order Confirmation, and/or in CCC's standard operating procedures, whether such writing is prepared prior to, simultaneously with or subsequent to the Order Confirmation, and whether such writing appears on a copy of the Order Confirmation or in a separate instrument.

e) The License described in the Order Confirmation shall be governed by and construed under the law of the State of New York, USA, without regard to the principles thereof of conflicts of law. Any case, controversy, suit, action, or proceeding arising out of, in connection with, or related to such License shall be brought, at CCC's sole discretion, in any federal or state court located in the County of New York, State of New York, USA, or in any federal or state court whose geographical jurisdiction covers the location of the Rightsholder set forth in the Order Confirmation. The parties expressly submit to the personal jurisdiction and venue of each such federal or state court.